Gold Nanorod based Nanoprobes for Biomedical Applications

A Thesis submitted to the University of Strathclyde for the degree of Doctor of Philosophy

By

Zendesha Stephen Mbalaha

Photophysics Research Group

Department of Physics

University of Strathclyde

Glasgow

2020

‘This thesis is the result of the author’s original research. It has been composed by the author and has not been previously submitted for examination which has led to the award of a degree.’

Signed:

Date:

Abstract

Small gold nanorods (SGNRs) are nanorods that are ~13-50 nm in length and less than 10 nm in diameter. The SGNRs manifest excellent optical properties arising from localised surface plasmon resonance including strong optical absorption and scattering tunable from the visible to the infrared region of electromagnetic spectrum. The SGNRs have higher absorption to scattering ratio compared to the large gold nanorods (LGNRs), making the SGNRs good photothermal agents. Moreover, the SGNRs have ease of subcellular accessibility, high internalization rate and large surface area to volume ratio for binding of analytes. These attributes make the SGNRs good candidates in various biomedical applications such as biosensing, imaging and delivery of drugs. This study is aimed at developing gold nanorod based nanoprobes for detecting molecular biomarkers at the single cell level, and characterization of the optical properties and the photothermal effects of gold nanorods for photothermal therapy of cancer.

A systematic study on the growth conditions was carried out and a reliable method has been developed for the synthesis of stable SGNRs with good control over size and shape, and high yield of rods. The SGNRs were successfully functionalized with hairpin DNA (hpDNA) for targeting messenger RNA (mRNA).

Moreover, this work investigated the influence of gold nanorods size and media on their photothermal effect. Theoretical calculation revealed that the SGNRs have higher photothermal efficiency than the LGNRs in solution. However, in solution the SGNRs generated slightly more heat at off-resonance illumination while the LGNRs generated more heat than SGNRs at plasmon resonance excitation. Nevertheless, the experimental study revealed that the SGNRs generated more heat than the LGNRs when both are in gel media that is close to cell enviroment. Furthermore, aptamer functionalized SGNRs nanoprobes were developed for targeting cancer cells. The SGNRs based nanoprobes were found to have higher photothermal effect in cancer cells compared to the LGNRs nanoprobes.

In addition, the SGNR based nanoprobes were found to be more sensitive than the LGNR based nanoprobes in detecting RNA cancer biomarkers in cells and exosomes.

This work demonstrates the capability of the gold nanorod based nanoprobes in detecting the cancer biomarker RNA in a blood serum.

Acknowledgements

I give thanks to the almighty God for sustaining me through the period of my study at the University of Strathclyde Glasgow, Scotland, United Kingdom. I remain very grateful to my supervisors, Dr. Yu Chen and Prof. David J. S. Birch for their encouragement, support, advice and inputs in making my study a reality. I also thank Dr. Jun Yu for his assistance. My appreciation goes to my wife, Iveren Agatha Mbalaha and my kids, Ngukuran Josephine Zendesha, Tordue David Zendesha, Myom Michelle Zendesha and Senajighjigh Daniel Zendesha for your prayers and moral support. I also appreciate my parents and siblings for the support given to me.

I would like to acknowledge the Federal University of Agriculture, Makurdi, Nigeria for sponsoring me to undertake a PhD study at the University of Strathclyde, Glasgow, Scotland, United Kingdom. This opportunity has made a significant positive difference in my professional career. In appreciation, I acknowledge hardship support fund from the University of Strathclyde Glasgow and Rank Prize Funds.

In addition, I would like to acknowledge Intisar Albanda, Dr. Ben Russell, Dr. Davy Alastair, Nora Alkudaisi, Natakorn Sapermsap, friends, well-wishers and others too numerous to mention for their assistance. I thank you all immensely.

List of Publication

1. Mbalaha, Z. S.; Edwards, P. R.; Birch, D. J. S.; Chen, Y., Synthesis of Small Gold Nanorods and Their Subsequent Functionalization with Hairpin Single Stranded DNA. *ACS Omega* **2019,** *4* (9), 13740-13746.

Papers in preparation.

1. Mbalaha, Z. S. et al. A study of the localised surface plasmon resonance and photothermal effects of small gold nanorods in agarose gel media.

2. Mbalaha, Z. S. et al. Targeting EpCAM over-expressed cancer cells with SYL3C aptamer functionalized small gold nanorods nanoprobes.

3. Mbalaha, Z. S. et al. Detection of NEAR1 biomaker in biological systems with small gold nanorods based nanoprobes.

4. Mbalaha, Z. S. et al. Size effect of the spectral and photophysical properties of Cy5-labelled gold nanorod based RNA nanoprobes: Implication for detecting exosome-derived mRNA.

Poster presentation

Small gold nanorod based SYL3C-aptamer nanoprobes for photothermal therapy of cancer being a poster presented at the 3rd Postgraduate Institute Conference held at the University of Strathclyde, Glasgow between 23-24th October 2018.

Abbreviations

AA- Ascorbic acid

AFM- Atomic force microscope

$AgNO_3$- Silver nitrate

AR- Androgen receptor

BSA- Bovine serum albumin

BSE- Backscatter electron

cDNA- Complementary DNA

CT- X-ray computed tomography

CTAB- Hexadecyltrimethylammonium bromide

Cy3- Cyanine 3

Cy5- Cyanine 5

DAPI-4', 6-Diamidine-2'-phenylindole

DDT- Dodecanethiol

DFM- Dark field microscopy

DNA- Deoxyribonucleic acid

DMEM- Dubecco's modified eagle's medium

DMF- N, N-dimethylformamide

DOX- Doxorubicin

ELISA- Enzyme-link immune sorbent assay

EpCAM- Epithelia cell adhesion molecule

FBS- Foetal bovine serum

FITC- Fluorescein isothiocynate

FLIM- Fluorescence lifetime imaging

FRET- Förster resonance energy transfer

FSC- Forward scatter

GNRs- Gold nanorods

$HAuCl_4$- Tetrachloroauric acid

HCl- Hydrochloric acid

HIV- Human immunodeficiency virus

hpDNA- Hairpin DNA

IRF- Instrument response function

LGNRs- Large GNRs

LSPR-Longitudinal surface plasmon resonance

MHA- Mercaptohexanoic acid

miRNA- Micro RNA

mRNA- Messenger RNA

$NaBH_4$- Sodium borohydride

NaCl- Sodium chloride

NEAR1- Neuroendocrine long non-coding RNA

NEPC- Neuroendocrine prostate cancer

NIR- Near infrared

NTA- Nanoparticle tracking analysis

OCT- Optical coherence tomography

PAT- Photoacoustic tomography

PBS- Phosphate buffered saline

PEG- Polyethylene glycol

PH- Potential of hydrogen

PSA- Prostate specific antigen

PVP- Polyyinylpyrrolidone

RNA- Ribonucleic acid

SE- Secondary electron

SEM –Scanning electron microscope

SELEX- Systematic evolution of ligands by exponential enrichment

SERS- Surface enhanced Raman scattering

SGNRs- Small GNRs

SiO_2- Silicon dioxide

SSC- Side scatter

ssDNA- Single strand DNA

TBE- Tris/Borate/ EDTA

TCEP- Tris (2-carboxyethyl) phosphine hydrochloride

TCAB- Tetradodecylammonium bromide

TCSPC- Time correlated single photon count

TDAB- Tetrakis (decyl)ammoniumbromide

TE- Tris EDTA

TPL- Two photon luminescence

TSPR- Transverse surface plasmon resonance

UV- Ultra-violet

WHO- World health organisation

Table of content

List of figures

List of Tables

Chapter 1

Introduction

1. 1. Aims and objectives

Gold nanorods have great potential in biomedical applications because of their biocompatibility, accessibility, chemical functionality and unique optical properties due to localised surface plasmons resonance. The aims and objectives of this study are to develop gold nanorods based nanoprobes for detecting molecular biomarkers at the single cell level, and characterize the optical properties and the photothermal effects of gold nanorods for photothermal therapy of cancer.

1. 2. Background

Cancer is one of the major causes of mortality in both developed and underdeveloped countries[1-2] due to late diagnosis[3-4], resistance to drugs and hormonal therapies[5] and re-occurrence of cancer due to residual tumour cells after surgery. In addition, some cancers such as oesophagus cancer are asymptomatic and can be detected very late after spreading beyond the oesophageal wall leading to approximately a 90% mortality rate[3, 6]. Moreover, the conventional screening methods for oesophagus cancer include cytology examination and endoscopy with mucosal iodine staining[3]. Cytology examination for example, can be very uncomfortable while endoscopy can cause bleeding and triggers an allergic reaction due to iodine staining[3]. These screening methods are generally expensive and lack the sensitivity to detect oesophagus cancer at the early stage[3]. Attempts to diagnose other forms of cancers such as neuroendocrine prostate cancer (NEPC) at the early stage have been challenging because the current screening methods (androgen receptor, AR and

prostate specific antigen, PSA tests) lack the specificity and sensitivity to detect NEPC at the early stage[4]. Furthermore, NEPC does not express AR nor PSA biomarkers making the diagnosis of NEPC very challenging. Furthermore, both the normal and the cancerous prostate cells express PSA; and an elevated PSA level does not necessarily implicate prostate cancer[7]. For example, prostatisis or urinary tract infection could induce an elevated PSA levels[8]. Moreover, a PSA test is susceptible to false positive or false negative results[8]. This obligates the use of other tests (e.g. transrectal ultrasound, x-ray and cystoscopy) to make informed prognosis[9]. The delay in conducting further tests to establish a prima facie case of prostate cancer could exacerbate the morbidity of the patient leading to death. Attempts to treat cancer through conventional means (surgery, chemotherapy and radiation therapy) have been challenging due to lack of sensitivity to discriminate between the cancerous and the non-cancerous cells, numerous side effects on the healthy cells leading to the death of the patients[2-3, 10]. This requires new techniques to enable sensitive and facile detection of cancer biomarkers and high efficacious therapy. Metal nanoparticles have demonstrated to be good candidates for screening and treatment of cancer because of their fascinating optical properties, high internalization rate, deep tissue penetration and biocompatibility with the biological systems[1, 11-13].

1. 3. Metal nanoparticles

Metal nanoparticles have gained attention in nanotechnology because of their utilization in catalysis, photonics, information storage, optoelectronics and biomedical applications[14-17]. Metal nanoparticles are nanoscale nanomaterials made from metal elements with at least one dimension in the range of 3-100 nm[18-19]. Nanoscale particles are of great interest in nanotechnology due to their unique size, shape, electrical, thermal,

magnetic and optical properties[20]. The size and shape of metal nanoparticles for example, are essential parameters in both synthesis and applications[21-22]. Examples of metal nanoparticles include zinc, cerium, titanium, and iron, [20, 23-24].

1. 3. 1. Noble metal nanoparticles

Noble metals nanoparticles are nanomaterials developed from noble metals and these include platinum, silver and gold nanoparticles. Noble metal nanoparticles are uniquely different from other metal nanoparticles because they exhibit the surface plasmons resonance (SPR) effect[18].

1. 3. 2. Bulk plasmons in metals and surface plasmons resonance in noble metal nanoparticles

Plasmons are collective oscillations of free conducting electrons in metals and metal nanoparticles[25-26]. Metals are 3-dimensional (3D) bulk structures with no confinement of electrons. Because the metallic electrons can move freely in 3 dimensions, the interaction of a metal with incident light results in an incoherent oscillations of the free conduction electrons, out of resonance with the wavelength of incident light leading to a faster collision with the lattice; thus, incident light is prevented from penetrating the depth of the metal. The incoherent oscillations of free conduction electrons along the bulk of a metal can thus be described as bulk plasmons. On the other hand, metal nanoparticles are 1-dimensional (1D) nanostructures with electron confinement in two directions. Because of the electron confinement effects, the optical properties of a metal nanoparticle are uniquely different from that of the bulk metal. Thus, surface plasmons can be described as the coherent oscillations of the free conduction electrons at the interface between the surface of a metal nanoparticle and dielectric medium in resonance with the wavelength of incident light[18, 26-27]. Because the oscillations of the free electrons are confined to the surface of a noble metal nanoparticle, hence the term localised surface plasmon resonance. The interaction of the noble metal nanoparticles with the incident light induces local electric field to the metal nanoparticles forcing the free electrons to separate from

the lattice structure[18]. The coherent oscillations of free electrons of noble metal nanoparticles in resonance with incident light leads to strong optical absorption and scattering of light[18]. Surface plasmon resonance in noble metal nanoparticles occurs only if the size of the nanoparticle is > 2 nm, smaller than the wavelength of incident light; and the frequency of the oscillating electrons must be in resonance with the frequency of incident light[22].

1. 4. Gold nanoparticles

Gold nanoparticles are nanomaterials fabricated from a precursor gold metal. Gold nanoparticles are preferred over other noble metal nanoparticles because the gold nanoparticles are non-toxic, chemically unreactive, good quenchers of fluorescence and biocompatible with biological systems[29-30]. The gold nanoparticles are particularly utilized in nanotechnology due their superior absorption and scattering properties when irradiated by an electromagnetic wave source[12-13, 31-34]. There are different types of gold nanoparticles and these include nanoshells, nanocages, nanocubes, nanostars, , nanospheres, and nanorods[1, 35].

1. 4. 1. Gold nanoshells

Gold nanoshells are 100-200 nm sized spherical nanoparticles with dielectric cores shielded by a metallic gold shell[36-37]. Gold nanoshells were fabricated by Halas and co-workers in 2003[38]. They are good contrast agents for imaging due to their large extinction cross section. They exhibit a single peak localized surface plasmon resonance from the visible to the near infrared wavelengths of the electromagnetic spectrum. Gold nanoshells are known to be tunable, photostable and non-cytotoxic[36]. These attributes render gold nanoshells very useful in cancer diagnosis, therapy, imaging and medical biosensing. In addition, gold nanoshells can be used as vehicle for delivery of drugs and enzymes[12].

1. 4. 2. Gold nanocages

Gold nanocages are hollow and porous nanosystems fabricated by Xia and co-workers[39]. Gold nanocages are typically 20-50 nm in size[39-40]. Gold nanocages can be synthesized by creating a silver nanoparticle template which can be replaced by gold[12, 40]. Gold nanocages have a single absorption peak that lies 400-1000 nm[41]. Gold nanocages have demonstrated photothermal effect in mice model infected with cancer cells[12].

1. 4. 3. Gold nanocubes

Gold nanocubes are cube-like nanostructures with tunable surface plasmon resonance from the visible to the infrared wavelengths of the electromagnetic spectrum. Typically, the size of gold nanocubes lies between 13- 80 nm[42]. Gold nanocubes can be synthesized by a three steps approach. These include preparing the gold seeds which are further grown sequentially by two growth solutions[42].

1. 4. 4. Gold nanostars

Gold nanostars are anisotropic gold nanoparticles with multiple sharp tips. The multiple tips enhance local field around the nanostars[43]. The surface plasmon resonance of gold nanostars can be tuned from the visible to the infrared wavelengths of the electromagnetic spectrum by adjusting the length of the tips, increasing the density and distance between the gold nanostars[43]. Gold nanostars can be synthesized by the seeded growth method[44]. The preformed gold seeds coated with polyvinylpyrrolidone (PVP) solution are added to a solution containing gold salt, PVP and N, N-dimethylformamide (DMF) to react for 24 hours. The size of gold nanostars ranges 120-250 nm[44].

1. 4. 5. Gold nanospheres

Gold nanospheres assume a spherical shape with a single absorption peak due to surface plasmon resonance in the visible electromagnetic spectrum between 510 nm to 550nm[1]. This limits the biomedical applications of gold nanospheres in the near infrared region[36].

1. 4. 6. Gold nanorods

Gold nanorods (GNRs) are rod-like shape nanoparticles with absorption peaks along the length axis and width axis[18, 45]. The absorptions along the length and width are the key feature that distinguished gold nanorods from other gold nanoparticles[46]. The absorption along the length axis is called longitudinal surface plasmon resonance (LSPR) while the absorption along the width axis is called transverse surface plasmon resonance (TSPR)[45]. The longitudinal surface plasmon resonance can be tuned from the visible to the infrared wavelengths of the electromagnetic spectrum by adjusting the synthetic parameters such as the amount of seeds, silver nitrate and CTAB etc. in the growth solution, while the transverse surface plasmon resonance lies in the visible region around 520-523 nm[12, 34, 46-48]. The longitudinal surface plasmon resonance of gold nanorods is dependent on the aspect ratio and dielectric constant of the surrounding environment. Gold nanorods are easier to synthesize with good control over size and shape as well as longer circulation time in comparison to gold nanosphere and nanoshell[49]. Gold nanorods are generally biocompatible, non-toxic, photostable, good quenchers of fluorescence and easy to synthesize[10, 12-13, 46, 50-51]. These properties make gold nanorods the ideal nanoagents for biomedical applications[10].

Gold nanorods can be classified based on size as large and small nanorods[34, 52]. The large gold nanorods (LGNRs) are nanorods with ~38 -100 nm in length and > 10 nm in diameter, while the smaller gold nanorods (SGNRs) are ~13-50 nm in length and < 10 nm in diameter[18, 34]. The large gold nanorods manifest more scattering features than the small gold nanorods and their longitudinal surface plasmon resonance is tunable to the near infrared[18, 52]. The small gold nanorods are absorption dominant gold nanorods with tunable longitudinal surface plasmon resonance to the near infrared electromagnetic spectrum[34, 52]. The small gold nanorods have higher absorption to scattering ratio compared to the large gold nanorods, making the small good nanorods good photothermal agents[13, 34]. Furthermore, the small gold nanorods have a large surface area to volume ratio, high cellular uptake, high clearance rate from the liver, spleen and the kidney, efficient diffusion through the blood vessels and ease of subcellular accessibility[10, 50, 52-58]. These attributes make the small gold nanorods essential nanomaterials for biomedical applications.

1. 5. Optical properties of gold nanorods

Surface plasmon resonance plays a critical role in the optical properties of gold nanorods. Surface plasmon resonance induces optical absorption and scattering of incident light by gold nanorods. The absorption and scattering properties of gold nanorods are functionally dependent on the size, shape and dielectric constant of the medium[51, 59]. The absorption and scattering effects of gold nanorods attenuate the intensity of incident light. The extent to which light is attenuated as it interacts with the gold nanorods is called the extinction coefficient, ε.

Previously, Gustav Mie developed a theoretical model to explain the interaction of incident electromagnetic light with the spherical particles via absorption and scattering cross-sections. The sum of the absorption and scattering cross-sections yields extinction cross-section. The extinction cross-section of the spherical nanoparticles smaller than 20 nm can be computed by Mie theory given as[18, 60]:

$$C_{ext} = \frac{24\pi^2 R^3 \varepsilon'^{\frac{3}{2}}_m}{\lambda} \cdot \frac{\varepsilon'_i}{(\varepsilon'_r + 2\varepsilon'_m)^2 + \varepsilon'^2_i} \qquad 1.1.$$

where C_{ext} is the extinction cross-section of nanosphere, R is the diameter of nanosphere, λ is the wavelength of incident light, ε′is the complex dielectric constant of the metal given by $\varepsilon' = \varepsilon'_r(\omega) + i\varepsilon'_i(\omega)$, $\varepsilon'_r(\omega)$ is the real part and $i\varepsilon'_i(\omega)$ is the imaginary part of the dielectric function of the metal respectively, and ε'_m is the dielectric constant of the surrounding medium. The real part of the dielectric constant of the metal determines the position of the surface plasmon resonance (SPR) while the imaginary part determines the bandwidth[18]. The wavelength at which the SPR condition of nanospheres is fulfilled is given by:

$$\varepsilon'_r = -2\varepsilon'_m \qquad 1.2.$$

Gans extended the Mie theory to analyse the extinction cross-section of nanoparticles with rod shape (nanorod). The extinction cross-section of gold nanorods less than 80 nm in length can be computed by Gans' model given as[18, 61-62]:

$$\gamma = \frac{2\pi NV\varepsilon'^{\frac{3}{2}}_m}{3\lambda}\sum_J \frac{\left(\frac{1}{p_j^2}\right)\varepsilon'_i}{\left(\varepsilon'_r + \frac{1-p_j}{p_j}\varepsilon'_m\right)^2 + \varepsilon'^2_i} \quad 1.3.$$

where N is the number of particles per unit volume, V is the volume of the particles, while λ, $\varepsilon'_r(\omega)$, $i\varepsilon'_i(\omega)$ and ε'_m have their usual meaning. $P_{j\,=\,(A,\,B)}$ is the depolarization factor given as:

$$P_A = \frac{1-e^2}{e^2}\left(\frac{1}{2e}\ln\frac{1+e}{1-e} - 1\right) \quad 1.4.$$

$$P_B = \frac{1-P_A}{2} \quad 1.5.$$

where $e = \sqrt{1 - \left(\frac{B}{A}\right)^2}$ 1.6.

A and B are the length and the diameter of the gold nanorods respectively. Gans' model predicted that the wavelength at which the SPR of gold nanorods occurs is given by:

$$\varepsilon'_r = -\left(\frac{1-P_j}{P_j}\right)\varepsilon'_m \quad 1.7.$$

Based on the SPR condition of nanorod (equation 1.7.) predicted by the Gans' model, Link and El-Sayed explicitly predicted the wavelength at which the SPR along the longitudinal axis of gold nanorods occurs by a solution of equation 1.7. Their prediction demonstrated the dependency of the SPR along the longitudinal axis on the gold nanorods aspect ratio and dielectric constant of the surrounding medium as encapsulated in the Gans' model (equation 1.3.). Link and El-Sayed[63] factored a linear relationship between the position of the SPR along the longitudinal axis (λ_m), and the nanorods aspect ratio (AR) and the dielectric constant of the medium (ε'_m). The relationship is given as:

$$\lambda_m = (53 \cdot 71AR - 42 \cdot 29)\varepsilon'_m + 495.14 \quad 1.8.$$

1. 6. Synthesis of gold nanorods

Gold nanorods can be synthesized by several methods, which include template, electrochemical, photochemical, seedless, and silver assisted seed mediated growth methods[32, 46, 64-67].

1. 6. 1. Template method

The template method is an electrochemical deposition based method introduced by Martins and co-workers[66]. It involves the electrochemical deposition of gold within the pores of nanoporous polycarbonate or alumina template membranes. The process begins with sputtering small amount of silver or copper onto the alumina template membrane as a conductive film for electrodeposition. This is followed by electrodeposition of gold within the nanopores of the alumina template. After the electrodeposition of gold into the nanopores, the synthesized gold nanorods contained in the template membrane are immersed in an organic solvent to dissolve the membrane while the silver or copper film is removed by wiping with the laboratory tissue[68]. Then, a polymeric stabilizer such as poly(vinylpyrrolidone) (PVP) is added to the solution of gold nanorods to enhance the stability of the nanorods' shape[66]. The diameter of the nanorods can be adjusted by tuning the diameter of the pores of alumina template[69], while the length can be controlled by the deposition time and the amount of gold deposited into the pores[68, 70]. Because the diameter of the pores of the template membrane is fixed, direct variability of the diameter of the synthesized metal nanorods is minimised by the template method. Cepak and Martin[68] synthesized gold nanorods with 40 nm and 90 nm in diameter by template method using polycarbonate filtration membranes, and a silver film as cathode. The length of the 40 nm and 90 nm diameter gold nanorods was changed by varying the deposition time. The longitudinal absorption of the 40 nm and the 90 nm diameter gold nanorods was limited to the visible wavelengths (520 nm-553 nm). It was found that the nanorods precipitated in the organic solvents (hexafluoro-2-propanol and chloroform) due to the loss of stability. In addition, it was found that the gold nanorods with higher aspect ratio precipitated much faster than the gold nanorods with lower aspect ratio. Van de Zande et al. synthesized gold nanorods by the template method by electrodepositing gold into the

nanopores of an alumina membrane[70]. Although, the longitudinal absorption of the gold nanorods was tuned to the near infrared, the nanorods were characterised by side branches and surface irregularities due to the pore geometry[70]. Evans et al.[71] adsorbed aluminium films on a silicon substrate. The aluminium films were anodized in a sulphuric acid. By etching process, nanopores were created in the anodized alumina template. Gold nanorods were grown by electrodepositing gold into the pores of the pre-etch alumina template. Pre-deposition etching whilst keeping the length and the spacing of the gold nanorods constant varied the diameter of the gold nanorods embedded in the anodized alumina template. Although, the aspect ratio of gold nanorods can be varied by this method, however, the procedure is very complicated, time consuming, very costly and over-reliance on equipment for synthesis of gold nanorods. Gao et al.[72] reported the synthesis of gold nanorods using silica nanotubes as hard template for seeding of the gold seeds. The gold nanorods were grown in the silica nanotubes after which the silica shell was etched by sodium hydroxide. Homogeneity in size and high yield of gold nanorods were achieved by this approach. However, multiple processes are required to obtain the final gold nanorods, and the etching of silica shell by sodium hydroxide could affect the surface quality of the synthesized gold nanorods[73].

1. 6. 2. Electrochemical method

The electrochemical method is based on the basic principle of electrolysis. It was developed by Wang and co-workers[74-75]. It involves inserting a gold metal plate and platinum plate as anode and cathode respectively into a solution containing hexadecyltrimethylammonium bromide (CTAB) and tetradodecylammonium bromide (TCAB) both acting as co-surfactants[66]. The electrolysis is preceded by addition of acetone and cyclohexane into the electrolytic solution. A typical 3 mA is passed for the electrolytic process for 30 minutes under controlled temperature. The gold metal anode reacts with the electrolyte to produce $AuBr_4^-$, which migrates to the cathode where reduction takes place. Addition of silver ions is needed for the formation of nanorods[65]. Yu et al.[74] synthesized gold nanorods of different aspect ratios via electrochemical method. The electrodes were gold metal plate (anode) and platinum plate (cathode) both

immersed in an electrochemical cell containing hexadecyltrimethylammonium bromide (C_{16}TAB), and a rod inducing co-surfactant as an electrolyte. In a bid to improve the yield and tunability of the length of gold nanorods, Chang et al.[75] introduced acetone and cyclohexane into the electrolytic solution whilst silver plate was immersed behind the platinum electrode. The silver plate induced the formation of silver ions necessary for an anisotropic growth of gold nanorods. Huang modified the electrochemical method by direct electroreduction of bulk $AuCl_4^-$ ions in the presence of poly(N-vinylpyrrolidone) (PVP). A platinum rod (cathode) and a platinum sheet (anode) were immersed in an electrolytic solution containing potassium nitrate (KNO_3), chloroauric acid ($HAuCl_4$) and PVP. Previous reports have shown that gold nanorods synthesized by this method were not homogenous in size and have a significant proportion of spherical particles[76-77]. In addition, the method is complicated and the procurement of an electrochemical cell can be very expensive[65]. A simplified method for synthesis of gold nanorods is needed.

1. 6. 3. Photochemical method

The photochemical method involves exciting the growth solution with an ultraviolet (UV) laser light. The reagents for synthesis of gold nanorods are mixed together in a one-pot growth solution. CTAB and silver ions are added to the growth solution to facilitate the formation of a soft CTAB template for an anisotropic growth, and preferential deposition of gold atoms for evolution of rod shape[65]. The final growth mixture is then exposed to a UV light of given intensity for photoreduction of gold ions[78]. Placido et al.[32] synthesized gold nanorods via a photochemical approach by preparing a solution containing $HAuCl_4$ acetone, cyclohexane, CTAB, Tetrakis (decyl)ammoniumbromide (TDAB) and varying amount of silver ions (Ag^+). The mixture was exposed to a UV light at room temperature at varying irradiation time. In the presence of Ag^+, the yield of gold nanorods was >60% and >68% of the entire population of gold nanoparticles for 17hours and 21 hours irradiation time respectively. The yield of gold nanoords declined further at longer irradiation time, with the population of spheres and spheroids reaching 75%-90%. Furthermore, more triangles and cubes shapes were formed at higher amount of Ag^+. A careful examination of the transmission electron microscope (TEM) images revealed that

the control of the size and the shape of the gold nanorods is difficult to achieve by the photochemical method due to the simultaneous formation and growth of gold seeds to nanorods[78]. Moreover, previous studies have shown that the photochemical method requires longer reaction time and the gold nanorods are highly susceptible to transform to nanospheres if the gold nanorods solution is exposed to a UV light for a longer irradiation time[32, 64-65]. Moreover, fluctuations of the UV light intensity could affect the growth of the nanorods.

1. 6. 4. Seedless growth method

The seedless growth method is also a one-pot method where all the reactants are mixed together in one growth mixture with the CTAB and the silver ions both binding on the selected facets of the nanorods. Furthermore, silver ions facilitate the preferential deposition of gold atoms on the selected facets of the nanorods[79]. The formation of gold seeds occurs simultaneously with growth into a rod shape. The seeds do not necessarily grow to a critical size before metamorphosing into rods. This method is very simple and less time is spent on producing the gold nanorods. Xu et al.[80] reported the synthesis of high yield of gold nanorods with high aspect ratio by seedless method. Recently. Li et al.[81] synthesized long-range gold nanorods with longitudinal surface plasmon resonance of 1200 nm by seedless method. The TEM images of the studies by Xu and Li groups revealed that the gold nanorods synthesized by seedless method were thinner with high aspect ratios compared to the gold nanorods synthesized by silver assisted seed mediated growth method[13, 76] due to a reduced width arising from the incomplete growth of the gold seeds to a critical size. This implies that the volume of thinner gold nanorods will be smaller in comparison to the thicker gold nanorods of the same aspect ratio. Based on the Gans' model, the extinction coefficient of thinner shape gold nanorods with similar aspect ratio as the thicker shape gold nanorods will be smaller because of reduced particle volume. A smaller extinction coefficient will reduce the absorption and scattering efficiencies of the gold nanorods.

1. 6. 5. Silver assisted seed mediated growth method

The silver assisted seed meditated growth method involves the preparation of seeds and growth solutions separately. The seeds solution is incubated for a period of time to allow the seeds to grow to a critical size in order to develop large facets sufficient for surfactant binding[77]. A proportion of the seeds solution is later added to the growth solution and incubated overnight for the seeds to grow sufficiently to an anisotropic shape. The silver assisted seed mediated growth method is commonly used for synthesis of GNRs because it is very simple, easy to control synthetic parameters and has a high yield of monodispersed GNRs[82-83]. Previously, Jana et al.[84] introduced the seed mediated growth method in 2001. In the Jana et al. protocol, the seeds solution was prepared with $HAuCl_4$, trisodium citrate and sodium borohydride ($NaBH_4$) and incubated for 4 hours before use. The seeds solution acts as both a reducing agent and a nucleation site[85] for the growth of nanorods. The growth solution was prepared with $HAuCl_4$, CTAB, cyclohexane and acetone. Different amounts of seeds solution were added to the same amount of growth solution in separate samples. Thereafter, ascorbic acid was added to the mixture containing the gold seeds and the growth solution. More gold nanospheres were formed than gold nanorods from Jana et al. protocol. Nikoobakht and El-Sayed[77] modified Jana et al. protocol by replacing trisodium citrate with CTAB in the seeds solution and added $AgNO_3$ to the growth solution before introducing the gold seeds in final growth mixture. The selective binding of CTAB surfactant and introduction of silver ions (Ag^+) improved the yield of gold nanorods by the Nikoobakht and El-Sayed protocol[77, 79]. This underscores the role of introducing CTAB and silver ions (Ag^+) in the growth solution before addition of the gold seeds. CTAB is a capping agent that provides a soft template for the growth of nanorods when seeds are introduced through the formation of a silver ion/CTAB complex on the {110} facets as demonstrated in fig. 1.1. [77, 79, 86]. The Ag^+ ions facilitate the preferential deposition of gold atoms on the {100} and {111} facets to enhance an anisotropic growth[77, 79, 86-87]. Since then, several modifications have been made to the silver assisted seed mediated growth method to synthesize gold nanorods for specific requirements. For example, the protocol for synthesis of large and small gold nanorods by silver assisted seed mediated growth method are different[34, 88-89].

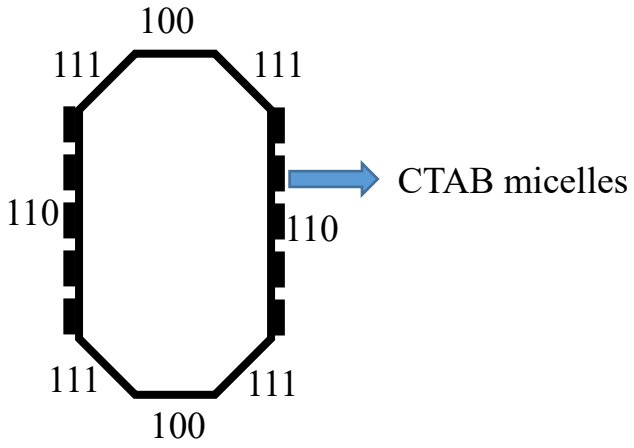

Figure 1.1. The facets of a gold nanorod.

Wei et al.[89] and Mackey et al.[88] synthesized the large gold nanorods with similar chemicals used in Nikoobakht and El-Sayed protocol, but with different concentrations for both the seeds and growth solutions. The seeds solution was incubated for at least 3 hours before use. On the other hand, Jia et al.[34] synthesized the small gold nanorods with similar chemicals by incubating the seeds solution for 2 hours, while the growth solution contained similar chemicals except hydrochloric acid, HCl. Figure 1.2 displays the scheme for synthesis of the small gold nanorod by silver assisted seed mediated growth method. The small gold nanorods synthesized by Jia et al. were 16-45 nm in length and 6-9 nm in diameter. The ratio of gold seeds solution to the growth solution and the age of the gold seeds played important roles in determining the final size and shape of the gold nanorods formed[90-91]. Synthesis of stable small gold nanorods with diameter < 6 nm, and an improved yield by silver assisted seed mediated growth method remains very challenging[10, 13]. Therefore, further improvement to the silver assisted seed mediated growth method for synthesis of smaller gold nanorods is needed.

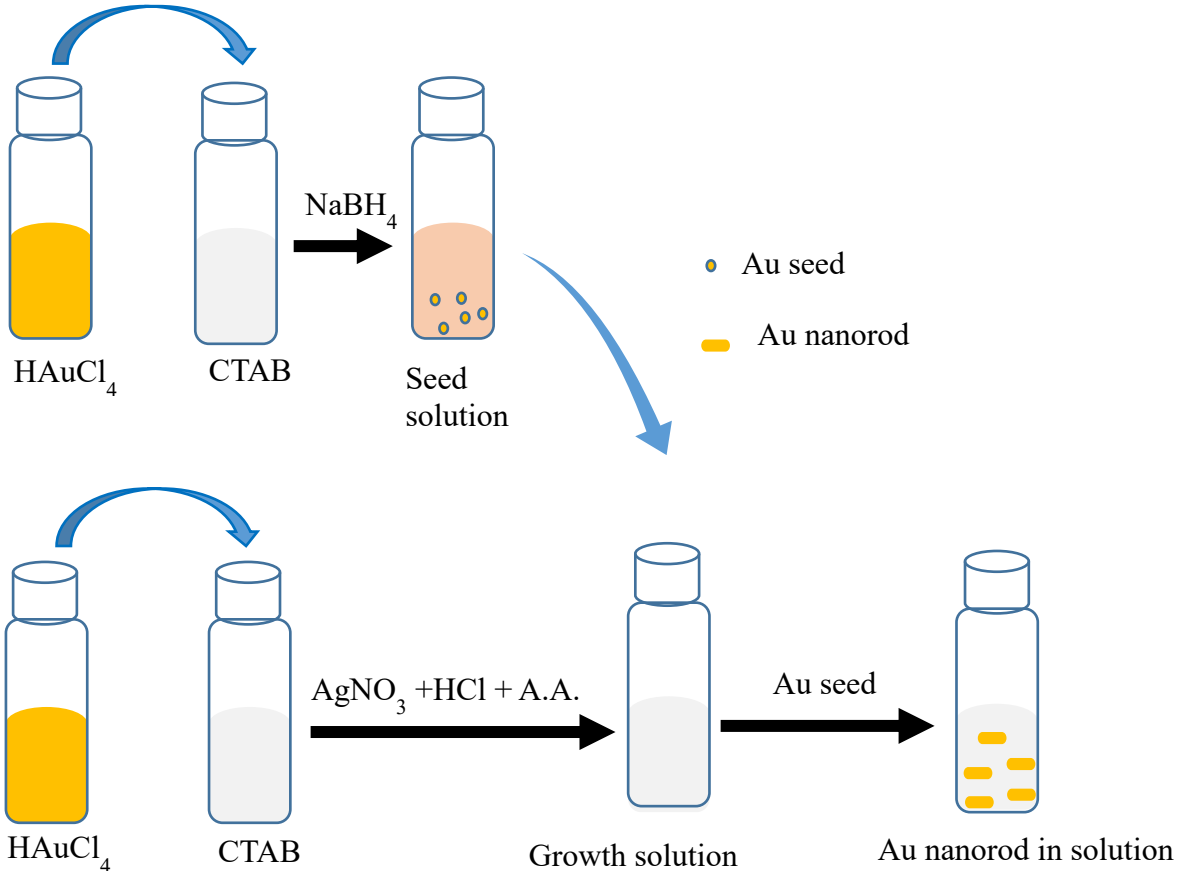

Figure 1.2. A scheme illustrating the synthesis of small gold nanorod by silver assisted seed mediated growth method.

1. 7. Surface modification of gold nanorods

Synthesized gold nanorods are often coated with CTAB surfactant. The toxicity of CTAB surfactant limits direct biological applications of synthesized gold nanorods[83, 92]. Thus, surface modification of gold nanorods can be performed to replace the CTAB surfactant with bio-friendly molecules and improve the stability of the gold nanorod structure. In addition, the surface modification of gold nanorods prepares the surface of gold nanorods for adsorption of biomaterials such as the deoxyribonucleic acid (DNA)[85]. Surface modification can be achieved by surface coating, ligand exchange, and electrostatic adsorption. Generally, surface modification of gold nanorods involves coating a

biocompatible molecule on the CTAB-GNR surface[56] or exchanging the CTAB surfactant with a biocompatible molecule[89, 93].

1. 7. 1. Surface coating

Surface coating of gold nanorods can be performed with silicon dioxide (SiO_2) and bovine serum albumin[34, 56] to reduce the toxicity of CTAB and prevent particle aggregation[83]. Silicon (SiO_2) coated gold nanorods have been demonstrated to enhance the photothermal performance, photoacoustic signal and optical responses of gold nanorods[56, 93-95]. Similarly, bovine serum albumin (BSA) coated gold nanorods have shown an improved biocompatibility and cellular uptake[10, 55, 96].

1. 7. 2. Ligand exchange

Ligand exchange could be seen as a technique for replacing the CTAB surfactant on the gold nanorods surface with bio-friendly molecules or ligands. Ligand exchange can be performed with polyethylene glycol (PEG) and mercaptohexanoic acid (MHA)[83]. PEGylated gold nanorods have been demonstrated to be highly soluble and stable for biological applications[83, 88, 97].

On the other hand, MHA is an organic molecule composed of a thio group (HS) and carboxylic group (COOH) as shown in figure 1.3. MHA has strong affinity for gold[98] and the carboxylic group of MHA facilitates the efficient adsorption of biomolecules such as DNA on the GNRs structures[83]. MHA binds to the GNRs surface covalently via thio chemistry[83]. Wei et al. and Mbalaha et al. demonstrated the assembly of hairpin DNA (hpDNA) on the GNRs platform for detecting messenger ribonucleic acid (mRNA) in solution phase[86, 89]. In this study, ligand exchange involves the transfer of the CTAB-GNR from the aqueous phase to an organic phase using a round-trip phase transfer ligand exchange method[86, 89].

Figure 1.3. The organic structure of mercaptohexanoic acid (MHA).

1. 7. 3. Functionalization of gold nanorods

Functionalization of GNRs could be defined as the assemblage of functional agents on the surface of GNRs for targeting and delivery of therapeutics substances. In this study, functionalization involves the adsorption of fluorophore labeled oligonucleotides of DNA onto the GNRs surface to target specific cancer cells receptors and prevent the nanostructure from degradation due to nuclease activity[99-101]. The oligonucleotides are designed with a thio group for linkage onto the GNRs by thio chemistry.

1. 8. DNA

A DNA is found in the nucleus of living cells[102]. It is the reservoir of genetic information in living systems and it is composed of polymer of nucleotides linked by a linear sequence or pattern[103]. A DNA is the building block for constructing new structures[104-105]. It can be synthesized by replication, enzymatic synthesis and solid-phase chemical synthesis [103, 106]. The structure of a DNA is organised into primary and secondary structures. The primary structure is organised into a linear sequence of nucleotides. The nucleotides constitute the building blocks for a DNA. A nucleotide is composed of phosphate, monosaccharides (D-2-deoxyribose) and nitrogenous organic base. The nitrogenous bases include **adenine (A)**, **guanine (G)**, **thymine (T)**, **cytosine (C)** and **uracil (U)**. The adenine and guanine are the purines while the thymine, cytosine and uracil are pyrimidines[103]. The phosphate group bonds covalently to the monosaccharide residue on the left by a phosphoester bond while the nitrogenous base group connects on the right by a N-glycosidic bond [103-104]. The carbon atoms of the monosaccharide residue are numbered 1', 2', 3', 4'and 5'. The phosphate group bonds to the monosaccharide residue at the 5' carbon atom and this is called the **5' terminus.** The phosphate group connects the nucleotides of a DNA at the 3' carbon atom. The linear sequence of nucleotides

terminates with OH on the 3’ carbon atom and this is called the **3’terminus.** A typical nucleotide is displayed in figure 1.4.

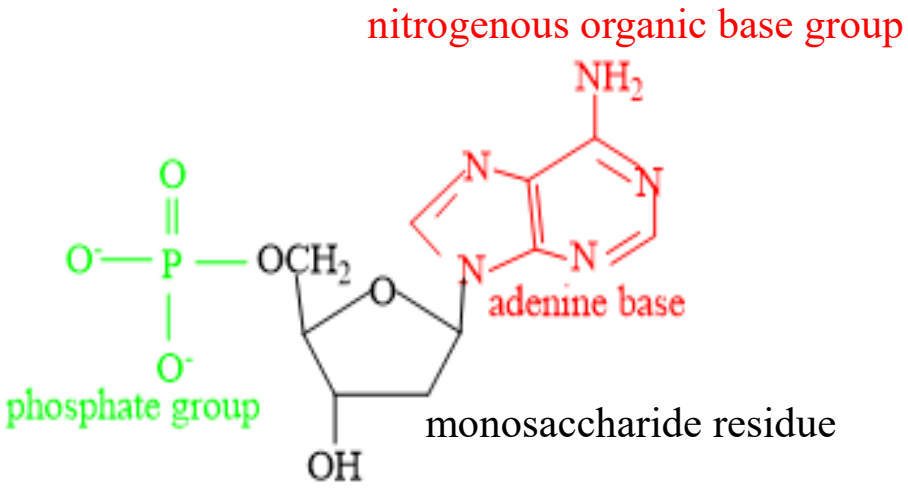

Figure 1.4. A typical primary structure of the nucleotide of a DNA.

The secondary structure of DNA represents the double strands oriented in antiparallel pattern with 5’, 3’ ends at the one end and 3’, 5’ ends at the other end. This pattern of arrangement produces a twisted double helical structure. The nucleotide bases from each strand face each other in an opposite pattern; hence, they are **complementary bases**. Guanine is always linked to cytosine, and adenine to thymine via a hydrogen bond[102]. This arrangement makes the double strands complementary to each other. Complementary bases pairing helps to maintain the constant width of the DNA double helix structure[103]. The secondary structure of a DNA is shown in the figure 1.5. below.

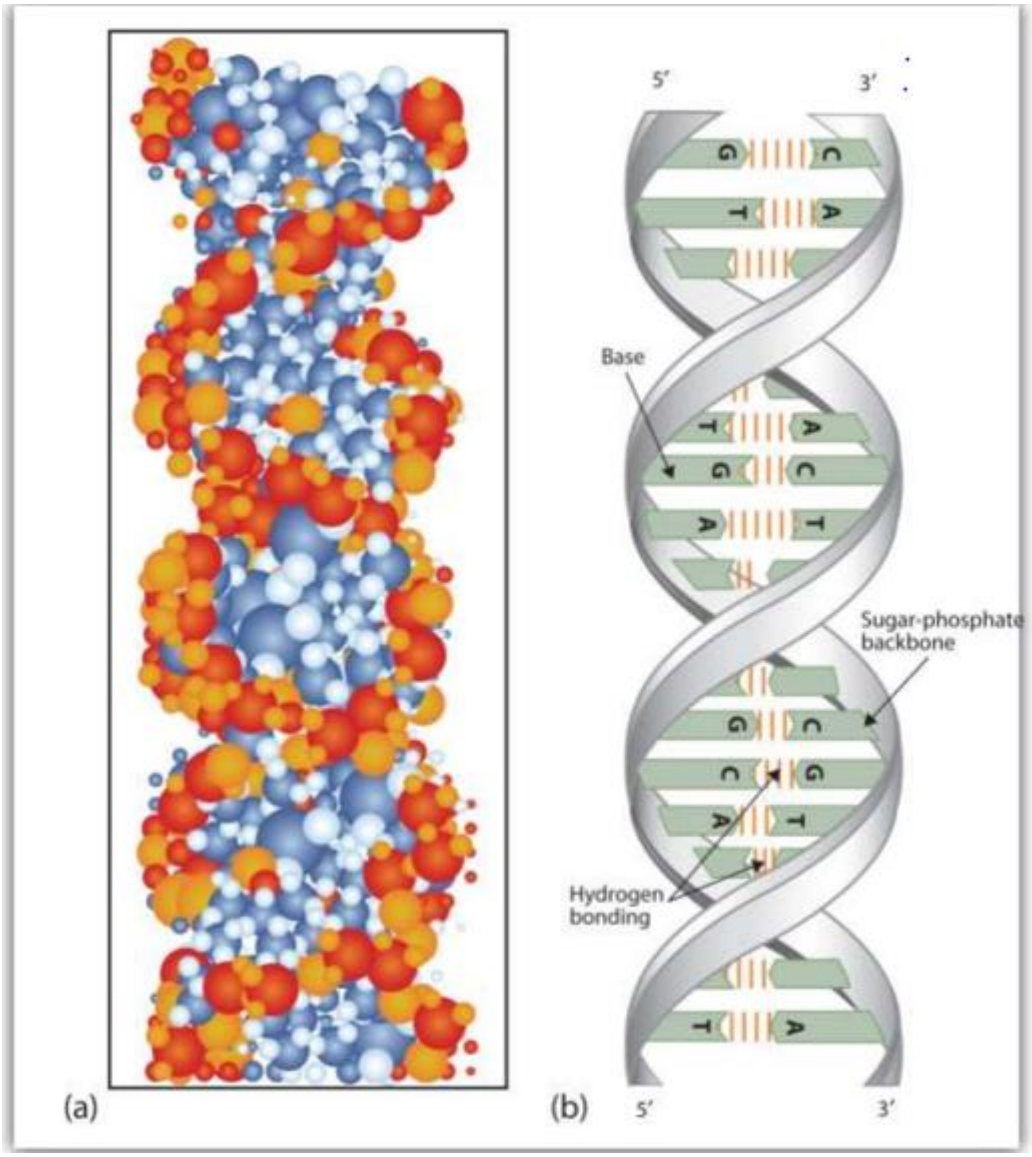

Figure 1.5. The secondary structure of a DNA; (a) model of the DNA double helix structure (b) DNA double helix structure showing the pattern of complementary bases[103].

1. 9. Molecular interactions of the gold nanorods with fluorophore labeled oligonucleotide

1. 9. 1. Hairpin DNA (hpDNA)

An oligonucleotide is characterised by a sequence of nucleic acid bases with two ends symoblized by 5' end and 3' end. For a typical molecular beacon, the oligonucleotide structure is conformed in a hairpin shape composed of a thio group, spacer, base sequence

and a fluorophore in a sytematically arranged order: 5′→ thio group (SH) →spacer→ base sequence → fluorophore →3′. The thio group links the oligonucleotide onto the GNRs surface by covalent bonding from the 3′ end while the 5′end brings the fluorophore closer to the GNRs surface as shown in the figure 1.6. below:

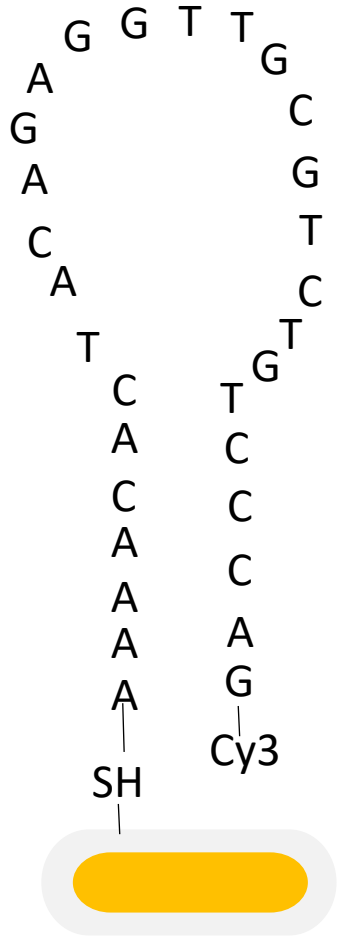

Figure 1.6. The description of the interaction of gold nanorods with a fluorophore labeled DNA.

The proximity of fluorophore to the GNRs surface enhances energy transfer interaction by Förster resonance energy transfer (FRET). FRET is a distant-dependent dipole-dipole molecular interaction and could be defined as the process by which energy is transferred from an excited donor to the acceptor[107]. The effective distance for which the FRET process occurs is 1-8 nm for organic dyes and this distance is called the Förster distance[108]. For FRET to occur, the emission spectrum of the donor must overlap the

absorption spectrum of the acceptor; the donor and acceptor must be in close proximity within the Förster distance[109-110]. In the case of GNR-fluorophore molecular interaction, the energy transfer from the excited fluorophore (donor) to the GNRs (acceptor) occurs via a dipole-dipole interaction[107, 111]. Gold nanorods extends the interaction range by 20 nm thus making it possible to study long-range molecular interaction in biological systems. The energy transfer by FRET process is the basis for fluorescence quenching abilities of GNRs. This makes GNRs ideal agents in fluorescence detection applications[108, 111-112]. For example, Wei et al. utilized the GNRs as a quenching agent in the detection of a targeted gene (c-myc) in mRNA in a homogenous solution[89]. This demonstrates the potential of utilizing the GNRs for the diagnosis of cancer.

1. 9. 2. Aptamer

Aptamers are synthetically created by Systematic Evolution of Ligands by Exponential Enrichment (SELEX). An aptamer is a single strand biological molecule obtained from either a DNA or RNA to target specific analytes. DNA aptamers are more stable than RNA aptamers because RNA aptamers undergo degradation due to enzyme activities[113-114]. An aptamer is composed of 20-70 nucleic acid bases. Aptamers bind various molecules such as proteins, cells, peptides and tissues with high specificity[115]. Aptamers are relatively small, non-immunogenic, non-toxic and very stable at room temperature[115-116]. Aptamers can be easily conjugated to nanomaterials such as gold nanorods[117-118]. These features make aptamers versatile biomolecules in biomedical applications. Displayed in table 1.1. is the list of DNA aptamers and their analytes.

Table 1.1. The list of DNA aptamers, cancer biomakers and host cancer cells.

DNA aptamer	**Cancer biomaker**	**Host cancer cell (cell line)**	**Ref.**
NU172	Thrombin	Hepatocellular carcinoma (HepG2)	[119-120]
Sgc8	Protein tyrosine kinase 7 (PTK7)	Leukemia (CCRF-CEM)	[116, 121]
AS1411	Nucleolin (NCL)	Breast cancer (MDA-MB-231)	[122-123]
AS1411	Nucleolin (NCL)	Pancreatic cancer (BxPC-3)	[123-124]
SYL3C	EpCAM	Gastric cancer (KATO lll)	[125]
SYL3C	EpCAM	Colorectal adenocarcinoma (HT-29)	[115]
SYL3C	EpCAM	Oesophageal adenocarcinoma (Flo-1)	[126]
SYL3C	EpCAM	Breast cancer (MCF-7)	[127]

1. 10. Incidence of cancer infections and mortality

Cancer is a generic term describing diseases with abnomal growth and spread of cells[128-129]. Cancer is one of the major causes of global mortality[130]. It has been predicted previously that the new cases of cancer will increase to >15million, with the mortality rising to 12 million by 2020[131]. The World health organization (WHO) cancer report for 2015 indicated that about 14 million new infections and 8.2 million cancer related deaths were recorded in 2012[132]. Furthermore, the WHO cancer report for 2020 estimated that 18. 1million new cases of cancer and 9.6 million deaths due to cancer occurred in 2018[133]. It is predicted that the new cases of cancer will rise to 29-37 million by 2040[133]. Table 1.2. for example, shows that oesophageal cancer has the highest percentage of global mortality among the common cancers. Thus, there is an urgent need to find effective screening modalities for early detection and treatment of cancer. The estimated incidence rate of cancer infections and mortality according to different types of cancers for 2018 are shown table 1.2.

Table 1.2. The estimated incidence rate of cancer infections and mortality.

Cancer type	New infection rate	Mortality rate (%)	Ref.
Lung cancer	2,093,876	1,761,007 (84)	[6, 128]
Breast cancer	2,088,849	626,679 (30)	[6, 128]
Colorectal cancer	1,800,000	862,000 (48)	[6, 128]
Prostate cancer	1,276,106	358, 989 (28)	[6, 128]
Skin cancer (non-melanoma)	1,042,056	65,155 (6)	[6, 128]
Stomach cancer	1,033,701	782,685 (76)	[6, 128]
Oesophageal ancer	572,034	508,585 (89)	[6]

1. 10. 1. Conventional methods for cancer diagnosis and therapy

Early diagnosis of cancer is very important for a successful cancer therapy. The conventional methods for diagnosis of cancer include blood sample test, biopsy, enzyme-link immune sorbent assay (ELISA), cytology examination, endoscopy and magnetic resonance imaging (MRI)[3, 134-135]. These methods can cause discomfort, bleeding, allergic reactions, high cost and are time-consuming[3, 134]. On the other hand, conventional treatment modalities for cancer are chemotherapy, radiation and surgery[136]. These modalities are limited by lack of specificity on target, drug resistance, tumour regeneration after surgery and other numerous side effects[2, 137-139]. Hence, the need for innovative diagnosis and treatment methods to target specific cancer cells is essential.

1. 10. 2. Cancer biomakers

A cancer biomaker is a molecule that determines the existence of a specific cancer type [140]. Cancer biomakers can occur as proteins and nucleic acids. Cancer biomakers are important tools in biomedical applications for early diagnosis and treatment of cancer diseases[99]. Cancer biomakers are very useful in identifying and targeting cancerous cells[141]. Cancer biomakers can be targeted with hpDNA and aptamers. Examples of cancer biomakers and their host cancer cells are shown in table 1.1. above.

1. 11. Biomedical applications of gold nanorods

Gold nanorods have been demonstrated as promising agents for various biomedical applications including drug loading and delivery, biosensing, imaging and photothermal therapy.

1. 11. 1. Drugs loading and delivery

The large surface area to volume ratio and absorption cross section of gold nanorods makes GNRs ideal agents as nanovectors for loading, delivery and release of therapeutic drugs to tumour sites[142-143]. For example, tumour growth in mice was inhited by polymer encapsulated gold nanorods loaded with Doxorubicin (Dox)[144]. Similarly, Chen et al. terminated tumour viability in mice with Dox coated gold nanorods[143].

1. 11. 2. Biosensing

The sensitivity of longitudinal surface plasmon resonance of GNRs to the refractive index of the surrounding medium has been exploited in biosensing applications[27]. The fundamental principle in biosensing applications with the GNRs is that, changes in the refractive index of the surrounding medium are detected by a shift of the longitudinal surface plasmon resonance of GNRs. Furthermore, binding interaction between the GNRs and the analytes in the microenvironment leads to a shift of the longitudinal surface plasmon resonance absorption of GNRs[27]. Omair and Talukder demonstrated that the biomakers of diseases such as cancer and human immunodificiency virus (HIV) can be detected at the single molecule level with a GNRs biosensor[145]. Peptide functionalized gold nanorods have also been demonstrated as biosensors for detecting cardiac biomaker troponin I in solution phase [146].

1. 11. 3. Cancer imaging

Gold nanorods scatter electromagnetic light intensely[18, 52]. The scattering cross section of GNRs is dependent on its size[52]. The scattering cross section of large gold nanorods is more than the small gold nanorods[18, 34, 52]. This makes the large gold nanorods ideal contrast agents for imaging applications. The scattering properties of gold nanorods have been exploited for imaging applications such as dark field microscopy (DFM), optical coherence tomography (OCT), two-photon luminescence (TPL), photoacoustic

tomography (PAT), X-ray computed tomography (CT) and surface-enhanced Raman scattering (SERS)[108, 147]. Gold nanorods have been demonstrated as good contrast agents in fluorescence lifetime imaging[148]. Yan et al. developed a GNRs based nanofibre system for delivery of cancer drugs and cell imaging[149]. Betzer et al. utilized gold nanorods as contrast agents to distinguish squamous carcinoma cells from non-cancerous cells using a hyperspectral imaging system[150].

1. 11. 4. Photothermal Therapy

Photothermal therapy is a treatment modality that utilizes the heat energy generated by a colloid of noble metal nanoparticles following excitation by a beam of laser to kill cancer cells and bacterial infections[49, 151-152]. That is, the free electrons in the conduction band of metal nanoparticles become agitated following excitation by an incident light of high intensity leading to the absorption of light. Because of the rapid phase loss in femtoseconds, the agitated free electrons collide with each other via electron-electron interaction, thus generating hot electrons with a rising temperature of ~1000K[18-49]. The hot electrons dissipate their heat energy to the lattice via electron-phonon relaxation in ~0.5-1 picoseconds[49]. The hot lattice dissipates the heat to the surrounding medium via phonon-phonon relaxation[49]. The heat released in the surrounding medium can be exploited to kill cancer cells and bacteria. Compared to the gold nanospheres, the gold nanorods absorb light in the near infrared region where tissue transmission is very high[49, 153]. Moreover, the gold nanorods generate heat 6 times faster and more efficient than the gold nanospheres and nanoshells because the optical absorption efficiency of the gold nanorod is 6 times higher than that of the gold nanospheres and the nanoshells of comparable size[49],[154]. These excellent attributes make the GNRs suitable agents for photothermal applications. Photothermal applications exploit the absorption efficiency of the GNRs to generate heat energy for therapeutic purposes. The SGNRs are absorption dominant, therefore, could be better phothermal agents compared to the LGNRs[34].

Few studies have reported photothermal therapy of cancer with aptamer funcntionalized gold nanorods. Huang et al. functionalized a 53x14 nm GNRs based nanocomposite with sgc8c aptamer to target protein tyrosine kinase in leukemia cancer cell (CCRF-CEM)[155].

The result showed that more CCR-CEM cells were killed after photothermal treatment with a 808 nm CW diode laser. Wang et al. demonstrated that 45x13 nm gold nanorods functionalized with CSC13 aptamer killed prostate cancer stem cells after irradiation with the NIR laser light (812 nm)[156]. Studies on the photothermal applications of the aptamer functionalized SGNRs are however somewhat lacking.

1. 12. Summary

Metal nanoparticles are nanoparticles obtained from metal elements with at least one dimension in the range of 3-100 nm. The noble metal nanoparticles exhibit localised surface plasmon resonance effect that makes them uniquely different from other metal nanoparticles. The noble metal nanoparticles are made from noble metal elements and these include platinum, silver and gold nanoparticles.

Gold nanoparticles are nanoscale particles with excellent optical properties. The optical properties of gold nanoparticles are very useful in biomedical applications particularly in the diagnosis and treatment of cancer. Gold nanoparticles exist in different sizes and shapes. The various forms of gold nanoparticles include gold nanoshells, gold nanocages, gold nanocubes, gold nanostars, gold nanospheres and gold nanorods. Gold nanorods are preferred over other gold nanoparticles because of ease to synthesize with a good control over the aspect ratio and longer circulation time. Moreover, the optical absorption of gold nanospheres is limited to the visible spectrum; hence, gold nanospheres cannot be used for applications in the near infrared region. However, the longitudinal absorption of gold nanorods can be tuned from the visible to the near infrared. These combined with biocompatibility and photostability make the gold nanorods ideal agents for biomedical applications. Gold nanorods can be synthesized by various methods such as template, electrochemical, photochemical, seedless and silver assisted seed mediated growth methods. The silver assisted seed mediated growth method is preferred over other methods because it is very simple to control synthetic parameters and the yield of monodisperse gold nanorods is very high.

References

1. Cai, W.; Gao, T.; Hong, H.; Sun, J., Applications of gold nanoparticles in cancer nanotechnology. *Nanotechnology, Science and Applications* **2008,** *1*, 17-32.

2. Kakde, D.; Jain, D.; Shrivastava, V.; Kakde, R.; Patil, T., Cancer therapeutics-opportunities, challenges and advances in drug delivery. *Journal of Applied Pharmaceutical Science* **2011,** *1* (9), 1-10.

3. Yang, S.; Wu, S.; Huang, Y.; Shao, Y.; Chen, X. Y.; Xian, L.; Zheng, J.; Wen, Y.; Chen, X.; Li, H.; et al., Screening for oesophageal cancer. *Cochrane Database of Systematic Reviews* **2012,** (12), 1-24.

4. Bai, V.; Kaseb, A.; Tejwani, S.; Divine, G.; Barrack, E.; Menon, M.; Pardee, A.; Reddy, G., Identification of prostate cancer mRNA markers by averaged differential expression and their detection in biopsies, blood, and urine. *Proceedings of the National Academy of Sciences of the United States of America* **2007,** *104*, 2343-2348.

5. Huang, Y.-H.; Zhang, Y.-Q.; Huang, J.-T., Neuroendocrine cells of prostate cancer: biologic functions and molecular mechanisms. *Asian Journal of Andrology* **2019,** *21* (3), 291-295.

6. Bray, F.; Ferlay, J.; Soerjomataram, I.; Siegel, R. L.; Torre, L. A.; Jemal, A., Global cancer statistics 2018: GLOBOCAN estimates of incidence and mortality worldwide for 36 cancers in 185 countries. *CA CANCER J. CLIN.* **2018,** *68*, 394-424.

7. Das, R.; Feng, F. Y.; Selth, L. A., Long non-coding RNAs in prostate cancer: biological and clinical implications. *Molecular and Cellular Endocrinology* **2019,** *480*, 142-152.

8. National Cancer Institute, Prostate specific antigen test. National Cancer Institute: 2017.

9. Caram, M. E. V.; Skolarus, T. A.; Cooney, K. A., Limitations of prostate-specific antigen testing after a prostate cancer diagnosis. *Eur Urol* **2016,** *70* (2), 209-210.

10. Li, Z.; Huang, H.; Tang, S.; Li, Y.; Yu, X.; Wang, H.; Li, P.; Sun, Z.; Zhang, H.; Liu, C.; Chu, P. K., Small gold nanorods laden macrophages for enhanced tumor coverage in photothermal therapy. *Biomaterials* **2016,** *74*, 144-154.

11. Popovtzer, R.; Agrawal, A.; Kotov, N. A.; Balter, J.; Carey, T. E.; Kopelman, R., Targeted gold nanoparticles enable molecular CT imaging of cancer. *Nano Letters* **2008,** *8* (12), 4593-4596.

12. Kennedy, L. C.; Bickford, L. R.; Lewinski, N. A.; Coughlin, A. J.; Hu, Y.; Day, E. S.; West, J. L.; Drezek, R. A., A new era for cancer treatment: gold-nanoparticle-mediated thermal therapies. *Small* **2011,** *7* (2), 169-183.

13. Ali, M. R. K.; Snyder, B.; El-Sayed, M. A., Synthesis and optical properties of small Au nanorods using a seedless growth technique. *Langmuir* **2012,** *28*, 9807-9815.

14. Formo, Y.; Lee, E.; Campbell, E.; Xia, D., Functionalization of electrospun Tio2 nanofibers with Pt nanoparticles and nanowires for catalytic applications. *Nano Lett.* **2008,** *2*, 668-672.

15. Shevchenko, A. P.; Ringler, E. V.; Schwemer, M.; Talapin, A.; Klar, D. V.; Rogach, T. A.; Feldmann, A. L.; Alivisatos, J., Self-assembled binary superlattices of CdSe and Au nanocrystals and their fluorescence properties. *J. Am. Chem. Soc.* **2008,** *130*, 3274-3275.

16. Murray, T.; Sun, C. B.; Doyle, S.; Betley, H., Monodisperse 3d transition-metal (Co, Ni, Fe) nanoparticles and their assembly into nanoparticles superlacttices. *Mater. Res. Soc. Bull* **2001,** *26* (12), 985-991.

17. Kamat, P. V., Photophysical, photochemical and photocatalytic aspects of metal nanoparticles. *J.Phys.Chem.* **2002,** *106*, 7724-7729.

18. Huang, X.; El-Sayed , M. A., Gold nanoparticles: optical properties and implementations in cancer diagnosis and photothermal therapy. *Journal of Advanced Research* **2010,** *1*, 13–28.

19. Qu, X.; Li, Y.; Li, L.; Wang, Y.; Liang, J.; Liang, J., Fluorescent gold nanoclusters: synthesis and recent biological application. *Journal of Nanomaterials* **2015,** *2015* (6), 1-23.

20. Mody, V. V.; Siwale, R.; Singh, A.; Mody, H. R., Introduction to metallic nanoparticles. *J. Pharm. Bioallied Sci.* **2010,** *2* (4), 282-289.

21. Tatini, F.; Landini, I.; Scaletti, F.; Massai, L.; Centi, S.; Ratto, F.; Nobili, S.; Romano, G.; Fusi, F.; Messori, L.; Mini, E.; Pini, R., Size dependent biological profiles of PEGylated gold nanorods. *Journal of Materials Chemistry B* **2014,** *2* (36), 6072-6080

22. Link, S.; Mohamed, M. B.; El-Sayed, M. A., Simulation of the optical absorption spectra of gold nanorods as a function of their aspect ratio and the effect of the medium dielectric constant. *J. Phys. Chem. B* **1999,** *103* (16), 3073-3077.

23. Pedone, D.; Moglianetti, M.; Luca, E. D.; Bardi, G.; Pompa, P. P., Platinum nanoparticles in nanobiomedicine. *Chem. Soc. Rev.* **2017,** *46*, 4951-4975.

24. Sturikova, H.; Krystofova, O.; Huska, D.; Adam, V., Zinc, zinc nanoparticles and plants. *Journal of Hazardous Materials* **2018,** *349*, 101-110.

25. Hong, Y.; Huh, Y.; Yoon, D. S.; Yang, J., Nanobiosensors based on localized surface plasmon resonance for biomarker detection. *Journal of Nanomaterials* **2012,** *2012* (111), 1-13.

26. Kumar, S.; Sood, A., Ultrafast Response of Plasmonic Nanostructures. In *Review in plasmonics*, Geddes, C. D., Ed. Springer: Cham, 2016; Vol. 2015, pp 131-167.

27. Cao, J.; Sun, T.; Grattan, K. T. V., Gold nanorod-based localized surface plasmon resonance biosensors: a review. *Sensors and Actuators B: Chemical* **2014,** *195*, 332-351.

28. Cao, J.; Galbraith, E. K.; Sun, T.; Grattan, K. T. V., Comparison of surface plasmon resonance and localized surface plasmon resonance-based optical fibre sensors. *Journal of Physics: Conference Series* **2011,** *307*, 012050.

29. Stensberg, M. C.; Wei, Q.; McLamore, E. S.; Porterfield, D. M.; Wei, A.; Sepúlveda, M. S., Toxicological studies on silver nanoparticles: challenges and opportunities in assessment, monitoring and imaging. *Nanomedicine (Lond)* **2011,** *6* (5), 879–898.

30. Alkilany, A.; Murphy, C., Toxicity and cellular uptake of gold nanoparticles: what we have learned so far? *Journal of nanoparticle research : an interdisciplinary forum for nanoscale science and technology* **2010,** *12*, 2313-2333.

31. Smith, D. A.; Korgel, B. A., The importance of the CTAB surfactant on the colloidal seed-mediated synthesis of gold nanorods. *Langmuir* **2008,** *24* (3), 644-649.

32. Placido, T.; Comparelli, R.; Giannici, F.; Cozzoli, P. D.; Capitani, G.; Striccoli, M.; Agostiano, A.; Curri, M. L., Photochemical synthesis of water-soluble gold nanorods: the role of silver in assisting anisotropic growth. *Chem. Mater.* **2009,** *21* (18), 4192-4202.

33. Alkilany, A. M.; Nagaria, P. K.; Hexel, C. R.; Shaw, T. J.; Murphy, C. J.; Wyatt, M. D., Cellular uptake and cytotoxicity of gold nanorods: molecular origin of cytotoxicity and surface effects. *Small* **2009,** *5* (6), 701-708.

34. Jia, H.; Fang, C.; Zhu, X. M.; Ruan, Q.; Wang, Y. X.; Wang, J., Synthesis of absorption-dominant small gold nanorods and their plasmonic properties. *Langmuir* **2015,** *31* (26), 7418-7426.

35. Khan, A. K.; Rashid, R.; Murtaza, G.; Zahra, A., Gold Nanoparticles: synthesis and applications in drug delivery. *Trop. J. Pharm. Res.* **2014,** *13* (7), 1169-1177.

36. Erickson, T. A.; Tunnell, J. W., *Gold nanoshells in biomedical applications*. John Wiley & Sons: Wienheim, 2009.

37. Loo, C.; Lin, A.; Hirsch, L.; Lee, M.; Barton, J.; Halas, N.; West, J.; Drezek, R., Nanoshell- enabled photonics-based imaging and therapy of cancer. *Technol. Cancer Res. Treat.* **2004,** *3* (1), 33-40.

38. Burgess, R., *Medical applications of nanoparticles and nanomaterials*. IOS Press: Netherlands, 2009.

39. Skrabalak, S. E.; Chen, J.; Sun, Y.; Lu, X.; Au, L.; Cobley, C. M.; Xia, Y., Gold nanocages: synthesis, properties, and applications. *Accounts of chemical research* **2008,** *41* (12), 1587-1595.

40. Cang, H.; Sun, T.; Li, Z.; Chen, J. C.; Wiley, B. J.; Xia, Y., Gold nanocagesas contrast agents for spectroscopic optical coherence tomography. *Optical Letters* **2005,** *30* (22), 3048-3050.

41. Pengo, P.; Pasquato, L., *Modified gold nanoparticles and surfaces*. John Wileys & Sons, Inc: New Jersey, 2010.

42. Thiele, M.; Soh, J. Z. E.; Knauer, A.; Malsch, D.; Stranik, O.; Muller, R.; Csaki, A.; Henkel, T.; Kohler, J. M.; Fritzsche, W., Gold nanocubes- direct comparison of synthesis approaches reveals the need for a microfluidic synthesis setup for a high reproducibility. *Chemical Engineering Journal* **2016,** *288*, 432-440.

43. Shan, F.; Zhang, T., Theoretical study on the surface plasmon propertiesof gold nanostars. *Materials Science and Engineering* **2018,** *322* (2), 1-6.

44. Montoto, A. H.; Montes, R.; Samadi, A.; Gorbe, M.; Terres, J. M.; Cao-Milan, R.; Aznar, E.; Ibanez, J.; R, M.; Marcos, M. D.; Orzaez, M.; Sancenon, F.; Oddershede, L. B.; Martinez-Manez, R., Gold nanostars coated with mesoporous silica are effective and

nontoxic phothermal agents capable of gate keeping and laser-induced drug release. *ACS Appl. Mater. Interfaces* **2018,** *10*, 27644-27656.

45. Akouibaa, A.; Benhamou, M.; Derouiche, A., Simulation of the optical properties of gold nanorods : comparison to experiment. *International Journal of Advanced Research in Computer Science and Software Engineering* **2013,** *3* (9), 657-671.

46. Ma, Z. Y.; Xia, H. X.; Liu, Y. P.; Liu, B.; Chen, W.; Zhao, Y. D., Applications of gold nanorods in biomedical imaging and related fields. *Chinese Sci. Bull* **2013,** *58* (21), 2530-2536.

47. Ni, W.; Kou, X.; Yang, Z.; Wang, J., Tailoring longitudinal surface plasmon wavelengths, scattering and absorption cross sections of gold nanorods. *ACS Nano* **2008,** *4*, 677-686.

48. Lee, K.-S.; El-Sayed, M. A., Dependence of the enhanced optical scattering efficiency relative to that of absorption for gold metal nanorods on aspect ratio, size, end-cap shape, and medium refractive index. *The Journal of Physical Chemistry B* **2005,** *109* (43), 20331-20338.

49. Huang, X.; El-Sayed, M. A., Plasmonic photo-thermal therapy (PPTT). *Alexandria Journal of Medicine* **2011,** *47* (1), 1-9.

50. Jiang, K.; Smith, D. A.; Pinchuk, A., Size-dependent photothermal conversion efficiencies of plasmonically heated gold nanoparticles. *J. Phys. Chem. C* **2013,** *117* (51), 27073-27080.

51. Wan, J.; Wang, J.-H.; Liu, T.; Xie, Z.; Yu, X.-F.; Li, W., Surface chemistry but not aspect ratiomediates the biological toxicity of gold nanorods in vitro and in vivo. *Science Reports* **2015,** *5* (1), 11398-1141.

52. Ungureanu, C.; Koning, G. A.; van Leeuwen, T. G.; Manohar, S., The 'nanobig rod' class of gold nanorods: optimized dimensions for improved in vivo therapeutic and imaging efficacy. *Nanotechnology* **2013,** *24* (21), 1-9.

53. Yue, K.; Nan, J.; Zhang, X.; Tang, J.; Zhang, X., Photothermal effects of gold nanoparticles induced by light emitting diodes. *Applied Thermal Engineering* **2016,** *99*, 1093-1100.

54. Shibu, E. S., Varkentina, N., Cognet, L., Lounis, B., Small gold nanorods with tunable absorption for photothermal microscopy in cells. *Adv. Sci.* **2017,** *4* (2), 1600280-1600285.

55. Li, Z.; Tang, S.; Wang, B.; Li, Y.; Huang, H.; Wang, H.; Li, P.; Li, C.; Chu, P. K.; Yu, X.-F., Metabolizable small gold nanorods: size-dependent cytotoxicity, cell uptake and *in vivo* biodistribution. *ACS Biomaterials Science & Engineering* **2016,** *2* (5), 789-797.

56. Cong, B.; Kan, C.; Wang, H.; Liu, J.; Xu, H.; Ke, S., Gold Nanorods : near-Infrared Plasmonic Photothermal Conversion and Surface Coating. *Journal of Materials Science and Chemical Engineering* **2014,** *2* (1), 20-25.

57. Pearce, M. E.; Melanko, J. B.; Salem, A. K., Multifunctional Nanorods for Biomedical Applications. *Pharmaceutical Research* **2007,** *24* (12), 2335-2352.

58. Warrier, P.; Yuan, Y.; Beck, M. P.; Teja, A. S., Heat transfer in nanoparticle suspensions: modeling the thermal conductivity of nanofluids. *AIChE Journal* **2010,** *56* (12), 3243-3256.

59. Yu, C.; Irudayaraj, J., Multiplex biosensor using gold nanorods. *Analytical Chemistry* **2007,** *79* (2), 572-579.

60. Mie, G., Beiträge zur Optik trüber Medien, speziell kolloidaler Metallösungen. *Ann. Phys.* **1980,** *330* (3), 377-445.

61. Nehl, C. L.; Hafner, J. H., Shape-dependent plasmon resonances of gold nanoparticles. *J. Mater. Chem.*, **2008,** *18*, 2415-2419.

62. Gans, R., Über die Form ultramikroskopischer Goldteilchen. *Ann. Phys.* **1912,** *342* (5), 881-900.

63. Link, S.; Mohamed, M. B.; El-Sayed, M. A., Addition and correction. *J. Phys. Chem. B* **2005,** *109* (20), 10531-10532.

64. Ahmed, M.; Narain, R., Rapid synthesis of gold nanorods using a one-step photochemical strategy. *Langmuir* **2010,** *26* (23), 18392-18399.

65. Kim, F.; Song, J. H.; Yang, P., Photochemical synthesis of gold nanorods. *J. Am. Chem. Soc.* **2002,** *124* (48), 14316-14317.

66. Pérez-Juste, J.; Pastoriza-Santos, I.; M. Liz-Marzán, L.; Mulvaney, P., Gold nanorods: synthesis, characterization and applications. *Coord. Chem. Rev.* **2005,** *249* (17-18), 1870-1901.

67. Köppl, S. Seed-mediated synthesis of high aspect ratio nanorods and nanowires of gold and silver. PhD thesis, ETH ZURICH, 2011.

68. Cepak, V. M.; Martin, C. R., Preparation and stability of template-synthesized metal nanorod sols in organic solvents. *The Journal of Physical Chemistry B* **1998,** *102* (49), 9985-9990.

69. Hulteen, J. C.; Martin, C. R., A general template-based method for the preparation of nanomaterials. *J. Mater. Chem.* **1997,** *7*, 1075-1087.

70. Van der Zande, B. M. I.; Böhmer, M. R.; Fokkink, L. G. J.; Schönenberger, C., Colloidal dispersions of gold rods: synthesis and optical properties. *Langmuir* **2000,** *16* (2), 451-458.

71. Evans, P.; Hendren, W. R.; Atkinson, R.; Wurtz, G. A.; Dickson, W.; Zayats, A. V.; Pollard, R. J., Growth and properties of gold and nickel nanorods in thin film alumina. *Nanotechnology* **2006,** *17* (23), 5746-5753.

72. Gao, C.; Zhang, Q.; Lu, Z.; Yin, Y., Templated synthesis of metal nanorods in silica nanotubes. *Journal of the American Chemical Society* **2011,** *133* (49), 19706-19709.

73. Wang, S.; Han, J.; Song, D.; Wang, X., Effect of NaOH solution concentration on the quality of controllable silicon nanowires array fabrication. *Materials Research Express* **2020,** *6* (12), 1250e9.

74. Yu; Chang, S.-S.; Lee, C.-L.; Wang, C. R. C., Gold nanorods: electrochemical synthesis and optical properties. *The Journal of Physical Chemistry B* **1997,** *101* (34), 6661-6664.

75. Chang, S.-S.; Shih, C.-W.; Chen, C.-D.; Lai, W.-C.; Wang, C. R. C., The shape transition of gold nanorods. *Langmuir* **1999,** *15* (3), 701-709.

76. Orendorff, C. J.; Murphy, C. J., Quantity of metal content in the silver-assisited growth of gold nanorods. *J. Phys. Chem. B* **2006,** *110*, 3990-3994.

77. Nikoobakht, B.; El-Sayed, M. A., Preparation and growth mechanism of gold nanorods (NRs) using seed-mediated growth method. *Chem. Mater.* **2003,** *15*, 1957-1962.

78. Abdelrasoul, G. N.; Cingolani, R.; Diaspro, A.; Athanassiou, A.; Pignatelli, F., Photochemical synthesis: effect of UV irradiation on gold nanorods morphology. *Journal of Photochemistry and Photobiology A: Chemistry* **2014,** *275*, 7-11.

79. Cheng, J.; Ge, L.; Xiong, B.; He, Y., Investigation of pH effect on gold nanorods synthesis. *Journal of the Chinese chemical Society* **2011,** *58*, 822-827.

80. Xu, X.; Zhao, Y.; Xue, X.; Huo, S.; Chen, F.; Zou, G.; Liang, X.-J., Seedless synthesis of high aspect ratio gold nanorods with high yield. *Journal of Materials Chemistry A* **2014,** *2* (10), 3528-3535.

81. Li, M.; Qian, L.; Han, C., Seedless synthesis of gold nanorods with longitudinal surface plasmon resonance wavelength of 1200 nm. *Spectroscopy Letters* **2017,** *50* (10), 585-590.

82. Yang, W.; Chen, Y.; Cheng, W., *Properties of DNA-capped nanoparticles*. Springer: Heidelberg, 2014.

83. An, L.; Wang, Y.; Tian, Q.; Yang, S., Small gold nanorods: recent advances in synthesis, biological imaging, and cancer therapy. *Materials* **2017,** *10* (12), 1372-1393.

84. Jana, N. R.; Gearheart, L.; Murphy, C. J., Seed-mediated growth approach for shape-controlled synthesis of spheroidal and rod-like gold nanoparticles using a surfactant template. *Adv. Mater.* **2001,** *13* (18), 1389-1392.

85. Guo, J.; Rahme, K.; He, Y.; Li, L.; Holmes, J. D.; O'Driscoll, C. M., Gold nanoparticles enlighten the future of cancer theranostics. *International Journal of Nanomedicine* **2017,** *12*, 6131-6152.

86. Mbalaha, Z. S.; Edwards, P. R.; Birch, D. J. S.; Chen, Y., Synthesis of small gold nanorods and their subsequent functionalization with hairpin single stranded DNA. *ACS Omega* **2019,** *4* (9), 13740-13746.

87. Chen, H.; Shao, L.; Li, Q.; Wang, J., Gold nanorods and their plasmonic properties. *Chemical Society Reviews* **2013,** *42* (7), 2679-2724.

88. Mackey, M. A.; Ali, M. R. K.; Austin, L. A.; Near, R. D.; El-Sayed, M. A., The most effective gold nanorod size for plasmonic photothermal therapy: theory and in vitro experiments. *J. Phys. Chem. B,* **2014,** *118* (5), 1319–1326.

89. Wei, G.; Yu, J.; Wang, J.; Gu, P.; Birch, D. J. S.; Chen, Y., Hairpin DNA-functionalized gold nanorods for mRNA detection in homogenous solution. *Journal of Biomedical Optics* **2016,** *21* (9), 09700-097009.

90. Watt, J.; Hance, B. G.; Anderson, R. S.; Huber, D. L., Effect of seed age on gold nanorod formation: a microfluidic, real-time investigation. *Chemistry of Materials* **2015,** *27* (18), 6442-6449.

91. Jin, W.; Liang, G.; Zhong, Y.; Yuan, Y.; Jian, Z.; Wu, Z.; Zhang, W., The influence of CTAB-capped seeds and their aging time on the morphologies of silver nanorparticles. *Nanoscale Research Letters* **2019,** *14* (81), 3-11.

92. Locatelli, E.; Monaco, I.; Franchini, M. C., Surface modifications of gold nanorods for applications in nanomedicine. *RSC Advances* **2015,** *5* (28), 21681-21699.

93. Wijaya, A.; Hamad-Schifferli, K., Ligand customization and DNA functionalization of gold nanorods via round-trip phase transfer ligand exchange. *Langmuir* **2008,** *24*, 9966-9969.

94. Chen, Y.-S.; Frey, W.; Kim, S.; Homan, K.; Kruizinga, P.; Sokolov, K.; Emelianov, S., Enhanced thermal stability of silica-coated gold nanorods for photoacoustic imaging and image-guided therapy. *Opt. Express* **2010,** *18* (9), 8867-8878.

95. Chen, Y. S.; Frey, W.; Kim, S.; Kruizinga, P.; Homan, K.; Emelianov, S., Silica-coated gold nanorods as photoacoustic signal nanoamplifiers. *Nano Lett* **2011,** *11* (2), 348-354.

96. Alam, S.; Mukhopadhyay, A., Conjugation of gold nanorods with bovine serum albumin protein. *The Journal of Physical Chemistry C* **2014,** *118* (47), 27459-27464.

97. Turcheniuk, K.; Dumych, T.; Bilyy, R.; Turcheniuk, V.; Bouckaert, J.; Vovk, V.; Chopyak, V.; Zaitsev, V.; Mariot, P.; Prevarskaya, N.; Boukherroub, R.; Szunerits, S., Plasmonic photothermal cancer therapy with gold nanorods/reduced graphene oxide core/shell nanocomposite. *RSC Adv.* **2016,** *6*, 1600-1610.

98. Marangoni, V.; Cancino, J.; Zucolotto, V., Synthesis, Physico-chemical properties, and biomedical applications of gold aanorods-a review. *Journal of Biomedical Nanotechnology* **2016,** *12*, 1136-1158.

99. Pu, Y.; Liu, Z.; Lu, Y.; Yuan, P.; Liu, J.; Yu, B.; Wang, G.; Yang, C. J.; Liu, H.; Tan, W., Using DNA aptamer probe for immunostaining of cancer frozen tissues. *Analytical Chemistry* **2015,** *87* (3), 1919-1924.

100. Saha, K.; Agasti, S. S.; Kim, C.; Li, X.; Rotello, V. M., Gold nanoparticles in chemical and biological sensing. *Chemical Reviews* **2012,** *112* (5), 2739-2779.

101. Unser, S.; Bruzas, I.; He, J.; Sagle, L., Localized surface plasmon resonance biosensing: current challenges and approaches. *Sensors* **2015,** *15* (7), 15684-15716.

102. Bryce, C. F. A.; Pacini, D., *The structure and function of nucleic acids*. Revised edition ed.; Holbrooks Printers: Portsmouth, 1998.

103. Ball, D.; Hill, J.; Scott, R., *The basics of general, organic, and biological chemistry*. Saylor Foundation: Washington, 2011.

104. Redmonds, G.; King, T.; Hey, D., *Surnames, DNA and family history*. Oxford University Press: Oxford, 2011.

105. Zhu, G.; Hu, R.; Zhao, Z.; Chen, Z.; Zhang, X.; Tan, W., Noncanonical self-assembly of multifunctional DNA nanoflowers for biomedical applications. *J. Am. Chem. Soc.* **2013,** *135* (44), 16438-16445.

106. Caruthers, M. H., Concepts in biochemistry. *Journal of Chemical Education* **1989,** *66* (7), 577-580.

107. Lakowicz, J. R., *Principles of Fluorescence Spectroscopy*. 3rd ed.; Springer: New York, 2006.

108. Zhang, Y.; Birch, D. J. S.; Chen, Y., Two-photon excited surface plasmon enhanced energy transfer between DAPI and gold nanoparticles: opportunities in intra-cellular imaging and sensing. *Appl. Phys. Lett.* **2011,** *99*, 103701-103703.

109. Swierczewskaa, M.; Lee, S.; Chen, X., The design and application of fluorophore–gold nanoparticle activatable probes. *Phys. Chem. Chem. Phys.* **2011,** *13* (21), 9929-9941.

110. Birch, D. J. S.; Rolinski, O. J., Fluorescence resonance energy transfer sensors. *Res. Chem. Intermed.* **2001,** *27* (45), 425-446.

111. Zhang, Y.; Wei, G.; Yu, J.; Birch, D. J. S.; Chen, Y., Surface plasmon enhanced energy transfer between gold nanorods and fluorophores: application to endocytosis study and RNA detection. *Faraday Discuss* **2015,** *178*, 383-394.

112. Zhang, Y.; Chen, Y.; Yu, J.; Birch, D. J. S., A surface plasmon enhanced FLIM-FRET imaging approach based on Au nanoparticles. *Med. Devices Diagn. Eng.* **2017,** *2* (1), 78-82.

113. Zhu, Q.; Liu, G.; Kai, M., DNA aptamers in the diagnosis and treatment of human diseases. *Molecules* **2015,** *20*, 20979-20997.

114. Base Pair DNA aptamer or RNA aptamer? https://www.basepairbio.com/dna-aptamers-rna-aptamers/ (accessed 30/05/2019).

115. Song, Y.; Zhu, Z.; An, Y.; Zhang, W.; Zhang, H.; Liu, D.; Yu, C.; Duan, W.; Yang, C. J., Selection of DNA aptamers against epithelial cell adhesion molecule for cancer cell imaging and circulating tumor cell capture. *Anal. Chem.* **2013,** *85*, 4141-4149.

116. Zhou, J.; Rossi, J. J., Cell-type-specific, aptamer-functionalized agents for targeted disease therapy. *Molecular Therapy - Nucleic Acids* **2014,** *3* (6), 1-17.

117. Ocsoy, I.; Yusufbeyoglu, S.; Yılmaz, V.; McLamore, E. S.; Ildız, N.; Ülgen, A., DNA aptamer functionalized gold nanostructures for molecular recognition and photothermal inactivation of methicillin-resistant staphylococcus aureus. *Colloids and surfaces. B, Biointerfaces* **2017,** *159*, 16-22.

118. Yasun, E.; Gulbakan, B.; Ocsoy, I.; Yuan, Q.; Shukoor, M. I.; Li, C.; Tan, W., Enrichment and detection of rare proteins with aptamer-conjugated gold nanorods. *Anal Chem* **2012,** *84* (14), 6008-6015.

119. Xue, Y. H.; Zhang, X. F.; Dong, Q. Z.; Sun, J.; Dai, C.; Zhou, H. J.; Ren, N.; Jia, H. L.; Ye, Q. H.; Qin, L. X., Thrombin is a therapeutic target for metastatic osteopontin-positive hepatocellular carcinoma. *Hepatology* **2010,** *52* (6), 2012-2022.

120. Yu, Y.; Liang, C.; Lv, Q.; Li, D.; Xu, X.; Liu, B.; Lu, A.; Zhang, G., Molecular selection, modification and development of therapeutic oligonucleotide aptamers. *International Journal of Molecular Sciences* **2016,** *17* (3), 358-377.

121. Kaur, H.; Bruno, J. G.; Kumar, A.; Sharma, T. K., Aptamers in the therapeutics and diagnostic pipelines. *Theranostics* **2018,** *8* (15), 4016-4032.

122. Palmieri, D.; Richmond, T.; Piovan, C.; Sheetz, T.; Zanesi, N.; Troise, F.; James, C.; Wernicke, D.; Nyei, F.; Gordon, T. J.; Consiglio, J.; Salvatore, F.; Coppola, V.; Pichiorri, F.; Lorenzo, C. D.; Croce, C. M., Human anti-nucleolin recombinant immunoagent for cancer therapy. *PNAS* **2015,** *112* (30), 9418-9423.

123. Esposito, C. L.; Catuogno, S.; Condorelli, G.; Ungaro, P.; Franciscis, V. D., Aptamer chimeras for therapeutic delivery: the challenging perspectives. *Genes* **2018,** *9* (529), 2-20.

124. Gilles, M.; Maione, F.; Cossutta, M.; Carpentier, G.; Caruana, L.; Maria, S. D.; Houppe, C.; Destouches, D.; Shchors, K.; Prochasson, C.; Mongelard, F.; Lamba, S.; Bardelli, A.; Bouvet, P.; Couvelard, A.; Courty, J.; Giraudo, E.; Cascone, l., Nucleolin targeting impairs the progression of pancreatic cancer and promotes the normalization of tumor vasculature. *Cancer Res.* **2016,** *76* (24), 7182-7193.

125. Song, Y.; Shi, Y.; Huang, M.; Wang, W.; Wang, Y.; Cheng, J.; Lei, Z.; Zhu, Z.; Yang, C., Bioinspired engineering of a multivalent aptamer-functionalized nanointerface

to enhance the capture and release of circulating tumor cells. *Angew. Chem. Int. Ed.* **2019,** *58*, 2236-2240.

126. Garcia, E.; Hayden, A.; Birts, C.; Britton, E.; Cowie, A.; Pickard, K.; Mellone, M.; Choh, C.; Derouet, M.; Duriez, P.; Noble, F.; White, M. J.; Primrose, J. N.; Strefford, J. C.; Rose-Zerilli, M.; Thomas, G. J.; Ang, Y.; Sharrocks, A. D.; Fitzgerald, R. C.; Underwood, T. J.; consortium, O.; MacRae, S.; Grehan, N.; Abdullahi, Z.; de la Rue, R.; Noorani, A.; Elliott, R. F.; de Silva, N.; Bornschein, J.; O'Donovan, M.; Contino, G.; Yang, T.-P.; Chettouh, H.; Crawte, J.; Nutzinger, B.; Edwards, P. A. W.; Smith, L.; Miremadi, A.; Malhotra, S.; Cluroe, A.; Hardwick, R.; Davies, J.; Ford, H.; Gilligan, D.; Safranek, P.; Hindmarsh, A.; Sujendran, V.; Carroll, N.; Turkington, R.; Hayes, S. J.; Ang, Y.; Preston, S. R.; Oakes, S.; Bagwan, I.; Save, V.; Skipworth, R. J. E.; Hupp, T. R.; O'Neill, J. R.; Tucker, O.; Taniere, P.; Owsley, J.; Crichton, C.; Schusterreiter, C.; Barr, H.; Shepherd, N.; Old, O.; Lagergren, J.; Gossage, J.; Davies, A.; Chang, F.; Zylstra, J.; Sanders, G.; Berrisford, R.; Harden, C.; Bunting, D.; Lewis, M.; Cheong, E.; Kumar, B.; Parsons, S. L.; Soomro, I.; Kaye, P.; Saunders, J.; Lovat, L.; Haidry, R.; Eneh, V.; Igali, L.; Welch, I.; Scott, M.; Sothi, S.; Suortamo, S.; Lishman, S.; Beardsmore, D.; Anderson, C.; Smith, M. L.; Secrier, M.; Eldridge, M. D.; Bower, L.; Achilleos, A.; Lynch, A. G.; Tavare, S., Authentication and characterisation of a new oesophageal adenocarcinoma cell line: MFD-1. *Scientific Reports* **2016,** *6*, 32417-32429.

127. Chen, Y.; Cheng, B.; He, Z.; Wang, S.; Wang, Z.; Sun, M.; Song, H.; Fang, Y.; Chen, F.; Xiong, B., Capture and identification of heterogeneous circulating tumor cells using transparent nanomaterials and quantum dots-based multiplexed imaging. *Journal of Cancer* **2016,** *7* (1), 69-79.

128. World Health Organization, Cancer. World Health Organization: 2018.

129. American Cancer Society, Cancer Facts & Figures 2018. American Cancer Society: Atlanta, 2018.

130. National Cancer Institute, Cancer statistics reports. Bethesda, 2016.

131. Kanavos, P., The rising burden of cancer in the developing world. *Annals of Oncology* **2006,** *17*, 815-823.

132. World Health Organization, Cancer report. Geneva, 2015.

133. World Health Organization, WHO report on cancer: setting priorities, investing wisely and providing care for all. Geneva, 2020.

134. Zhao, Y.; Tong, L.; Li, Y.; Pan, H.; Zhang, W.; Guan, M.; Li, W.; Chen, Y.; Li, Q.; Li, Z.; Wang, H.; Yu, X. F.; Chu, P. K., Lactose-functionalized gold nanorods for sensitive and rapid serological diagnosis of cancer. *ACS Appl. Mater. Interfaces* **2016,** *8* (9), 5813-5820.

135. Nounou, M. I.; ElAmrawy, F.; Ahmed, N.; Abdelraouf, K.; Goda, S.; Syed-Sha-Qhattal, H., Breast cancer: conventional diagnosis and treatment modalities and recent patents and technologies. *Breast Cancer: Basic and Clinical Research* **2015,** *9* (S2), 17-34.

136. Damyanov, C. A.; Maslev, I. K.; Pavlov, V. S.; Avramov, L., Conventional treatment of cancer realities and problems. *Annals of Complementary and Alternative Medicine* **2018,** *1* (1), 1-9.

137. Nguyen, K. T., Targeted nanoparticles for cancer therapy: promises and challenges. *Journal of Nanomedicine & Nanotechnology* **2011,** *2* (5), 1000103e-1000104e.

138. Williams, D., Essential biomaterials science. Cambridge University Press: Cambridge, 2014.

139. Chandrashekara, S., The treatment strategies of autoimmune disease may need a different approach from conventional protocol: a review. *Indian Journal of Pharmacology* **2012,** *44* (6), 665-671.

140. Alagiri, M.; Rameshkumar, P.; Pandikuma, A., Gold nanorod-based electrochemical sensing of small biomolecules: a review. *Microchim Acta* **2017,** *184*, 1-24.

141. Minhee, K.; Kim, D.; Kim, K.; Jung, W.; Kim, D., Applications of cancer cell-specific aptamers in targeted delivery of anticancer therapeutic agents. *Molecules* **2018,** *23* (830), 1-20.

142. Chen, J.; Li, X.; Zhao, X.; Wu, Q.; Zhu, H.; Mao, Z.; Gao, C., Doxorubicin-conjugated pH-responsive gold nanorods for combinedphotothermal therapy and chemotherapy of cancer. *Bioactive Materials* **2018,** *3*, 347-354.

143. Chen, H.; Chi, X.; Li, B.; Zhang, M.; Ma, Y.; Achilefu, S.; Gu, Y., Drug loaded multilayered gold nanorods for combined photothermal and chemotherapy. *Biomaterials Science* **2014,** *2* (7), 996-1006.

144. Zhang, Z.; Wang, J.; Nie, X.; Wen, T.; Ji, Y.; Wu, X.; Zhao, Y.; Chen, C., Near infrared laser-induced targeted cancer therapy using thermoresponsive polymer encapsulated gold nanorods. *Journal of the American Chemical Society* **2014,** *136* (20), 7317-7326.

145. Omair, Z.; Talukder, M. A., Sensitivity analysis of gold nanorod biosensors for single molecule detection. *Plasmonics* **2019,** *14* (6), 1611-1619.

146. Tadepalli, S.; Kuang, Z.; Jiang, Q.; Liu, K.-K.; Fisher, M. A.; Morrissey, J. J.; Kharasch, E. D.; Slocik, J. M.; Naik, R. R.; Singamaneni, S., Peptide functionalized gold nanorods for the sensitive detection of a cardiac biomarker using plasmonic paper devices. *Scientific Reports* **2015,** *5*, 16206-16217.

147. Chiu, M. J.; Chu, L. K., Quantifying the photothermal efficiency of gold nanoparticles using tryptophan as an in situ fluorescent thermometer. *Phys. Chem.* **2015,** *17* (26), 17090-17100.

148. Zhang, Y.; Yu, J.; Birch, D.; Chen, Y., Gold nanorods for fluorescence lifetime imaging in biology. *Journal of Biomedical Optics* **2010,** *15* (2), 020504-020506.

149. Yan, E.; Cao, M.; Wang, Y.; Hao, X.; Pei, S.; Gao, J.; Wang, Y.; Zhang, Z.; Zhang, D., Gold nanorods contained polyvinyl alcohol/chitosan nanofiber matrix for cell imaging and drug delivery. *Materials Science and Engineering: C* **2016,** *58*, 1090-1097.

150. Betzer, O.; Ankri, R.; Motiei, M.; Popovtzer, R., Theranostic approach for cancer treatment: multifunctional gold nanorods for optical imaging and photothermal therapy. *Journal of Nanomaterials* **2015,** *16* (1), 1-7.

151. Al-Bakri, A. G.; Mahmoud, N. N., Photothermal-induced antibacterial activity of gold nanorods loaded into polymeric hydrogel against pseudomonas aeruginosa iofilm. *Molecules* **2019,** *24* (14), 2661-2680.

152. Yang, T.; Wang, D.; Liu, X., Assembled gold nanorods for the photothermal killing of bacteria. *Colloids and Surfaces B: Biointerfaces* **2019,** *173*, 833-841.

153. Manivasagan, P.; Hoang, G.; Moorthy, M. S.; Mondal, S.; Doan, V. H. M.; Kim, H.; Phan, T. T. V.; P, N. T.; Oh, J., Chitosan/fucoidan multilayer coating of gold nanorods as highly efficient near infrared photothermal agents for cancer therapy. *Carbohydrate Polymers* **2019,** *211*, 360-369.

154. Jain, P. K.; Lee, K. S.; El-Sayed, I. H.; El-Sayed, M. A., Calculated absorption and sacttering properties of gold nanoparticles of different size, shape and composition:

application in biomedical imaging and biomedicine. *J.Phys. Chem. B.* **2006,** *110*, 7238-7248.

155. Huang, Y.; Sefah, K.; Bamrungsap, S.; Chang, H.; Tan, W., Selective photothermal therapy for mixed cancer cells using aptamer-conjugated nanorods. *Langmuir* **2008,** *24*, 11860-11865.

156. Wang, J.; Sefah, K.; Altman, M. B.; Chen, T.; You, M.; Zhao, Z.; Huang, C. Z.; Tan, W., Aptamer-conjugated nanorods for targeted photothermal therapy of prostate cancer stem cells. *Chem. Asian J.* **2013,** *8*, 2417-2422.

Chapter 2

Characterization techniques

2. 1. Introduction

Gold nanorods manifest fascinating photo-physical properties such as absorption, scattering, fluorescence emission and fluorescence lifetime. Therefore, the characterization techniques employed to characterize the photophysical properties of the gold nanorods are absorption spectroscopy, fluorescence spectroscopy and microscopy.

2. 2. Absorption spectroscopy

Spectroscopy could be defined as the study of interaction between electromagnetic wave and matter. Fundamentally, the interaction of electromagnetic wave with matter results in light absorption, scattering, transmission and emission. Absorption spectroscopy involves the absorption of an electromagnetic wave by a molecule following excitation at a particular wavelength from an appropriate electromagnetic wave source. The range of wavelengths over which electromagnetic wave is absorbed by molecules can be referred to as the absorption spectrum. The amount of light absorbed by molecules depends on the molecules' concentration, molar extinction coefficient and optical path length. The amount of light absorbed by a molecule is directly proportional to the molecule's molar extinction coefficient, concentration, and the path length of the solution through which light is transmitted[1]; and this is known as the Beer-Lambert law, described quantitatively as:

$$A = \varepsilon l c \qquad 2.1.$$

where A is the absorbance of the molecule, ε is the molar extinction coefficient of the molecule, l is the optical path length usually 1cm for a conventional cuvette in which the solution is held, and c is the concentration of the molecule in moles per cm^3.

Gold nanorods absorb electromagnetic light from the visible to the infrared of the electromagnetic spectrum. The optical absorption of gold nanorods is measured in the range of 400 nm - 1100 nm with a spectrophotometer. A spectrophotometer is an optical device for measuring absorbance of light by a sample as a function of wavelength. It is

made up of double excitation sources (lamps) for excitation in the ultraviolet/visible electromagnetic spectrum, a monochromator (wavelength selector), sample chamber(s), detector(s) and a signal processor. Examples of lamps used in spectrophotometers include halogen and deuterium for excitations ranging from 300 nm -1100 nm, and 190 nm -350 nm respectively[1]. Light from the deuterium lamp can be blocked by adjusting the position of a planar mirror, P1 in synchronization with the monochromator wavelength, thus, allowing the light from the halogen lamp to be reflected on a toroidal mirror[2]. The toroidal mirror focuses the light via the filter wheel, via an entry slit onto the monochromator[2]. By means of a diffraction grating, the monochromator allows a specific wavelength of light to exit via the slit onto the spherical mirror. By virtue of a beam splitter, light emanating from the spherical mirror is split by 50 % to the two planar mirrors, P2 and P3 respectively[2]. Simultaneously, P2 and P3 focus their light to the respective sample chambers (sample chamber and reference chamber) where a fraction of the light is absorbed by an analyte suspended in a cuvette. The transmitted light from the sample strikes the detector and the information is processed in the signal processor unit where it is converted to a digital signal. The working principle of a spectrophotometer is illustrated in fig. 2.1. Prior to measuring the absorbance of an analyte, a spectrophotometer is calibrated with a blank solution to set the instrument to zero absorbance and 100 % transmittance[3].

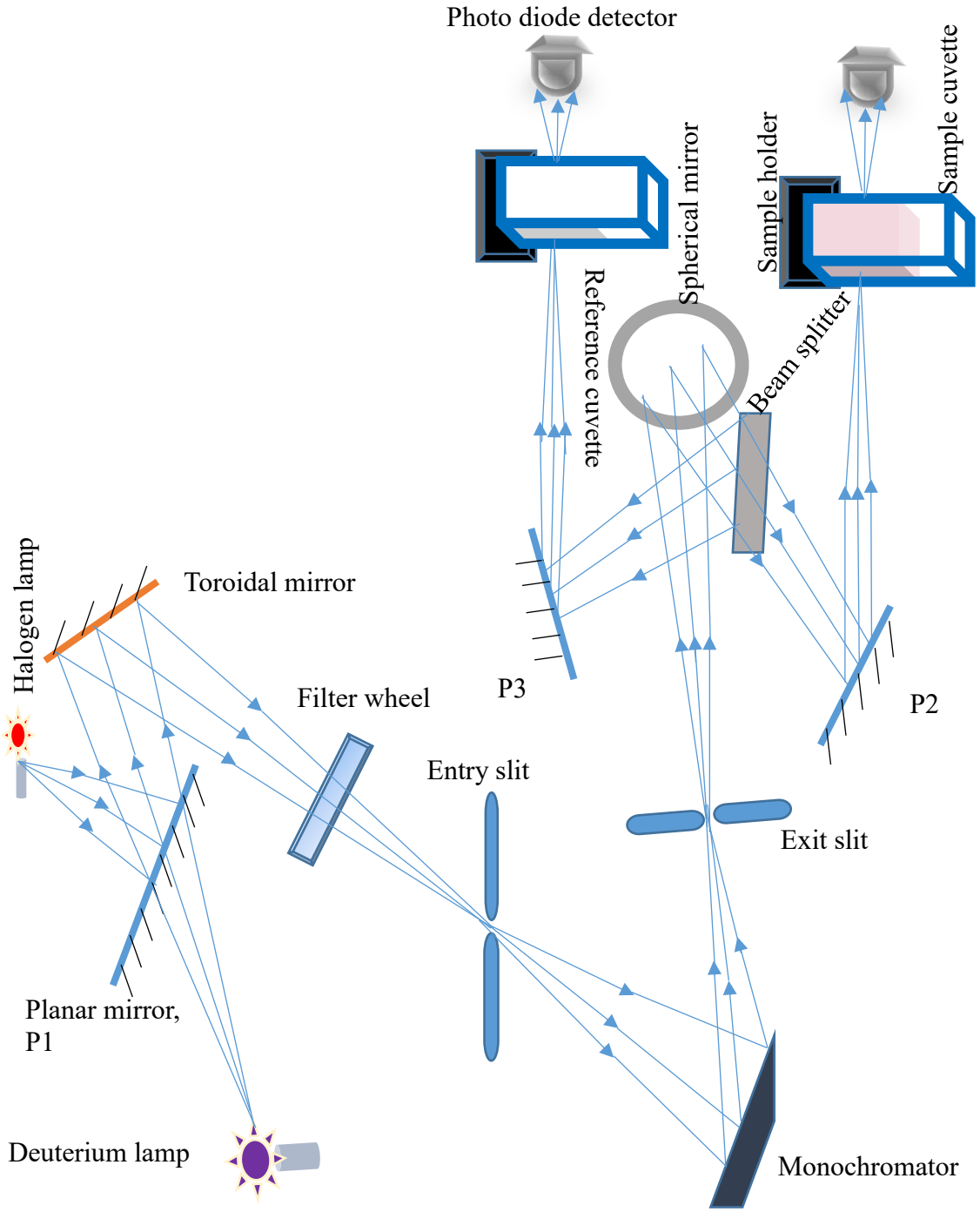

Figure 2.1. The working principle of a UV-vis spectrophotometer showing the optical path of light.

2. 3. Fluorescence spectroscopy

Fluorescence is the emission of a photon by a molecule from the lowest energy level of a singlet excited state (S_1) to the ground state (S_0)[4]. Internal conversion from the higher excited electronic states such as S_2 can also occur and this is a non-radiative process through which energy is lost as heat, therefore the excited electron returns to S_1 where it relaxes shortly before emitting a photon. The electrons of molecules in the singlet excited state return to the ground state by emitting a photon because both the excited state electron and ground state electron are paired in opposite spin orientation. The return of the excited electron to the ground state can be described as a radiative decay process because a photon of light is emitted. Fluorescence is a rapid event that occurs in ~10^8 s^{-1}. Displayed in fig. 2.2. is the Jablonski diagram describing the fluorescence process following optical absorption of light from the ground state by a molecule. It can be seen from the Jablonski diagram that optical absorption occurs at lower wavelength while emission occurs at higher wavelength. The difference between emission wavelength and absorption wavelength is known as the Stokes shift.

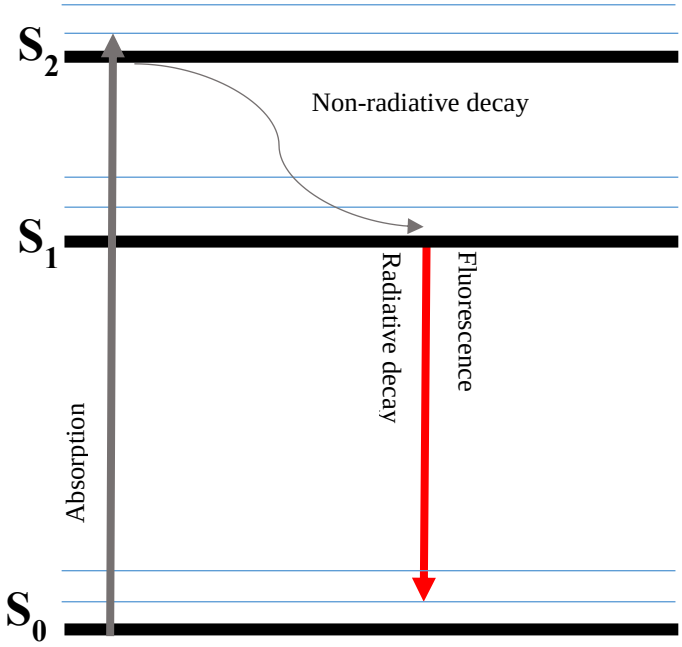

Figure 2.2. Jablonski diagram describing absorption and fluorescence processes.

Fluorescence spectroscopy is a powerful technique in biochemical applications such as sensing, cell imaging and clinical diagnosis[4-5]. Fluorescence spectroscopy can be divided into steady-state spectroscopy and time-domain fluorescence spectroscopy.

2. 3. 1. Steady-state spectroscopy

Steady-state spectroscopy involves a constant illumination of a sample with a lamp to measure the fluorescence intensity as a function of wavelength. Changes in the fluorescence intensity can be used to recognise the binding of nanoprobes to a target[6]. The range of wavelengths for which fluorescence intensity is measured is called the emission spectrum[4]. Fluorescence emission intensity can be measured with a spectrofluorometer. A spectrofluorometer is composed of a lamp source, an excitation monochromator, a sample chamber, an emission monochromator, an amplifier and a recorder. These components are schematically shown in fig. 2.3.

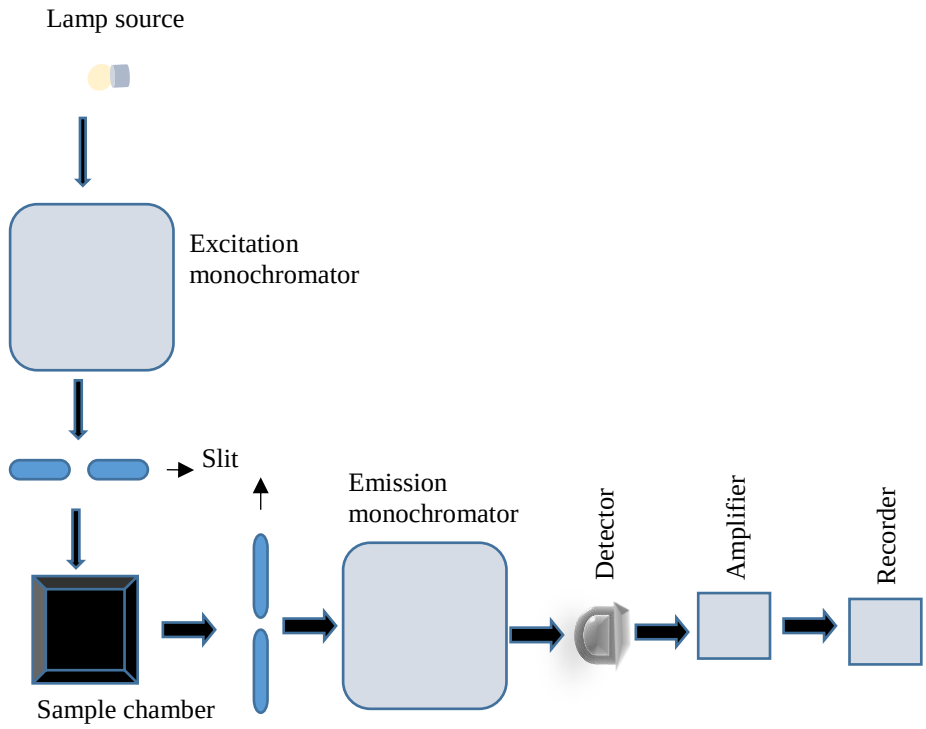

Figure 2. 3. A schematic set-up of a spectrofluorometer.

2. 3. 2. Time-resolved fluorescence spectroscopy

Time-resolved fluorescence lifetime spectroscopy is a useful technique for resolving molecules that exist in different conformations using fluorescence lifetimes as a contrast parameter[4]. It can be used to resolve different species with different lifetimes in a heterogenous environment. These advantages make time-resolved fluorescence lifetime measurement a very useful tool in fluorescence lifetime based sensing of analyte and fluorescence lifetime imaging (FLIM)[7]. Time-resolved fluorescence lifetime spectroscopy can be performed using a time correlated single photon counting (TCSPC) technique with an IBH Fluorocube fluorescence lifetime system shown in fig. 2.4. The TCSPC technique involves a pulsed excitation of a sample with a NanoLED or a laser diode light source. The sample is excited by a pulsed ligth source and the arrival time of the observed emitted photon is measured and stored in a histogram. The histogram depicts the intensity decay of the sample. The intensity decay can be written as:

$$I(t) = I_0 e^{-t/\tau} \qquad 2.2.$$

where I_0 is the intensity at $t = 0$ and τ is the decay time.

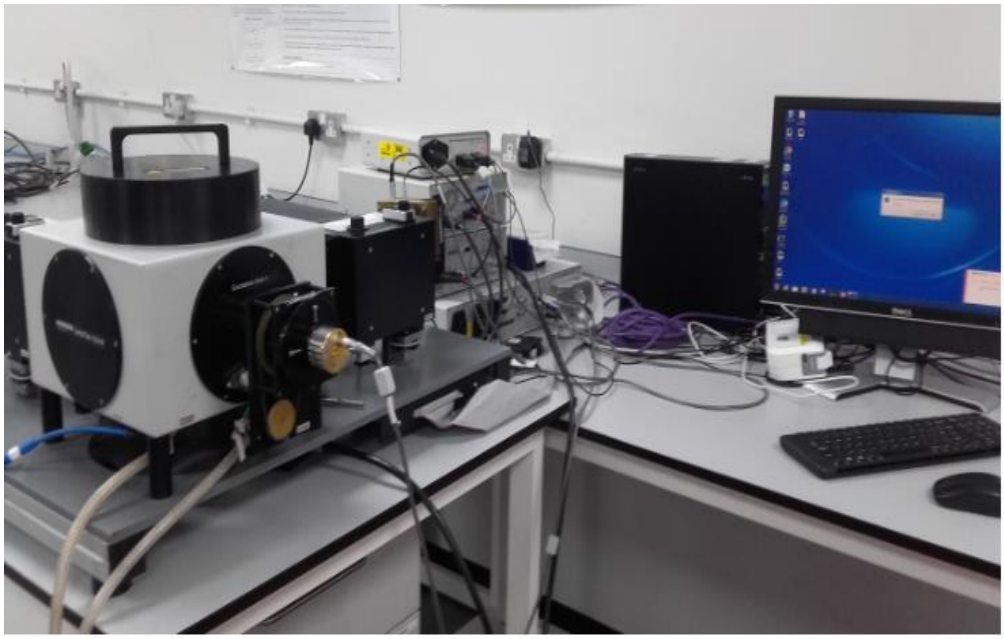

Figure 2.4. A Fluorocube fluorescence lifetime system.

Prior to a fluorescence decay measurement, the instrument response function (IRF) is performed with a zero fluorescence lifetime sample to ascertain the shortest time profile the instrument can measure for use in reconvolution. The excitation and emission-motorized polarizers are set to 0^0. Both excitation and emission monochromators are set at the excitation wavelength of the NanoLED laser source during the IRF (prompt) measurement. For fluorescence decay measurement, the excitation motorized polarizer remains at 0^0 while the emission-motorized polarizer is set to the magic angle (54.7^0) to avoid polarization artefacts. The emission monochromator is set at the emission wavelength of the sample. Data analysis can be performed using DAS6 software to fit fluorescence lifetimes decay curves to a multi-exponential decay model given as:

$$I(t) = \sum_i B_i \, exp\left(-\frac{t}{\tau_i}\right) \qquad 2.3.$$

where τ_i are the decay times and B_i the associated amplitudes. The fractional contribution of each lifetime component to the steady-state intensity is represented by:

$$\int_i = B_i\tau_i \Big/ \sum_i B_i \, \tau_i \qquad 2.4.$$

The average lifetime ($\bar{\tau}$) is calculated as:

$$\bar{\tau} = \sum_i \int_i \tau_i \qquad 2.5.$$

The procedures for fitting fluorescence lifetime decays are presented in appendix 4.

2. 4. Flow cytometry

Floating particles such as cells carrying fluorescent nanoprobes can scatter light and emit fluorescent signals as they pass through a beam of laser light. The scattered light and emitted fluorescent signals from the cells yield useful information about the physico-chemical characteristics of the flowing cells using the flow cytometry technique[8]. A flow cyotometer shown in figure 2.5. utilizes the scattered light and fluorescence emission signals from the flowing cells to generate information about the complexity and size of the cells[9] and the fluorescent signal of nanoprobes binding on the cells. The signals from the flowing cells can be collected by specific detectors placed in front of the laser source.

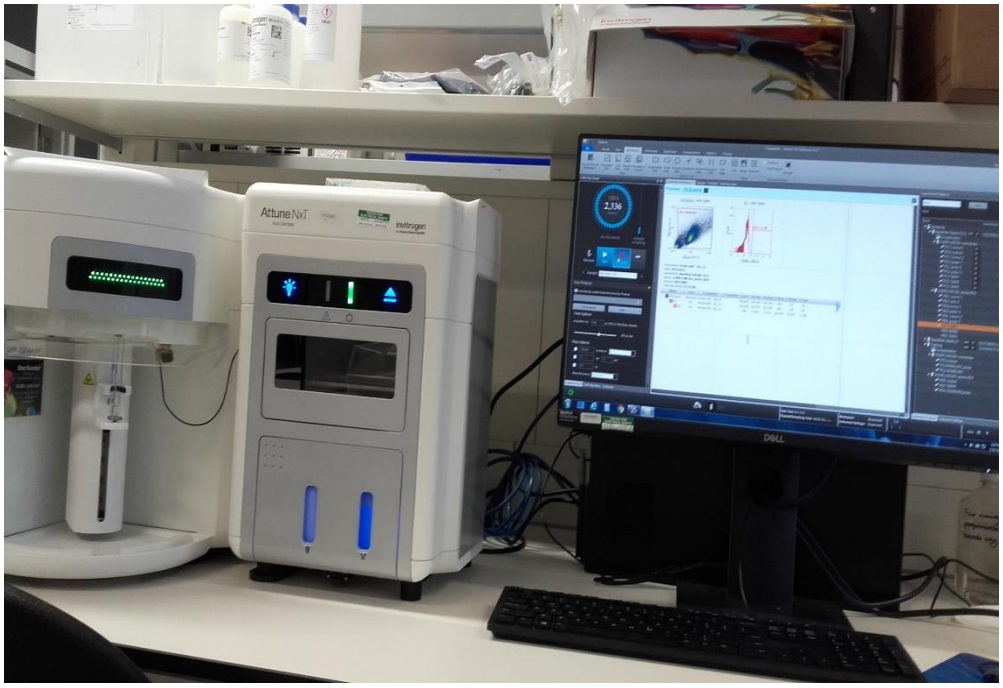

Figure 2.5. An Attune Nxt flow cytometer.

As shown in figure 2.6., the cells are hydrodynamically focused in a single narrow channel down the column by sheath fluids so that at any given time, only a single cell is intercepted by the beam of a laser light propagated perpendicular to the narrow channel containing cells[8]. The interception between the cells and the beam of a laser light results in forward scatter (FSC) and side scatter (SSC) respectively. The FSC could be due to the resultant effect of light diffraction and it is propagated in the same direction as the beam of incident laser light. The FSC intensity is proportional to the size of the cell. On the other hand, SSC intensity could be due to the effect of refraction and reflection of light and it yields information about the complexity of the cell[8]. The data collected by the detectors can be analysed by computer software and represented as a density plot and histogram plot. The density plot reflects the SSC and FSC intensities by the cells, while the histogram depicts cell count versus fluorescent intensity emitted by the fluorescent probes bound to the cells.

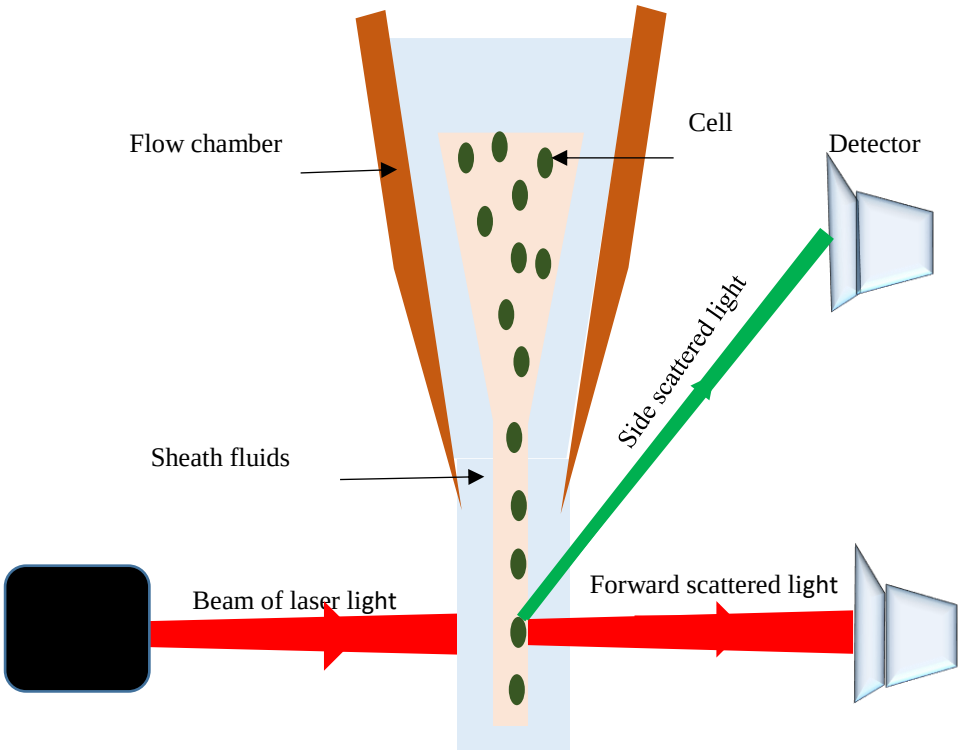

Figure 2.6. The working principle of a flow cytometer.

2. 5. Microscopy

Microscopy is a useful technique for observing the structure of microscopic substances. Microscopic techniques employed in this study are confocal fluorescence microscopy and scanning electron microscopy.

2. 5. 1. Confocal fluorescence microscopy

Confocal microscopy is an imaging technique involving a confocal fluorescence microscope. A confocal microscope has a higher axial resolution (0.5μm)[10] compared to a conventional widefield microscope. It has a pinhole in front of the detector for rejecting out-of-focus ligth. These features make the confocal microscope images sharper and crystal clear compared to the images generated by a conventional widefield microscope. The working principle of a confocal microscope is that the laser light passes through an aperture to the dichroic mirror where the light is reflected down the column of the objective to the sample spot (stage). The emitted light from the sample returns back through the dichroic mirror to the pinhole where out-of focus light (background light) is rejected. Only focused light from the sample is allowed to pass through the pinhole to the

detector. The working principle of a confocal fluorescence microscope is demonstrated in figure 2.7.

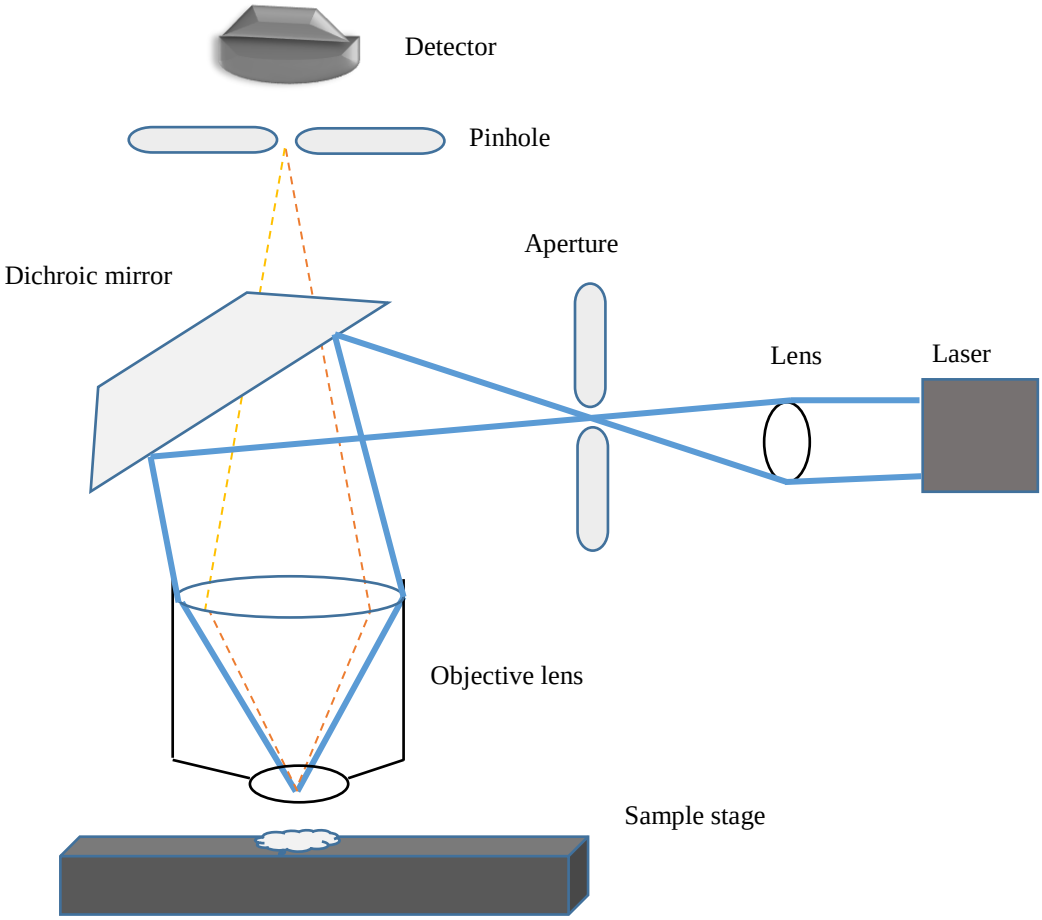

Figure 2.7. A schematic illustration of the working of a confocal microscope.

2. 5. 2. Scanning electron microscopy (SEM)

Scanning electron microscopy is an imaging technique with a scanning electron microscope (SEM). A scanning electron microscope is an analytical tool that generates images about the morphology of a sample. SEM has a resolution of 10 nm[11] and it is composed of an electron gun, two condensers, an objective aperture, objective lens, scanning coils, a sample holder and scintillator-photomultiplier detectors for different signals. The working principle of SEM is based on using the emitted electrons from a sample to reconstruct an image of the surface features of the sample. A high-energy electron beam is generated by an electron gun (tungsten filament). The high-energy

electrons generated from the electron gun are known as primary electrons. The beam of electrons are accelerated down the column by high voltage through the two condensers and sets of apertures to the sample chamber. Then, the scanning coils scan the electron beam on the surface of the sample and send the signal to the detector to generate the image of the sample. The interaction of primary electrons with the sample yields backscattered electrons (BSE), secondary electrons (SE), as well as x-rays from electron ionization. Backscattered electrons are reflected primary electrons due to elastic scattering after interacting with the sample. BSE re-emerge from the interior of the sample via the entry surface and thus, yield information about the crystallography and magnetic field of the sample[12]. The SE are emitted from the surface of the sample, therefore SE yields information about the surface features of the sample. The X-rays are emitted from the core of the sample, therefore X-rays yield information about the chemical composition of the sample. An SEM operates in two imaging modes: secondary electron mode and backscattered electron mode. The intensity of the backscattered electrons is usually high but the resolution of the BSE imaging mode is very poor due to a large angle scattering. The brightness of the BSE imaging mode depends on the atomic number of the sample. On the other hand, the intensity of the SE is low; therefore, it generates morphological information about the shape and the size of the sample. Thus, the resolution of the SE imaging mode is better than the BSE. The set-up of SEM is shown in figure 2.8.

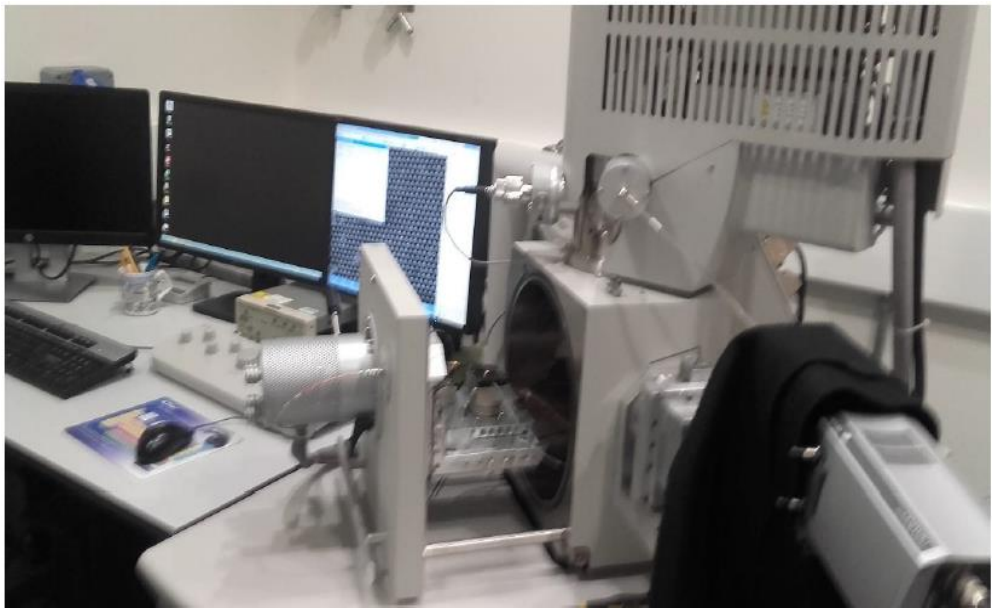

Figure 2.8. The set-up of a scanning electron microscope.

2. 5. 3. Nanosight LM10

A Nanosight is an optical device for visualizing nanoparticles undergoing Brownian motion in a liquid suspension. Basically, it is composed of a LM10 viewing unit, an optical microscope and a SCMOS camera as shown in figure 2.9. The Nanosight uses nanoparticle tracking analysis (NTA 3.0) software to analysed the size (ranging from 10 nm-1000 nm) and the concentration of the nanoparticles.

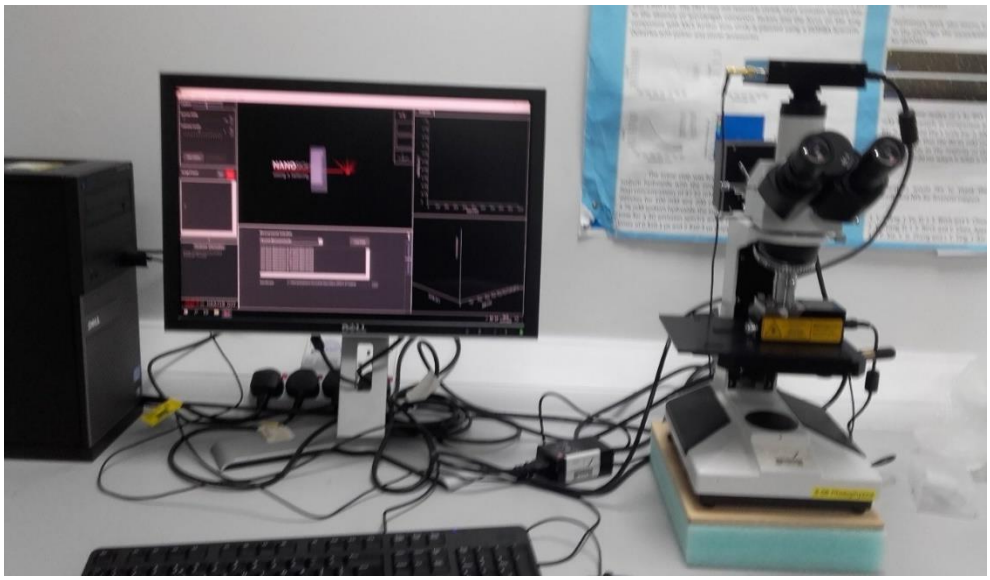

Figure 2.9. A Nanosight LM10 system.

Figure 2.10. displays the working principle of a Nanosight system. A sample of nanoparticles is introduced into the chamber of LM10 viewing unit by a syringe. The LM10 vewing unit encapsulates the laser excitation source that provides illumination to the nanoparticles. Illuminated nanoparticles undergo Brownian motion and pass through the beam path of the incident light. The motion of nanoparticles passing through the beam path can be visualized by the SCMOS camera fitted above the optical microscope. The camera captures the video clips of the nanoparticles which can be analysed by NTA 3. 0 software. The NTA analytical software tracks the trajectory of a single nanoparticle to the centre of the nanoparticle and determines the mean square displacement of each nanoparticle in the field of view. The mean square displacement of each nanoparticle is reconstructed by NTA software to generate average nanoparticle size while the nanoparticle concentration is determine by counting the individual particles.

Theorectically, NTA software determines the mean square displacement of each nanoparticle and calculates the diffusion coefficients of nanoparticles using the Einsten-Smuluchowski diffusion equation given as[13-14]:

$$\langle|\Delta x(t)|^2\rangle = \langle|x(t) - x(0)|^2\rangle = 2Dt \qquad 2.6.$$

where $\langle|\Delta x(t)|^2\rangle$ is the mean square displacement at a time (t), and D is diffusion coefficient of the nanoparticle. The diffusion coefficient of the nanoparticle is used to determine the hydrodynamic size of the nanoparticle according to Stokes-Einsten equation given as :

$$D = \frac{k_B T}{6\pi\eta r_h} \qquad 2.7.$$

where k_B is the Boltzmann constant, T is the temperature, η is the viscosity and r_h is the hydrodynamic radius of the nanoparticle.

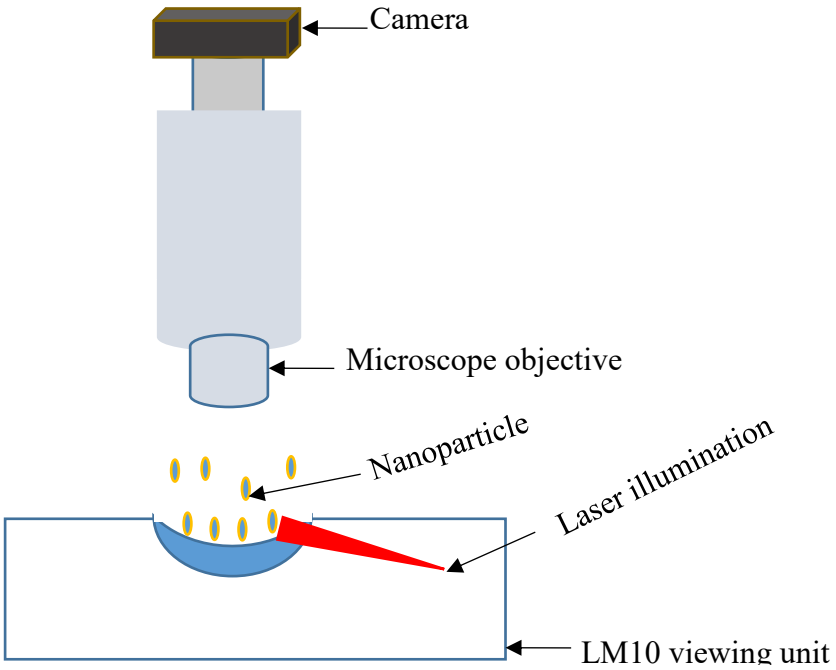

Figure 2.10. A scheme showing the working principle of a Nanosight LM10 system.

2. 6. Summary

Characterization of gold nanorods nanoprobes is very important in understanding their physico-chemical properties. Absorption, scattering fluorescenece spectroscopic techniques were employed in this study to characterize the gold nanorods based nanoprobes. Microscopic techniques were equally explored to visualize the morpohology of the gold nanorods structures and the binding of gold nanorods nanoprobes by the cells.

References

1. Russell, B. A. Protein Encapsulated Gold Nanoclusters for Biological Applications. PhD thesis, University of Strathclyde, 2017.

2. Morris, S., A UV/Vis Lambda 2 spectrometer operational manual. Bodenseewerk Perkin-Elmer & Co GmbH: Überlingen: Germany 1989.

3. JENWAY Spectrophotometers models 7300 & 7305 operating manual. http://www.jenway.com/adminimages/Jenway_7300_7305_Spectro_Manual_LO(5).pdf (accessed 07/06/2019).

4. Lakowicz, J. R., *Principles of Fluorescence Spectroscopy*. 3rd ed.; Springer: New York, 2006.

5. Ray, K.; Zhang, J.; Lakowicz, J. R., Fluorescence lifetime correlation spectroscopic study of fluorophore-labeled silver nanoparticles. *Analytical Chemistry* **2008,** *80* (19), 7313–7318.

6. Wei, G.; Yu, J.; Wang, J.; Gu, P.; Birch, D. J. S.; Chen, Y., Hairpin DNA-functionalized gold nanorods for mRNA detection in homogenous solution. *Journal of Biomedical Optics* **2016,** *21* (9), 09700-097009.

7. Szmacinski, H.; Lakowicz, J. R., Fluorescence lifetime-based sensing and imaging. *Sensors and Actuators B* **1995,** *29*, 16-24.

8. Adan, A.; Alizada, G.; Kiraz, Y.; Baran, Y.; Nalbant, A., Flow cytometry: basic principles and applications. *Critical Reviews in Biotechnology* **2017,** *37* (2), 163-176.

9. Behzadi, S.; Serpooshan, V.; Tao, W.; Hamaly, M. A.; Alkawareek, M. Y.; Dreaden, E. C.; Brown, D.; Alkilany, A. M.; Farokhzad, O. C.; Mahmoudi, M., Cellular uptake of nanoparticles: journey inside the cell. *Chemical Society Reviews* **2017,** *46* (14), 4218-4244.

10. ZMB Introduction to confocal laser scanning microscopy (LEICA). https://www.umassmed.edu/globalassets/maps/documents/confocal-explanation.pdf (accessed 12/06/2019).

11. Raval, N.; Maheshwari, R.; Kalyane, D.; Youngren-Ortiz, S. R.; Chougule, M. B.; Tekade, R. K., Importance of physicochemical characterization of nanoparticles in pharmaceutical product development. In *Basic Fundamentals of Drug Delivery*, Tekade, R. K., Ed. Academic Press: India, 2019; pp 369-400.

12. Nanakoudis, A. SEM: types of electrons, their detection and the information they provide. https://www.thermofisher.com/blog/microscopy/sem-signal-types-electrons-and-the-information-they-provide/ (accessed 06/01/2021).

13. Islam, M. A., Einstein–Smoluchowski diffusion equation: a discussion. *Physica Scripta* **2004,** *70* (2-3), 120-125.

14. Li, T.; Raizen, M., Brownian motion at short time scales. *Ann. Phys.* **2013,** *525* (4), 284-295.

Chapter 3

Synthesis of small gold nanorods and their subsequent functionalization with hairpin single stranded DNA

3. 1. Introduction

Gold nanorods (GNRs) are one type of gold nanoparticles with two absorption bands (transverse band and longitudinal band). Gold nanorods have excellent optoelectronic properties occasioned by localised surface plasmon resonance and these properties include larger absorption and scattering cross sections; tunable longitudinal surface plasmon resonance from the visible to the NIR wavelengths of the electromagnetic spectrum, and an enhanced local electric field in comparison to the gold nanospheres[1-2]. Furthermore, the refractive index sensitivity of GNRs is higher than that of the gold nanospheres[3-5]. In addition, their low toxicity and biocompatibility have made gold nanorods versatile nanomaterials for various biomedical applications[6-8]. For example, the GNRs are better photothermal agents because the absorption efficiency of GNR is 2-3 times stronger than that of the gold nanoshells of similar size [9-10]. GNR based biosensors have been utilized in detecting the presence of Escherichia coli in solution phase[11].

Research has shown that the size of GNRs influences the ratio of absorption-to-scattering [1, 10, 12-14]. For example, the SGNRs have higher absorption to scattering ratio than that of the LGNRs, therefore convert more energy to heat [1, 14-15] and this makes the SGNRs better photothermal agents[14, 16]. In addition, the small size gold nanorods have a larger surface area to volume ratio making the SGNRs better candidates for drug loading and binding of biological targets from blood serum or plasma[17]. Moreover, the SGNRs have high cellular uptake[3], high clearance rate from the liver, spleen and the kidney, and ease of subcellular accessibility[13, 15, 18-23]. The SGNRs are therefore, the ideal agents for photothermal therapy, diagnostic, biosensing and drugs delivery.[10]

Conversely, the LGNRs have higher ratio of scattering-to-absorption relative to the SGNRs[10, 24]. Therefore, the LGNRs are more suitable for dark field imaging applications because of their strong surface plasmon enhanced scattering[10, 24]. Furthermore, the LGNR are more suitable for surface enhanced Raman scattering (SERS) applications[10, 25]. Moreover, the extension of the local field from the surface of metal nanoparticles

increases as the size of the metal nanoparticles increases[1, 26-28], thus, the LGNRs can be good candidates for distant-dependent sensing of analytes[26-27].

GNRs can be synthesized by various methods such as template, electrochemical, seedless, seed-mediated growth methods[3, 29-33]. Recently, Ali et al.[32] synthesized small gold nanorods (18-25 nm in length and 4-5 nm in diameter) via a seedless growth method by adjusting the pH, concentration of sodium borohydride ($NaBH_4$) and hexadecyltrimethylammonium bromide (CTAB) respectively. Compared to other synthetic methods, the silver assisted seed-mediated growth method is simple, has an ease of controlling synthesis parameters and has a higher yield of monodisperse GNRs[34-35]. Jia et al.[14] synthesized small gold nanorods with diameter less than 10 nm via the seed-mediated method by simultaneously varying both the amount of seeds and CTAB added to the growth solutions to tune the diameter of the gold nanorods. The SGNRs were coated with SiO_2 to prevent particle aggregation. It was found that the SGNRs exhibited a higher photothermal effect in killing cancer cells compared to the LGNRs[14]. Song et al.[36] demonstrated that the SGNRs based vesicles enhanced the efficacy of photothermal therapy of cancer in mice, and improved the photoacoustic signal at the tumour microenvironment due to high uptake of the SGNRs vesicles. Shibu et al.[37] developed a photothermal imaging technique based on the NIR absorption of SGNRs as contrast agents. The SGNRs displayed a distinctive photothermal imaging signal from the cell mitochondria. The photothermal effect of bovine serum albumin (BSA)-coated SGNRs on the tumor cells was investigated. The SGNRs circulated through the tumour pores and covered the entire tumour microenvironment after intra-tumoral injection, thus, inducing a strong photothermal effect of SGNRs on the entire tumour region[22]. Recently, Chang et al.[12] demonstrated the synthesis of SGNRs by using ascorbic acid and hydroquinone as reducing agent to tune the longitudinal surface plasmon resonance from 600-1300 nm. However, the synthesis of stable, SGNRs with controlled aspect ratios is very delicate and challenging to achieve[,35, 37].

GNRs can be functionalized with targeting ligands to increase the sensitivity and specificity of the GNRs based nanoprobes in detecting targets in complex bio-systems such as blood plasma; stabilization of the nanostructure to reduce degradation from nuclease activity[5, 35, 38-41]. Previously, Wei et al. reported the synthesis of LGNRs by a

silver assisted seed-mediated growth method[42]. The LGNRs were functionalized with hairpin DNA (hpDNA) via a salting process[42]. The sensitivity of the LGNR-hpDNA nanoprobes in detecting c-myc gene expression in messenger RNA (mRNA) was demonstrated by the changes in the fluorescence emission intensities and the fluorescence lifetimes of the nanoprobes after hybridization with the complementary DNA[42]. We report, for the first time, the functionalization of SGNR with hairpin single stranded DNA (hpDNA).

In this chapter, we have demonstrated the synthesis of stable SGNRs with controlled aspect ratios in comparison to the LGNRs by a silver assisted seed-mediated growth method. The SGNRs were functionalized with a Cy5-hpDNA for enhancing the targeting abilities of the SGNRs nanoprobes. Therefore, this demonstrates the possibility of functionalizing the small gold nanorods with targeting ligands such as aptamer for photothermal therapy.

3. 2. Experimental section

3. 2. 1. Materials

All chemicals were used as received without further purification. Chloroauric acid ($HAuCl_4$, 49%), hexadecyltrimethylammonium bromide (CTAB, 99%), ascorbic acid (AA), sodium borohydride ($NaBH_4$, 99.8%), silver nitrate ($AgNO_3$), dodecanethiol (DDT, 98%), mercaptohexanoic acid (MHA, 99.8%), acetone (99.9%), isopropanol (99.5%), toluene (99.8%), methanol, thiolated oligonucleotide and the complementary oligonucleotide were all purchased from Sigma Aldrich while hydrochloric acid (HCL) was purchased from Fluka.

C-myc-Cy5-hpDNA:

5’-Cy5-CTGACTTGGTGAAGCTAACGTTGAGCAAGTCAG-AA-$(CH_2)_6$-HS-3’

cDNA: 5’- CCT CAA CGT TAG CTT CAC CAA- 3’. The c-myc-hpDNA and cDNA were purchased from Sigma Aldrich.

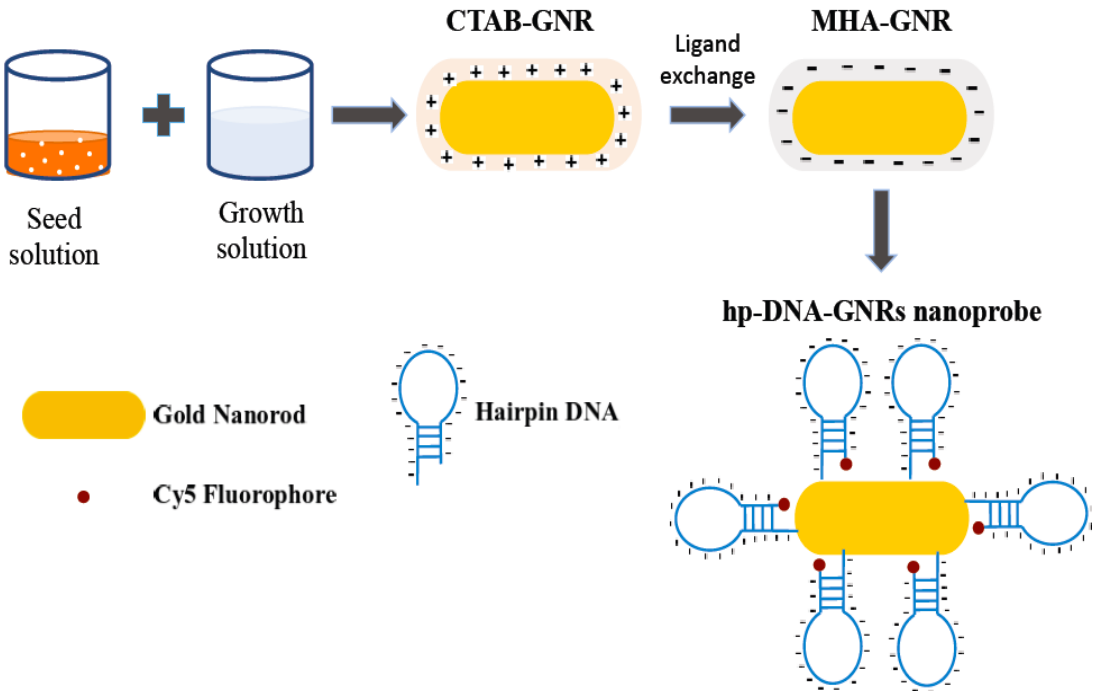

Figure 3.1. A scheme showing the synthesis and the functionalization of the small gold nanorods with a hpDNA[39].

3. 2. 2. Synthesis of SGNRs

The influence of seeds and CTAB on the growth of SGNRs was studied by varying the amount of seeds and the CTAB in the growth solution as reported[14]. The seeds solution was prepared as reported[14]. The growth solutions of the SGNRs samples (G_9S_1, G_8S_2, and G_6S_4) were prepared by adding $HAuCl_4$ (0.01 M; 0.5 ml) to CTAB solutions (0.1 M; 9.0 ml, 8.0 ml, 6.0 ml) respectively. Then, $AgNO_3$ (0.01 M; 0.1 ml) and HCl (1.0 M; 0.2 ml) were sequentially added to each solution respectively. Stirring continued until the mixture turned colourless[44]. Lastly, 1ml, 2ml and 4ml of the seeds solution was added to each sample respectively and these were then kept at room temperature overnight. The chemicals used for preparing G_9S_1, G_8S_2, and G_6S_4 are listed in Table 3.1.

Table 3.1. The list of reagents used to investigate the influence of seeds and the concentration of CTAB on the size of SGNRs samples.

Reagents		$HAuCl_4$ (0.01M; ml)	CTAB (0.1M; ml)	$NaBH_4$ (0.01M; ml)	$AgNO_3$ (0.01M; ml)	HCl (1.0M; ml)	A.A (0.1M; ml)	Seeds (ml)
Seeds solution		0.25	9.75	0.60	-	-	-	-
Growth solution	G_9S_1	0.50	9.00	-	0.060	0.20	0.08	1.00
	G_8S_2	0.50	8.00	-	0.075	0.20	0.08	1.00
	G_6S_4	0.50	9.00	-	0.090	0.20	0.08	1.00

The recipe of G_9S_1 was modified by varying the amount of silver ions added in the growth solution to tune the size of the SGNRs. That is, $HAuCl_4$ (0.01 M; 0.5 ml) was added to a solution of CTAB (0.1 M; 9.0 ml) in nine separate samples. Varying amounts of $AgNO_3$ (0.01M; 0.150 ml, 0.135 ml, 0.120 ml, 0.080 ml, 0.065 ml, 0.050 ml, 0.035 ml, 0.025 ml and 0.020 ml) were added to each growth solution respectively, followed by adding the same amount of HCl (1.0 M; 0.2 ml) and ascorbic acid (0.1 M; 0.08 ml) under continuous stirring. Thereafter, 1ml of the gold seeds for SGNRs prepared as above was added to each solution and kept at room temperature overnight. The samples were labeled as G_9S_1-150, G_9S_1-135, G_9S_1-120, G_9S_1-80, G_9S_1-65, G_9S_1-50, G_9S_1-35, G_9S_1-25 and G_9S_1-20. Table 3.2. lists all the reagents for investigating the influence of silver ions on the size of SGNRs.

Table 3.2. The list of reagents for investigating the influence of silver ions on the size of SGNRs.

Reagents		$HAuCl_4$ (0.01M; ml)	CTAB (0.1M; ml)	$NaBH_4$ (0.01M; ml)	$AgNO_3$ (0.01M; ml)	HCl (1.0M; ml)	A.A (0.1M; ml)	Seeds (ml)
Seeds solution		0.25	9.75	0.60	-	-	-	-
Growth solution	G_9S_1-150	0.50	9.00	-	0.150	0.20	0.08	1.00
	G_9S_1-135	0.50	8.00	-	0.135	0.20	0.08	1.00
	G_9S_1-120	0.50	9.00	-	0.120	0.20	0.08	1.00
	G_9S_1-80	0.50	9.00	-	0.080	0.20	0.08	1.00
	G_9S_1-65	0.50	9.00	-	0.065	0.20	0.08	1.00
	G_9S_1-50	0.50	9.00	-	0.050	0.20	0.08	1.00
	G_9S_1-35	0.50	9.00	-	0.035	0.20	0.08	1.00
	G_9S_1-25	0.50	9.00	-	0.025	0.20	0.08	1.00
	G_9S_1-20	0.50	9.00	-	0.020	0.20	0.08	1.00

SGNRs and LGNRs of similar surface plasmon resonance were synthesized to investigate their physical and spectral difference. A sample of the SGNRs was synthesized by our modified silver-assisted seed mediated growth method[39]. The seeds solution was prepared by adding $HAuCl_4$ (0.01 M; 0.25 ml) to a solution of CTAB (0.1 M; 9.75 ml). Freshly prepared ice-cold $NaBH_4$ solution (0.01 M; 0.6 ml) was added to the mixture and stirred with a magnetic stirrer for 2-3 minutes until the seeds solution turned to a dark brown

colour. The solution was incubated at room temperature for 2 hours to initiate the growth of gold seeds before use. The growth solution was prepared by adding $HAuCl_4$ (0.01 M; 0.5 ml) to a solution of CTAB (0.1 M; 9 ml) followed by $AgNO_3$ (0.01 M; 0.090 ml), HCl (1.0 M; 0.2 ml) and ascorbic acid (0.1 M, 0.08 ml). After stirring for few minutes, 1.0 ml of the gold seeds solution was added to the growth solution and kept at room temperature overnight. Table 3.3. lists all the chemicals used for synthesis of SGNR.

Table 3.3. The list of reagents used to prepare the seeds and the growth solutions of the SGNRs sample.

Reagents	$HAuCl_4$ (0.01M; ml)	CTAB (0.1M; ml)	$NaBH_4$ (0.01M; ml)	$AgNO_3$ (0.01M; ml)	HCl (1.0M; ml)	A.A (0.1M; ml)	Seeds (ml)
Seeds solution	0.25	9.75	0.60	-	-	-	-
Growth solution	0.50	9.00	-	0.090	0.20	0.08	1.00

On the other hand, a sample of the LGNRs was synthesized according to a reported protocol[42] with some adjustments. The seeds solution of the LGNRs was prepared by adding $HAuCl_4$ (0.001 M; 2.5 ml) to a solution of CTAB (0.2 M; 7.5 ml). Thereafter, a freshly prepared ice-cold $NaBH_4$ solution (0.01 M; 0.6 ml) was added to the mixture and stirred with a magnetic stirrer for 2-3 minutes until the seeds solution turned to a dark-brown colour. The seeds solution was incubated at room temperature for 3 hours before used. The growth solution was prepared by scaling down (20x) the volume of the chemicals used for growth solution as follows; $HAuCl_4$ (0.001 M; 10 ml) was added to CTAB (0.2 M; 10 ml) followed by $AgNO_3$ (0.004 M; 0.380 ml), ascorbic acid (0.0778M, 0.140 ml) under continuous stirring until the growth solution turned colourless. The addition of ascorbic acid partially reduced the gold ions from Au^{+3} to Au^{+1}. After stirring for few minutes, 0.02 ml of the gold seeds were added to the growth solution and kept at room temperature overnight. The seeds solution acts as a template for growth of nanorod and reduces Au^{+1} to Au^{0} [45]. Table 3.4. lists all the chemicals used for sample preparation.

Table 3.4. The list of reagents used to prepare the seeds and the growth solutions of the LGNRs sample.

Reagents	$HAuCl_4$ (0.001M; ml)	CTAB (0.2M; ml)	$NaBH_4$ (0.01M ; ml)	$AgNO_3$ (0.004M; ml)	A.A (0.0778 M; ml)	Seeds (ml)
Seeds solution	2.50	7.50	0.60	-	-	-
Growth solution	10.00	10.00	-	0.380	0.14	0.02

3. 2. 3. Ligand exchange for small gold nanorods

The CTAB surfactant on the surface of gold nanorods is toxic and could prevent direct assembly of hairpin DNA to gold nanorods' surface, therefore ligand exchange was performed to replace the CTAB surfactant via a ligand exchange approach[42]. We performed ligand exchange for two samples of the SGNRs ($SGNR_1$ and $SGNR_2$) using a round-trip phase transfer ligand exchange protocol previously reported in the literature[42, 45]. Specifically, the ligand exchange for SGNRs was performed in two phases.

In phase 1, the CTAB-SGNRs were centrifuged at 12000 rpm for 15 minutes. The absorption spectrum of the CTAB-SGNRs was measured to ascertain the sample concentration. Then, the SGNRs (1ml) pellets, DDT (1 ml), acetone (4 ml) were mixed together in the ratio 1:1:4 and shaken to extract the CTAB coated SGNRs from the aqueous phase to an organic phase. DDT-SGNRs pellets of known volume were mixed with equal volumes of acetone and methanol 5 times the volume of DDT-SGNRs in the ratio 1:1:5 and left undisturbed for at least 3 hours for sedimentation of the nanorods after which the nanorods sediments were extracted from the mixture and re-suspended in toluene (1 ml).

In phase 2, toluene (9 ml) was heated in a water bath on a hot plate (shown in fig.3.2.) until the temperature of ~93^{o}C was attained, then MHA (20 μl) was added to the heated toluene solution. After 2-3 minutes of vigorously stirring the mixture (toluene and MHA), the SGNRs already re-suspended in 1 ml of toluene were added to the 9ml of toluene in

the heated bath maintained at 90°C-93°C while stirring continued until visible aggregation was seen within 10-11 minutes. Then, heating was suspended and the mixture was allowed to cool for few minutes. The SGNR sediments were extracted and washed twice in toluene (2 ml) after which the SGNR pellets were re-suspended in isopropanol (1 ml) and centrifuged at 8000 rpm for 6 minutes. The supernatant was discarded, but the pellets of the ligand-exchanged SGNRs were suspended in a TBE (pH 8.5; 50 µl) buffer to prevent aggregation.

Figure 3.2. The experimental set-up for ligand exchange on the surface of GNRs.

3. 2. 4. Functionalization of SGNRs

The SGNRs were functionalized with thiolated hairpin DNA (hpDNA) labeled with Cy5 according to a previous protocol[42] as described in fig. 3.1. The hpDNA is composed of Cy5 label located at the 5' end and the thiol group at the 3' end (5'-Cy5- CTGACTTG GTG AAG CTA ACG TTG AG CAAGTCAG-AA-$(CH_2)_6$-HS -3'). The thiolated hairpin DNA (10^5 nM, 10 µl) was activated with tris (2-carboxyethyl) phosphine hydrochloride (TCEP, 10 µl) in 1x TE buffer (pH 8.0.) in the molar ratio TCEP: DNA (100:1) to reduce the disulfide bond of hpDNA[42]. Then, TCEP-hpDNA was placed on a shaker for 1 hour at room temperature. Next, the TCEP-hpDNA was mixed with sodium acetate (3 M) and

ethanol (100%) in the ratio 2: 1: 7 respectively and incubated further for 3 hours at 4ºC. After the incubation, the mixture was centrifuged at 13000 rpm for 15 minutes at 4ºC. The supernatant was removed and the pellets of hpDNA were re-suspended in 100 µl of distilled water. The hpDNA was conjugated with the SGNRs (5 nM) in the molar ratio 400:1 using a previously reported salt aging procedure[42], [46-47]. That is, each sample contained the same concentration of hairpin DNA (100000 nM; 100 µl), phosphate buffer solution (10 mM; 50 µl), Sodium dodecyl sulfate (SDS, 0.02%; 50 µl) and distilled water (200 µl), 100 µl of each sample of the SGNRs ($SGNR_1$ and $SGNR_2$). The samples were incubated on a shaker over night at room temperature. Salting resumed the following day with the same salting solution containing (NaCl, 500 mM, SDS 0.02 %, phosphate buffer, 10 mM). For each tube, 5 µl of the salting solution was added to the mixture hourly for the first 4 hours, followed by 10 µl hourly for 3 hours and finally 12.5 µl making a total of 125 µl (100%) per 500 µl of hpDNA-SGNRs conjugation mixture until the final NaCl (125 mM) concentration was attained. The salted sample remained under incubation for another 16 hours at room temperature. The hpDNA-SGNRs conjugates were washed 3x with buffer (Na phosphate buffer pH 7.5, 10 mM and SDS 0.02 %) and another three times with phosphate buffer (pH 7.5, 10 mM) at 13000 rpm for 15 minutes at 4 ºC to get rid of unbound reagents. The conjugates were finally re-suspended in phosphate buffer (pH 7.5, 10 mM; 50 µl) for each sample.

.

3. 2. 5. Hybridization of hpDNA-GNRs nanoprobes with complementary DNA (cDNA)

Complementary DNA (cDNA) was incubated with hpDNA-SGNRs nanoprobes in the ratio 1000:1 for 2 hours at 37 ºC for each sample prior to measuring the fluorescence intensity and the lifetime response of the nanoprobes**.**

3. 2. 6. Characterization of gold nanorods and GNR- hpDNA nanoprobes

The extinction spectra of gold nanorods covering 400-1100 nm wavelength was measured with a UV-visible spectrophotometer (Lambda 2, Perkin Elmer). A scanning electron microscope (SEM, FEI Quanta FEG 250) was used for morphological characterization of

the gold nanorods using a 30kV electron beam and bright field/dark field scanning transmission electron detectors. ImageJ was used for size analysis to obtain the average length and diameter. Zeta potential of the SGNRs was measured using a Zetasizer Nano-ZS (Malvern Panalytical, UK). A spectrofluorometer (Horiba Jobin Yvon Ltd., Middlesex, UK) was used to measure the fluorescence spectra of gold nanorods nanoprobes at 635 nm excitation wavelength.

Time-resolved fluorescence lifetime measurements were conducted before and after hybridization with a cDNA using the time-correlated single-photon counting (TCSPC) technique with IBH Fluorocube fluorescence lifetime system (Horiba Jobin Yvon IBH Ltd., Glasgow, UK). This system is equipped with monochromators for excitation and emission. The excitation-motorized polarizer was maintained at 0^o for both Instrument Response Function (IRF) and fluorescence decay measurements. While the emission-motorized polarizer was fixed at magic angle (54.7^o) during fluorescence decay measurement to avoid polarization artefact. The nanoprobes were excited with 638nm pulsed light-emitting diode (NanoLED) source operating at measurement range 100 ns and repetition rate 1 MHz. Data analysis was performed with DAS6 package. Fluorescence lifetimes were analyzed by fitting the decay curves to multi-exponentials decay model given in equation 2.3. while the average time was calculated using equation 2.5. The procedures for fitting the fluorescence decay curves are outlined in appendix 4. The fluorescence decay curves of the nanoprobes were fit to 3-exponentials model to account for the fluorescence lifetimes arising from the closed and the opened Cy5-hpDNA and the gold cores. The fluorescence lifetime of the gold cores was fixed at 0.5 channel to eliminate the scattering contribution to the average fluorescence lifetime.

3. 3. Results and Discussion

3. 3. 1. Influence of seeds and CTAB on the size of SGNRs

The seeds and the solution of CTAB in the growth solution were varied to investigate their influence on the size of the SGNRs. Fig. 3.3. shows the UV-vis extinction spectra and the SEM images of the SGNRs samples synthesized. The longitudinal surface

plasmon resonances of the SGNRs (G_9S_1, G_8S_2 and G_6S_4) were found to be 776 nm, 744 nm and 717 nm respectively. Moreover, G_6S_4 was found to be unstable after few days of synthesis. Fig. 3.3a shows that the UV-vis extinction spectrum of G_6S_4 transformed from the initial two surface plasmon resonance peaks to one peak (*G_6S_4) after 24 days of synthesis, indicating the morphological change of the gold nanorods to the gold nanospheres. This illustrates the limitation of synthesising small gold nanorods by merely increasing the seeds to growth solution ratio. Table 3.5. shows the physical dimensions of G_9S_1, G_8S_2 and G_6S_4 samples. It can be seen that the average length of the SGNRs is < 17 nm and the average width < 6 nm. Both the length and the width decreased as the amount of seeds added to the growth solution increased. The decrease in the size as the seeds increased could be due to the increased nucleation sites, thus depleting the amount of gold atoms available to grow each nanorod[43, 48]. Similarly, the aspect ratio decreased as the amount of seeds in the growth solution increased because the length decreases[14, 29] leading to a blue shift in the longitudinal surface plasmon resonance peaks from 776 nm to 717 nm. The size distributions of the SGNRs for all the samples are shown in appendix 1 (fig. 1). In addition, the growth yield of the SGNRs (number of nanorods / number of total particles) decreased from 69% for G_9S_1 to 12% for G_6S_4 as the seeds to CTAB ratio in the growth solution increased. This could be due to the insufficient amount of the CTAB surfactant selectively binding to the sides of each nanorod, thus yielding less anisotropic growth and generating more nanospheres. It has been demonstrated previously that more by-products of nanospheres can be formed than gold nanorods as the amount of seeds solution in the final growth mixture increases[14, 32, 49].

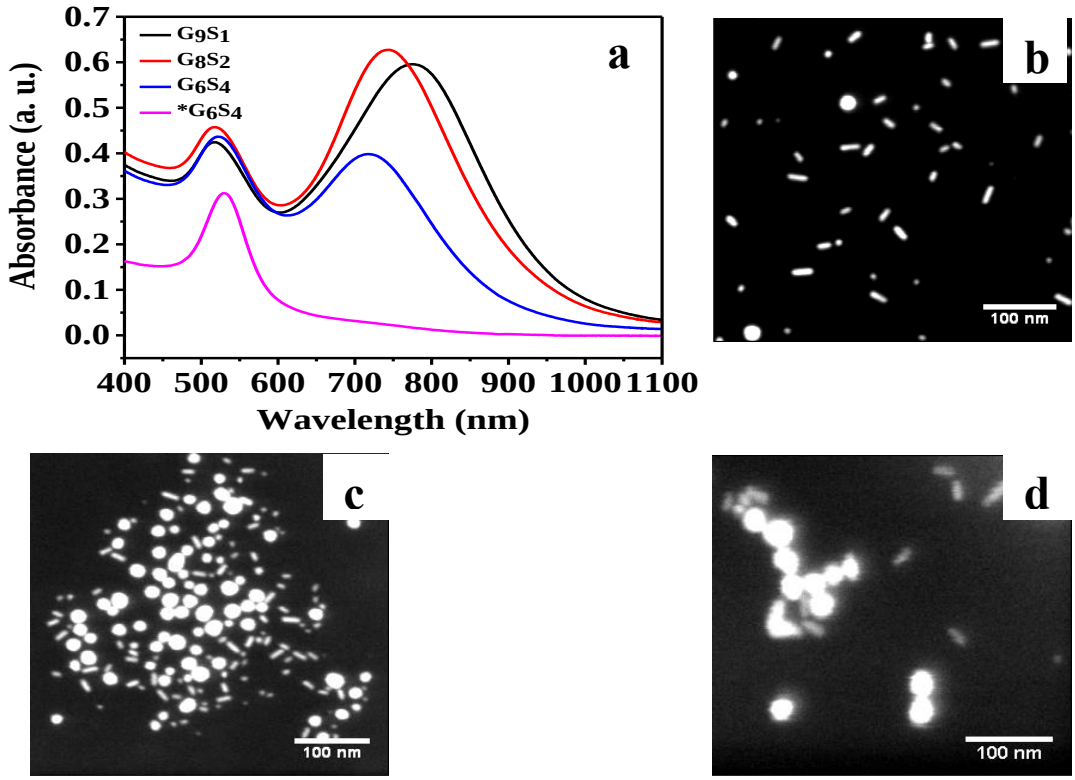

Figure 3.3. The SEM images of small gold nanorods prepared by varying the ratio of growth solution (G) to seeds solution (S); (a) UV-vis extinction spectra (b) G_9S_1 (c) G_8S_2 and (d) G_6S_4.

Table 3.5. The size distribution, longitudinal mode wavelength, and growth yield of the small gold nanorods at varying seeds to CTAB solution ratios.

Samples	LSPR (nm)	Length (nm)	Diameter (nm)	Yield (%)
G_9S_1	776	16.3±2.9	6.0±1.4	69
G_8S_2	744	14.9±2.9	6.0±1.2	51
G_6S_4	717	13.1±2.8	5.0±1.4	12

3. 3. 2. Influence of silver ions on the growth of SGNRs

Silver ions are very essential in tuning the aspect ratios and the growth yields of gold nanorods[44]. Silver ions form complexes with CTAB to control structural evolution of gold seeds to rod-like shape and improve the yield of nanorod[50-51]. Fig. 3.4a depicts the UV-vis extinction spectra taken from the nine samples. It can be seen that the longitudinal surface plasmon resonance blue shifts from 912 nm to 613 nm as the amount of the silver nitrate decreases from 150 µl to 20 µl. A monotonic relationship was found between the wavelength of the longitudinal surface plasmon mode and the silver nitrate as depicted in fig.3.4b. Table 3.6. shows the average length, average diameter and the yield of nanorods. It can be seen that the average length of nanorods blue shifts from about 25 nm to 14 nm as the silver nitrate decreased from 150 µl to 20 µl; while the average diameter varies slightly alternating between 6.6-5.0 nm. The silver ions were found to promote the anisotropic growth to a nanorod shape although the specific role of the silver ions in the synthesis is still not fully understood [44, 52-53]. Three mechanisms proposed so far include the under-potential deposition to favour growth on the longitudinal facets, face-specific capping to block specific facets and modification of the CTAB micelle formation through silver-bromide integrations[44, 54]. At higher silver nitrate concentration (> 100 µl), the average lengths of nanorods were found to fluctuate between 24-25 nm. Nikoobakht and El-Sayed have shown previously that a new species (e.g. $AgCl_4$) with less efficiency could be formed at higher silver ions concentration, thus yielding gold nanorods with reduced aspect ratio[44]. Tong et. al. recently found that the control of silver ions on the aspect ratio of conventional gold nanorods occurs during the symmetry breaking period and the length of the final nanorods formed is dependent on the available gold atom concentration[50]. Therefore, the unchanged length at higher silver ions concentration suggests the depletion of the available gold atoms. These findings are consistent with previous reports on the growth of large gold nanorods[43-44]. This demonstrates that silver ions have similar effect on the longitudinal surface plasmon mode of the small gold nanorods and the conventional gold nanorods. The size distributions of the synthesized SGNRs are displayed in appendix 1(fig.2). Moreover, high yields of nanorod formation (>85%) were found for all the nine samples. Fig. 3.4c-k displays the SEM images taken from these nine

samples. The dependence of size of the SGNRs on the amount of silver ions observed in this work is in line with previous study on the conventional (large) gold nanorods[55].

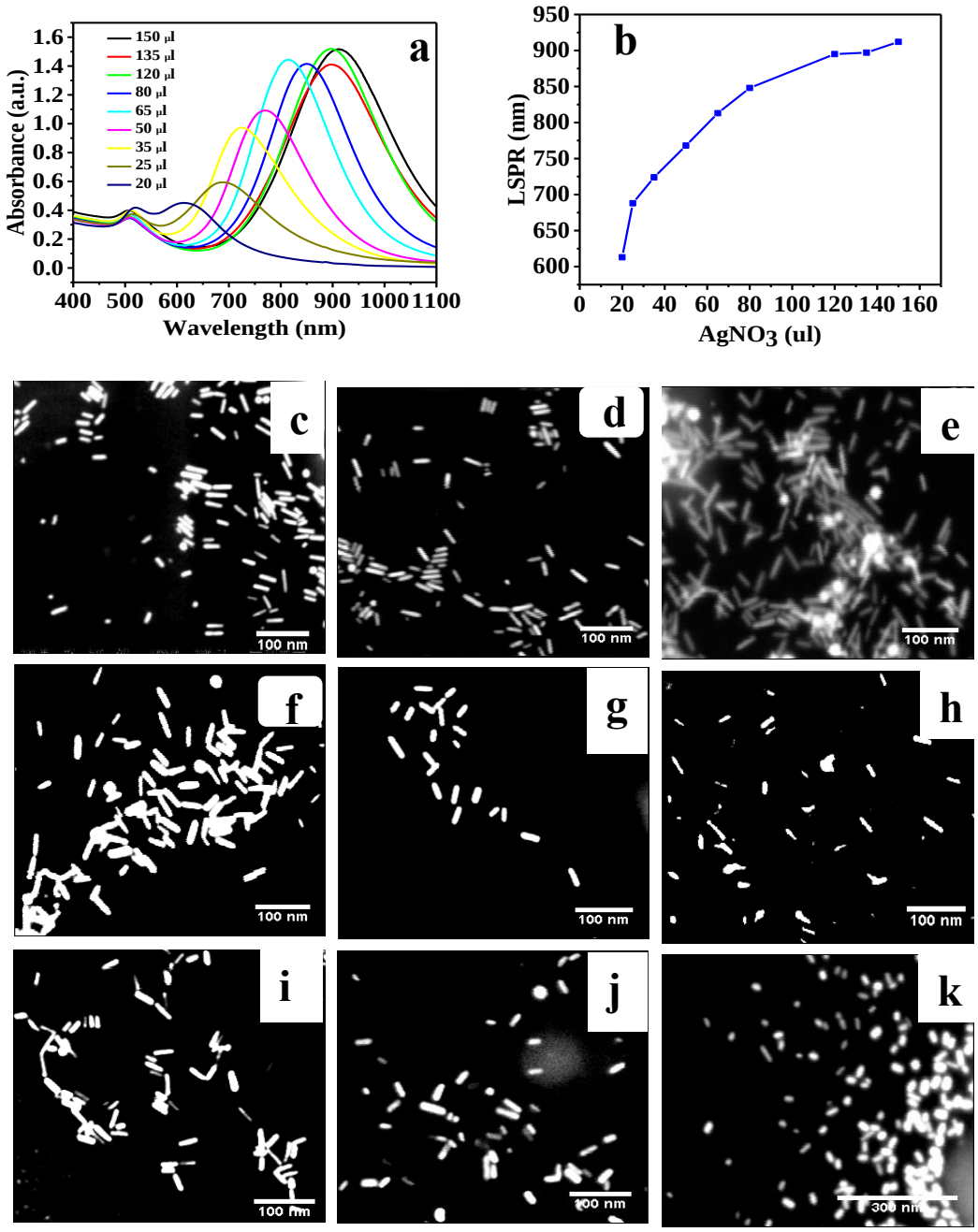

Figure 3.4. The SEM images of small gold nanorods prepared by varying the amount of silver nitrate in the growth solution; (a) UV-vis extinction spectra of the samples; (b) the relationship between the amount of silver nitrate in the growth solution and longitudinal surface plasmon resonance wavelength. (c) G_9S_1-150µl$AgNO_3$; (d) G_9S_1-135µl$AgNO_3$;

(e) G_9S_1-120µl$AgNO_3$; (f) G_9S_1-80µl$AgNO_3$ (g) G_9S_1-65µl$AgNO_3$; (h) G_9S_1-50µl$AgNO_3$; (i) G_9S_1-35µl$AgNO_3$; (j) G_9S_1 -25µl$AgNO_3$ (k) G_9S_1-20µl$AgNO_3$.

Table 3.6. The size distribution of the wavelength of longitudinal absorption, the average length, the average diameter and the nanorod yield at different amount of silver nitrate ($AgNO_3$, 0.01 M).

$AgNO_3$ (ul)	LSPR (nm)	Length (nm)	Diameter (nm)	Yield (%)
150	912	25.7± 5.5	5.9± 1.1	85.28
135	897	25.0± 5.6	6.3± 1.4	90.95
120	895	24.6± 4.7	5.8± 1.0	87.20
80	848	23.3± 4.2	5.7± 1.4	97.94
65	813	23.9± 3.9	6.6± 1.1	94.33
50	768	22.8± 4.4	5.5± 1.3	92.11
35	724	22. 0± 4.5	5.6± 1.3	98.94
25	688	18.3± 4.6	5.2± 1.3	93.10
20	613	14.2± 4.0	5.1± 1.5	90.60

3. 3. 3. Physical and spectral features of the SGNRs and the LGNRs

SGNRs and LGNRs of similar surface plasmon resonance were synthesized by a silver-assisted seed mediated growth method. Physical and spectral features of the SGNRs were examined in comparison to the LGNRs to depict the difference between the SGNRs and the LGNRs. Figure 3.5a-b. show the SEM of SGNRs and LGNRs respectively. It can be seen that the SGNRs and the LGNRs are stable and monodispered. The physical dimensions of the SGNRs and the LGNRs were determined from the SEM images using ImageJ software. The average length and the average width of the SGNRs are 24.03±6.5 nm and 5.96±1.0 nm respectively, while the average length and the average width of the LGNRs are 46.24±8.4 nm and 11.54±1.5 nm respectively. The size distributions of L816

and S817 are shown in fig. 3 of appendix 1. The apparent size difference in the two samples can be attributed to the different ratio of seeds-to-growth solution used in the synthesis of the LGNRs and the SGNRs. The smaller ratio of the seeds-to-growth solution for the synthesis of LGNRs allows a higher amount of gold atoms to grow the seeds to LGNRs, hence the larger size of the LGNRs compared to the SGNRs.

In addition, the aging of the seeds before addition to the growth solution could affect the size of synthesized LGNRs and SGNRs. Gold seeds are very important parameter because they provide soft templates and nucleation sites for the growth of rods shape[39, 56]. The size of the gold seeds increases with increasing incubation time[56]. The seeds solution of the SGNRs sample was incubated for 2 hours before adding to the growth solution of the SGNRs, while the seeds solution for LGNRs was incubated for 3 hours.

Furthermore, the pH of the growth solution has been found to affect the size of the gold nanorod formed[57-58]. Therefore, we measured the pH of the growth solution of the LGNRs and the SGNRs before the gold seeds were added respectively with a pH meter (HORIBA pH meter D-51, Kyoto Japan). The pH of the growth solution of the LGNRs was found to be 3.96 while the pH of the growth solution of the SGNRs was 2.86. It has been reported that, increase in the pH of the growth solution reduces the capping strength of the CTAB making the (110) facet unstable, hence the gold nanorods grow larger[58]. Cheng et al. reported that increase in the pH of the growth solution reduces the stability and the strength of the CTAB capping on the facet (110) of gold nanoseeds, inducing a faster and a wider deposition of gold atoms to the other facets including (110) facet[58]. This could induce a larger growth of the gold nanorod. However, for the SGNRs, the addition of the hydrochloric acid (HCl) to the growth solution of the SGNRs decreases the pH of the growth solution, favouring stronger CTAB capping on the (110) facet and thus, restricting the larger growth of the size of the SGNRs [35, 59].

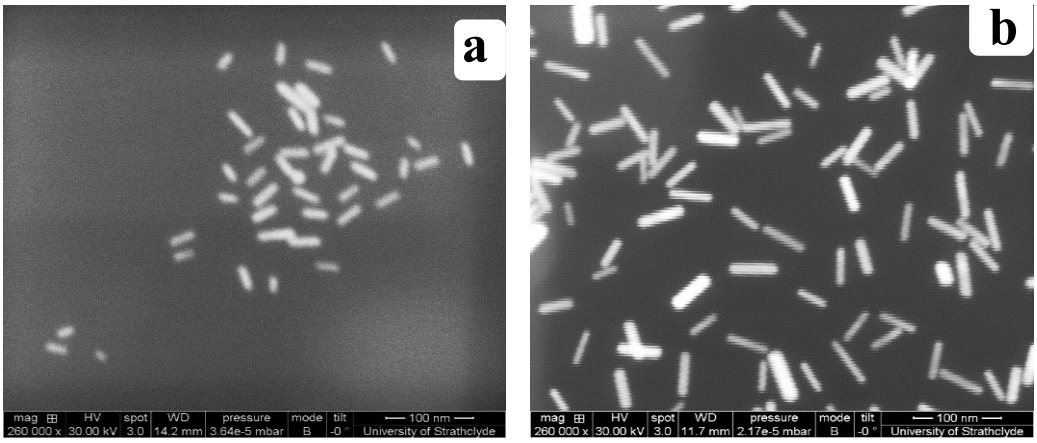

Figure 3.5. The SEM images; (a) S817 and (b) L816.

Figure 3.6. shows the normalized UV-vis extinction spectra of the SGNRs and the LGNRs measured with a spectrophotometer. It can be seen that the longitudinal surface plasmon resonances of the SGNRs and the LGNRs are 817 nm and 816 nm respectively. The SGNRs are denoted by S817 while the LGNRs are denoted by L816. Moreover, the spectral peak of the longitudinal surface plasmon resonance of the SGNRs is broader compared to the spectral peak of the LGNRs. This is because the SGNRs have higher damping due to a higher surface scattering[60-61].

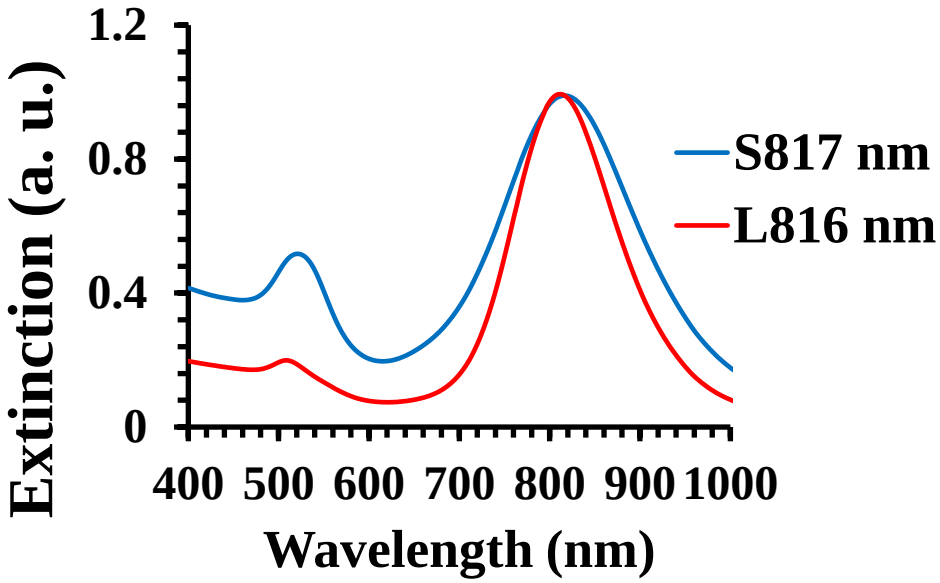

Figure 3.6. The UV-vis extinction spectra of S817 and L816.

3. 3. 4. Spectroscopic study of the small gold nanorods based nanoprobes.

The functionalization of gold nanoparticles is important for biological and biomedical applications, thus the SGNRs ($SGNR_1$ and $SGNR_2$) were functionalized with Cy5-hpDNA. The longitudinal surface plasmon resonance of the $SGNR_1$ (661nm) was matched with the fluorescence emission of Cy5 (665 nm), while the longitudinal surface plasmon resonance of the $SGNR_2$ (857 nm) was tuned away from the emission of Cy5 as shown fig. 3.7. The average dimensions of the $SGNR_1$ and the $SGNR_2$ are 13.1 ± 2.1 nm by 4.9 ± 1.0 nm and 20.6 ± 4.7 nm by 5.7 ± 1.1 nm respectively.

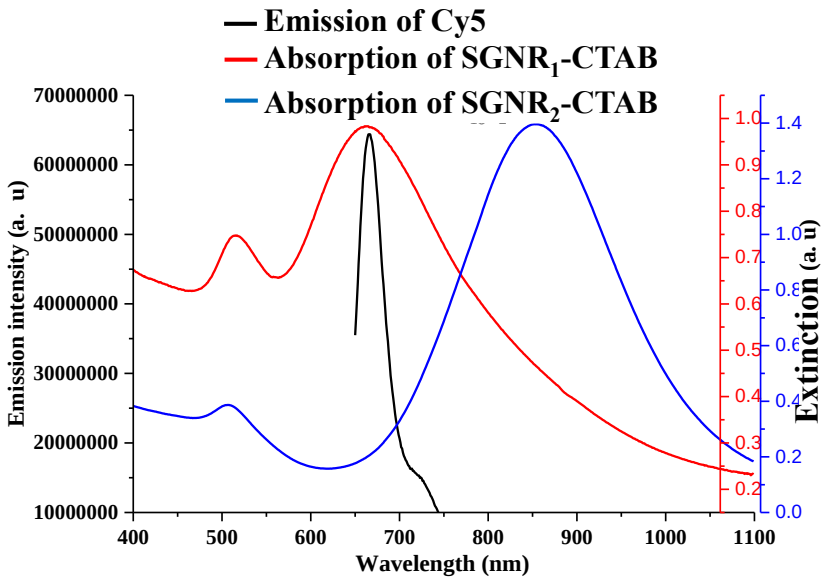

Figure 3.7. The overlap of emission of Cy5 with the extinction spectra of the $SGNR_1$ and the $SGNR_2$.

The UV-vis extinction spectra of the $SGNR_1$ and the $SGNR_2$ before and after ligand exchange are shown fig. 3.8a-b respectively. It can be seen that the longitudinal surface plasmon resonance bands of the $SGNR_1$ and the $SGNR_2$ blue shifted to 653 nm and 839nm respectively without significant broadening after the ligand exchange process, due to the shortening of the length of $SGNR_1$ and $SGNR_2$ after ligand exchange[43]. Prior to the ligand exchange, zeta potential measurement show that the surface charge of the $SGNR_1$ was 25.7±2.7 mV, while the surface charge of the $SGNR_2$ was 36.0±1.1 mV. After the ligand

exchange, the surface charge of the $SGNR_1$ was -12.9±0.3 mV, while that of the $SGNR_2$ was -20.1±6.7 mV indicating the replacement of CTAB by MHA.

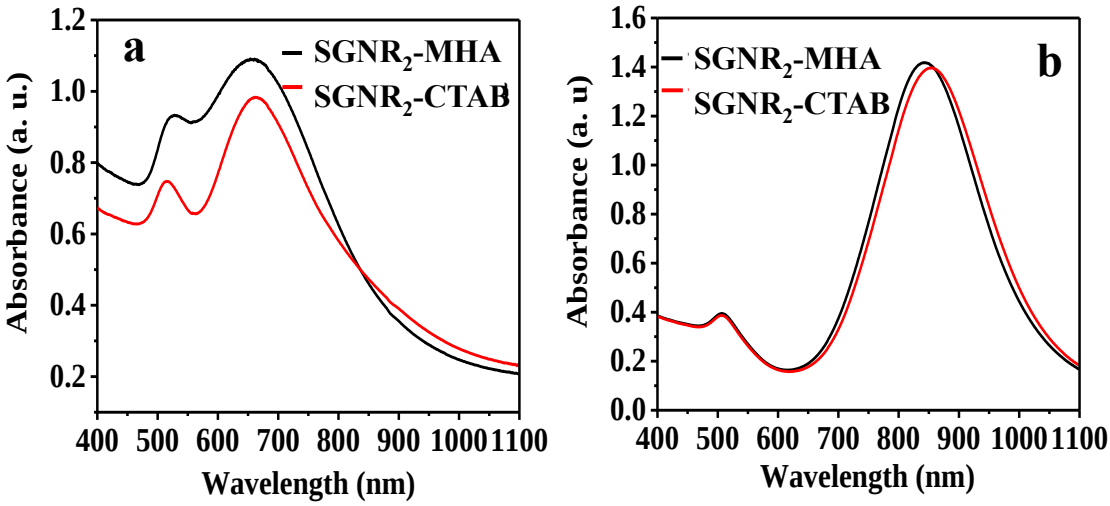

Figure 3.8. The UV-vis extinction spectra of the $SGNR_1$ and the $SGNR_2$ before and after ligand exchange.

A typical extinction spectrum of the small gold nanorods ($SGNR_1$) functionalized with Cy5-hpDNA is shown in figure 3.9. It was found that the longitudinal surface plasmon resonance of the $SGNR_1$ was 654 nm while the $SGNR_2$ was 851 nm after functionalization. A peak was found at 260 nm representing the absorption peak of hpDNA. Upon addition of a cDNA to the $SGNR_1$-Cy5-hpDNA and the $SGNR_2$-Cy5-hpDNA, the intensity of the absorption peak of both nanoprobes increased. The Cy5-hpDNA functionalized small gold nanorods were stable with no visible sign of aggregation.

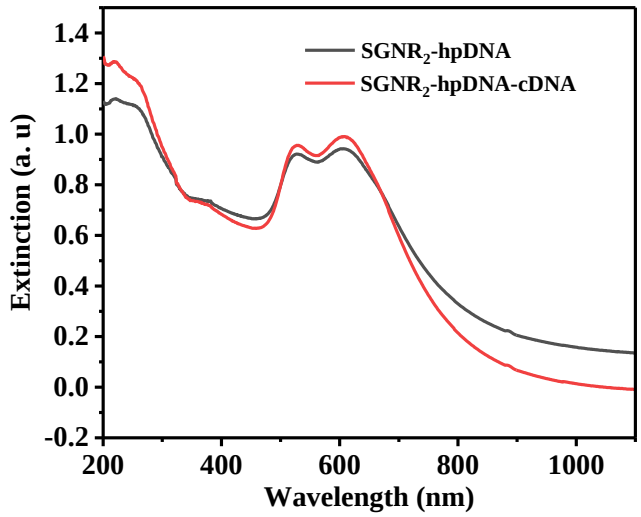

Figure 3.9. A typical UV-vis extinction spectrum of the small gold nanorods ($SGNR_1$) functionalized with Cy5-hpDNA.

The performance of the SGNRs based nanoprobes was evaluated by hybridizing the nanoprobes with a cDNA in the molar ratio 1000:1 (cDNA to SGNRs-Cy5-hpDNA). The hybridization of the cDNA with the $SGNR_1$-Cy5-hpDNA and the $SGNR_2$-Cy5-hpDNA opens the hairpin structure, separating the Cy5 from the gold surface. Thus, the Cy5-fluorophore is switched from its initial dark state (quenched) to an opened bright state (emission). The fluorescence emission spectra taken from both samples before and after hybridization are presented in fig. 3.10a-b. The emission wavelength of both nanoprobes ($SGNR_1$-Cy5-hpDNA and that of $SGNR_2$-Cy5-hpDNA) was found centred at 665 nm. A significant increase in the fluorescence intensity in the presence of a cDNA is apparent in both cases, indicating the successful assembly of the Cy5-hpDNA onto the SGNRs. A larger fluorescence increase (1.8 fold) was observed for the $SGNR_1$-Cy5-hpDNA nanoprobe where the longitudinal surface plasmon resonance overlaps the emission of the Cy5 fluorophore and the excitation wavelength. On the other hand, a smaller fluorescence increase (1.4 fold) was observed for the $SGNR_2$-Cy5-hpDNA nanoprobe because the longitudinal surface plasmon resonance is away from the emission of Cy5 and the excitation wavelength. The overlap of the longitudinal surface plasmon resonance of the $SGNR_1$-Cy5-hpDNA nanoprobe with the emission of the Cy5 fluorophore and the

excitation wavelength induces a faster and an efficient fluorescence emission rate of the $SGNR_1$-Cy5-hpDNA nanoprobe compared to the $SGNR_2$-Cy5-hpDNA nanoprobe[62], hence the higher fluorescence intensity of the $SGNR_1$-Cy5-hpDNA nanoprobe. It has been demonstrated previously that the fluorescence emission of a fluorophore is significantly enhanced when the fluorophore is within the influence of the metal's local field[28].

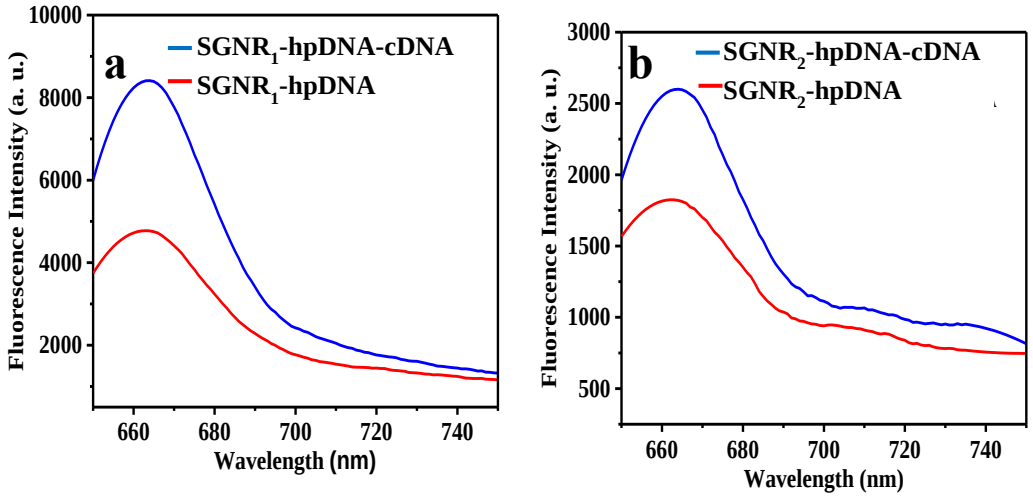

Figure 3.10. The fluorescence emission spectra of the small gold nanorods nanoprobes. (a) $SGNR_1$-Cy5-hpDNA nanoprobe and (b) $SGNR_2$-Cy5-hpDNA nanoprobe with/out cDNA.

The fluorescence decay curves of the $SGNR_1$-Cy5-hpDNA nanoprobe and $SGNR_2$-Cy5-hpDNA nanoprobe are presented in figure 3.11, while the fittings of the fluorescence decays of $SGNR_1$-Cy5-hpDNA nanoprobe and $SGNR_2$-Cy5-hpDNA nanoprobe are presented in figure 1 of appendix 5. Obviously, the fluorescence decays of the $SGNR_1$-Cy5-hpDNA nanoprobe and the $SGNR_2$-Cy5-hpDNA nanoprobe after hybridization are longer than those before hybridization indicating the binding of the nanoprobes with the target. Table 3.7. shows the fluorescence lifetime components of the SGNRs nanoprobes. The short and the long fluorescence lifetimes of the Cy5 fluorophore denoted by τ_1 and τ_2 respectively. The fluorescence lifetime from gold cores represented by τ_3 arises from the detection of scattered excitation while $\bar{\tau}$ represents the average lifetime. The fluorescence lifetime of the free Cy5 fluorophore has been reported to be approximately

1.8 ns[62]. The sub-nanosecond lifetime, τ_1 can be attributed to the Cy5 near the gold surface in a closed hairpin structure.[63-64]. The longer nanosecond lifetime, τ_2 arises from the Cy5 in an opened hairpin that is relatively away from the gold surface. Prior to the hybridization, it can be seen that the average fluorescence lifetime of the Cy5 fluorophore from the $SGNR_1$-Cy5-hpDNA nanoprobe (0.62 ns) is shorter than that of the $SGNR_2$-Cy5-hpDNA nanoprobe (0.82 ns). Previous studies have shown that energy transfer is stronger when the longitudinal mode of the metal nanoprobe matches the emission of the fluorophore and the excitation wavelength due to a faster fluorescence emission rate, hence, the shorter average fluorescence lifetime of the $SGNR_1$-Cy5-hpDNA nanoprobe compared to the $SGNR_2$-Cy5-hpDNA nanoprobe[28, 62]. After the hybridization, the average lifetime of $SGNR_1$-Cy5-hpDNA nanoprobe increased to 0.90 ns, while that of $SGNR_2$-Cy5-hpDNA nanoprobe increased to 1.16 ns indicating the binding of the $SGNR_1$-Cy5-hpDNA and the $SGNR_2$-Cy5-hpDNA nanoprobes with the target. The increase of the average lifetime of both nanoprobes upon hybridization is consistent with the steady state measurement, confirming the hybridization of the nanoprobe with the targeted DNA.

In comparison, the fluorescence lifetimes of both $SGNR_1$-Cy5-hpDNA and $SGNR_2$-Cy5-hpDNA nanoprobes in the closed state are shorter relative to the lifetime of free Cy5 fluorophore. This is due to the stronger energy transfer from the Cy5 fluorophore to the gold nanorods surface leading to shorter fluorescence lifetimes of the nanoprobes compared to the free Cy5 fluorophore. Moreover, the local field around the $SGNR_1$-Cy5-hpDNA and the $SGNR_2$-Cy5-hpDNA nanoprobes is significantly enhanced, therefore the fluorescence emission rate of the Cy5 fluorophore attached to the nanoprobes is faster and very efficient leading to shorter fluorescence lifetimes[62]. These findings demonstrates the potential of the SGNRs based nanoprobes in detecting targets. Furthermore, the synthesis and functionalization approach reported here can be used to develop functional small gold nanorods based nanoprobes for fluorescence biosensing, targeted delivery of drugs and photothermal therapy.

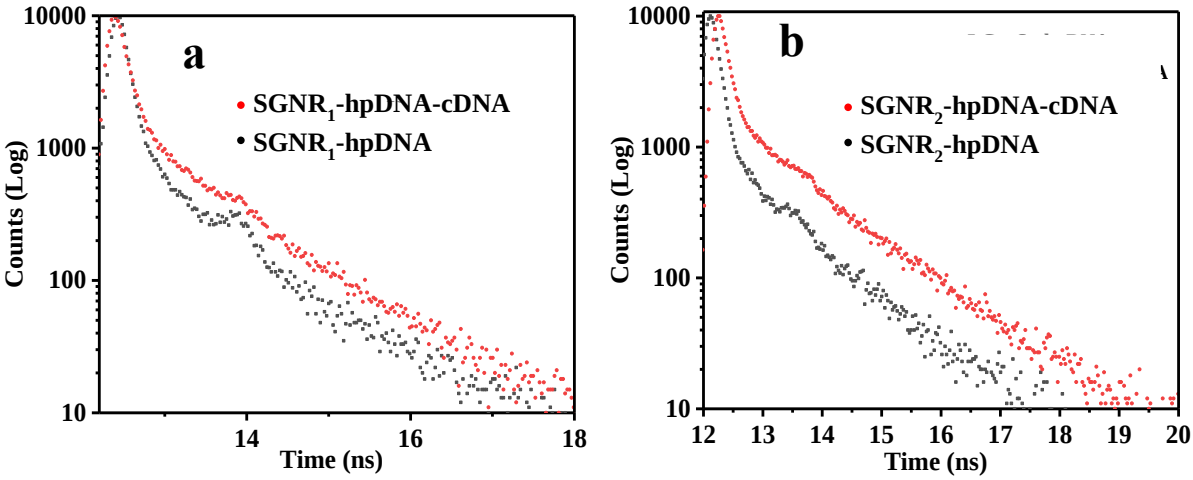

Figure 3.11. The fluorescence decay curves; (a) $SGNR_1$ and (b) $SGNR_2$ nanoprobes.

Table 3.7. The fluorescence lifetimes of the SGNRs nanoprobes before and after hybridization with the cDNA.

Sample	τ_1 (ns)	B_1 (%)	τ_2 (ns)	B_2 (%)	τ_3 (ns)	B_3 (%)	$\bar{\tau}$ (ns)	χ^2
$SGNR_1$-hpDNA	0.21±0.016	8.24	1.19±0.018	6.24	0.01	85.52	0.62	1.03
$SGNR_1$-hpDNA-cDNA	0.38±0.031	9.65	1.24±0.017	14.39	0.01	75.96	0.90	1.00
$SGNR_2$-hpDNA	0.25±0.015	6.23	1.27±0.015	7.77	0.01	86.00	0.82	1.01
$SGNR_2$-hpDNA-cDNA	0.53±0.047	7.47	1.44±0.015	16.86	0.01	75.67	1.16	0.93

3. 4. Conclusion

We have demonstrated the synthesis of SGNRs with tunable longitudinal surface plasmon resonance from 613 nm to 912 nm by the silver-assisted seed-mediated growth method. The bandwidth of the longitudinal absorption peak of SGNRs is broader than that of the LGNRs. It was found that a decrease in the amount of silver ions in the growth solution

decreases the length of SGNRs. Moreover, the SGNRs were functionalized with a Cy5 labeled thiol- modified hpDNA. Significant changes in the fluorescence intensities and the lifetimes of nanoprobes upon hybridization with the cDNA indicate the successful functionalization of the SGNRs with the Cy5-hpDNA and the capability of the SGNRs based nanoprobes in detecting potential targets such as mRNA, microRNA and ssDNA. Fluorescence intensity measurements show an enhanced signal/background ratio when the longitudinal surface plasmon resonance of the SGNRs overlaps the emission wavelength of Cy5 fluorophore and the excitation wavelength, manifesting the surface plasmon enhanced energy transfer and of benefit to the optical tunability of the SGNRs nanoprobes. The overlap of the longitudinal surface plasmon resonance of the SGNRs with the emission of Cy5 fluorophore and the excitation wavelength induces a faster and an efficient fluorescence emission rate of the Cy5 fluorophore leading to a shorter average lifetime relative to the average lifetime of free Cy5 fluorophore. The synthesis and the functionalization methods reported in this work should shine light on further development of functionalized SGNRs for applications in biomedical sensing, drugs delivery and photothermal therapy.

References

1. Mackey, M. A.; Ali, M. R. K.; Austin, L. A.; Near, R. D.; El-Sayed, M. A., The most effective gold nanorod size for plasmonic photothermal therapy: theory and in vitro experiments. *J. Phys. Chem. B,* **2014,** *118* (5), 1319–1326.

2. Jain, P. K.; Lee, K. S.; El-Sayed, I. H.; El-Sayed, M. A., Calculated absorption and scattering properties of gold nanoparticles of different size, shape and composition: application in biomedical imaging and biomedicine. *J.Phys. Chem. B.* **2006,** *110*, 7238-7248.

3. Li, Z.; Tang, S.; Wang, B.; Li, Y.; Huang, H.; Wang, H.; Li, P.; Li, C.; Chu, P. K.; Yu, X.-F., Metabolizable small gold nanorods: size-dependent cytotoxicity, cell uptake and *in vivo* biodistribution. *ACS Biomaterials Science & Engineering* **2016,** *2* (5), 789-797.

4. Velasco-Aguirre, C.; Morales Zavala, F.; Salas-Huenuleo, E.; Gallardo-Toledo, E.; Andonie, O.; Muñoz, L.; Rojas, X.; Acosta, G.; Sánchez-Navarro, M.; Giralt, E.;

Araya, E.; Albericio, F.; Kogan, M., Improving gold nanorod delivery to the central nervous system by conjugation to the shuttle Angiopep-2. *Nanomedicine (London, England)* **2017,** *12* (20), 2503-2517.

5. Unser, S.; Bruzas, I.; He, J.; Sagle, L., Localized surface plasmon resonance biosensing: current challenges and approaches. *Sensors* **2015,** *15* (7), 15684-15716.

6. Zhang, Y.; Chen, Y.; Yu, J.; Birch, D. J. S., A surface plasmon enhanced FLIM-FRET imaging approach based on Au nanoparticles. *Med. Devices Diagn. Eng.* **2017,** *2* (1), 78-82.

7. Nima, Z. A.; Alwbari, A. M.; Dantuluri, V.; Hamzah, R. N.; Sra, N.; Motwani, P.; Arnaoutakis, K.; Levy, R. A.; Bohliqa, A. F.; Nedosekin, D.; Zharov, V. P.; Makhoul, I.; Biris, A. S., Targetin g nano drug delivery to cancer cells using tunable,multi-layer, silver-decorated gold nanorods. *J. Appl. Toxicol.* **2017,** *37*, 1370–1378.

8. Haine, A. T.; Niidome, T., Gold nanorods as nanodevices for bioimaging, photothermal therapeutics, and drug delivery. *Chem. Pharm. Bull.* **2017,** *65* (7), 625–628.

9. Huang, X.; El-Sayed, M. A., Plasmonic photo-thermal therapy (PPTT). *Alexandria Journal of Medicine* **2011,** *47* (1), 1-9.

10. Huang, X.; El-Sayed , M. A., Gold nanoparticles: optical properties and implementations in cancer diagnosis and photothermal therapy. *Journal of Advanced Research* **2010,** *1*, 13–28.

11. Singh, A. K.; Senapati, D.; Wang, S.; Griffin, J.; Neely, A.; Candice, P.; Naylor, K. M.; Varisli, B.; Kalluri, J. R.; Ray, P. C., Gold nanorod based selective identification of Escherichia coli bacteria using two-photon Rayleigh scattering spectroscopy. *ACS Nano* **2009,** *3* (7), 1906-1912.

12. Chang, H.; Murphy, C. J., Mini gold nanorods with tunable plasmonic peaks beyond 1000 nm. *Chem. Mater.* **2018,** *30*, 1427-1435.

13. Ungureanu, C.; Koning, G. A.; van Leeuwen, T. G.; Manohar, S., The 'nanobig rod' class of gold nanorods: optimized dimensions for improved in vivo therapeutic and imaging efficacy. *Nanotechnology* **2013,** *24* (21), 1-9.

14. Jia, H.; Fang, C.; Zhu, X.-M.; Ruan, Q.; Wang, Y.-X. J.; Wang, J., Synthesis of absorption-dominant small gold nanorods and their plasmonic properties. *Langmuir* **2015,** *31* (26), 7418-7426.

15. Jiang, K.; Smith, D. A.; Pinchuk, A., Size-dependent photothermal conversion efficiencies of plasmonically heated gold nanoparticles. *J. Phys. Chem. C* **2013,** *117* (51), 27073-27080.

16. Ali, H. R.; Ali, M. R. K.; Wu, Y.; Selim, S. A.; Abdelaal, H. F. M.; Nasr, E. A.; El-Sayed, M. A., Gold nanorods as drug delivery vehicles for rifampicin greatly improve the efficacy of combating mycobacterium tuberculosis with good biocompatibility with the host cells. *Bioconjugate Chem.* **2016,** *27*, 2486−2492.

17. Singh, P.; Pandit, S.; Mokkapati, V. R. S. S.; Garg, A.; Ravikumar, V.; Mijakovic, I., Gold nanoparticles in diagnostics and therapeutics for human cancer. *International journal of molecular sciences* **2018,** *19* (7), 1979-1995.

18. Yue, K.; Nan, J.; Zhang, X.; Tang, J.; Zhang, X., Photothermal effects of gold nanoparticles induced by light emitting diodes. *Applied Thermal Engineering* **2016,** *99*, 1093-1100.

19. Shibu, E. S., Varkentina, N., Cognet, L., Lounis, B., Small gold nanorods with tunable absorption for photothermal microscopy in cells. *Adv. Sci.* **2017,** *4*, 1-5.

20. Cong, B.; Kan, C.; Wang, H.; Liu, J.; Xu, H.; Ke, S., Gold Nanorods : near-infrared plasmonic photothermal conversion and surface coating. *Journal of Materials Science and Chemical Engineering* **2014,** *2* (1), 20-25.

21. Pearce, M. E.; Melanko, J. B.; Salem, A. K., Multifunctional nanorods for biomedical applications. *Pharmaceutical Research* **2007,** *24* (12), 2335-2352.

22. Li, Z.; Huang, H.; Tang, S.; Li, Y.; Yu, X.; Wang, H.; Li, P.; Sun, Z.; Zhang, H.; Liu, C.; Chu, P. K., Small gold nanorods laden macrophages for enhanced tumor coverage in photothermal therapy. *Biomaterials* **2016,** *74*, 144-154.

23. Warrier, P.; Yuan, Y.; Beck, M. P.; Teja, A. S., Heat transfer in nanoparticle suspensions: modeling the thermal conductivity of nanofluids. *AIChE Journal* **2010,** *56* (12), 3243-3256.

24. Lin, K.-Q.; Yi, J.; Hu, S.; Liu, B.-J.; Liu, J.-Y.; Wang, X.; Ren, B., Size effect on SERS of gold nanorods demonstrated via single nanoparticle spectroscopy. *The Journal of Physical Chemistry C* **2016,** *120* (37), 20806-20813.

25. Saute, B.; Premasiri, R.; Ziegler, L.; Narayanan, R., Gold nanorods as surface enhanced Raman spectroscopy substrates for sensitive and selective detection of ultra-low levels of dithiocarbamate pesticides. *Analyst* **2012,** *137* (21), 5082-5087.

26. Kedem, O.; Vaskevich, A.; Rubinstein, I., Critical issues in localized plasmon sensing. *The Journal of Physical Chemistry C* **2014,** *118* (16), 8227-8244.

27. Tian, L.; Chen, E.; Gandra, N.; Abbas, A.; Singamaneni, S., Gold nanorods as plasmonic nanotransducers: distance-dependent refractive index sensitivity. *Langmuir* **2012,** *28* (50), 17435-17442.

28. Zhang, J.; Fu, Y.; Chowdhury, M. H.; Lakowicz, J. R., Single-molecule studies on fluorescently labeled silver particles: effects of particle size. *The Journal of Physical Chemistry C* **2008,** *112* (1), 18-26.

29. Pérez-Juste, J.; Pastoriza-Santos, I.; M. Liz-Marzán, L.; Mulvaney, P., Gold nanorods: synthesis, characterization and applications. *Coord. Chem. Rev.* **2005,** *249* (17-18), 1870-1901.

30. Yu; Chang, S.-S.; Lee, C.-L.; Wang, C. R. C., Gold nanorods: electrochemical synthesis and optical properties. *The Journal of Physical Chemistry B* **1997,** *101* (34), 6661-6664.

31. Chang, S.-S.; Shih, C.-W.; Chen, C.-D.; Lai, W.-C.; Wang, C. R. C., The shape transition of gold nanorods. *Langmuir* **1999,** *15* (3), 701-709.

32. Ali, M. R. K.; Snyder, B.; El-Sayed, M. A., Synthesis and optical properties of small Au nanorods using a seedless growth technique. *Langmuir* **2012,** *28*, 9807-9815.

33. Jana, N. R.; Gearheart, L.; Murphy, C. J., Seed-mediated growth approach for shape-controlled synthesis of spheroidal and rod-like gold nanoparticles using a surfactant template. *Adv. Mater.* **2001,** *13* (18), 1389-1392.

34. Yang, W.; Chen, Y.; Cheng, W., *Properties of DNA-capped nanoparticles*. Springer: Heidelberg, 2014.

35. An, L.; Wang, Y.; Tian, Q.; Yang, S., Small gold nanorods: recent advances in synthesis, biological imaging, and cancer therapy. *Materials* **2017,** *10* (12), 1372-1392.

36. Song, J.; Yang, X.; Jacobson, O.; Huang, P.; Sun, X. L., L; Yan, X.; Niu, G.; Ma, Q.; Chen, X., Ultrasmall gold nanorod vesicles with enhanced tumor accumulation and fast excretion from the body for cancer therapy. *Adv. Mater.* **2015,** *27*, 4910-4917.

37. Shibu, E. S.; Varkentina, N.; Cognet, L.; Lounis, B., Small gold nanorods with tunable absorption for photothermal microscopy in cells. *Adv. Sci.* **2017,** *4* (2), 1600280-1600285.

38. Saha, K.; Agasti, S. S.; Kim, C.; Li, X.; Rotello, V. M., Gold nanoparticles in chemical and biological sensing. *Chemical Reviews* **2012,** *112* (5), 2739-2779.

39. Mbalaha, Z. S.; Edwards, P. R.; Birch, D. J. S.; Chen, Y., Synthesis of small gold nanorods and their subsequent functionalization with hairpin single stranded DNA. *ACS Omega* **2019,** *4* (9), 13740-13746.

40. Song, Y.; Shi, Y.; Huang, M.; Wang, W.; Wang, Y.; Cheng, J.; Lei, Z.; Zhu, Z.; Yang, C., Bioinspired engineering of a multivalent aptamer-functionalized nanointerface to enhance the capture and release of circulating tumor cells. *Angew. Chem. Int. Ed.* **2019,** *58*, 2236-2240.

41. Pu, Y.; Liu, Z.; Lu, Y.; Yuan, P.; Liu, J.; Yu, B.; Wang, G.; Yang, C. J.; Liu, H.; Tan, W., Using DNA aptamer probe for immunostaining of cancer frozen tissues. *Analytical Chemistry* **2015,** *87* (3), 1919-1924.

42. Wei, G.; Yu, J.; Wang, J.; Gu, P.; Birch, D. J. S.; Chen, Y., Hairpin DNA-functionalized gold nanorods for mRNA detection in homogenous solution. *Journal of Biomedical Optics* **2016,** *21* (9), 097001-097009.

43. Burrows, N. D.; Harvey, S.; Idesis, F. A.; Murphy, C. J., Understanding the seed-mediated growth of gold nanorods through a fractional factorial design of experiments. *Langmuir* **2017,** *33*, 1891-1907.

44. Nikoobakht, B.; El-Sayed, M. A., Preparation and growth mechanism of gold nanorods (NRs) using seed-mediated growth method. *Chem. Mater.* **2003,** *15*, 1957-1962.

45. Wijaya, A.; Hamad-Schifferli, K., Ligand customization and DNA functionalization of gold nanorods via round-trip phase transfer ligand exchange. *Langmuir* **2008,** *24*, 9966-9969.

46. Hurst, S. J.; Lytton-Jean, A. K. R.; Mirkin, C. A., Maximizing DNA loading on a range of gold nanoparticle sizes. *Anal. Chem.* **2006,** *78* (24), 8313-8318.

47. Wijaya, A.; Schaffer, S. B.; Pallares, I. G.; Hamad-Schifferli, K., Selective release of multiple DNA oligonucleotides from gold nanorods. *ACS Nano.* **2009,** *3* (1), 80-86.

48. Sau, T. K.; Murphy, C. J., Seeded high yield synthesis of short Au nanorods in aqueous solution. *Langmuir* **2004,** *20*, 6414-6420.

49. Park, K.; Hsiao, M.; Yi, Y.; Izor, S.; Koerner, H.; Jawaid, A.; Vaia, R. A., Highly concentrated seed-mediated synthesis of monodispersed gold nanorods. *ACS Appl. Mater. & Interfaces* **2017,** *9* (31), 26363-26371.

50. Tong, W.; Walsh, M. J.; Mulvaney, P.; Etheridge, J.; Funston, A. M., Control of symmetry breaking size and aspect ratio in gold nanorods: underlying role of silver nitrate. *The Journal of Physical Chemistry C* **2017,** *121*, 3549-3559.

51. Zhang, Q.; Jing, H.; Li, G. G.; Lin, Y.; Blom, D. A.; Wang, H., Intertwining roles of silver Ions, surfactants, and reducing agents in gold nanorod overgrowth: pathway switch between silver underpotential deposition and gold–silver codeposition. *Chem. Mater.*, **2016,** *28* (8), 2728-2741.

52. Gole, A.; Murphy, C. J., Seed-Mediated Synthesis of Gold Nanorods: Role of the Size and Nature of the Seed. *Chem. Mater.* **2004,** *16* (19), 3633–3640.

53. Smith, D. A.; Korgel, B. A., The importance of the CTAB surfactant on the colloidal seed-mediated synthesis of gold nanorods. *Langmuir* **2008,** *24* (3), 644-649.

54. Scarabelli, L.; Sánchez-Iglesias, A.; Pérez-Juste, J.; Liz-Marzán, L. M., A "tips and tricks" practical guide to the synthesis of gold nanorods. *J. Phys. Chem. Lett.* **2015,** *6* (21), 4270-4279.

55. Shi, W.; Casas, J.; Venkataramasubramani, M.; Tang, L., Synthesis and characterization of gold nanoparticles with plasmon absorbance wavelength tunable from visible to near infrared region. *ISRN Nanomaterials* **2012,** *2012*, 659043-659052.

56. Watt, J.; Hance, B. G.; Anderson, R. S.; Huber, D. L., Effect of seed age on gold nanorod formation: a microfluidic, real-time investigation. *Chemistry of Materials* **2015,** *27* (18), 6442-6449.

57. Thambi, V.; Kar, A.; Ghosh, P.; Paital, D.; Gautam, A. R. S.; Khatua, S., Synthesis of complex nanoparticle geometries via pH-controlled overgrowth of gold nanorods. *ACS Omega* **2019,** *4* (9), 13733-13739.

58. Cheng, J.; Ge, L.; Xiong, B.; He, Y., Investigation of pH effect on gold nanorods synthesis. *Journal of the Chinese chemical Society* **2011,** *58*, 822-827.

59. Shi, D.; Song, C.; Jiang, Q.; Wang, Z.-G.; Ding, B., A facile and efficient method to modify gold nanorods with thiolated DNA at a low pH value. *Chemical Communications* **2013,** *49* (25), 2533-2535.

60. Novo, C.; Gomez, D.; Perez-Juste, J.; Zhang, Z.; Petrova, H.; Reismann, M.; Mulvaney, P.; Hartland, G. V., Contributions from radiation damping and surface scattering to the linewidth of the longitudinal plasmon band of gold nanorods: a single particle study. *Physical Chemistry Chemical Physics* **2006,** *8* (30), 3540-3546.

61. Ye, Y.; Chen, T. P.; Liu, Z.; Yuan, X., Effect of surface scattering of electrons on ratios of optical absorption and scattering to extinction of gold nanoshell. *Nanoscale Research Letters* **2018,** *13* (1), 299-310.

62. Ray, K.; Zhang, J.; Lakowicz, J. R., Fluorescence lifetime correlation spectroscopic study of fluorophore-labeled silver nanoparticles. *Analytical Chemistry* **2008,** *80* (19), 7313–7318.

63. Racknor, C.; Singh, M. R.; Zhang, Y.; Birch, D. J. S.; Chen, Y., Energy transfer between a biological labelling dye and gold nanorods. *Methods and Applications in Fluorescence* **2014,** *2* (1), 015002-015008.

64. Zhang, Y.; Wei, G.; Yu, J.; Birch, D. J. S.; Chen, Y., Surface plasmon enhanced energy transfer between gold nanorods and fluorophores: application to endocytosis study and RNA detection. *Faraday Discuss* **2015,** *178*, 383-394.

Chapter 4

Characterization of the optical properties and the photothermal effects of gold nanorods

4. 1. Introduction

Gold nanorods (GNRs) have attracted great attention because of their excellent physical and chemical properties and these properties have been exploited for biomedical applications such as bio-sensing, cell imaging, remote release of drugs and photothermal therapy of cancer[1-5]. GNRs have longer period (~17 hours) of circulation in the blood than other gold nanoparticles (nanospheres, nanoshells and nanocages) due to their anisotropic shape[6-7].

GNRs can be excited from the visible to the near infrared (NIR) wavelengths by a continuous laser illumination[7-8]. The excited free electrons in the gold nanorods oscillate coherently in resonance with the incident light leading to strong absorption and scattering of light from the visible to the near infrared wavelengths of the electromagnetic spectrum where the biological tissue transmission efficiency is very high[7, 9]. The surface plasmon resonance (SPR) effect of GNRs enhances light absorption and scattering efficiency a million times more intense than the organic dyes (e.g. indocyanine green and porphyins) [1, 7, 10].

In comparison, GNRs have superior properties than other gold nanoparticles of comparable size [11]. For example, the extinction cross-section of the GNRs is around 2-3 times higher than that of the gold nanosphere and the gold nanoshells of comparable size[7, 11]. Gold nanorods have been found to generate heat ~6 times faster than the gold nanospheres[9, 12]. In addition, the longitudinal absorption band of the GNRs can be tuned to the near infrared wavelengths, while the absorption band of the gold nanospheres is limited to the visible wavelengths, making the GNRs a better candidate for biomedical applications in the near infrared of the electromagnetic spectrum[7]. Although the absorption band of gold nanoshells can be tuned to the near infrared wavelengths, they are much larger in size (100-200 nm) compared to the GNRs[7], thus, limiting their

possibility of crossing biological barriers. These excellent attributes of the GNRs informed the choice of GNRs for this study to gain further insight into the optical absorption and scattering properties of GNRs and their photothermal effects to optimize their performance in biomedical applications.

Large gold nanorods (LGNRs) with > 10 nm in diameter have higher extinction cross-sections than that of the small gold nanorod (SGNRs) with < 10 nm in diameter as predicted by the Gans model because the LGNRs have a larger particle volume compared to the SGNRs [11, 14]. In fact, the LGNRs have a higher scattering cross-section compared to the SGNRs [1, 11, 13, 15], thus are good contrast agents for biological imaging. On the other hand, the optical properties of the SGNRs are absorption dominant[2, 14], thus, the SGNRs are more suitable for photothermal applications. Optical absorption in GNRs triggers the generation of thermal energy by the GNRs via a non-radiative process[16-17]. That is, the free electrons in gold nanorods become excited following laser illumination. By means of a rapid phase loss in femtoseconds[1], the excited electrons collide with neighbouring electrons via electron-electron interactions leading to hot electrons with a temperature as high as 1000K[1, 7, 18]. The hot electrons transmit their heat energy to the phonons via electron-phonon interactions in about 0.5-1.0ps, heating up the lattice with rising temperature of about tens of degrees[1, 7]. The lattice dissipates the heat energy to the surrounding medium via phonon-phonon relaxation in about 100ps[1, 7, 16, 19]. The heat of the surrounding medium of the GNRs can be exploited for photothermal treatment of cancer[7]. The ability of GNRs to convert the absorbed photons to heat is called photothermal conversion efficiency. The photothermal conversion of the GNRs depends on the size and shape of the GNRs[16, 20], therefore it is important to select a suitable size and shape of the GNRs for optimal photothermal applications[21]. It has been established that the efficiency of photothermal conversion decreases with the increase of the size of GNRs because of strong scattering effects associated with the larger size gold nanorods[16, 21].

The photothermal effects of the LGNRs in water and biological media[2, 5, 22] have been studied previously. In water for example, Cong et al. have demonstrated that by increasing the power density of laser irradiation, the temperature of a conventional gold nanorod suspension rises quickly and the shape of the gold nanorods could be deformed, causing

the disappearance of the longitudinal surface plasmon resonance[23]. GNRs based nanoprobes have been found to destroy tumours in mice via the photothermal process[4, 7, 24].

Moreover, the artificial hydrogels and the biological hydrogels exhibit similar optical characteristics as the interstitial tissues[25-28] and can therefore be used as model systems to study the photothermal effect of gold nanorods. Previous studies found the changes of opto-electronic properties of gold nanoparticles in these model systems. It has been shown that the surface plasmon resonance of a gold nanosphere is red shifted in agarose gel due to the change of environmental refractive index and nanoparticle aggregation[29]. The effect of plasmon resonance excitation, laser density and particle concentration on the local temperature of a colloid of LGNRs has been investigated[16, 23, 30]. However, to the best of our knowledge, the photothermal effect of the different sizes of GNRs in hydrogels has not been investigated.

This chapter focuses on the study of the optical properties and the photothermal effects of the small gold nanorods in water and agarose hydrogel in comparison with the large gold nanorods. Theoretical calculations were performed to estimate the optical properties of the SGNRs and the LGNRs, and the influence of the optical properties on the photothermal effects. Moreover, experimental study revealed the influence of surface plasmon resonance, size of the GNRs and the surrounding medium on the photothermal effects.

4. 2. Experimental section

4. 2. 1. Materials

All chemicals were used as received without further purification. Chloroauric acid ($HAuCl_4$, 49%), hexadecyltrimethylammonium bromide (CTAB, 99%), ascorbic acid (AA), sodium borohydride ($NaBH_4$, 99.8%), silver nitrate ($AgNO_3$) and agarose gel were all purchased from Sigma Aldrich while hydrochloric acid (HCl) was purchased from Fluka.

4. 2. 2. Synthesis of gold nanorods

Both the LGNRs and the SGNRs were synthesized by different silver-assisted seed mediated growth methods. The LGNRs were synthesized according to a reported protocol[31] with some adjustments. The seeds solution for the LGNR was prepared by adding $HAuCl_4$ (0.001 M; 2.5 ml) to a solution of the CTAB (0.2 M; 7.5 ml). Thereafter, a freshly prepared ice-cold $NaBH_4$ solution (0.01 M; 0.6 ml) was added to the mixture and stirred with a magnetic stirrer for 2-3 minutes until the seeds solution turned dark-brown colour. The seeds solution was incubated at room temperature for 3 hours before being used. The growth solution was prepared by scaling down (20x) the volume of the chemicals used for the growth solution as follows; $HAuCl_4$ (0.001 M; 10.0 ml) was added to the solution of CTAB (0.2 M; 10.0 ml) in three separate samples. To each solution, varying amounts of $AgNO_3$ (0.004 M; 0.158 ml, 0.200 ml and 0.380 ml) were added respectively, follow by ascorbic acid (0.0778 M; 0.140 ml). After stirring for few minutes, 0.020 ml of the gold seeds solution were added to each solution and kept at room temperature overnight. Table 4.1. lists all the chemicals used for sample preparation.

Table 4.1. The list of reagents used to prepare the seeds and the growth solutions of the LGNRs.

Reagents		$HAuCl_4$ (0.001M; ml)	CTAB (0.2M; ml)	$NaBH_4$ (0.01M; ml)	$AgNO_3$ (0.004M; ml)	A.A (0.0778M; ml)	Seeds (ml)
Seeds solution		2.50	7.50	0.60	-	-	-
Growth solution	LGNR-158	10.00	10.00	-	0.158	0.14	0.02
	LGNR-200	10.00	10.00	-	0.200	0.14	0.02
	LGNR-380	10.00	10.00	-	0.380	0.14	0.02

The SGNRs were synthesized by our modified silver-assisted seed growth method[13]. The seeds solution was prepared and incubated as reported in chapter 3. The growth solution was prepared by adding $HAuCl_4$ (0.01 M; 0.5 ml) to the solution of CTAB (0.1 M; 9.0 ml) in three separate samples. To each solution, varying amounts of $AgNO_3$ (0.01 M; 0.060 ml, 0.075 ml and 0.090 ml) were added respectively, followed by adding the same amount of HCl (1.0 M; 0.2 ml) and ascorbic acid (0.1 M; 0.08 ml). After stirring for few minutes, 1 ml of the gold seeds solution was added to each solution and kept at room temperature overnight. Table 4.2. lists all the chemicals used for sample preparation.

Table 4.2. The list of reagents used to prepare the seeds and growth solutions of the SGNRs.

Reagents		$HAuCl_4$ (0.01M; ml)	CTAB (0.1M; ml)	$NaBH_4$ (0.01M; ml)	$AgNO_3$ (0.01M; ml)	HCl (1.0M; ml)	A.A (0.1M; ml)	Seeds (ml)
Seeds solution		0.25	9.75	0.60	-	-	-	-
Growth solution	G_9S_1-60	0.50	9.00	-	0.060	0.20	0.08	1.00
	G_9S_1-75	0.50	9.00	-	0.075	0.20	0.08	1.00
	G_9S_1-90	0.50	9.00	-	0.090	0.20	0.08	1.00

4. 2. 3. Sample preparation and experimental setting for photothermal study in water

The synthesized LGNRs and SGNRs were centrifuged at room temperature at 13000 rpm for 15 minutes to purify the GNRs. The pellets of the bare GNRs were suspended in 3.3 ml of water in a transparent plastic cuvette (1 cm path length) to measure the extinction using a UV-vis spectrophotometer. The pellets of GNRs were added to the 3.3 ml of water until the extinction was raised to an optical density of 0.99. The entire mixture was emptied into a glass cuvette (4.2x1.2 cm) mounted on a magnetic stirring plate for excitation. The room temperature of CTAB stabilized LGNRs and SGNRs was 19.80 ^oC and these were excited both on-resonance and off-resonance at 715 nm, 750 nm and 800 nm using a femtosecond Ti: Sapphire continuous-wave laser (Chameleon, Coherent, Santa Clara, California) for 16 minutes. A magnetic stirrer and a thermocouple (Omega, HH804) were both inserted into the glass cuvette to ensure uniform distribution of heat and record the temperature rise respectively. The depth of the thermocouple's probe was maintained at the same position 1.4 cm from the top of the cuvette for each measurement.

The excitation beam was propagated perpendicular to the glass cuvette containing colloid of SGNRs and LGNRs. A coherent laser power meter (FieldMax$_{II}$) was used to measure the incident power density. The experimental set up for photoexcitation of the gold nanorods is shown in figure 4. 1.

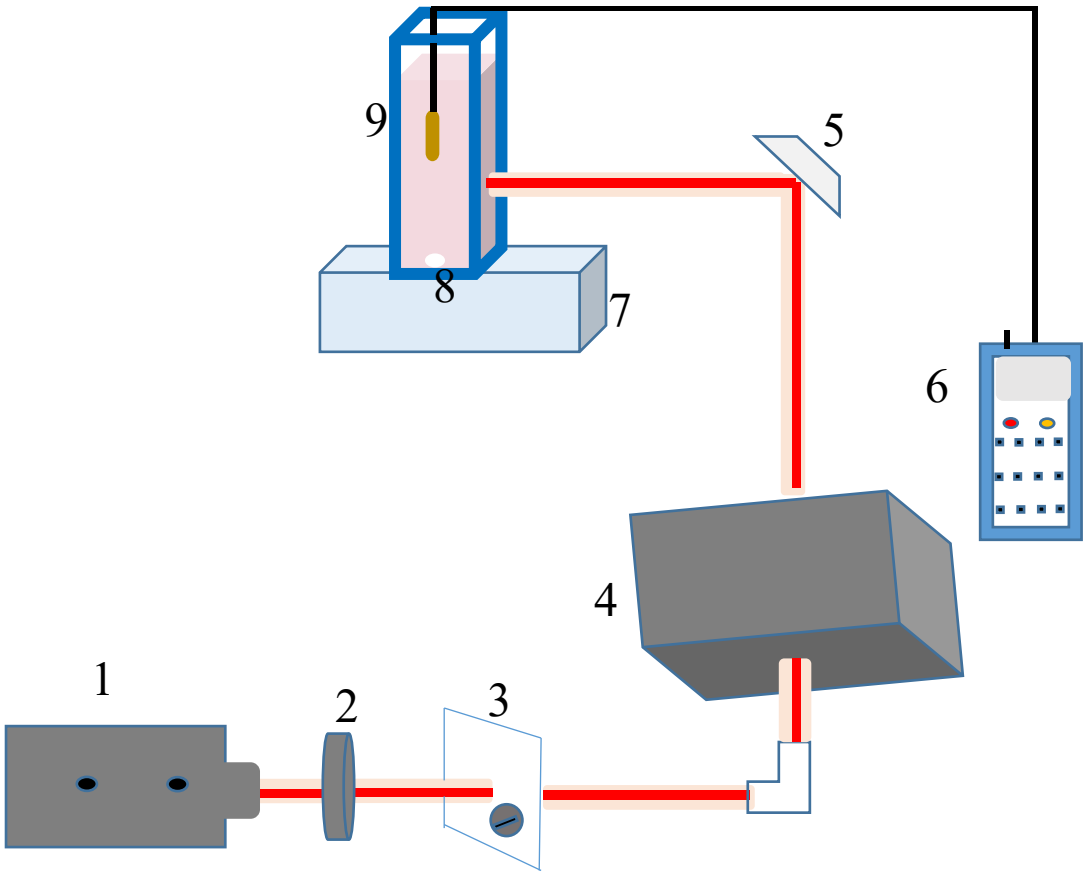

1. Coherent Laser
2. Beam splitter
3. Switch
4. Optical lens box
5. Optical mirror
6. Thermocouple
7. Magnetic Stirring Plate
8. Magnetic stirrer
9. Glass cuvette

Figure 4. 1. The experimental set up for laser excitation of gold nanorods.

4. 2. 4. Sample preparation for photothermal effect study in agarose gel

The longitudinal surface plasmon resonance (LSPR) of the LGNRs in TBE buffer-agarose gel and water-agarose gel of varying concentration was studied. Firstly, agarose

powder (2.5%, 0.5g) was dissolved in 20ml of TBE buffer and water as stocks of agarose gel respectively at 70 ^{o}C and allowed to cool at 21 ^{o}C-22 ^{o}C. Then appropriate volumes of TBE buffer and water were added to dilute the respective stocks of agarose gel into varying concentrations ranging from 0.3% - 2.5%. The LGNRs were then dispersed into the different concentrations of TBE buffer and water agarose gel, while the extinction was measured at an optical density of 0.9-1.0.

The concentration of agarose gel commonly used for biological applications ranges from 0.5% - 2%[32]. This is because agarose gel possesses physicochemical characteristics similar to the cellular cytoplasm and the biological fluids in this range[33]. Thus, 0.7% concentration of agarose gel was chosen. Agarose (0.7%, 0.14g) powder was dissolved in 20 ml of TBE buffer at 70 ^{o}C and allowed to cool at room temperature. Then, 3.3 ml of agarose gel were placed into a plastic cuvette. The pellets of the LGNR and the SGNR were cast into the 3.3 ml of agarose gel while the UV-vis extinction spectra were measured until the extinction was raised to an optical density of 0.99. Thereafter, the 3.3 ml of agarose-gold nanorods mixture were transferred to a glass cuvette and excited under similar experimental conditions as described in section 4. 2. 3.

4. 3. Optical characterization of gold nanorods

The extinction spectra of the GNRs samples were measured with a UV-vis spectrophotometer (Lambda 2, Perkin Elmer). The sizes of the LGNRs and the SGNRs were determined by a linear fitting to a standard calibration curve of gold nanorods reported in literature[13-14, 16, 31]. The standard calibration curve of the LGNRs and the SGNRs derived from reported GNRs samples are shown in figure 1 and 2 of appendix 2.

4. 4. Theoretical background

The ability of gold nanorods to absorb and scatter incident light is determined by their absorption and scattering cross-sections respectively. Theoretically, the absorption and scattering cross-sections of gold nanorods can be determined by Gans' model. The

absorption cross-section (σ_{abs}) of a single gold nanorod randomly polarized can be written as[3, 34-35]:

$$\sigma_{abs} = \frac{2\pi V \varepsilon'^{\frac{3}{2}}_m}{3\lambda} \sum_{\mathrm{J}} \frac{\left(\frac{1}{\mathrm{p}_j^2}\right)\varepsilon'_i}{\left(\varepsilon'_r + \frac{1-\mathrm{p}_j}{\mathrm{p}_j}\varepsilon'_m\right)^2 + \varepsilon'^2_i} \qquad 4.1.$$

while the scattering cross-section (σ_{sca}) of a single gold nanorod can be written as[34]:

$$\sigma_{sca} = \frac{8\pi^3 \mathrm{v}^2 \varepsilon'^2_m}{9\lambda^4} \sum_{\mathrm{J}} \frac{1}{\mathrm{p}_j^2} \frac{(\varepsilon'_r - \varepsilon'_m)^2 + \varepsilon'^2_i}{\left(\varepsilon'_r + \frac{1-\mathrm{p}_j}{\mathrm{p}_j}\varepsilon'_m\right)^2 + \varepsilon'^2_i} \qquad 4.2.$$

where all the symbols have their usual meaning. Localised surface plasmon resonance in gold nanorods occurs if the resonance condition displayed in equation 1.7. is satisfied. The equation 1.7. can be re-written as:

$$\mathrm{P}_J^* = -\left(\frac{\varepsilon'_r}{\varepsilon'_m} - 1\right)^{-1} \qquad 4.3.$$

where P_j^* is the depolarization factor along the axes of gold nanorods at surface plasmon resonance.

4. 5. Results and Discussion

4. 5. 1. The contribution of the simulated absorption cross-section, scattering cross-section to the extinction cross-section of GNRs

The absorption and scattering cross-sections of the GNRs can be defined as the surface area upon which the GNRs either absorb or scatter incident light[34]. The absorption and scattering cross-sections of a single gold nanorod was computed for wavelengths of incident light between 700-850 nm to accommodate the LSPR of the synthesized GNRs. A single gold nanorod was considered for this study because the number density of the

SGNRs and the LGNRs with the same O.D. varies as demonstrated in table 4.5. Therefore, inclusion of the number density of the GNRs will not give a correct estimation of the absorption and scattering cross-sections of a single SGNR and LGNR of comparable aspect ratio, hence the consideration of a single SGNR and LGNR for computation.

By considering the single gold nanorod suspended in water whose refractive index is 1.332, and assuming the polarization of the single gold nanorod to be oriented along the longitudinal axis, the absorption and scattering cross-sections of GNRs (SGNRs and LGNRs of comparable LSPR) of different aspect ratios were computed using equations 4.1. and 4.2. respectively. Figure 4.2a-c shows the absorption cross-section (σ_{abs}), the scattering cross (σ_{sca}) and the extinction cross-section (γ_{ext}) spectra of the small gold nanorod (SGNRs). It is clear that the extinction cross-section of the SGNRs is dominated by absorption cross-section.

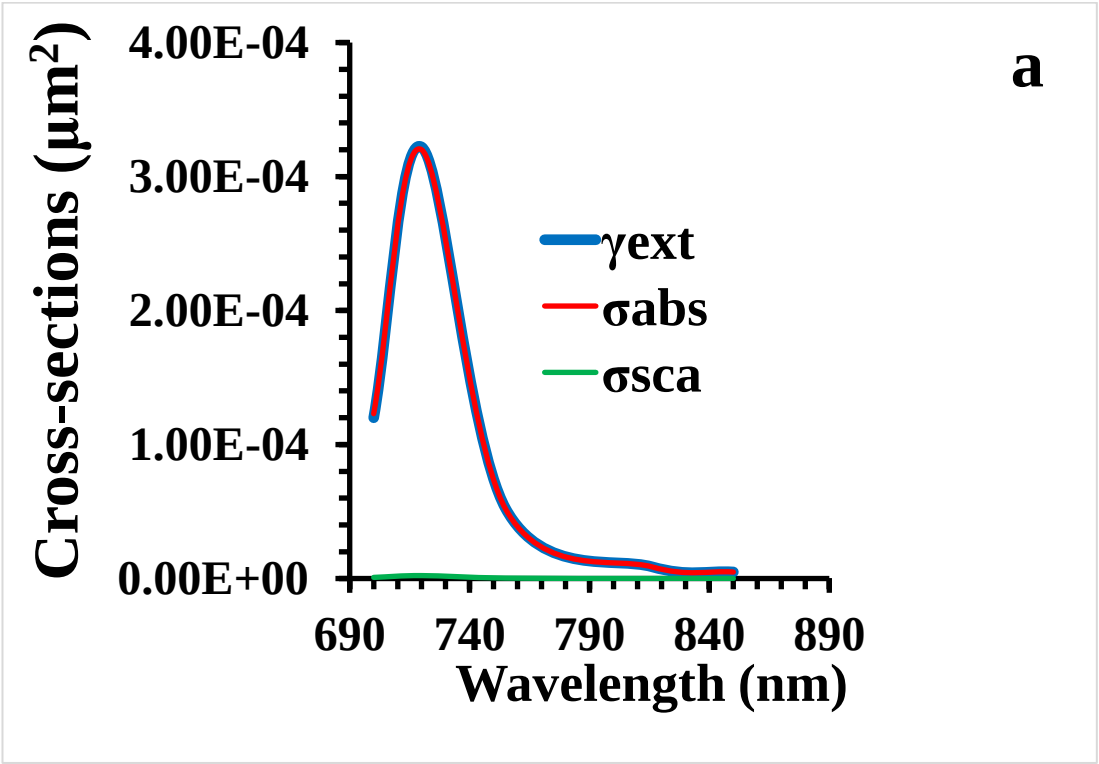

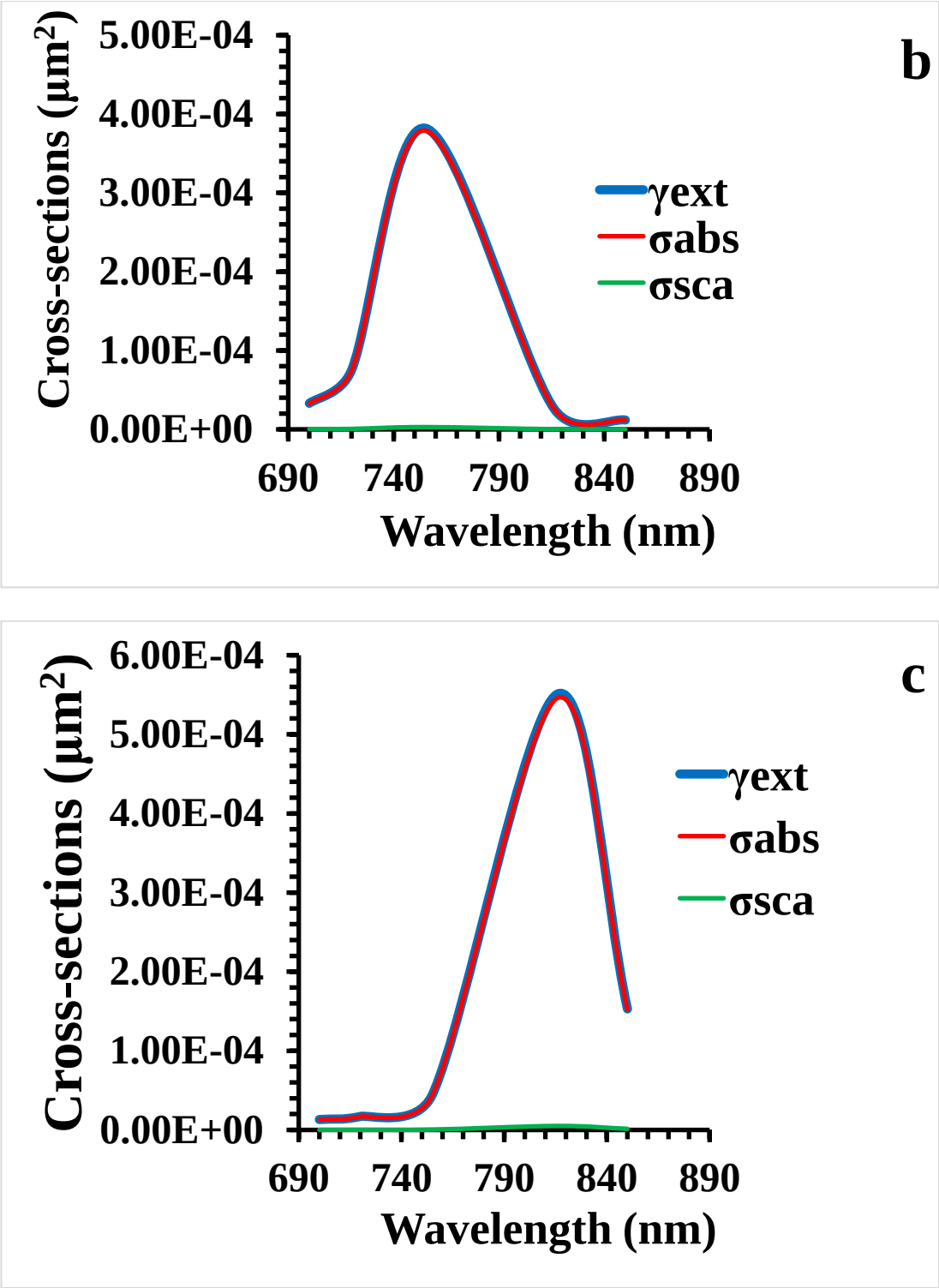

Figure 4.2. The absorption, scattering and extinction cross-sections of SGNRs; (a) S720, (b) S754 and (c) S817.

Figure 4.3a-c displays the absorption, scattering and extinction cross-sections of the LGNRs. It can be seen that the calculated extinction spectra of sample L719, L755 and L816 matched well with their experimental spectra (fig. 4.4c). The absorption cross-sections of L719, L755 and L816 are larger than their scattering cross-sections as previously observed from the SGNRs. However, the contribution of scattering cross-section to the extinction cross-section is seen to increase as the particle size increases in the LGNRs regime, significantly larger than that from the SGNRs. This is due to the larger volume of the LGNRs compared to the SGNRs. This finding is in agreement with previous reports[1, 11, 15].

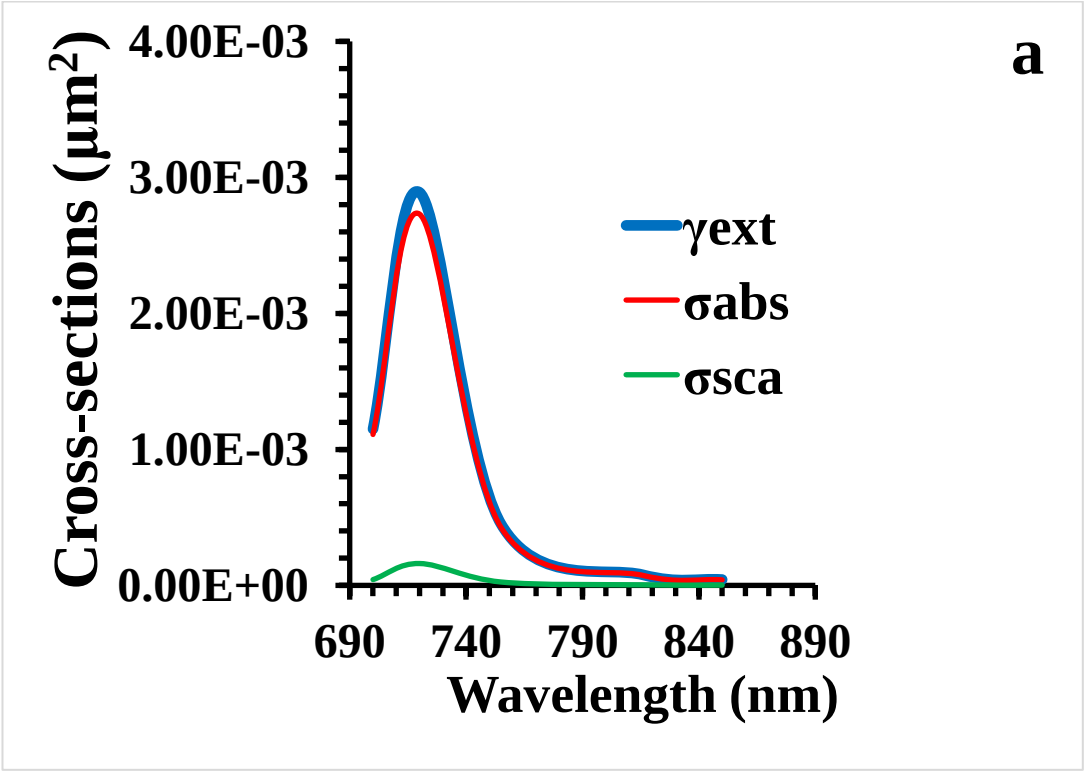

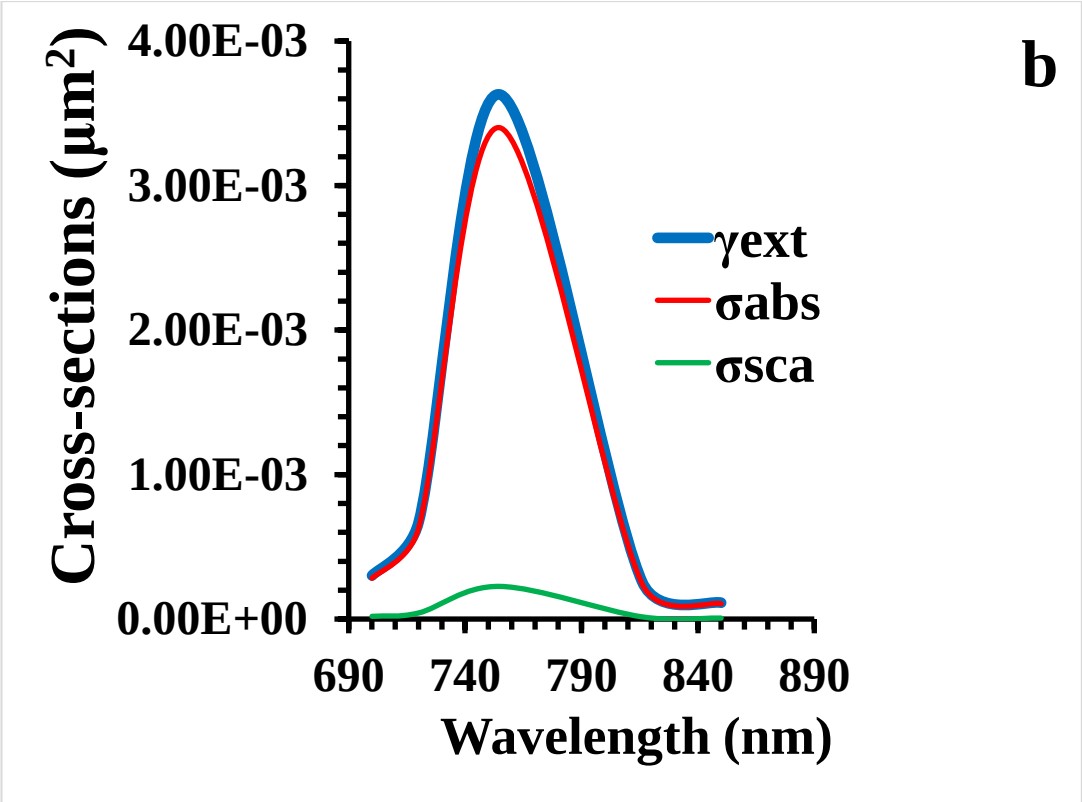

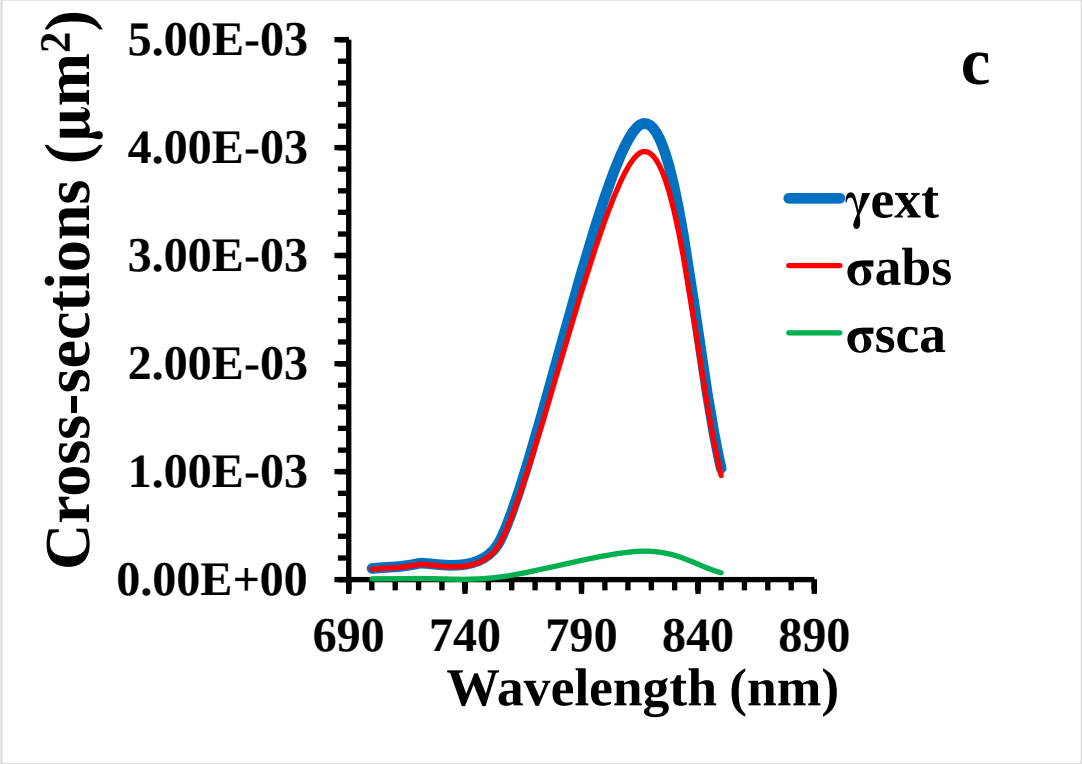

Figure 4.3. The absorption, scattering and extinction cross-sections of LGNRs; (a) L719, (b) L755 and (c) L816.

4. 5. 2. The extinction spectra of GNRs determined by the experimental and the simulation study

The SGNRs and LGNRs of comparable LSPR were synthesized and the position of their LSPR determined by experiment was compared with that obtained by simulation. The UV-vis extinction spectra in fig. 4.4. discloses the longitudinal absorption band of three SGNRs samples centred at 720 nm, 754 nm and 817 , while the LGNRs are centred at 719 nm, 755 nm and 816 nm respectively. The samples were denoted as S720, S754, S817, L719, L755 and L816. The decision of tuning the longitudinal surface plasmon resonance (LSPR) of GNRs to the near-infrared of the electromagnetic spectrum stems from the fact that tissue transmission is high in the biological transparency window (650 nm-950 nm)[7, 36]. It can be seen that the extinction spectra of the SGNRs samples (S720, S754 and S817) and LGNRs (L719, L755 and L816) determined by experimental study matched well with that predicted by Gans' model (fig. 4.4a vs 4.4b and 4.4c vs 4.4d). Furthermore, the peaks of the simulated extinction spectra of SGNRs and LGNRs indicated that the extinction cross-section is enhanced at the longitudinal surface plasmon resonance wavelength. It can be observed further that the extinction cross-section of both the SGNRs and the LGNRs increases as the size of particles increases as predicted by Gans' model. This finding is also consistent with the previous experimental studies[16, 23]. Table 4.3. shows the average length and the average width of SGNRs and LGNRs.

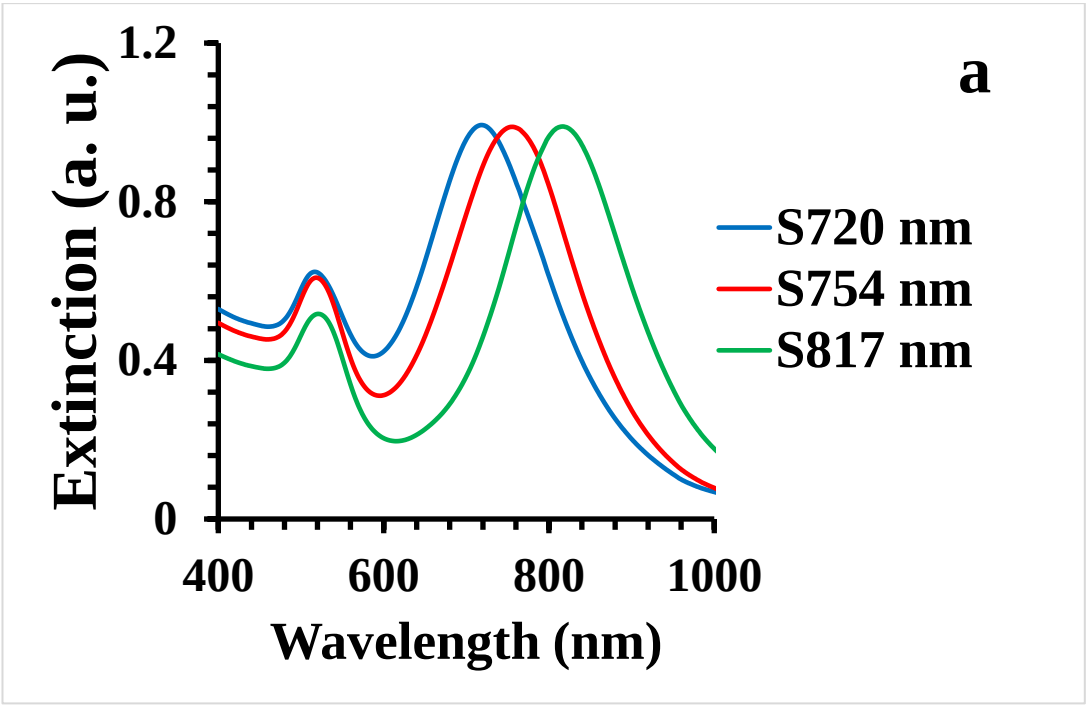
a
Extinction (a. u.)
1.2
0.8
0.4
0
400
600
800
1000
Wavelength (nm)
S720 nm
S754 nm
S817 nm

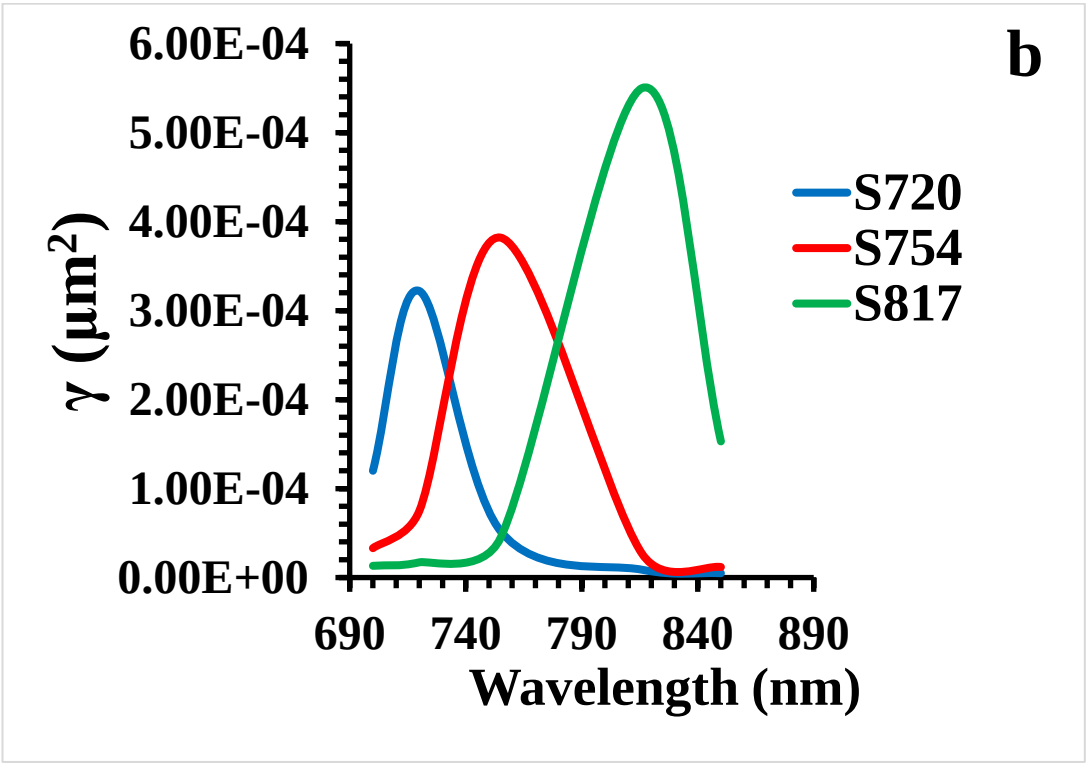
b
γ (μm²)
6.00E-04
5.00E-04
4.00E-04
3.00E-04
2.00E-04
1.00E-04
0.00E+00
690
740
790
840
890
Wavelength (nm)
S720
S754
S817

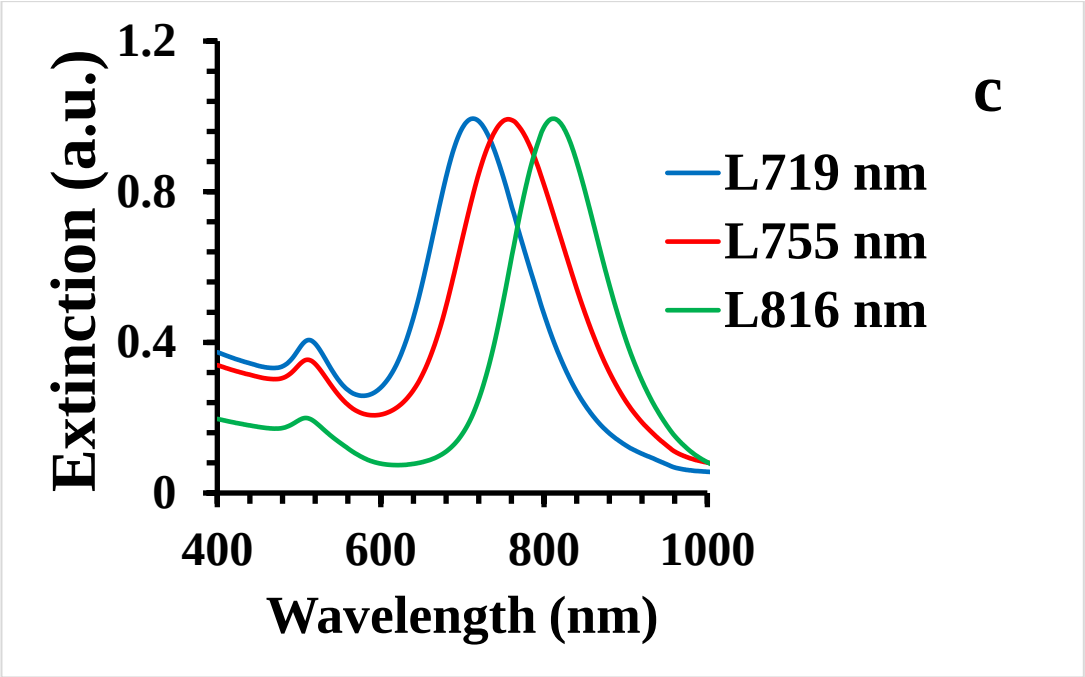

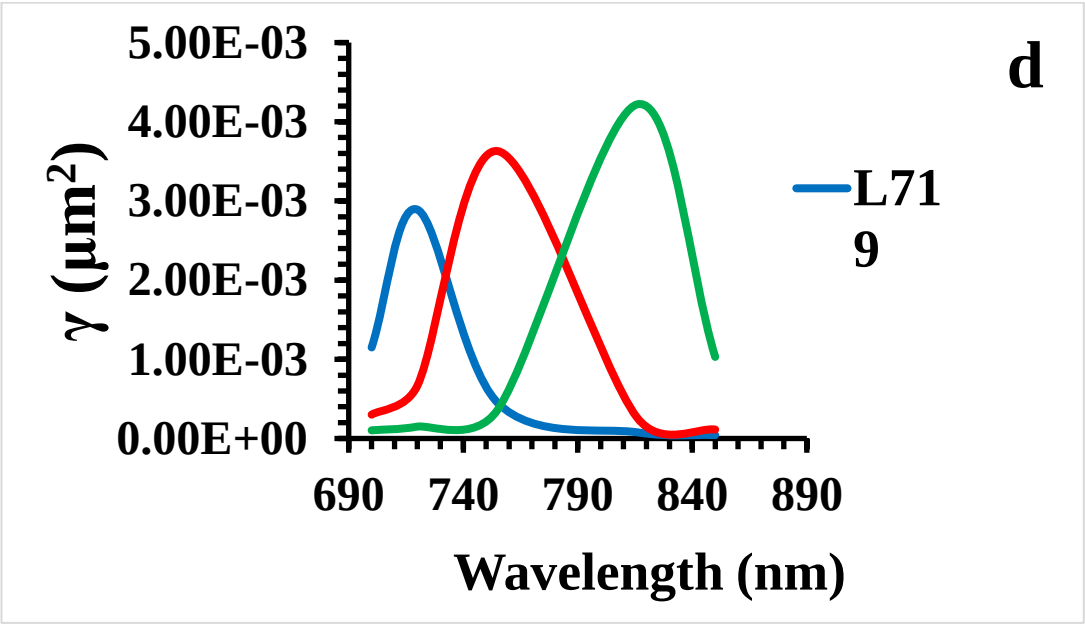

Figure 4.4. The UV-vis and the simulated extinction spectra of GNRs; (a) the UV-vis extinction spectra of SGNRs, (b) the simulated extinction spectra of SGNRs, (c) the UV-vis extinction spectra of LGNRs and (d) the simulated extinction spectra of LGNRs.

Table 4.3. The longitudinal absorption, average length, and the average width of SGNRs and LGNRs.

Samples	LSPR (nm)	Length (nm)	Width (nm)
S720	720	19.7±4.3	5.5±1.3
S754	754	20.9±4.5	5.6±1.3
S817	817	24.0±6.5	6.0±1.0
L719	719	41.1±6.8	11.2±2.2
L755	755	44.5±7.1	11.4±2.0
L816	816	46.2±8.4	11.5±1.5

Figure 4.5. compares the extinction cross-sections of the SGNRs and the LGNRs respectively at three plasmon resonance wavelengths, namely 720 nm, 755 nm and 816 nm. It can be seen that the extinction cross-section of both the SGNRs and the LGNRs is enhanced when the wavelength of incident light matches the longitudinal surface plasmon resonance of the gold nanorods, while at non-plasmon resonance excitation the optical extinction efficiency of GNRs is very weak due to a reduced field at the metal surface[37-38].

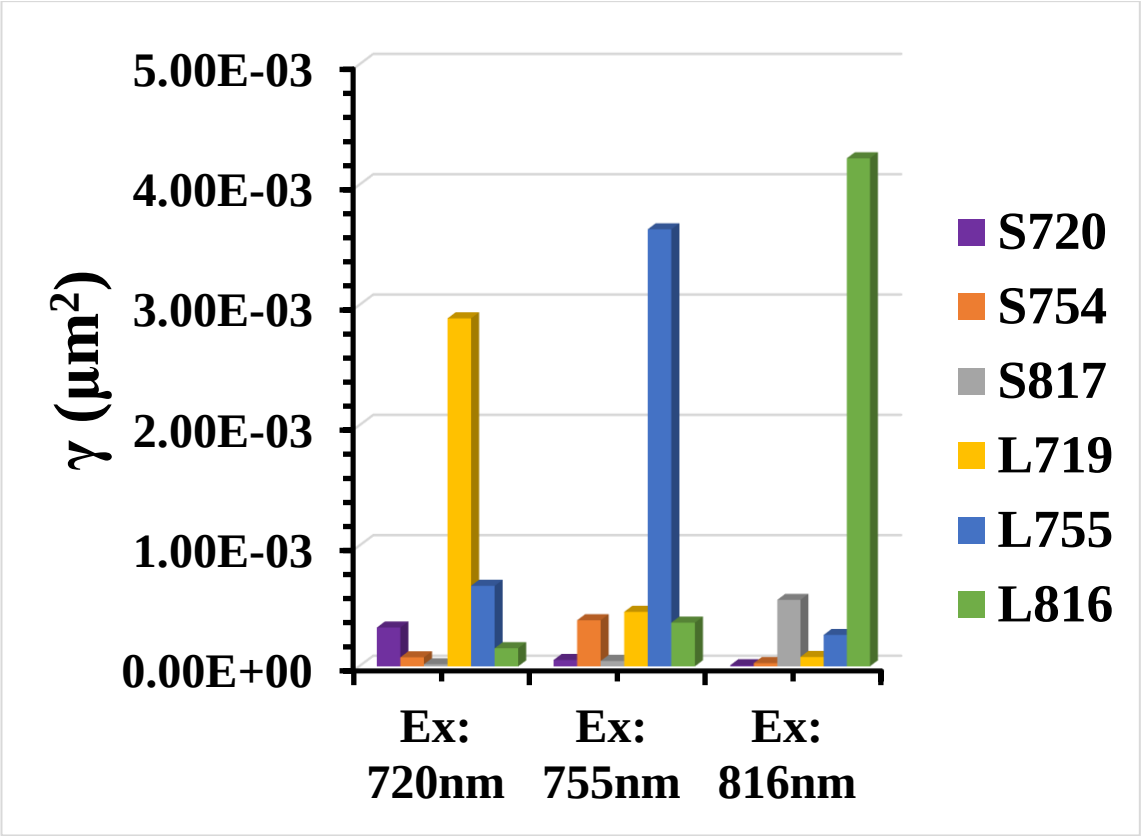

Figure 4.5. The extinction cross-sections of SGNRs and LGNRs at plasmon resonance and non-plasmon resonance excitation wavelengths.

Displayed in figure 4.6. is the scattering-to-absorption ratio of the SGNRs and the LGNRs at the three plasmon resonance wavelengths. We found that the ratio of scattering-to-absorption increases as the size of the gold nanorods increases and the ratio of scattering-to-absorption of the LGNRs is higher compared to the SGNRs as previously reported[1, 15, 39]. Moreover, the ratio of scattering-to-absorption decreases as the excitation wavelength increases. This is because the ratio of scattering-to-absorption is inversely propotional to λ^3 (dividing equation 4.2. with equation 4.1).

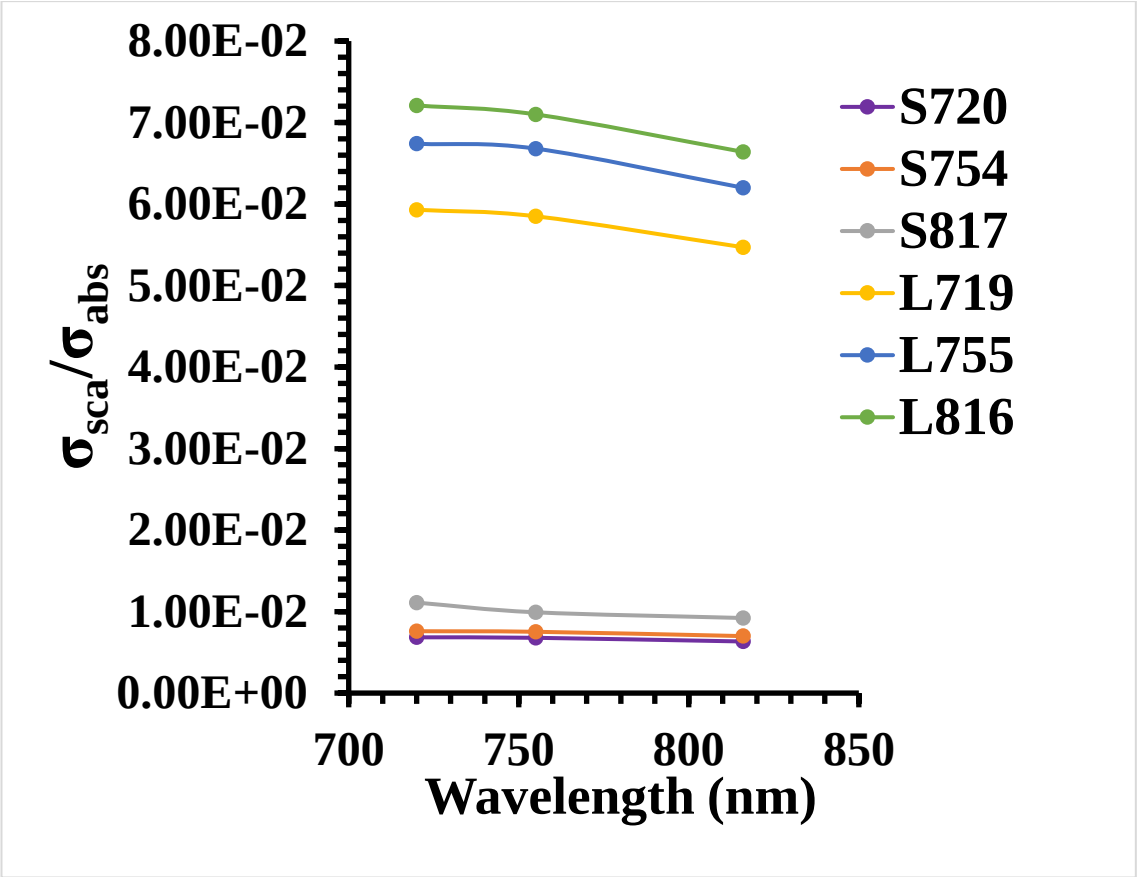

Figure 4.6. The ratio of scattering-to-absorption of SGNRs and LGNRs at plasmon resonance wavelengths.

Figure 4. 7. shows the ratio of absorption-to-extinction of the SGNRs and the LGNRs at the plasmon resonance wavelengths. It can be observed that the ratio of absorption-to-extinction of GNRs increases as the size of the gold nanorods decreases and the ratio of absorption-to-extinction of SGNRs is higher than that of the LGNRs due to a reduced scattering effect as the size of the gold nanorods decreases. Moreover, the ratio of absorption-to-extinction of the SGNRs and the LGNRs slightly increases as the wavelength of incident light increases.

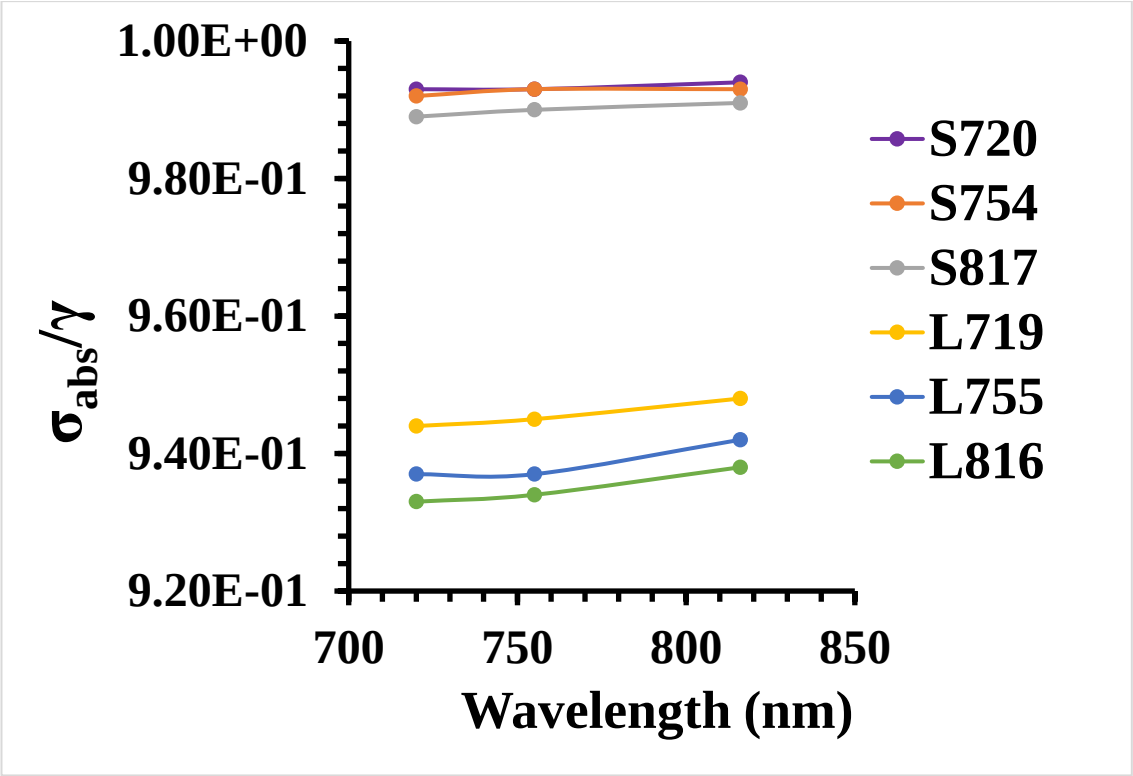

Figure 4.7. The ratio of absorption-to-extinction cross-sections of SGNRs and LGNRs at plasmon resonance wavelengths.

4. 5. 3. Molar extinction coefficients of GNRs

The extinction cross-sections of the GNRs were converted to their molar extinction coefficients (ε) using equation 4.4 given as[9]:

$$\gamma = 3.82 \times 10^{-21} \varepsilon \qquad 4.4.$$

where γ is the extinction cross-section (cm^2) of the gold nanorods and ε is the molar extinction coefficient ($mol^{-1}cm^{-1}$) of the gold nanorods. Table 4.4. displays the molar extinction coefficients of the SGNRs and the LGNRs at three excitation wavelengths 720 nm, 755 nm and 816 nm.

Table 4.4. The molar extinction coefficients of gold nanorods at longitudinal surface plasmon resonance wavelengths in water.

Excitation wavelength (nm)	Molar extinction coefficient, ε ($mol^{-1}cm^{-1}$)					
	S720	**S754**	**S817**	**L719**	**L755**	**L816**
720	$8.43E^{8}$	$1.96E^{8}$	$4.48E^{7}$	$7.57E^{9}$	$1.75E^{9}$	$3.93E^{8}$
755	$1.37E^{8}$	$1.00E^{9}$	$1.16E^{8}$	$1.18E^{9}$	$9.50E^{9}$	$9.48E^{8}$
816	$2.30E^{7}$	$7.02E^{7}$	$1.44E^{9}$	$2.03E^{8}$	$6.81E^{8}$	$1.10E^{10}$

4. 5. 4. Photothermal effect

4. 5. 4. 1. Photothermal conversion efficiency of GNRs

The photothermal conversion efficiency of the gold nanorods has been shown to be dependent on the optical properties of gold nanorods[20]. Theoretically, the photothermal conversion efficiency, η of the GNRs can be expressed as the ratio of absorption-to-extinction cross-sections given as[20]:

$$\eta = \frac{\sigma_{abs}}{\gamma} \qquad 4.5.$$

where σ_{abs} and γ are the absorption and extinction cross-sections of the gold nanorods respectively. The photothermal conversion efficiencies of the GNRs are displayed in fig. 4.8. It is clear that the photothermal conversion efficiency depends on the size of the gold nanorods; the SGNRs have higher photothermal conversion efficiency than the LGNRs because the ratio of absorption-to-extinction of the SGNRs is higher compared to the LGNRs. This finding is consistent with the previous experimental studies[16, 40]. Furthermore, the photothermal conversion efficiency is not significantly altered by the particle size in the regime of SGNRs. However, there is apparent decrease in the photothermal conversion efficiency as the particle size increases in the LGNRs regime, consistent with the previous reports [20-21, 40]. Moreover, the photothermal conversion

efficiency of the SGNRs and the LGNRs is less dependent on the wavelength of incident light [20].

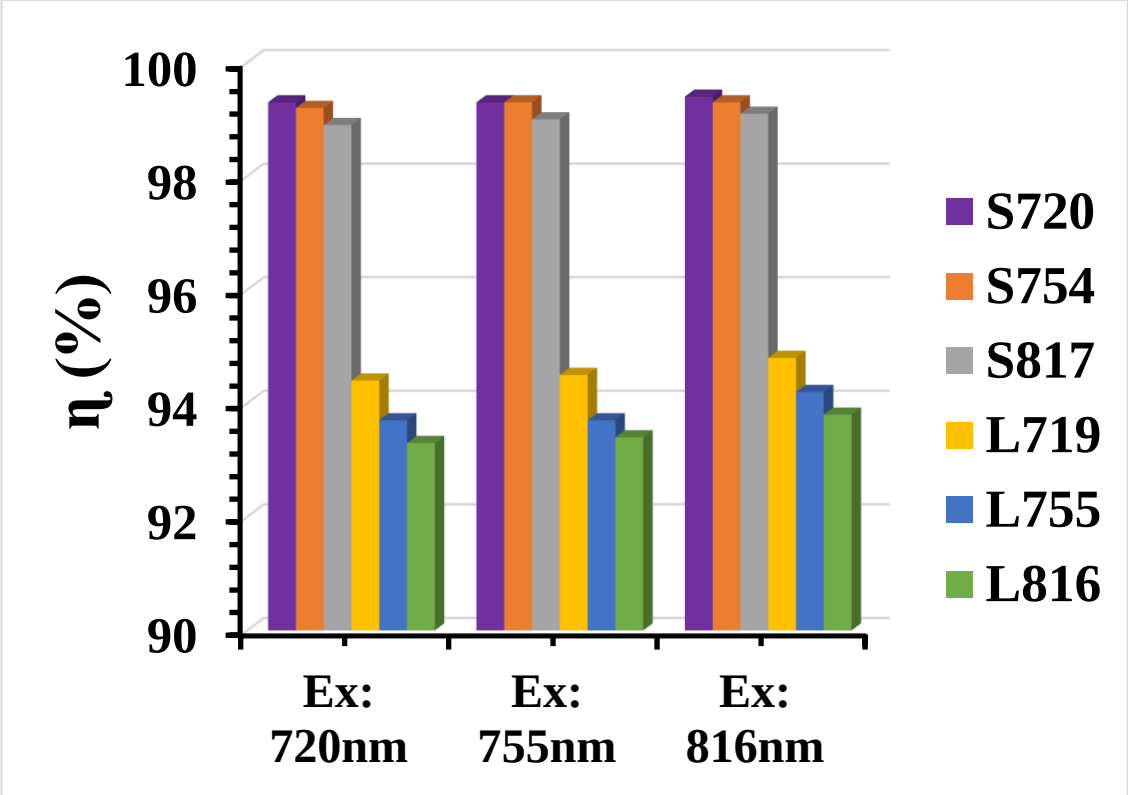

Figure 4. 8. The photothermal conversion efficiencies of the SGNRs and the LGNRs at three plasmon resonance wavelengths.

4. 5 .4. 2. Heat generation via a photothermal process of GNRs

Laser light of a selected wavelength can be used to excite GNRs. The heat generated by the GNRs, Q, correlates to the absorption cross section as[20]:

$$\sigma_{abs} = \frac{Q}{NIV} \qquad 4.6.$$

where σ_{abs} is the absorption cross section (cm^2) of the GNRs, N is the number density of the GNRs (cm^{-3}), I is laser power density (W/cm^2) and V is the volume (cm^3) of the GNRs solution. The absorption cross-sections were calculated at the LSPR of SGNRs and LGNRs respectively, while the optical density (O.D.) of 0.99 was measured with a spectrophotometer and this was used to determine the nanorods' concentration using

equation 2.1. Thus, the number density of particles was calculated by equation 4.7. given as[14]:

$$N = N_A C \times 10^{-3} \qquad 4.7.$$

where N_A is the Avogadro's constant (N_A= 6.022 x 10^{23} Mol^{-1}), C is the concentration of the GNRs in Mol/cm^3 determined from Beer's law. The power density used to calculate Q was 2.74±0.16W/cm^2 at 715 nm, 750 nm and 800 nm laser wavelengths respectively, while the volume of the SGNRs and the LGNRs solution was 3.3 cm^3.

Table 4.5. lists σ_{abs}, N, and V used to calculate Q. Figure 4. 9. shows the heat generated by a colloid of the SGNRs and the LGNRs at 715 nm, 750 nm and 800 nm. It can be observed that heat generation is enhanced when the excitation wavelength matches the longitudinal surface plasmon wavelength of the GNRs. This is because light absorption by both the SGNRs and the LGNRs is significantly enhanced at the surface plasmon resonance[10, 37-38]. Moreover, the heat generated by the SGNRs is slightly higher compared to the heat generated by the LGNRs. Based on Gans' model, we found that the ratio of absorption-to-extinction (fig. 4.7.) of the SGNRs is higher than that of the LGNRs leading to a higher photothermal conversion of the SGNRs as demonstrated in figure 4.8. Thus, the higher photothermal conversion of the SGNRs results to a higher photothermal energy of the SGNRs in contrast to that of the LGNRs. Moreover, the number density of the SGNRs are slightly larger than that of the LGNRs in the solutions with the same optical density (O.D.; 0.99).

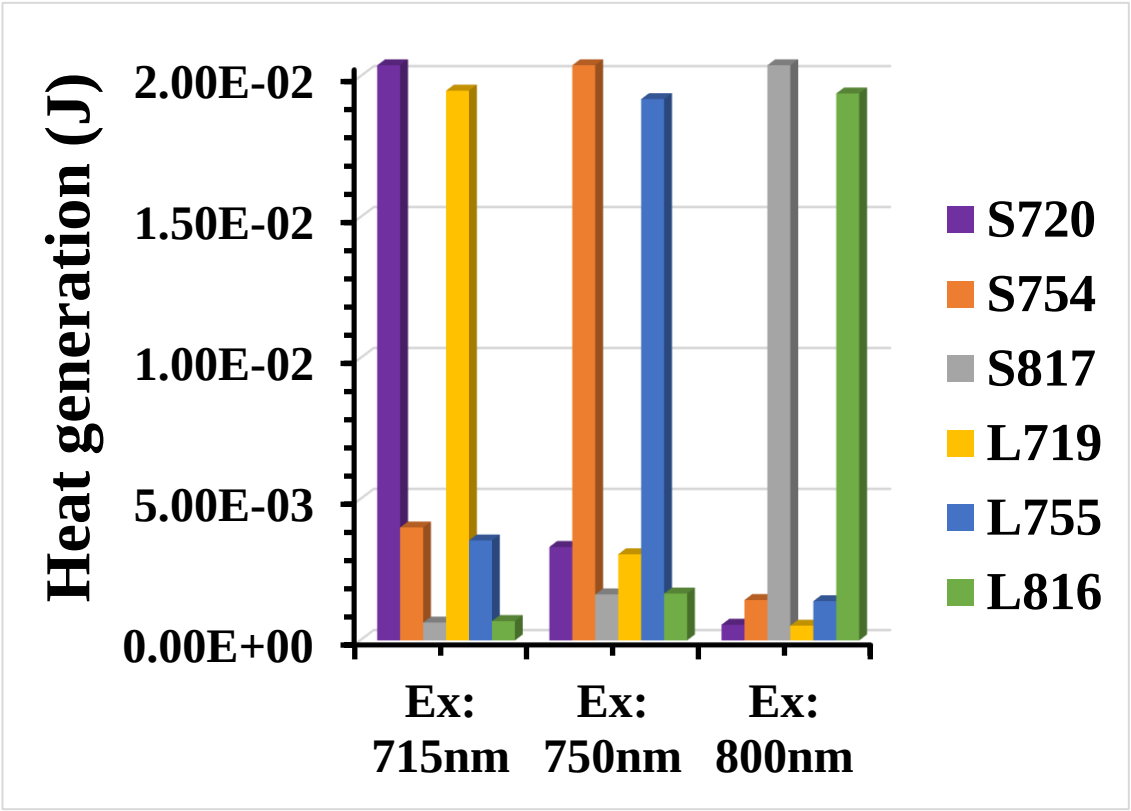

Figure 4.9. The heat generated by a colloid of SGNRs and LGNRs illuminated at 715 nm, 750 nm and 800 nm.

Table 4.5. The list of the parameters for calculating the heat generation of the SGNRs and the LGNRs. The absorption cross-section of the SGNRs and the LGNRs was calculated at their LSPR.

Sample	S720	S754	S817	L719	L755	L816
σ_{abs} (μm^2)	$3.20E^{-4}$	$3.79E^{-4}$	$5.46E^{-4}$	$2.73E^{-3}$	$3.40E^{-3}$	$3.96E^{-3}$
C ($mol/\mu m^3$) ($x10^{-24}$)	1.17	0.99	0.688	0.131	0.104	0.090
N (μm^{-3})	$7.05E^{-4}$	$5.96E^{-4}$	$4.14E^{-4}$	$7.89E^{-5}$	$6.26E^{-5}$	$5.42E^{-5}$
V (μm^3)	$3.30E^{12}$	$3.30E^{12}$	$3.30E^{12}$	$3.30E^{12}$	$3.30E^{12}$	$3.30E^{12}$

4. 5. 5. Photothermal effect of SGNRs and LGNRs illuminated in water suspension

Figure 4.10. illustrates the UV-vis extinction spectra of the gold nanorods before and after illumination in water suspension for 16 minutes at wavelengths (715 nm, 750 nm and 800 nm) close to their corresponding surface plasmon resonance wavelength. It can be observed that the longitudinal absorption of both the SGNRs and the LGNRs blue shift slightly after illumination without a clear change in the peak width, indicating the photostability of the gold nanorods. The small blue shift could be ascribed to the slight shortening of the GNRs due to laser induced heating. Gans' model[35] had predicted that the optical absorption of gold nanorods is linearly dependent on the aspect ratio (A.R.) of the gold nanorods. The shortening of the length of gold nanorods reduces the A.R. of gold nanorods, hence, the blue shift of both SGNRs and LGNRs after photoexcitation in solution. Moreover, Link and El-Sayed[41] predicted that the longitudinal absorption of gold nanorods is linearly dependent on the A.R. and dielectric constant of the surrounding medium (equation 1.7.). A decrease of the A.R. of the gold nanorods reduces the longitudinal absorption of the gold nanorods leading to a blue shift. In comparison, the peak intensity of the SGNRs remains relatively unchanged after laser illumination at plasmon resonance (fig.4.10a). However, the peak intensity of the LGNRs increased after laser illumination (fig.4.10b). This suggests an increase of particle concentration due to the evaporation of water. Moreover, the increase in the peak intensity of L755 is higher than that of L816 and L719, possibly due to a slightly higher laser power density at 750 nm ($2.74\pm0.16 W/cm^2$) than that at 800nm ($2.74\pm0.16 W/cm^2$) and 715nm ($2.74\pm0.16 W/cm^2$). The normalised temperature rise of the laser illuminated SGNRs and LGNRs in water solution are displayed in table 1a and 1b respectively of appendix 2.

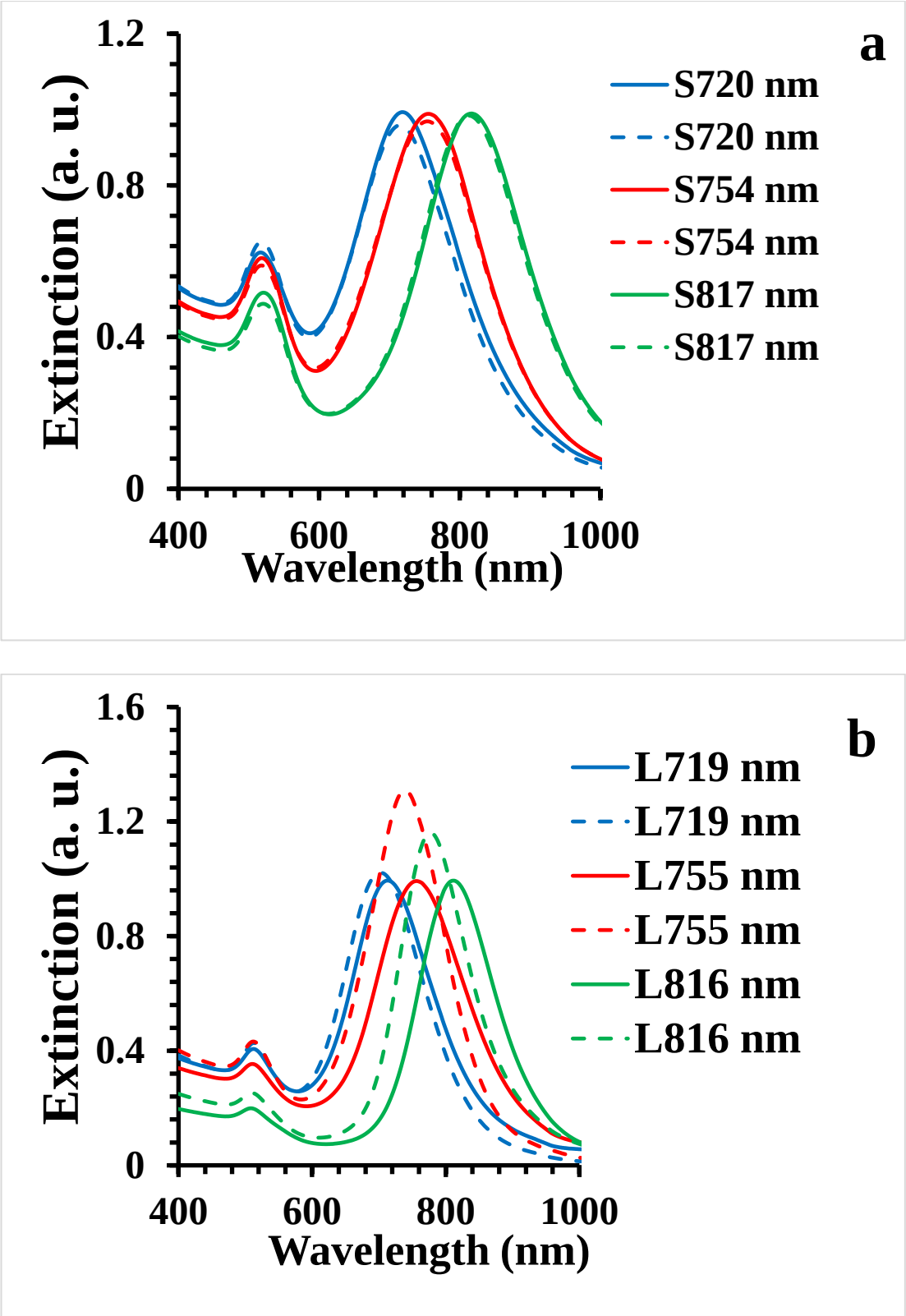

Figure 4.10. The UV-vis extinction spectra of the GNRs; (a) SGNRS and (b) LGNRs in water before (solid line) and after (dashed line) laser irradiation.

Figure 4.11. shows the temperature response of the SGNRs and the LGNRs versus illumination time. Three laser wavelengths were chosen, namely 715 nm, 750 nm and 800 nm, as they overlapped with the longitudinal surface plasmon resonance of S720/L719, S754/L755 and S817/L816 respectively. The temperature responses of the SGNRs and the LGNRs were normalised against 2.74±0.16W/cm^2 laser intensity because the laser intensities at 715 nm and 800 nm laser wavelengths were 2.57±0.15W/cm^2 and 2.78±0.05W/cm^2 respectively, while the laser intensity at 750 nm laser wavelength was 2.74±0.16W/cm^2. It can be seen that the temperature of all the samples increased with irradiation time and there is an initial fast rise, followed by a slow increase before reaching saturation. There is no obvious surface plasmon effect for the SGNRs; the temperature profiles of the SGNRs on resonance excitations are close to that of the SGNRs at off-resonance excitations. This is likely due to the broad surface plasmon bands and slight mismatch of the irradiation wavelength with the surface plasmon resonance wavelength. For example, as shown in fig 4.10., the extinction of S754 is close to that of S720 and both are clearly larger than the extinction of S817 at 715nm, in line with the trend in fig 4.11a. In addition, likely experimental uncertainty in the laser intensity, particle concentration and illumination time also make the surface plasmon effect less obvious. However, the surface plasmon enhancement effect can be observed for the LGNRs where relatively larger temperature increase was observed when the excitation wavelength is in resonance with the longitudinal surface plasmon resonance. This surface plasmon effect in the LGNRs regime is less significant in comparison with the simulation (fig. 4.9).

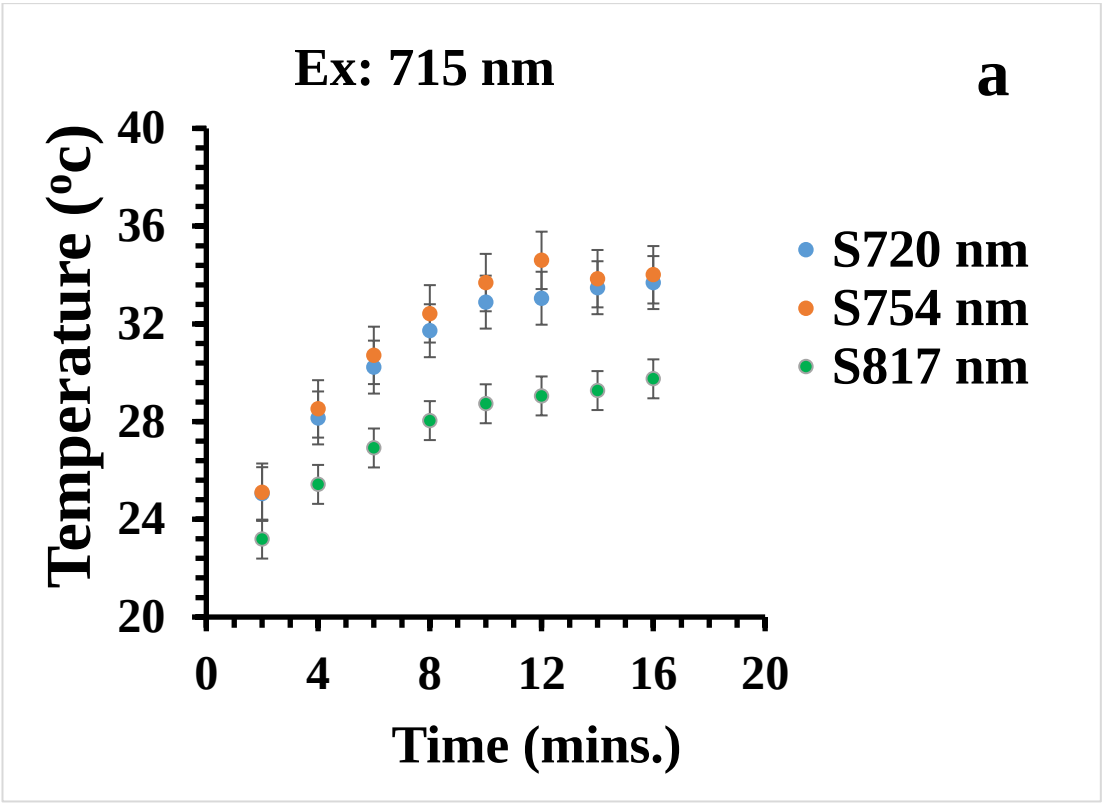
Ex: 715 nm
a
Temperature (°c)
40
36
32
28
24
20
0
4
8
12
16
20
Time (mins.)
S720 nm
S754 nm
S817 nm

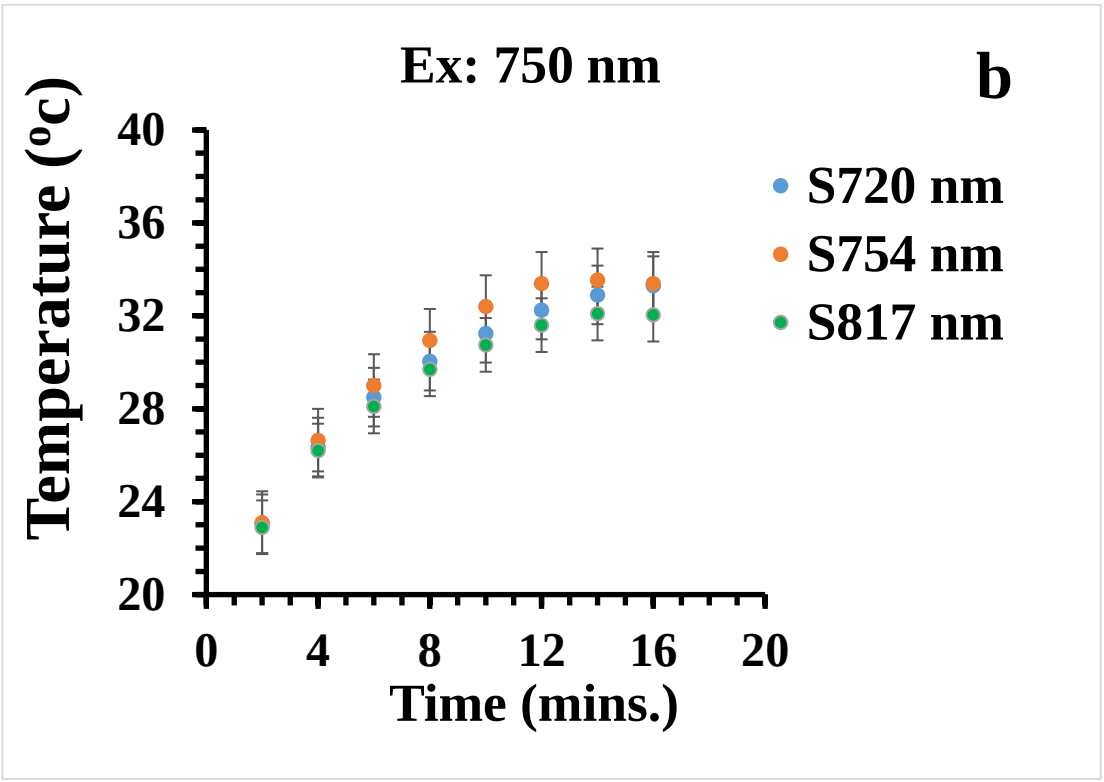
Ex: 750 nm
b
Temperature (°c)
40
36
32
28
24
20
0
4
8
12
16
20
Time (mins.)
S720 nm
S754 nm
S817 nm

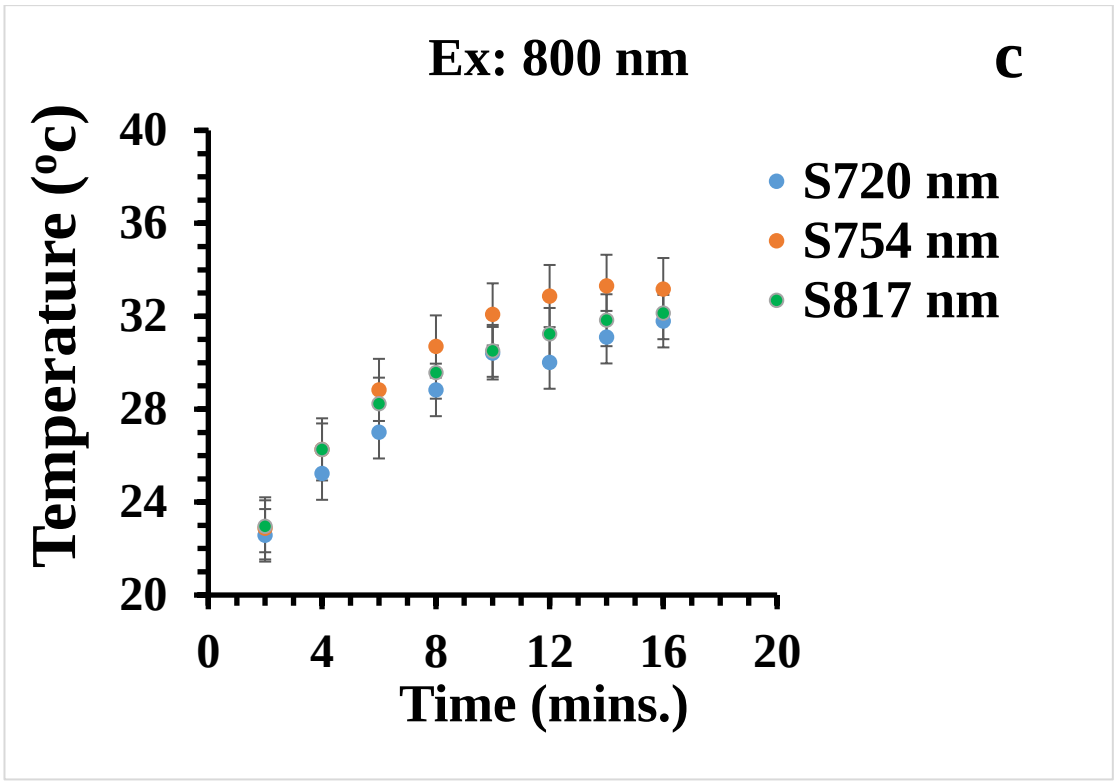
Ex: 800 nm
c
Temperature (°c)
40
36
32
28
24
20
0
4
8
12
16
20
Time (mins.)
S720 nm
S754 nm
S817 nm

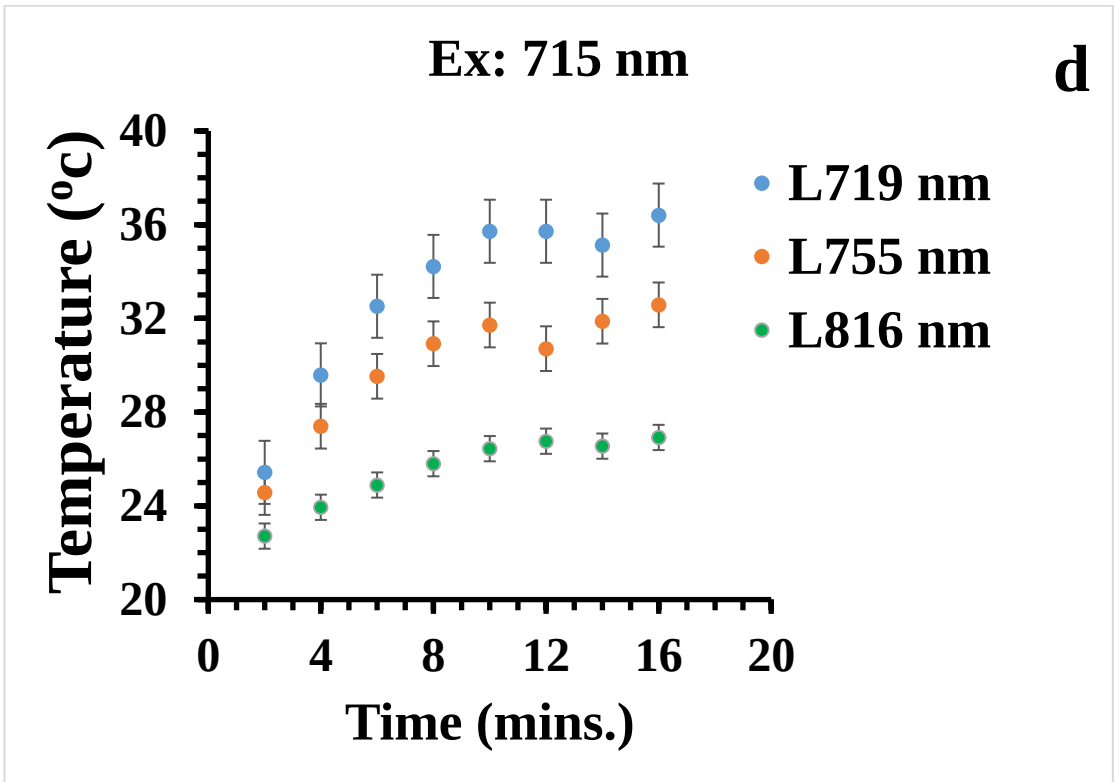
Ex: 715 nm
d
Temperature (°c)
40
36
32
28
24
20
0
4
8
12
16
20
Time (mins.)
L719 nm
L755 nm
L816 nm

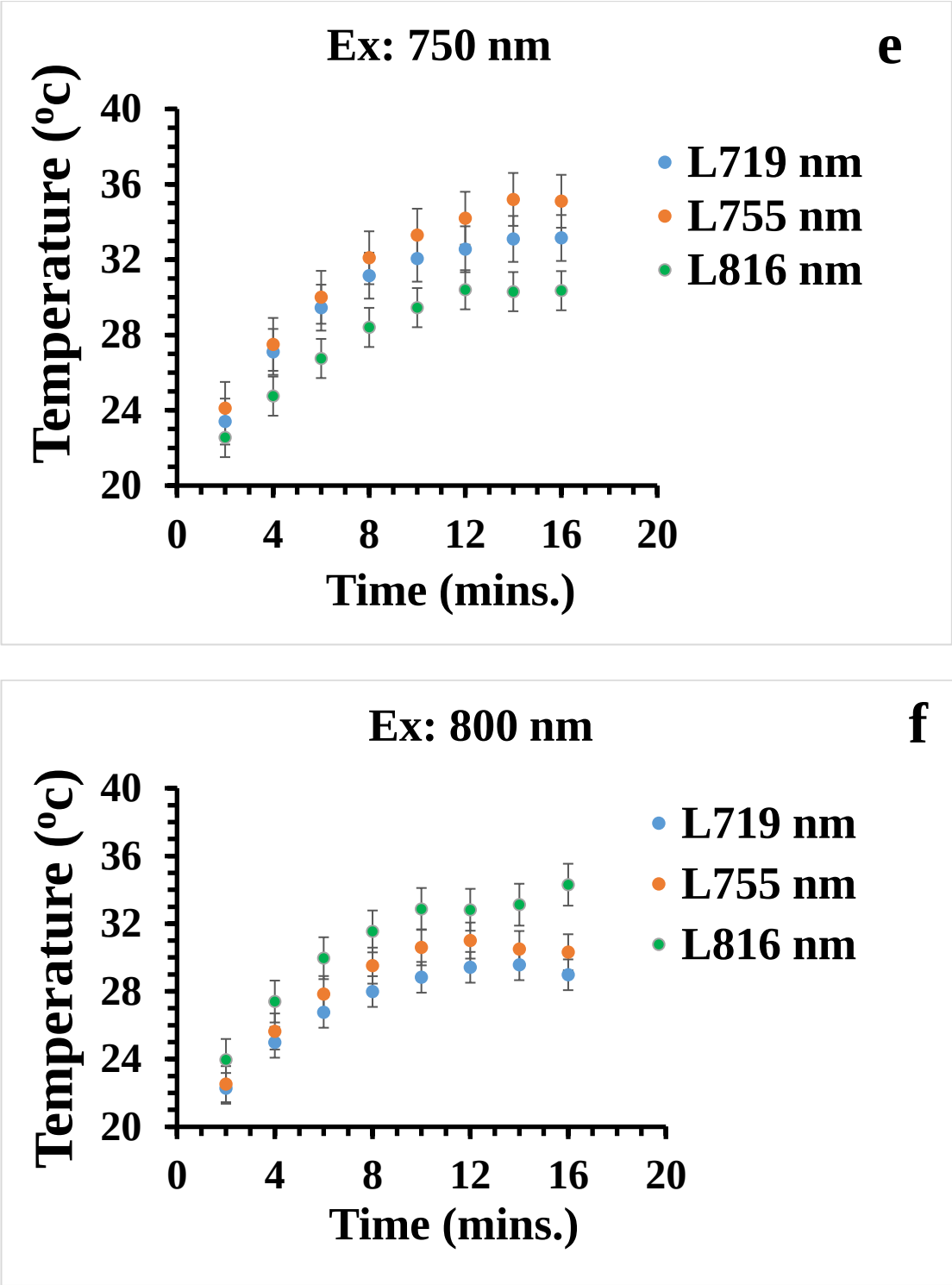

Figure 4.11. The time-dependent temperature changes of the SGNRs and the LGNRs after laser illumination in water; (a) SGNRs-Ex: 715 nm, (b) SGNRs-Ex: 750 nm, (c) SGNRs-Ex: 800 nm, (d) LGNRs-Ex: 715 nm, (e) LGNRs-Ex: 750 nm and (f) LGNRs-Ex: 800 nm. The temperature profiles are normalised against their laser intensities.

Figure 4.12. compares the temperature profiles of the SGNRs and the LGNRs excited on resonance. It can be seen that the temperatures of L719 and L816 are slightly higher than their SGNRs counterparts, while that of L755 is similar to S754. However, this is different from the theoretical calculation showing that the heat generated by the SGNRs is higher than that of the LGNRs (figure 4. 9.). It was reported that the field coupling between neighbouring GNRs generates strong electric field that enhances the heating of the GNRs solution[10, 16, 37-38]. Despite a relative strong absorption, SGNRs have shorter field length. On the other hand, the LGNRs have electric field extending further away from the surface of the GNRs. Thus, the field coupling of the LGNRs is stronger than the SGNRs at plasmon resonance excitation[16, 42]. This could explain the slightly higher temperature rise in the solution of the LGNRs than that in the solution of the SGNRs observed in fig. 4.12.

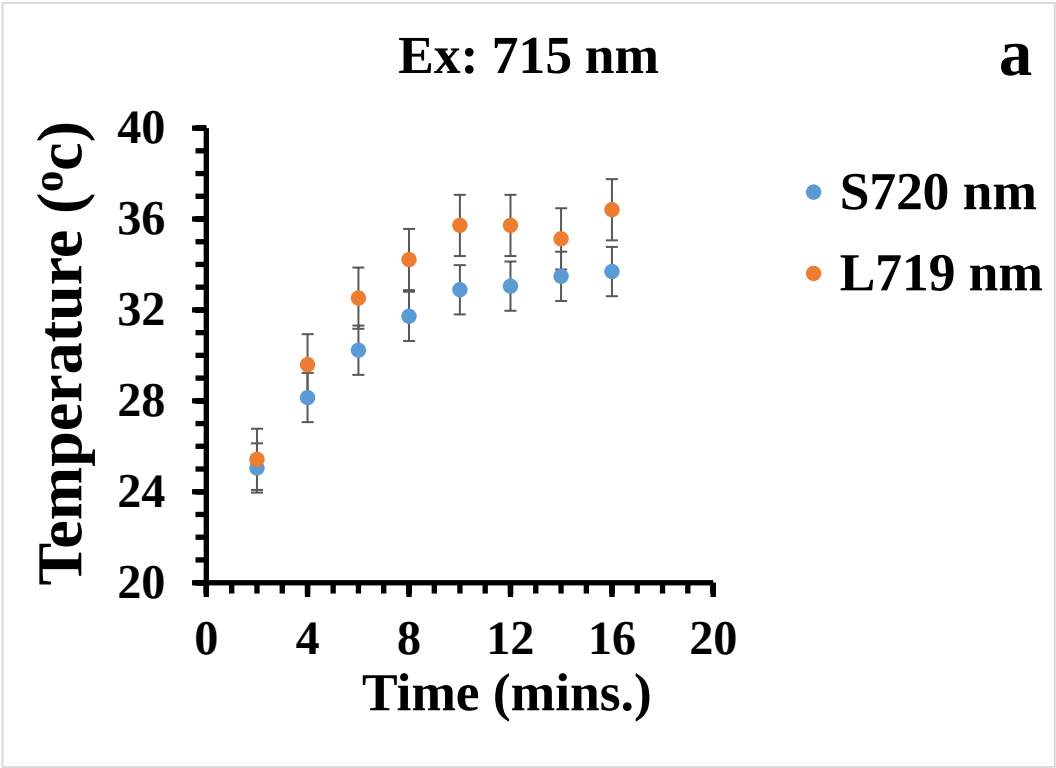

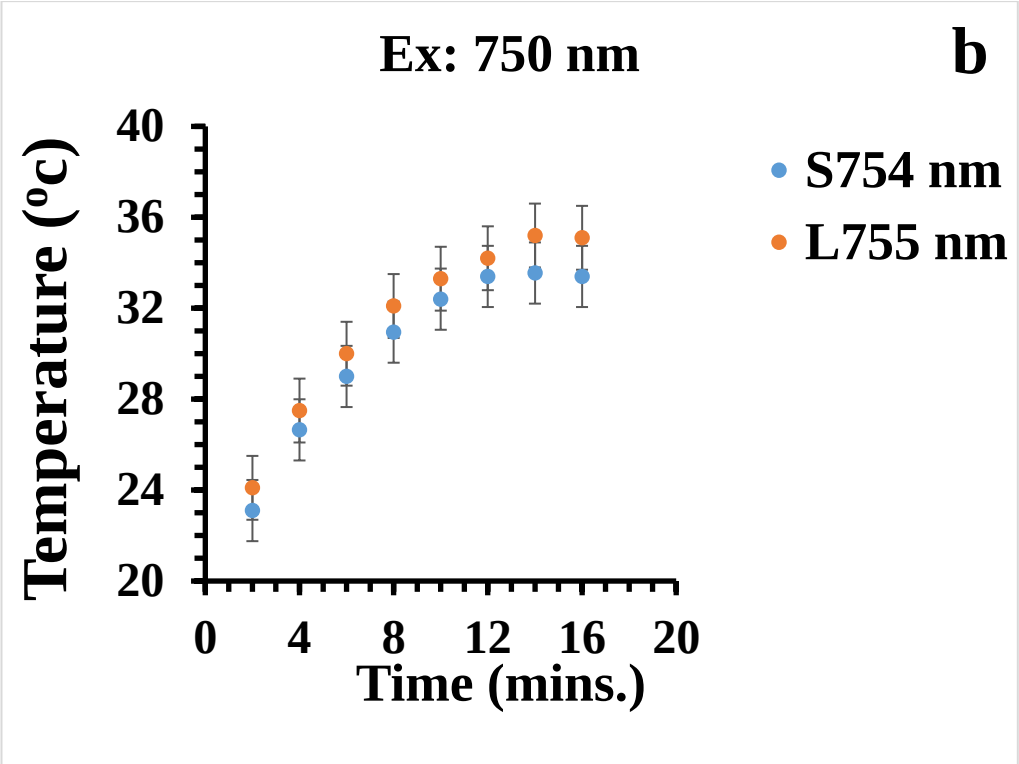

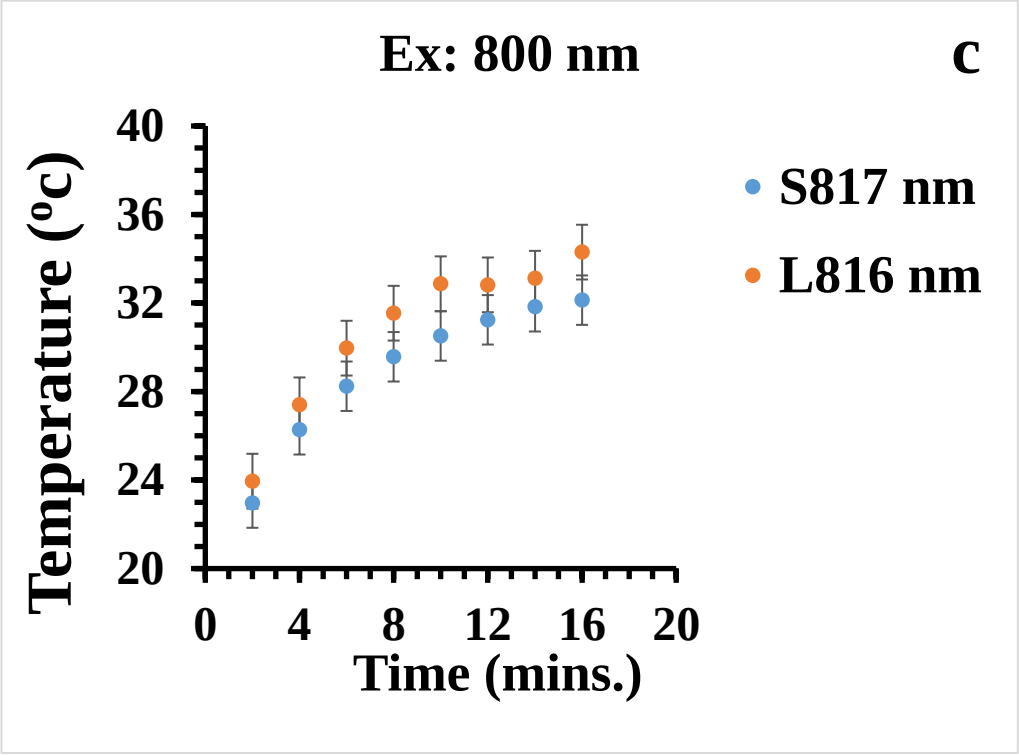

Figure 4.12. A comparison of the temperature profiles of the SGNRs and the LGNRs colloid at resonance excitations; (a) Ex: 715 nm, (b) Ex: 750 nm and (c) Ex: 800 nm.

Figure 4.13. displays a comparison of the temperature profiles of the SGNRs and the LGNRs at off-resonance excitations. In contrast to the on-resonance excitation, we observed that the temperature of the SGNRs increased slightly more or close to that of the LGNRs at the off-resonance excitation, in line with the calculation shown in fig. 4.9. This could be due to the weaker local electric field at off-resonance excitation leading to a reduced absorption, thus, the contribution of field coupling of the GNRs in the heating is negligible. Therefore, the SGNRs have higher temperature rise than the LGNRS at the off-resonance excitation.

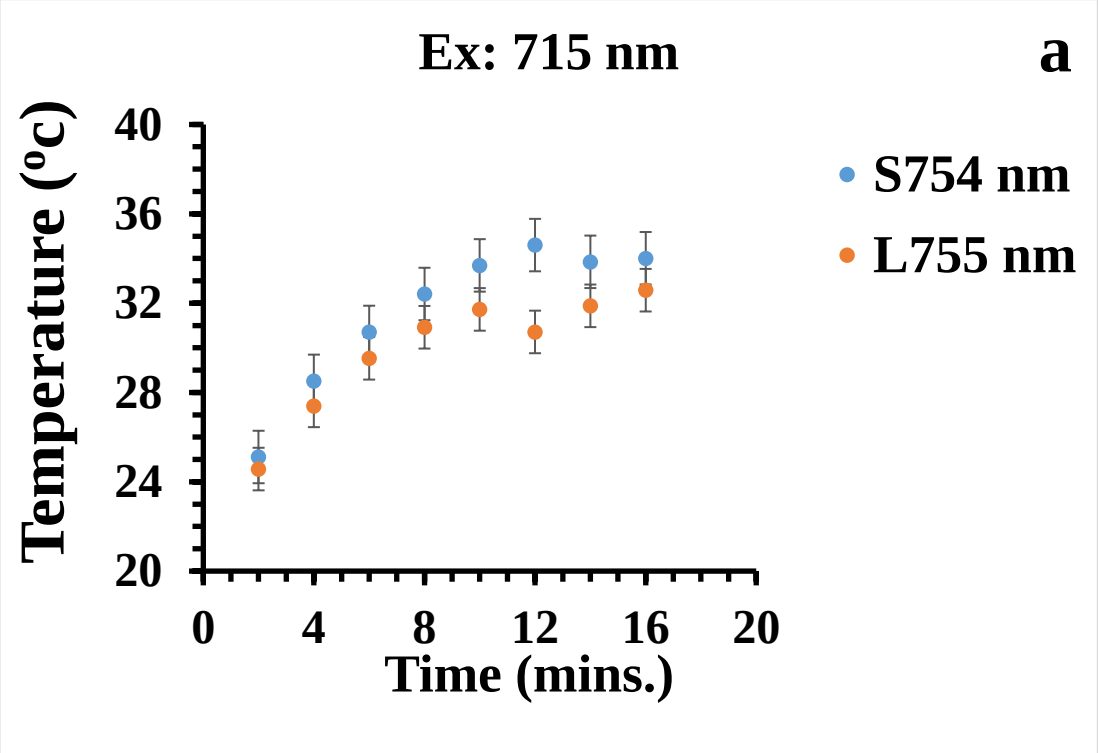

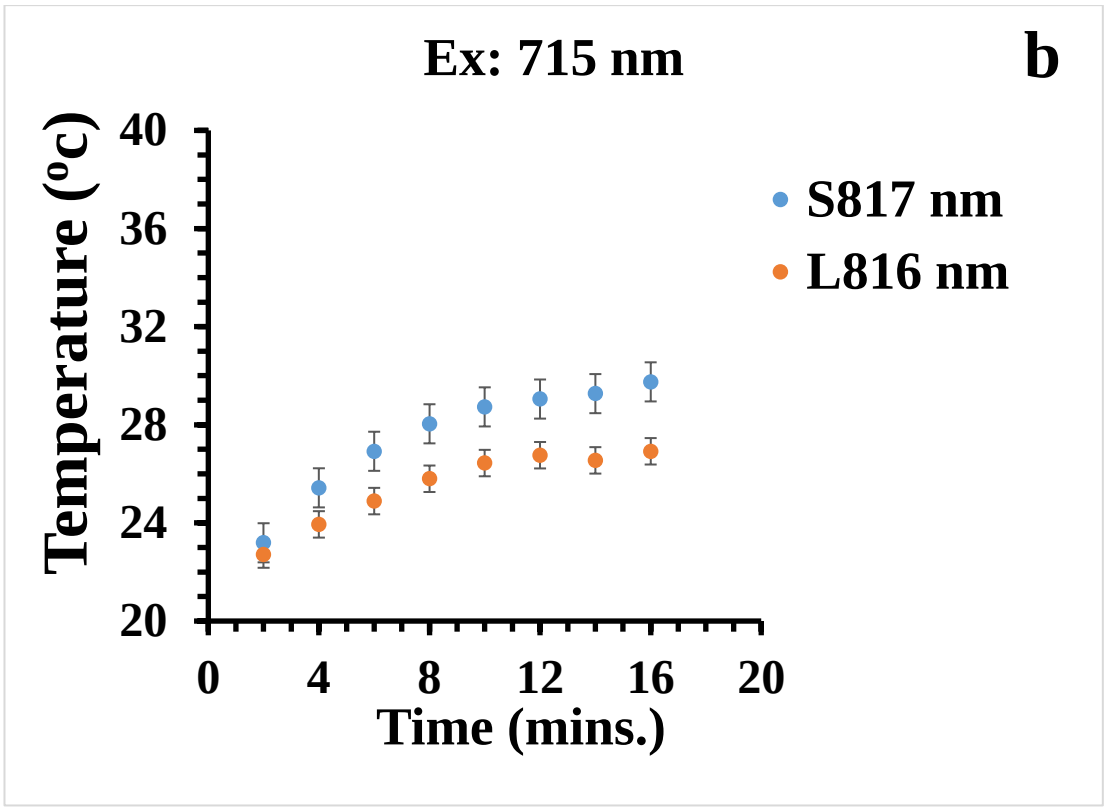
Ex: 715 nm
b
Temperature (°c)
40
36
32
28
24
20
0
4
8
12
16
20
Time (mins.)
S817 nm
L816 nm

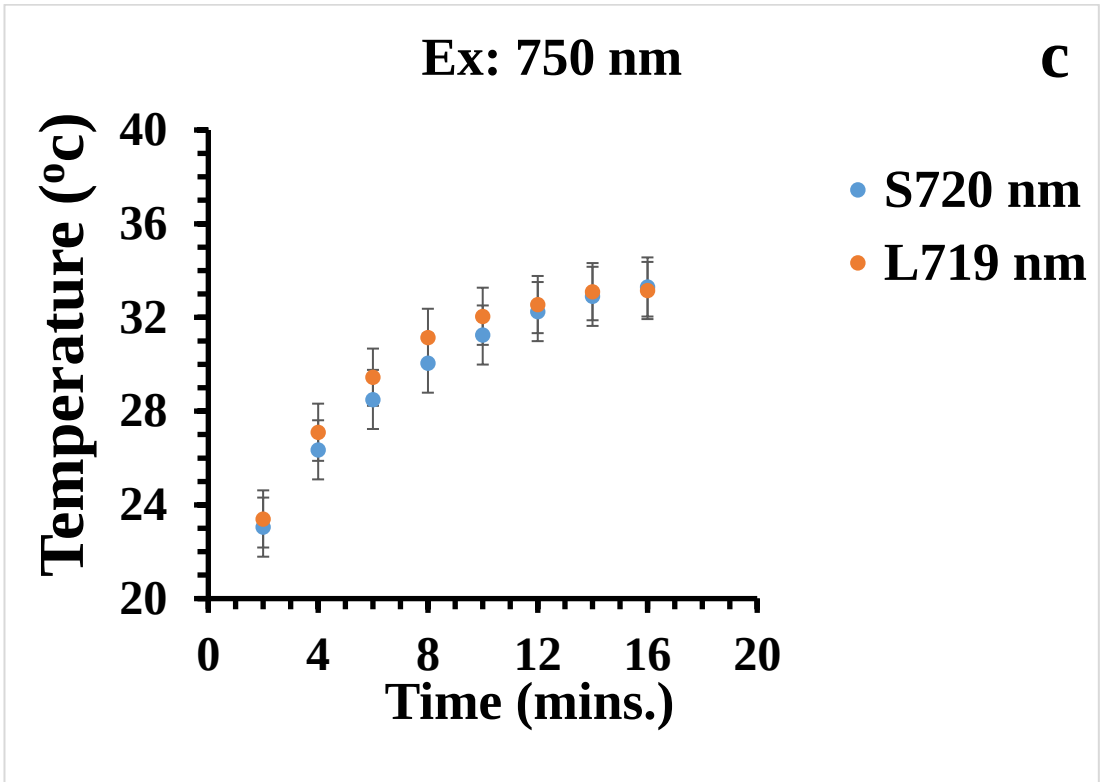
Ex: 750 nm
c
Temperature (°c)
40
36
32
28
24
20
0
4
8
12
16
20
Time (mins.)
S720 nm
L719 nm

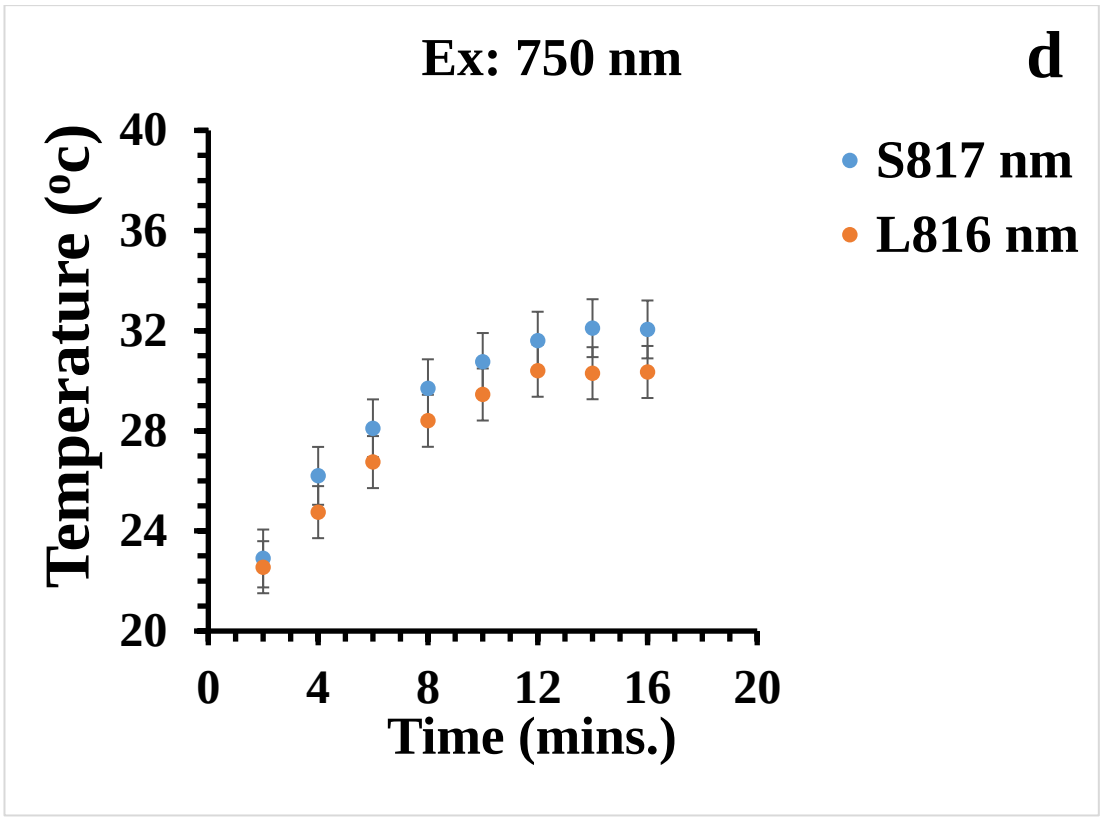
Ex: 750 nm
d
S817 nm
L816 nm
Temperature (°c)
40
36
32
28
24
20
0
4
8
12
16
20
Time (mins.)

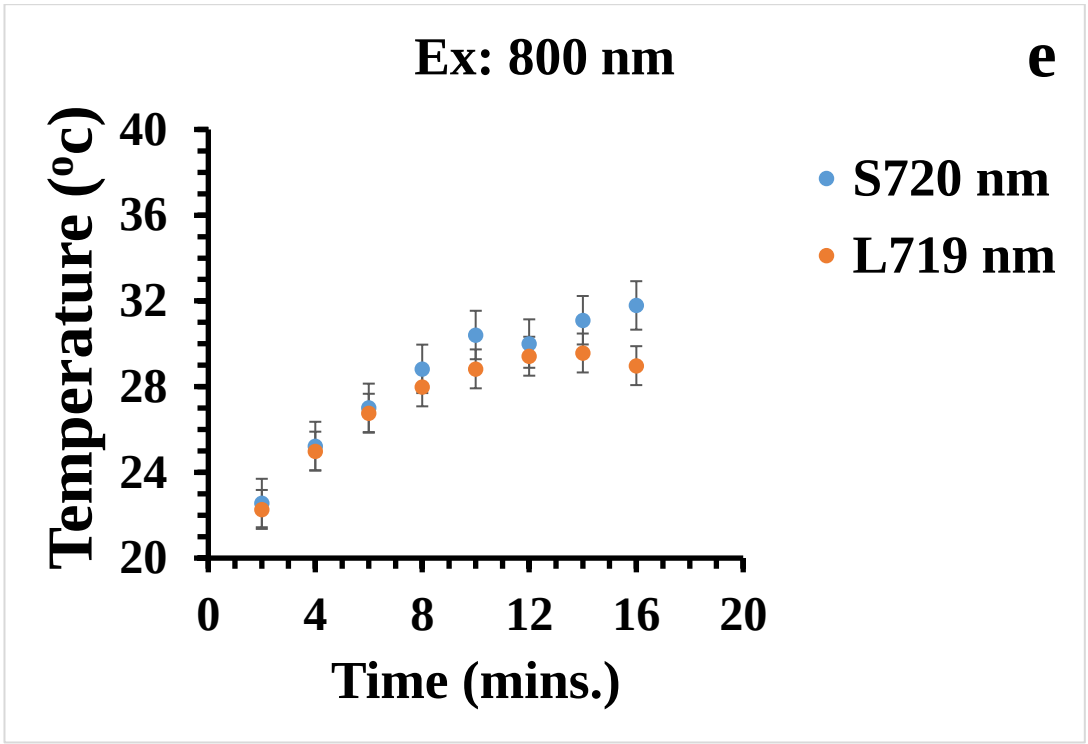
Ex: 800 nm
e
S720 nm
L719 nm
Temperature (°c)
40
36
32
28
24
20
0
4
8
12
16
20
Time (mins.)

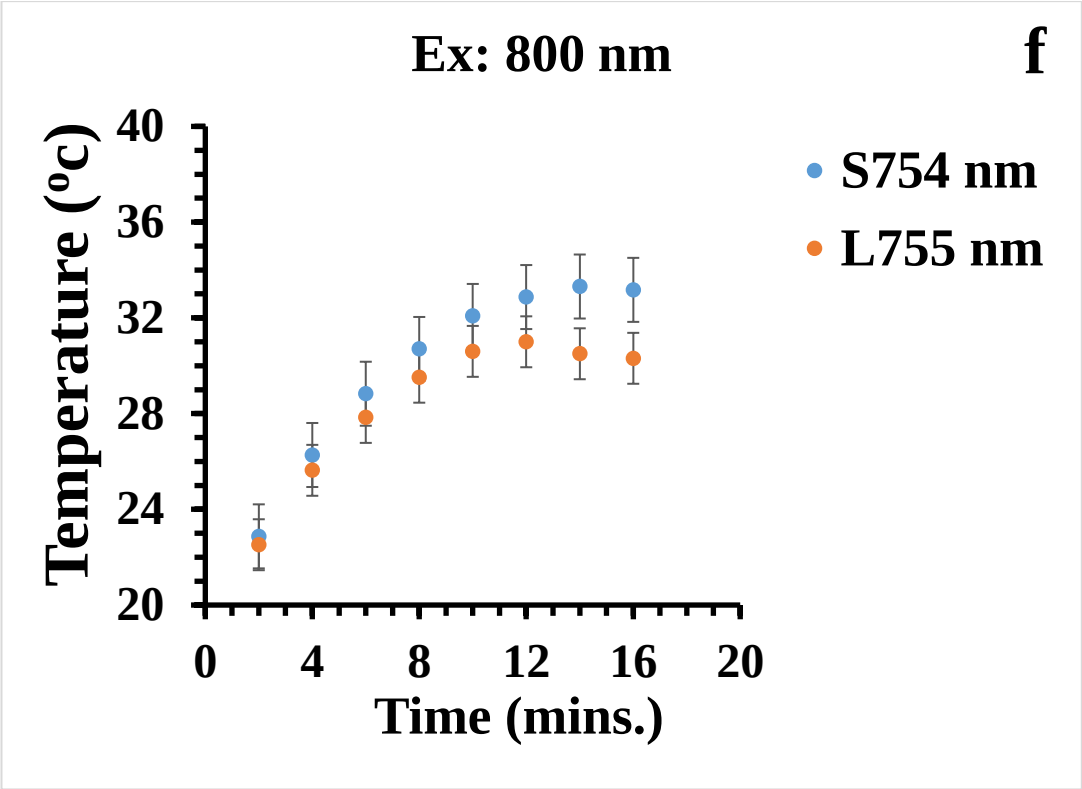

Figure 4.13. A comparison of the temperatures of the SGNRs and the LGNRs colloids at the off-resonance excitations**;** (a) S754/L755-Ex: 715 nm, (b) S817/L816-Ex: 715 nm, (c) S720/L719-Ex: 750 nm, (d) S817/L816-Ex: 750 nm, (e) S720/L719-Ex: 800 nm and (f) S754/L755-Ex: 800 nm.

4. 5. 6. Photothermal effect of SGNRs and LGNRs illuminated in agarose hydrogel

Agarose is a polysaccharide obtained from the red seaweed[47] and has been used in cell culturing applications to replicate the natural environment of mammalian cells[27-28, 32, 44-45]. Agarose hydrogel is non-cytotoxic and chemically unreactive to biomolecules. In this study, agarose hydrogel has been utilized to mimic the extracellular environment because agarose gel responds to incident light in a similar manner as the natural cell environment[25-26]. Agarose hydrogel is turbid and can scatter incident light intensely[46]. It can be dissolved either in TBE buffer or water at 70 ºC- 90 ºC and gels at 38 ºC-40 ºC. It is composed of polymer chains, which aggregate into helical agarose fibres upon gelation. The alignment of the fibres create a network of microscopic pores. The pore sizes are in

ten to hundreds of nanometers depending on the concentration and temperature of agarose hydrogel[47]. The porosity of agarose hydrogel has been employed in gel electrophoresis for separating biological molecules such as DNA fragments and melanin from genomic DNA[27, 48]. Agarose gel has a specific heat capacity of 4200J/kgK and density 1000kg/m^3 similar to that of water[49].

4. 5. 6. 1. Influence of solvents and concentration of agarose hydrogel on the longitudinal surface plasmon resonance of LGNR

The surface plasmon resonance of gold nanorods in agarose gel can be influence by the refractive index, the concentration and the temperature of the gel[29, 50-51]. The refractive index of agarose gel is directly proportional to its concentration[52-53]. Figure 4.14. shows the UV-vis extinction spectra of L784 measured at 21 ^oC-22 ^oC of different concentrations of the agarose gel dissolved in TBE buffer and water solvents. It can be seen that the LSPR of L784 blue shifts in both TBE buffer and water dissolved agarose gel relative to their solution counterparts. The blue shift increases as the concentration of agarose increases. This is because the refractive index of the agarose gel increases as the concentration of the agarose gel increases leading to an increase of scattered light, thus affecting the optical extinction of L784 sample[53-54]. Furthermore, the increase of the concentration of the agarose gel could cause a severe aggregation of the gold nanorods thereby inducing a further decrease of the A.R. leading to an increase of blue shift as predicted by Gans' model[35], and Link and El-Sayed[41]. The blue shift of L784 at varying concentrations of TBE buffer and water dissolved agarose gel is shown in table 2 of the appendix 2. Figure 4.15. displays the concentration dependent blue shift of the LSPR of L784 in TBE buffer and water agarose gel media. It can be seen that the LSPR of L784 remains stable until 1.5% of water-agarose gel media then, an increase of blue shift to 26 nm at 2.5%. In the case of buffer-agarose gel, there is an obvious change of the LSPR in 0.3% - 1.3% in comparison to that in solution. A rise of the blue shift is observed at 1.5%-2.0% and there is no further blue shift larger than at 2%. The large blue shift of the sample L784 in the TBE buffer-agarose gel compared to the water-agarose gel suggests a higher degree of the aggregation of gold nanorods in the TBE buffer-agarose gel media

compared to the water-agarose gel media. This study reveals the influence of the gel media on the optical characteristics of the GNRs. To avoid a large blue shift, an agarose concentration of 0.7% was chosen for photothermal study in this work.

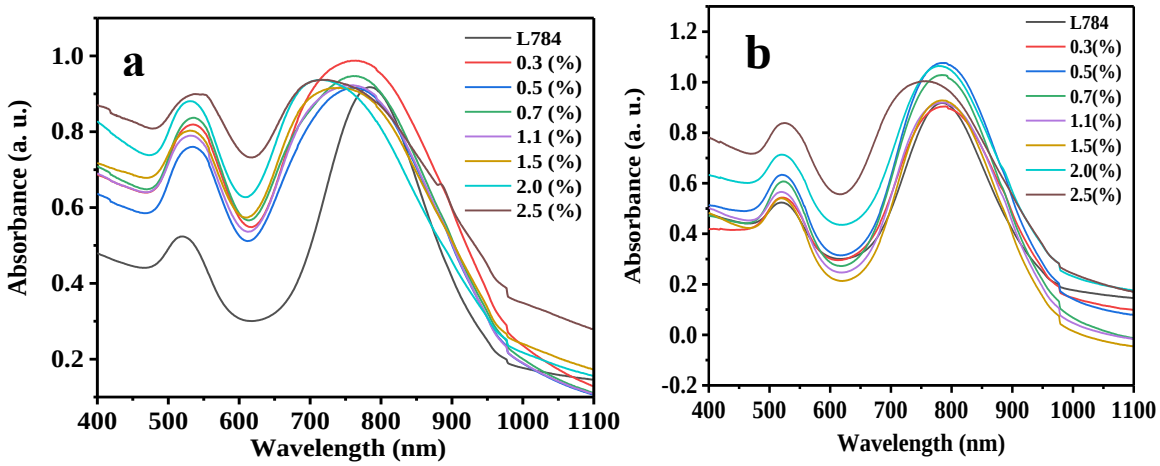

Figure 4.14. The extinction spectra of L784 at the different concentrations of agarose hydrogel; (a) UV-vis extinction spectra of sample L784 in the TBE buffer-agarose gel media. (b) UV-vis extinction spectra of sample L784 in the water-agarose gel media.

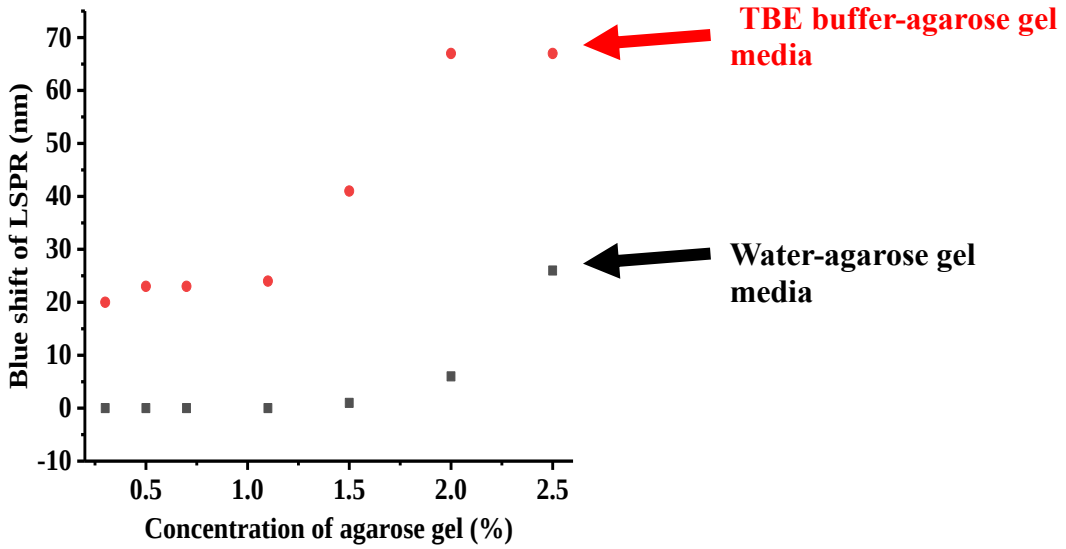

Figure 4.15. The effect of the concentration of agarose hydrogel dissolved in the TBE buffer and the water solvents on the longitudinal surface plasmon resonance of L784.

4. 5. 6. 2. Surface plasmon resonance and photothermal effect of SGNRs and LGNRs in agarose gel

By fitting to the calibration curve of the reported refractive indices and the concentrations of agarose gel[53], the refractive index of 0.7% agarose gel was found to be 1.334. Figure 4.16. shows the UV-vis extinction spectra of the SGNRs (AS720, AS754 and AS817) and the LGNRs (AL719, AL755 and AL816) in agarose gel of room temperature in comparison to those in water suspension. The optical densities (O.D.) of the AS720 and the AS754 were normalised against O.D. of 0.99 because their original O.D. were ~0.8. It can be seen that, the LSPR of both the SGNRs and the LGNRs are sensitive to the change of their surrounding medium. We observed a broadened extinction spectra and a blue shift of the longitudinal absorption band of both the SGNRs and the LGNRs dispersed in agarose gel. This could be ascribed to the aggregation of SGNRs and LGNRs, thus, affecting the surface plasmon resonance response of the SGNRs and the LGNRs[50-51, 55]. Furthermore, the aggregation could affect the A.R of the gold nanorods leading to a reduced longitudinal absorption of the gold nanorods as predicted by Gans' model[35], and Link and El-Sayed[41]. Table 4.6. shows that the blue shift is more pronounced for the LGNRs compared to the SGNRs. This is because the LGNRs are larger in size compared to the SGNRs, thus, the LGNRs form larger aggregators than the SGNRs[55].

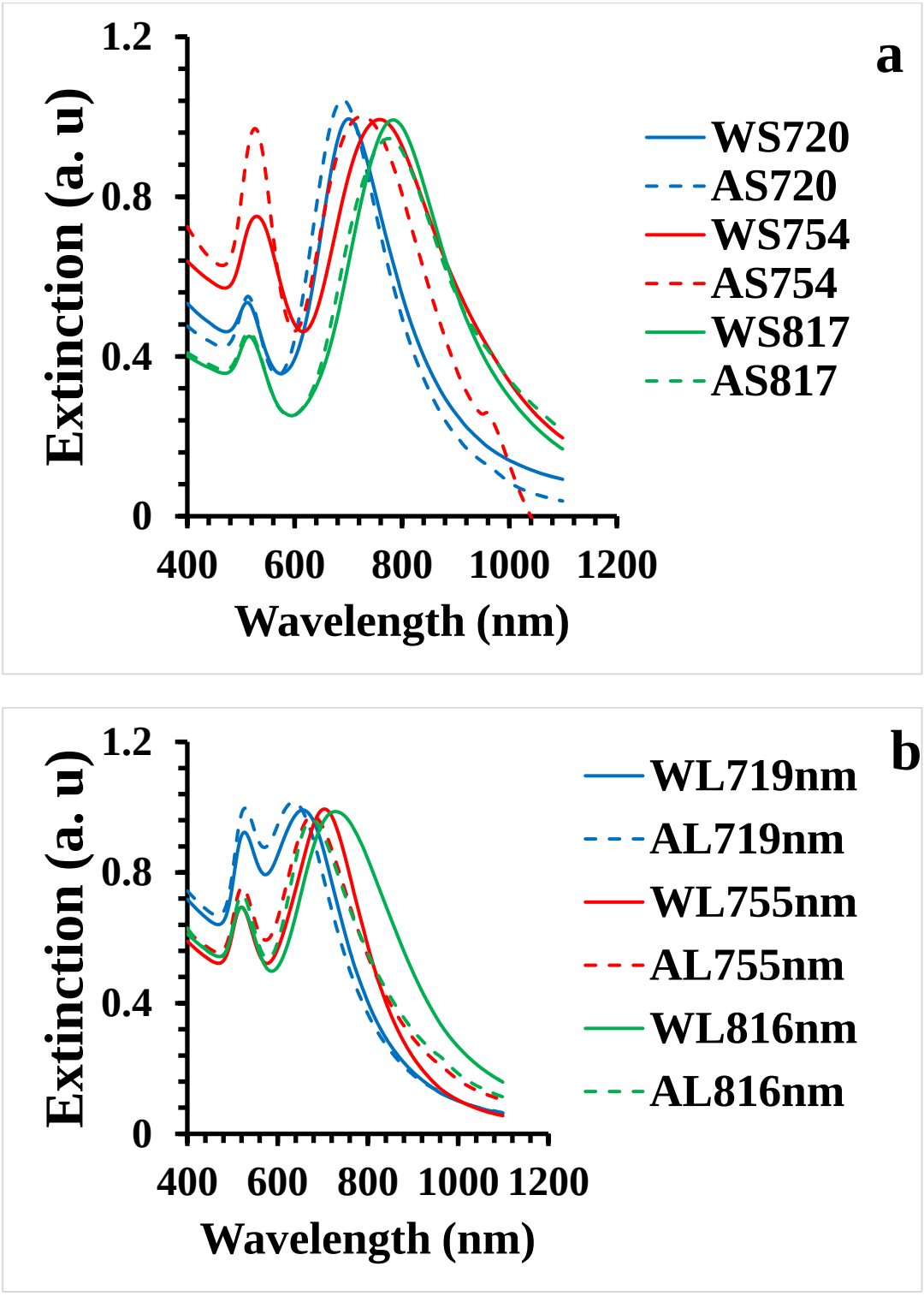

Figure 4.16. The UV-vis extinction spectra of gold nanorods in water and agarose gel media (0.7%); (a) SGNRs (b) LGNRs. Note W and A represent sample in water and agarose gel media respectively.

Table 4.6. The longitudinal absorptions of the SGNRs and the LGNRs in water and agarose hydrogel media.

Sample	LSPR (nm)		
	Water medium	Agarose gel medium	Blue shift in agarose hydrogel
S720	720	701	19
S754	754	749	05
S817	817	785	32
L719	719	657	62
L755	755	704	51
L816	816	730	86

Figure 4.17. depicts the temperature profiles of the gold nanorods in 0.7% TBE buffer agarose gel illuminated at 715 nm, 750 nm and 800 nm laser wavelengths. The temperature profiles of the SGNRs and the LGNRs in agarose gel were normalised against 2.74±0.16W/cm^2 laser intensity as explained above. The temperatures of the SGNRs in agarose gel (AS720, AS754 and AS817) are enhanced when their LSPR partially overlaps the excitation wavelengths at 715 nm, 750 and 800 nm (fig. 4.17a-c) due to strong absorption of light, in agreement with the theoretical prediction (figure 4.9.). However, no obvious surface plasmon (SP) enhancement in temperature rise was observed for the LGNRs colloids in agarose gel (AL719 and AL755; fig.4.17d. and 4.17e.) except AL816 (fig. 4.17f.) whose temperature is slightly higher than that of the AL755 and the AL719 at 800 nm illumination. This is not surprising as the absorption decreases when the illumination wavelength moves away from the surface plasmon resonance wavelength, resulting in a reduced heat generation. The temperature profiles of the SGNRs and the LGNRs in the TBE buffer agarose gel can be found in tables 3a and 3b respectively of appendix 2.

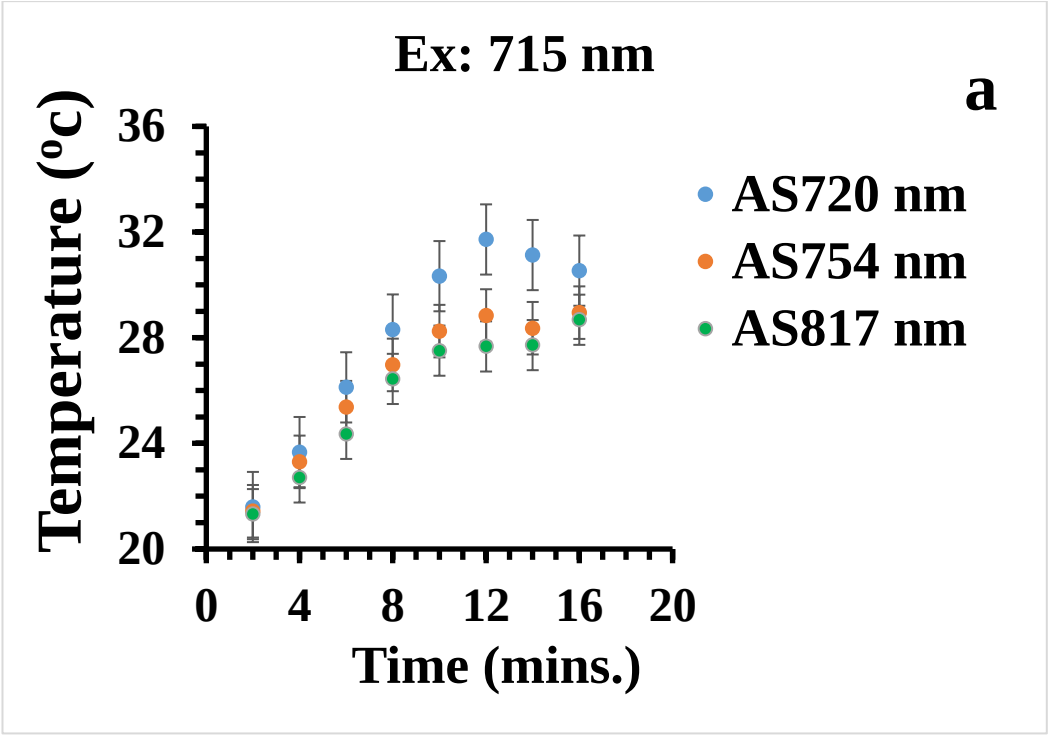
Ex: 715 nm
a
Temperature (°c)
36
32
28
24
20
0
4
8
12
16
20
Time (mins.)
AS720 nm
AS754 nm
AS817 nm

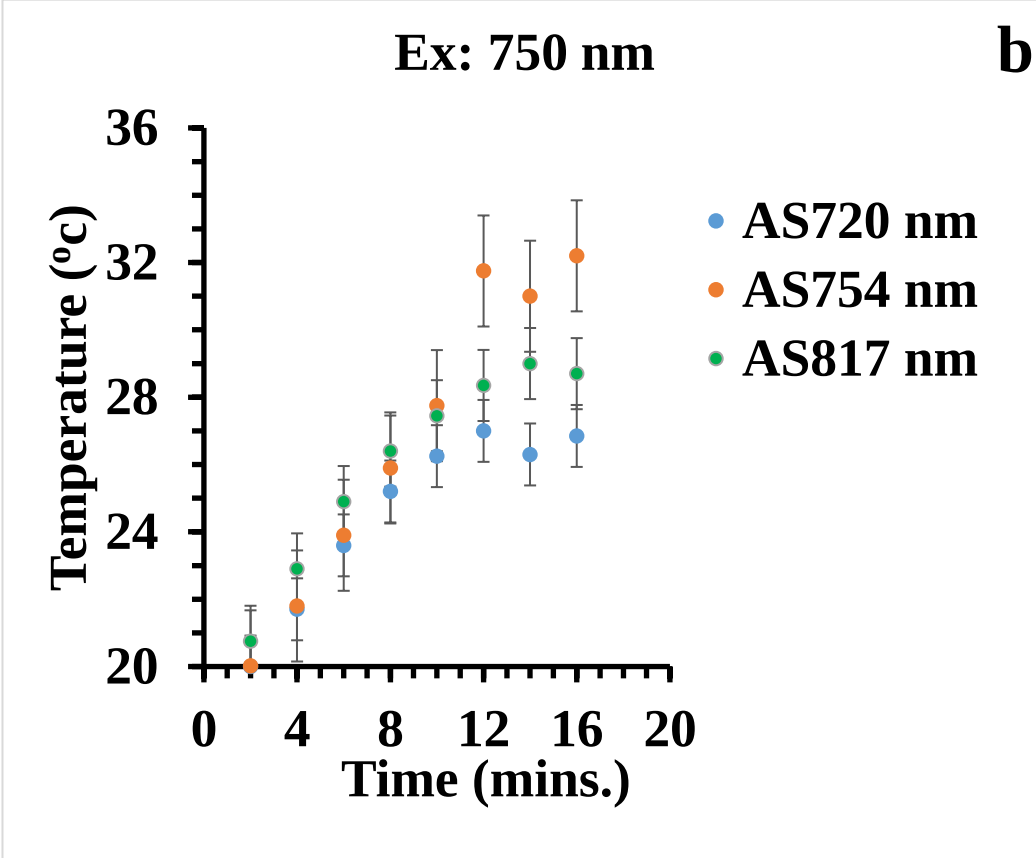
Ex: 750 nm
b
Temperature (°c)
36
32
28
24
20
0
4
8
12
16
20
Time (mins.)
AS720 nm
AS754 nm
AS817 nm

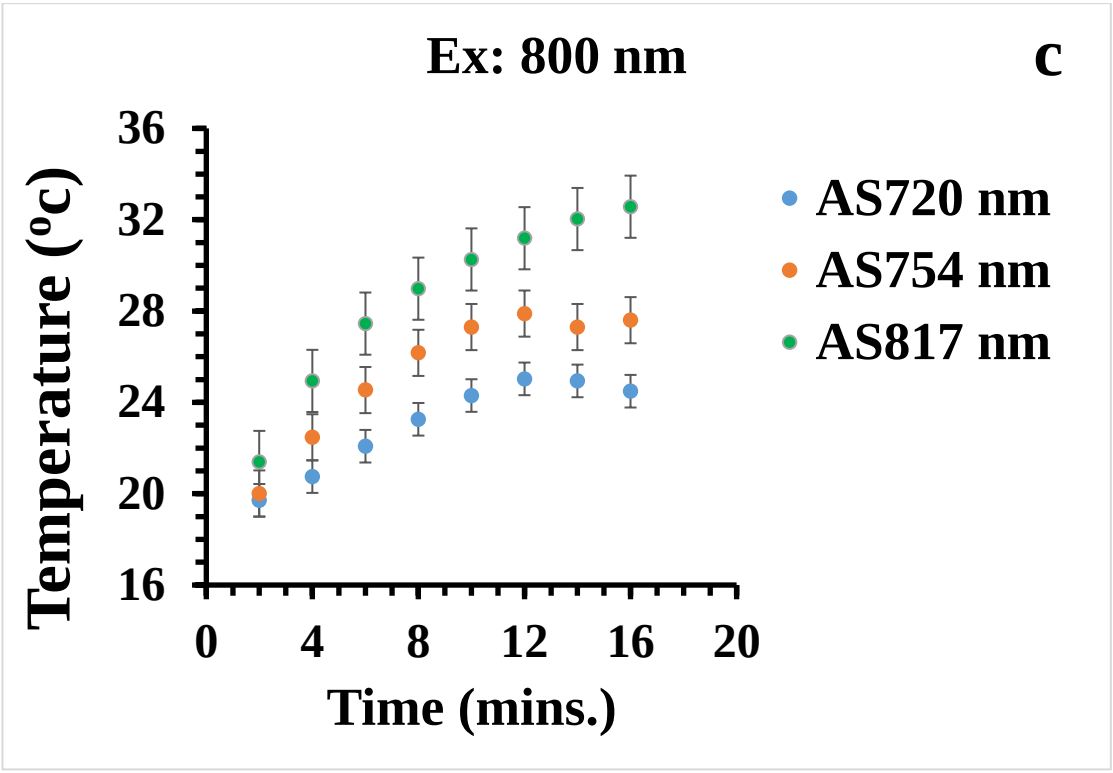
Ex: 800 nm
c
Temperature (°c)
36
32
28
24
20
16
0
4
8
12
16
20
Time (mins.)
AS720 nm
AS754 nm
AS817 nm

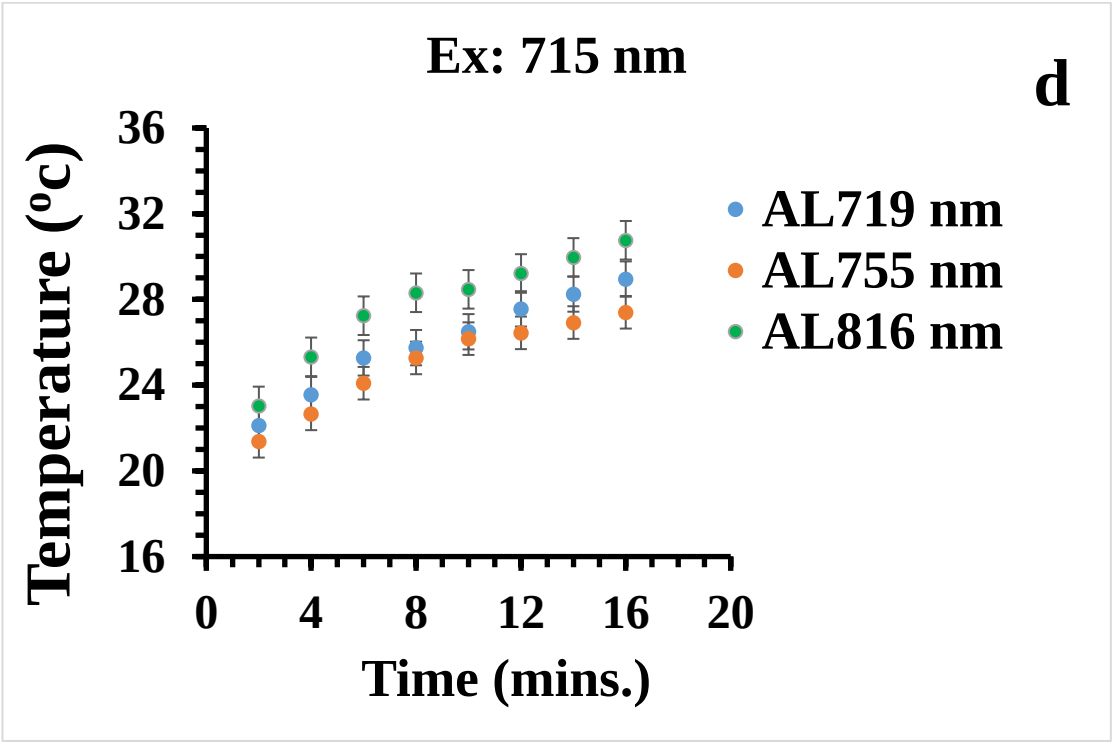
Ex: 715 nm
d
Temperature (°c)
36
32
28
24
20
16
0
4
8
12
16
20
Time (mins.)
AL719 nm
AL755 nm
AL816 nm

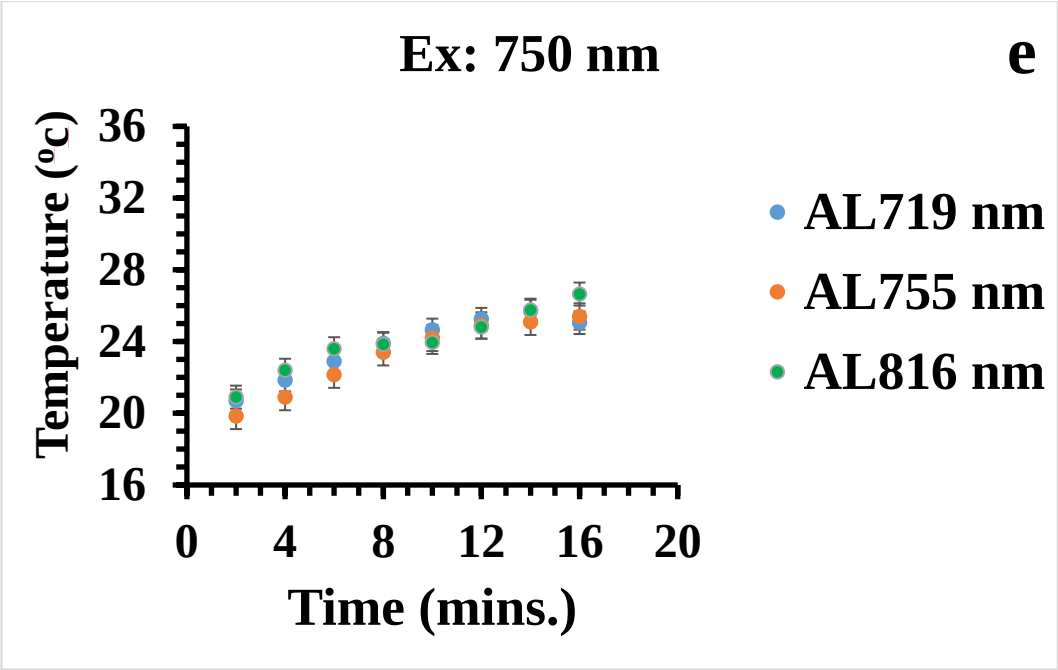

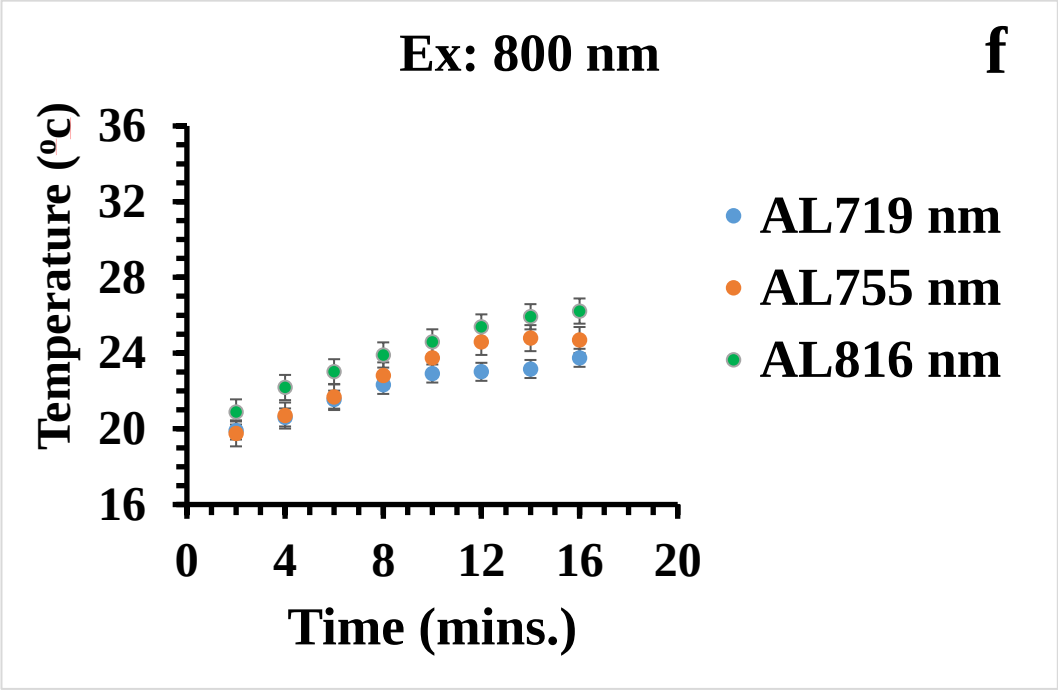

Figure 4.17. The time-dependent temperature changes of the SGNRs and the LGNRs in TBE buffer agarose gel after laser illumination; (a) SGNRs-Ex: 715 nm, (b) SGNRs-Ex: 750 nm, (c) SGNRs-Ex: 800 nm, (d) LGNRs-Ex: 715 nm, (e) LGNRs-Ex: 750 nm and (f) LGNRs-Ex: 800 nm. Note AS and AL represent small and large gold nanorods in agarose gel media respectively.

Figure 4.18. compares the temperature changes of the AS720 and the AL755 with similar LSPR (701 nm and 704 nm respectively) at 715 nm, 750 nm and 800 nm laser illumination. It can be seen that the temperature of the AS720 sample is more enhanced than that of the AL755 sample at 715 nm and 750 nm laser illuminations. In comparison to the AL755, AS720 shows a faster temperature rise from 2 minutes until reaching saturation temperature after 12 minutes. This could be due to a higher absorption to extinction ratio of the SGNRs compared to the LGNRs, thus a larger heat generation, consistent with the simulation (fig.4.9). It is found that the saturation temperature of the AS720 decreases from 31 ^{o}C (Ex:715 nm) to 27 ^{o}C (Ex: 750 nm) and finally 24 ^{o}C (Ex: 800 nm) as the wavelength of the laser moves away from its LSPR. Moreover, the temperature difference between the two samples also decreases as the illumination wavelength increases and both temperature profiles overlap at 800 nm illumination. This is believed to be due to a higher extinction of AL755 than that of the AS720 at 800nm because the band width of AL755 is larger than that of the AS720 although the latter has a high absorption to extinction ratio.

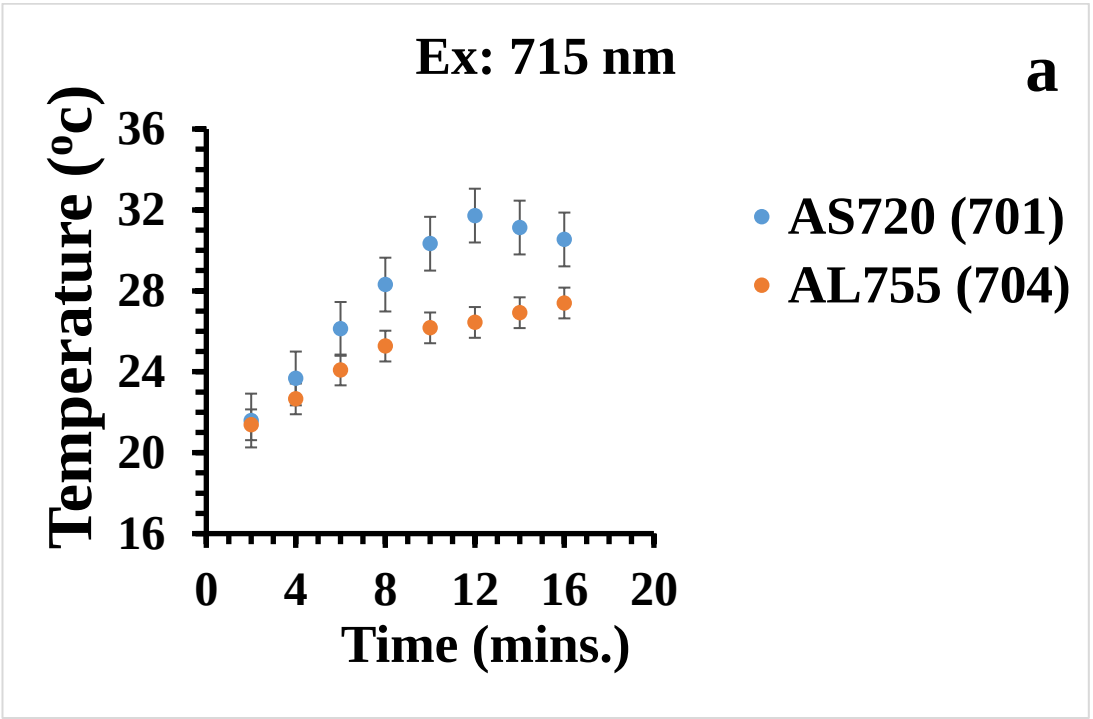

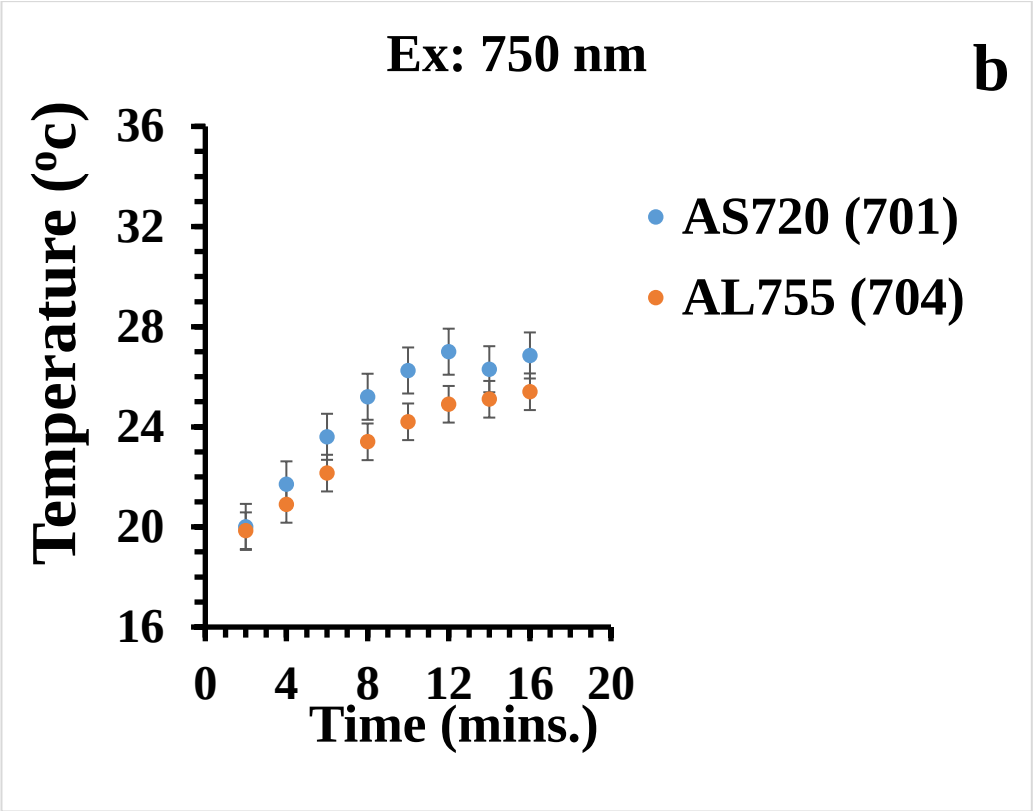

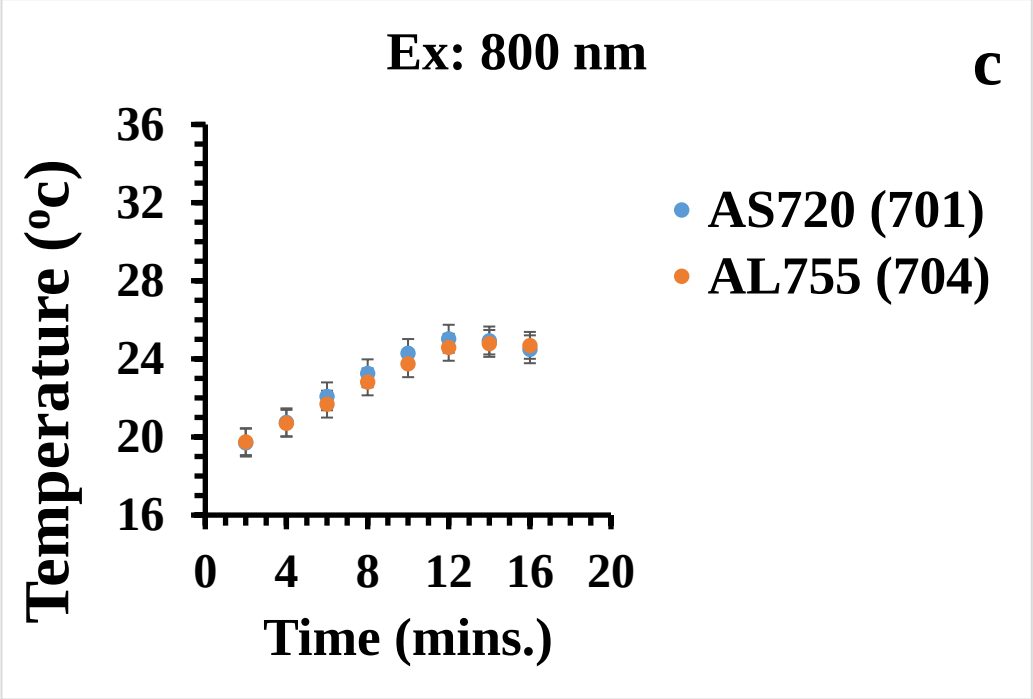

Figure 4.18. A comparison of the temperature profiles of the ASGNRs and the ALGNRs with similar LSPR at; (a) 715 nm, (b) 750 nm and (c) 800 nm illuminations.

Figure 4.19. compares the temperature profile of the SGNRs colloids in water and agarose gel. It can be seen that the temperature profiles of the S817 in the water and TBE buffer-agarose gel overlaps at 800 nm excitation wavelength. This is due to similar extinction of both samples, WS817 and AS817 at the 800 nm incident wavelength (figure 4.14a).

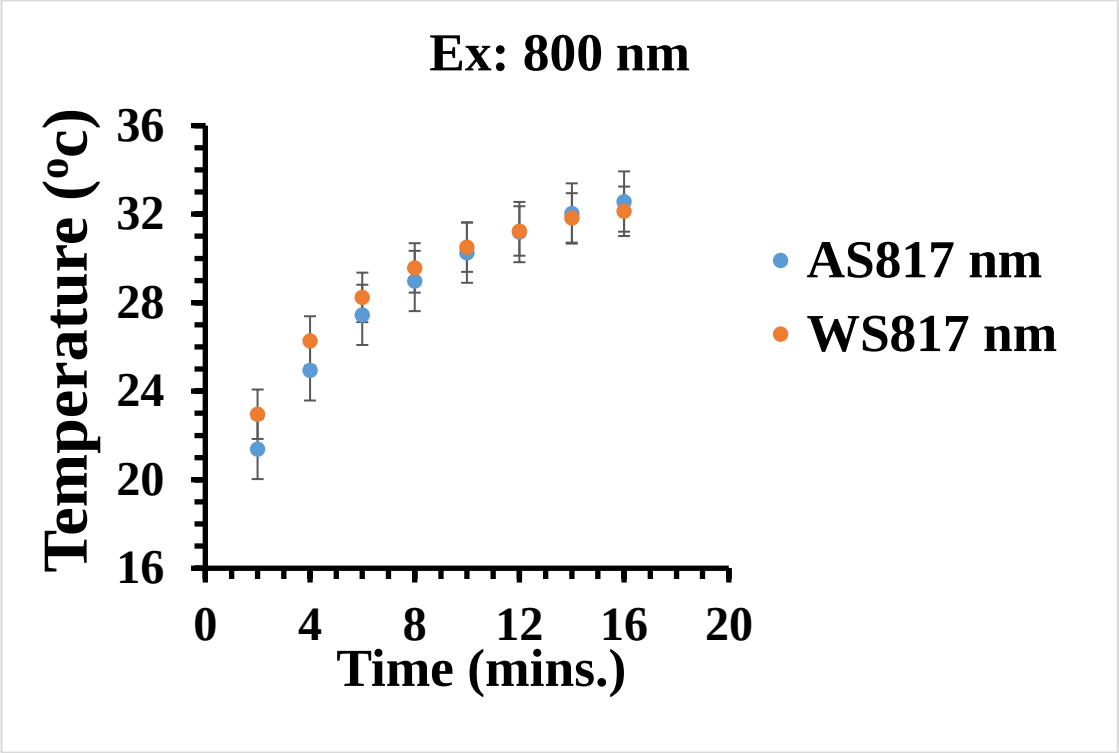

Figure 4.19. A comparison of the temperature of S817 colloid in the water (WS817) with it in the TBE buffer-agarose gel (AS817) at 800 nm illumination.

Figure 4.20. compares the temperature profile of the WL719 in water with that of the AL816 in TBE buffer-agarose gel at 715 nm, 750 nm and 800 nm excitation wavelengths. AL816 has a SP centred at 730 nm that is comparable to the SP of WL719 at 719 nm. It can be seen that sample WL719 shows a faster temperature rise from 2 minutes until saturation temperature is reached after 12 minutes. Apparently, the temperature of WL719 in solution is higher than that of the AL816 in the TBE buffer- agarose gel at 715 nm, 750 nm and 800 nm laser illuminations. As observed before, the LGNRs in solution have large electric field coupling under light excitation that could be reduced in the gel because the LGRNs are less mobile in the gel matrix. Furthermore, the extinction

coefficient of the AL816 in the gel could be lesser than that in solution due to a decrease of its A.R. as predicted by Gans' model[35], and Link and El-Sayed[41]; thus limiting the extinction efficiency of the AL816 compared to the WL719. In addition, the heat transfer efficiency of the gel is reduced compared to that in solution. It has been reported previously that gels reduce the efficiency of heat transfer because of the limited contact of granules in the gels[56-57]. Moreover, the thermal conductivity of the agarose gel (0.55W/m ºC at 20 -80 ºC) is slightly less than that of the water (0.6 W/m ºC at 20 ºC)[58-59], implying a reduced heat transfer of the agarose gel in comparison to the water solution.

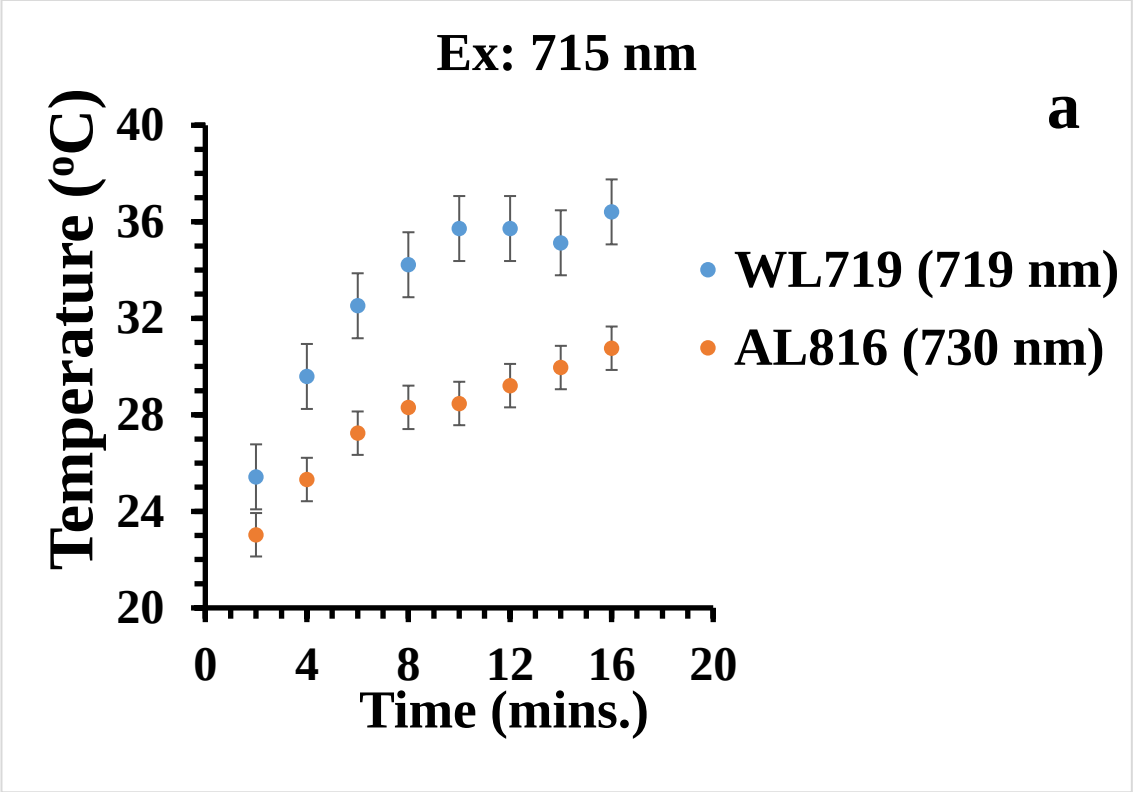

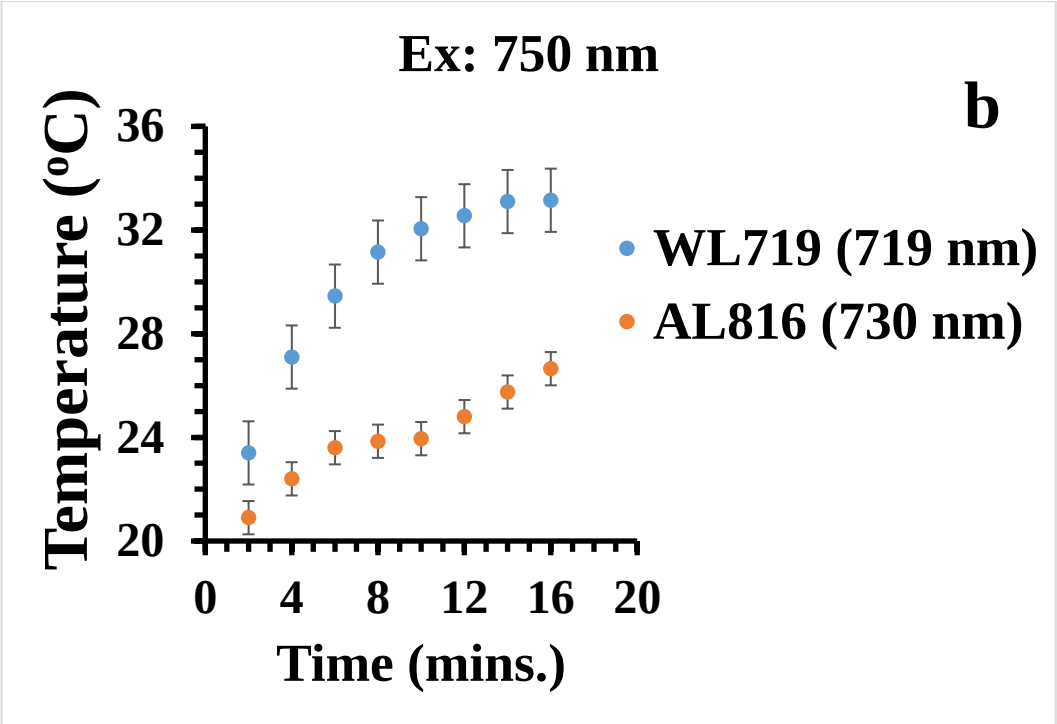

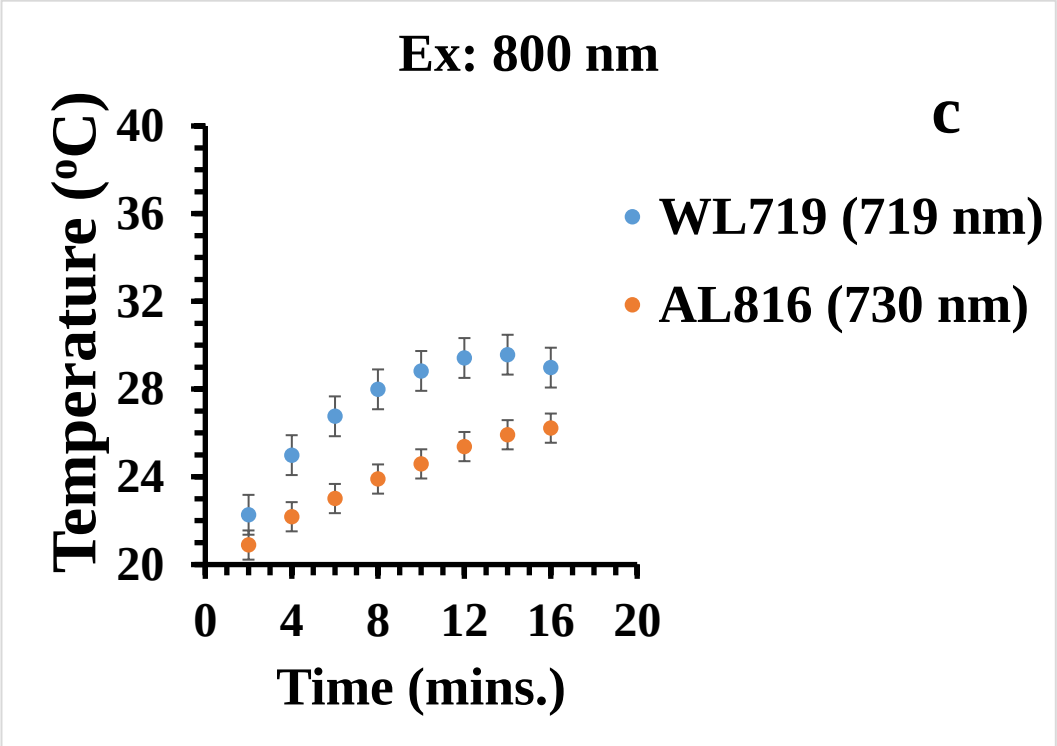

Figure 4.20. A comparison of the temperature of the WL719 colloids in the water with the AL816 in the TBE buffer-agarose gel at varying excitation wavelengths; (a) Ex: 715 nm, WL719/AL816, (b) Ex: 750 nm WL719/AL816 and (c) Ex: 800 nm, WL719/AL816.

4. 6. Conclusion

The optical properties and photothermal effects of the gold nanorods have been investigated. It is found that the calculated peak positions of the extinction cross-sections spectra of the SGNRs and the LGNRs predicted by Gans' model matched well with the peak positions of the SGNRs and the LGNRs derived experimentally. The ratio of the absorption-to extinction of the single SGNR is higher than that of the single LGNR, thus enhancing the photothermal conversion efficiency of SGNRs. Theoretical calculation shows that the SGNRs generate more heat than the LGNRs at both the plasmon resonance and off plasmon resonance excitations in the water. However, findings from the experiment revealed that the SGNRs generated slightly more heat than the LGRNs at the off-resonance illumination, while the LGNRs generated more heat than the SGNRs at the plasmon resonance excitation because of the stronger coupling of the local field of neighbouring LGNRs in the solution. The LSPR of both the SGNRs and the LGNRs showed a blue shift in the agarose gel. The degree of the blue shift is dependent on the size of GNRs and the concentration of agarose gel. It is found that the photothermal effect of the SGNRs is more enhanced than that of the LGNRs with similar LSPR in the gel when the LSPR overlaps with the illumination wavelength. This enhancement decreases as the excitation wavelength shifts away from the resonance wavelength. The photothermal effect of the SGNRs in solution is similar to that in the gel; however, the photothermal effect of LGNRs in solution is more enhanced than that in the gel. These findings help in shining light on tailoring the gold nanorod-based nanoprobes for optimal photothemal efficiency to enhance their performance in cancer therapy and other photothermal applications.

Reference

1. Huang, X.; El-Sayed , M. A., Gold nanoparticles: optical properties and implementations in cancer diagnosis and photothermal therapy. *Journal of Advanced Research* **2010,** *1*, 13–28.

2. Jia, H.; Fang, C.; Zhu, X.-M.; Ruan, Q.; Wang, Y.-X. J.; Wang, J., Synthesis of absorption-dominant small gold nanorods and their plasmonic properties. *Langmuir* **2015,** *31* (26), 7418-7426.

3. Hong, Y.; Huh, Y.; Yoon, D. S.; Yang, J., Nanobiosensors based on localized surface plasmon resonance for biomarker detection. *Journal of Nanomaterials* **2012,** *2012* (111), 1-13.

4. Manivasagan, P.; Hoang, G.; Moorthy, M. S.; Mondal, S.; Doan, V. H. M.; Kim, H.; Phan, T. T. V.; P, N. T.; Oh, J., Chitosan/fucoidan multilayer coating of gold nanorods as highly efficient near infrared photothermal agents for cancer therapy. *Carbohydrate Polymers* **2019,** *211*, 360-369.

5. Turcheniuk, K.; Dumych, T.; Bilyy, R.; Turcheniuk, V.; Bouckaert, J.; Vovk, V.; Chopyak, V.; Zaitsev, V.; Mariot, P.; Prevarskaya, N.; Boukherroub, R.; Szunerits, S., Plasmonic photothermal cancer therapy with gold nanorods/reduced graphene oxide core/shell nanocomposite. *RSC Adv.* **2016,** *6*, 1600-1610.

6. Lankveld, D.; Rayavarapu, R.; Krystek, P.; Oomen, A.; Verharen, H.; van Leeuwen, T.; Jong, W. H.; Manohar, S., Blood clearance and tissue distribution of PEGylated and non-PEGylated gold nanorods after intravenous administration in rats. *Nanomedicine (London, England)* **2011,** *6*, 339-349.

7. Huang, X.; El-Sayed, M. A., Plasmonic photo-thermal therapy (PPTT). *Alexandria Journal of Medicine* **2011,** *47* (1), 1-9.

8. Al-Bakri, A. G.; Mahmoud, N. N., Photothermal-induced antibacterial activity of gold nanorods loaded into polymeric hydrogel against pseudomonas aeruginosa biofilm. *Molecules* **2019,** *24* (14), 2661-2680.

9. Park, K.; Biswas, S.; Kanel, S.; Nepal, D.; Vaia, R. A., Engineering the optical properties of gold nanorods: independent tuning of surface plasmon energy, extinction coefficient and scattering cross-section. *J. Phys. Chem. C* **2014,** *118*, 5918-5926.

10. Chen, H.; Shao, L.; Li, Q.; Wang, J., Gold nanorods and their plasmonic properties. *Chemical Society Reviews* **2013,** *42* (7), 2679-2724.

11. Jain, P. K.; Lee, K. S.; El-Sayed, I. H.; El-Sayed, M. A., Calculated absorption and sacttering properties of gold nanoparticles of different size, shape and composition: application in biomedical imaging and biomedicine. *J.Phys. Chem. B.* **2006,** *110*, 7238-7248.

12. Baffou, G.; Quidant, R.; Girard, C., Heat generation in plasmonic nanostructures: Influence of morphology. *Appl. Phys. Lett.* **2009,** *94,* 153109-153111.

13. Mbalaha, Z. S.; Edwards, P. R.; Birch, D. J. S.; Chen, Y., Synthesis of small gold nanorods and their subsequent functionalization with hairpin single stranded DNA. *ACS Omega* **2019,** *4* (9), 13740-13746.

14. Ali, M. R. K.; Snyder, B.; El-Sayed, M. A., Synthesis and optical properties of small Au nanorods using a seedless growth technique. *Langmuir* **2012,** *28,* 9807-9815.

15. Ungureanu, C.; Koning, G. A.; van Leeuwen, T. G.; Manohar, S., The 'nanobig rod' class of gold nanorods: optimized dimensions for improved in vivo therapeutic and imaging efficacy. *Nanotechnology* **2013,** *24* (21), 1-9.

16. Mackey, M. A.; Ali, M. R. K.; Austin, L. A.; Near, R. D.; El-Sayed, M. A., The most effective gold nanorod size for plasmonic photothermal therapy: theory and in vitro experiments. *J. Phys. Chem. B,* **2014,** *118* (5), 1319–1326.

17. Nguyen, S. C.; Zhang, Q.; Manthiram, K.; Ye, X.; Lomont, J. P.; Harris, C. B.; Weller, H.; Alivisatos, A. P., Study of heat transfer dynamics from gold nanorods to the environment via time-resolved infrared spectroscopy. *ACS Nano* **2016,** *10,* 2144-2151.

18. Ekici, O.; Harrison, R. K.; Durr, N. J.; Eversole, D. S.; Lee, M.; Ben-Yakar, A., Thermal analysis of gold nanorods heated with femtosecond laser pulses. *Journal of Physics D: Applied Physics* **2008,** *41* (18), 185501-185511.

19. Link, S.; El-Sayed, M. A., Shape and size dependence of radiative, non-radiative and photothermal properties of gold nanocrystals. *International Reviews in Physical Chemistry* **2000,** *19* (3), 409-453.

20. Qin, Z.; Wang, Y.; Randrianalisoa, J.; Raeesi, V.; Chan, W. C. W.; Lipinski, W.; Bischof, J. C., Quantitative comparison of photothermal heat generation between gold nanospheres and nanorods. *Scientific Reports* **2016,** *6*, 29836-298348.

21. Chen, H.; Shao, L.; Ming, T.; Sun, Z.; Zhao, C.; Yang, B.; Wang, J., Understanding the photothermal conversion efficiency of gold nanocrystals *Small* **2010,** *6* (20), 2272-2280.

22. Heidari, Z.; Salouti, M.; Sariri, R., Breast cancer photothermal therapy based on gold nanorods target by covalently-coupled bombesin peptide. *Nanotechnology* **2015,** *26* (19), 195101-195111.

23. Cong, B.; Kan, C.; Wang, H.; Liu, J.; Xu, H.; Ke, S., Gold Nanorods : near-infrared plasmonic photothermal conversion and surface coating. *Journal of Materials Science and Chemical Engineering* **2014,** *2* (1), 20-25.

24. Kang, X.; Guo, X.; Niu, X.; An, W.; Li, S.; Liu, Z.; Yang, Y.; Wang, N.; Jiang, Q.; Yan, C.; Wang, H.; Zhang, Q., Photothermal therapeutic application of gold nanorods-porphyrin-trastuzumab complexes in HER2-positive breast cancer. *Scientific Reports* **2017,** *7*, 42069-42082.

25. Zhang, R.; Zhang, J.; Xie, M.; Chen, J., Optical characteristics of Agarose gel. *Infrared and Laser Engineering* **2016,** *45* (7), 721003-07121003.

26. Seliktar, D., Designing cell-compatible hydrogels for biomedical applications. *Science* **2012,** *336*, 1124-1128.

27. Fatin-Rouge, N.; Starchev, K.; Buffle, J., Size effects on diffusion processes with Agarose gel. *Biophysical Journal* **2004,** *86*, 2710-2719.

28. Tibbitt, M. W.; Anseth, K. S., Hydrogels as extracellular matrix mimics for 3D cell culture. *Biotechnology and Bioengineering* **2009,** *103* (4), 655-663.

29. Ma, X.; Xia, Y.; Song, L.; Wang, Z., Preparation of gold nanoparticles-Agarose gel composite and its application in SERS detection. *Spectrochimica Acta Part A: Molecular and Biomolecular Spectroscopy* **2014,** *121*, 657-661.

30. Singh, M.; Harris-Birtill, D. C. C.; Zhou, Y.; Gallina, M. E.; Cass, A. E. G.; Hanna, G. B.; Elson, D. S., Application of gold nanorods for photothermal therapy in ex vivo human oesophagogastric adenocarcinoma. *Journal of Biomedical Nanotechnology*

2016, *12*, 481–490.

31. Wei, G.; Yu, J.; Wang, J.; Gu, P.; Birch, D. J. S.; Chen, Y., Hairpin DNA functionalized gold nanorods for mRNA detection in homogenous solution *J. Biomed. Opt.* **2016,** *21* (9), 097001-097009.

32. Lee, P. Y.; Costumbrado, J.; Hsu, C.; Kim, Y. H., Agarose gel electrophoresis for the separation of DNA fragments. *Journal of Visualized Experiments* **2012,** (62), 3923-3927.

33. Latreille, P.-L.; Adibnia, V.; Nour, A.; Rabanel, J.-M.; Lalloz, A.; Arlt, J.; Poon, W.; Hildgen, P.; Martinez, V.; Banquy, X., Spontaneous shrinking of soft nanoparticles

boosts their diffusion in confined media. *Nature Communications* **2019,** *10* (1), 4294-4301.

34. Olson, J.; Dominguez-Medina, S.; Hoggard, A.; Wang, L.-Y.; Chang, W.-S.; Link, S., Optical characterization of single plasmonic nanoparticles. *Chemical Society Reviews* **2015,** *44* (1), 40-57.

35. Gans, R., Über die Form ultramikroskopischer Goldteilchen. *Ann. Phys.* **1912,** *342* (5), 881-900.

36. Morales-Dalmau, J.; Vilches, C.; de Miguel, I.; Sanz, V.; Quidant, R., Optimum morphology of gold nanorods for light-induced hyperthermia. *Nanoscale* **2018,** *10* (5), 2632-2638.

37. Giannini, V.; Fernández-Domínguez, A. I.; Heck, S. C.; Maier, S. A., Plasmonic Nanoantennas: Fundamentals and Their Use in Controlling the Radiative Properties of Nanoemitters. *Chemical Reviews* **2011,** *111* (6), 3888-3912.

38. Schuller, J.; Barnard, E.; Cai, W.; Jun, Y.; White, J.; Brongersma, M., Plasmonics for extreme light concentration and manipulation. *Nature Materials* **2010,** *9*, 193-204.

39. Danan, Y.; Ramon, Y.; Azougi, J.; Douplik, A.; Zalevsky, Z., Decoupling and tuning the light absorption and scattering resonances in metallic composite nanostructures. *Opt. Express* **2015,** *23* (22), 29089-29099.

40. Sheng, Y.; Lin, M.; Li, X.; Hao, H.; Lin, X.; Sun, H.; Zhang, H., Enhancement of the 808 nm photothermal effect of gold nanorods by thiol-induced self-assembly. *Part. Part. Syst. Charact.* **2014,** *31*, 788–793.

41. Link, S.; Mohamed, M. B.; El-Sayed, M. A., Addition and correction. *J. Phys. Chem. B* **2005,** *109* (20), 10531-10532.

42. Davis, T. J.; Vernon, K. C.; Gómez, D. E., Effect of retardation on localized surface plasmon resonances in a metallic nanorod. *Optics Express* **2009,** *17* (26), 23655-23663.

43. Jeppson, J. O.; Laurell, C. B.; Franzen, B., Agarose gel electrophoresis. *Clinical Chemistry* **1979,** *25* (4), 629-638.

44. Mirab, F.; Kang, Y. J.; Majd, S., Preparation and characterization of size-controlled glioma spheroids using agarose hydrogel microwells. *PLoS ONE* **2019,** *14* (1), 0211078-0211089.

45. Tsou, Y.; Khoneisser; Huang, P.; Xu, X., Hydrogel as a bioactive material to regulate stem cell fate. *Bioactive Materials* **2016,** *1*, 39-55.

46. Bica, C.; Borsali, R.; Rochas, C.; Geissler, E., Dynamics of cellulose whiskers spatially trapped in Agarose hydrogels. *MACROMOLECULES* **2006,** *39*, 3622-3627.

47. Narayanan, J.; Xiong, J.; Liu, X., Determination of agarose gel pore size: absorbance measurements vis a vis other techniques. *J.Phys.: Conf.Ser.* **2006,** *28*, 83-86.

48. Vicente, A. L. S. A.; Bianchini, R. A.; Laus, A. C.; Macedo, G.; Reis, R. M.; Vazquez, V., Comparison of the protocol for removal of melanin from genomic DNA to optimize PCR amplification of DNA purified from highly pigmented lesions. *Histology and Histopathology* **2019,** *34* (9), 1089-1096.

49. Haemmerich, D.; Schutt, D. J.; Santos, I. D.; Webster, J. G.; Mahvi, D. M., Measurement of temperature-dependent specific heat of biological tissues. *Physiol. Meas.* **2005,** *26*, 59–67

50. Lázár, I.; Szabó, H. J., Prevention of the aggregation of nanoparticles during the synthesis of nanogold-containing silica aerogels. *Gels* **2018,** *4* (2), 55-64

51. Liao, H.; Nehl, C. L.; Hafner, J. H., Biomedical applications of plasmon resonant metal nanoparticles. *Nanomedicine* **2006,** *1* (2), 201-208.

52. Wang, Y.; Wang, R. K., High-resolution computed tomography of refractive index distribution by transillumination low coherence interferometry. *Opt. Lett.* **2010,** *35* (1), 91-93.

53. Fujiwara, E.; Cabral, T. D.; Sato, M.; Oku, H.; Cordeiro, C. M. B., Agarose-based structured optical fibre. *Scientific Reports* **2020,** *10* (1), 7035-7042.

54. Lakowicz, J. R., *Principles of Fluorescence Spectroscopy*. 3rd ed.; Springer: New York, 2006.

55. Anderson, M. L.; Morris, C. A.; Stroud, R. M.; Merzbacher, C. I.; Rolison, D. R., Colloidal gold aerogels: preparation, properties, and characterization. *Langmuir* **1999,** *15* (3), 674-681.

56. Freni, A.; Calabrese, L.; Malara, A.; Frontera, P.; Bonaccorsi, L., Silica gel microfibres by electrospinning for adsorption chillers. *Energy* **2019,** *187*, 115971-115979.

57. Noroozi, M.; Panahi-Sarmad, M.; Abrisham, M.; Amirkiai, A.; Asghari, N.; Golbaten-Mofrad, H.; Karimpour-Motlagh, N.; Goodarzi, V.; Bahramian, A. R.; Zahiri,

B., Nanostructure of aerogels and their applications in thermal energy insulation. *ACS Applied Energy Materials* **2019,** *2* (8), 5319-5349.

58. Soto-Reyes, N.; Temis-P´erez, A. L.; L´opez-Malo, A.; Rojas-Laguna, R.; Sosa-Morales, M. E., Effects of shape and size of agar gels on heating uniformity during pulsed microwave treatment. *Journal of Food Science* **2015,** *80* (5), E1021-E1025.

59. Ramires, M. L. V.; Nieto de Castro, C. A.; Nagasaka, Y.; Nagashima, A.; Assael, M. J.; Wakeham, W. A., Standard reference data for the thermal conductivity of water. *Journal of Physical and Chemical Reference Data* **1995,** *24*, 1377-1381.

Chapter 5

Targeting EpCAM over-expressed cancer cells with SYL3C aptamer functionalised small gold nanorod based nanoprobes

5. 1. Introduction

Targeting cancerous cells for photothermal therapy could be a promising approach in destroying specific cancerous cells. This can be achieved by attaching single strand DNA such as aptamers on to the small gold nanorods (SGNRs) for targeting cancerous cells, because aptamers have a high binding affinity and specificity for targets[1-2]. Small gold nanorods are considered suitable agents because the absorption-to-extinction ratio of the SGNRs is high compared to the LGNRs. Therefore, the SGNRs are expected to have a superior photothermal effect compared to the LGNRs for photothermal therapy of cancers such as oesophagus cancer. Moreover, the SGNRs have demonstrated attractive features such as biocompatibility, deep tissue penetration, photostability and large surface area to volume ratio for effective binding to smaller targets[3-4]. These features make the SGNRs based nanoprobes ideal agents for targeting receptors, delivery of therapeutic drugs and photothermal therapy[5-6].

Previously, it has been reported that less laser energy is required to kill cancer cells when the GNRs bind on the cell membrane than when internalized into the cytoplasm[7]. Furthermore, rupturing cell membrane kills cancer cells faster because the metabolic activities of the cancerous cell is disrupted thereby leading to cell death[7], hence the need to target biomarkers on the membrane of the cancer cells. Cell membranes are characterised by cancer biomarkers such as membrane proteins (e.g. epidermal growth factor receptor, EGFR and epithelia cell adhesion molecule (EpCAM)[1, 8]. The membrane proteins facilitate the transportation of ions, nutrients, drugs and other small molecules into the cell[8-9]. The expression level of the membrane proteins could implicate cellular disorders such as cancers, making the membrane proteins useful biomarker for diagnosis and prognosis of disease[9].

Aptamers have been reported to bind to a variety of targets including proteins, nucleic acids and metal ions[10]. Aptamers have been utilized as bio-molecular nanocargo for transporting therapeutic agents, targeting RNAs and proteins[1-2]. Aptamers have demonstrated stability at ambient temperature and facile conjugation with nanomaterials[2]. Aptamers are non-immunogenic, non-toxic, smaller size (1.2 nm- 3 nm) for effective binding and deep tissue penetration[1-2]. These physicochemical features make aptamers very versatile nanomaterials for various applications including targeting disease biomarkers and detecting the presence of prohibited substances and contaminants in food[1, 11-12]. Aptamers are single stranded biological molecules synthetically created by systematic evolution of ligands by exponential enrichment (SELEX) from either a DNA or RNA to bind a variety of targets. DNA aptamers are preferred in most clinical applications because they are very stable and invincible to nuclease degradation[13]. SYL3C aptamer for example, is a dual-loop hairpin DNA based aptamer that binds to epithelia cell adhesion molecule (EpCAM)[1]. EpCAM is a transmembrane glycoprotein that is expressed on the cell membrane of cells of epithelia origin[14]. EpCAM over-expression is very common in prostate cancer, breast cancer, colorectal cancer and oesophagus cancer[1, 14-17] making EpCAM a versatile biomarker for detecting various cancer[13]. Recently, Song et al.[1] identified SYL3C aptamer for targeting EpCAM over-expression in human breast, colorectal and gastric cancer cells. SYL3C binds to EpCAM over-expressed cancer cells with high affinity and specificity, but negative to non-EpCAM over-expressed cells[15]. Thus, SYL3C is a promising molecular tool for early detection of EpCAM over-expressed cancer[13]. Following the discovery of SYL3C by Song et al., the utilization of SYL3C has been documented in various studies[15, 18-19]. For example, Zheng et al.[15] developed an electrochemical cytosensor for capturing EpCAM over-expressed circulating tumor cells. The cytosensor nanostructure was made by assembling gold nanospheres on the surface of glassy carbon electrode. The gold nanospheres were then functionalized with SYL3C for detecting cancer cells with high levels of EpCAM expression. The cytosensor shows high efficiency and specificity in capturing circulating tumour cells with high levels of EpCAM expression. Similarly, Song et al. demonstrated that gold nanoparticles functionalized with SYL3C could be very efficient in capturing circulating tumour cells[19]. Furthermore, Pu et al. observed that SYL3C is sensitive to EpCAM over-expression in frozen colorectal cancer tissues[13]. Liu

et al.[20] investigated the staining pattern of SYL3C in oesophagus squamous cell carcinoma, oesophagus adenocarcinoma and normal oesophagus epithelium. SYL3C was found to detect 98% of EpCAM over-expression in both oesophagus squamous cell carcinoma and oesophagus adenocarcinoma, but negative to normal oesophagus epithelium[20]. The molecular interaction between SYL3C and EpCAM was investigated by single molecular recognition force spectroscopy using atomic force microscopy (AFM)[10]. The SYL3C fit to AFM tip specifically recognized the EpCAM immobilized on the silicon substrate, indicating the sensitivity of SYL3C aptamer to EpCAM. In addition, the study found that SYL3C /EpCAM complexes could be stable in PBS binding buffer containing Mg^{2+}. Conventional sized gold nanorods encapsulated in graphitic shell were functionalized with FAM-labeled SYL3C by strong π-π interaction[18]. The nanoprobes show brighter Raman imaging signals for EpCAM positive cancerous cells compared to normal tissues.

The photothermal effect of large gold nanorods LGNRs (> 50 nm in length and > 10 nm in width) in killing cancer cells has been demonstrated. Manivasagan et al. demonstrated that cancer cells in the cell culture and a mouse treated with chitosan and fucoidan coated gold nanorods could be killed due to the photothermal effect of the gold nanorods [21]. Bucharskaya et al. showed that increasing the concentration of polyethylene glycol functionalized gold nanorods in tumour cells could enhance the local temperature rise of the tumour microenvironment upon laser irradiation thereby suppressing tumour growth and eventual tumour elimination[22]. Gold nanorods functionalized with polyethylene glycol reduced graphene oxide were used to destroyed human glioblastoma (U87MG) cancer cells upon irradiation by a continuous wave laser beam[23]. On the other hand, Jia et al.[6] have shown that silica coated SGNRs (< 50 nm in length and < 10 nm in width) have more photothermal effect than silica coated LGNRs in the photothermal therapy of cancer. However, it has been found that gold nanorods functionalized with targeting ligands have better cellular uptake/binding in comparison to gold nanorods without targeting ligands[24]. Moreover, gold nanoparticles functionalized with targeting ligands could have higher binding affinity and specificity for cancerous cell thereby minimising side effects on healthy cells, hence the functionalization of SGNRs with SYL3C aptamer.

The present study investigated the capability of SYL3C functionalized small gold nanorod nanoprobes in targeting EpCAM over-expression in cancer cells and the size effect of SYL3C functionalized gold nanorods on the photothermal therapy of cancer. Steady state and time-resolved spectroscopies were utilized to understand the hybridization kinetics of the GNRs-SYL3C nanoprobes. Flow cytometry and fluorescence microscopy were employed to assess the binding of the GNRs-SYL3C on the cancer cells, and the cell viability under laser irradiation.

5. 2. Experimental section.

5. 2. 1. Materials

All chemicals were used as received without further purification. Chloroauric acid ($HAuCl_4$, 49%), Hexadecyltrimethylammonium bromide (CTAB, 99%), Ascorbic acid (AA), Sodium borohydride ($NaBH_4$, 99.8%), Silver nitrate ($AgNO_3$), Dodecanethiol (DDT, 98%), Mercaptohexanoic acid (MHA, 99.8%), Acetone (99.9%), Isopropanol (99.5%), Toluene (99.8%) and methanol were purchased from Sigma Aldrich while hydrochloric acid (HCL) was purchased from Fluka.

Cy3-SYL3C aptamer:

5'[ThiC6]AAAAAACACTACAGAGGTTGCGTCTGTCCCACGTTGTCATGGGGGGTTGGCCTG[Cy3]-3',

cDNA:

5'-CAGGCCAACCCCCCATGACAACGTGGGACAGACAGACGCAACCTCTGTAGTG-3'. The aptamer and the cDNA were purchased from Sigma Aldrich.

5. 2. 2. Synthesis of gold nanorods

We synthesized large gold nanorods (LGNR) by a reported protocol[25]. Two samples of the small gold nanorods ($SGNR_1$ and $SGNR_2$) were synthesized by our modified silver

assisted seed-mediated growth method reported in the literature[26]. The seeds solution of the LGNR and the small gold nanorods ($SGNR_1$ and $SGNR_2$) were prepared and incubated as reported in section 3. 2. 2. of chapter 3. Table 5.1. and 5.2. list all the reagents used to prepare the gold seeds, the growth solutions and the amount of seeds used for the synthesis of LGNR, $SGNR_1$ and $SGNR_2$.

Table 5.1. The list of reagents used to prepare the seeds and the growth solutions of the LGNR.

Reagents	$HAuCl_4$ (0.001M; ml)	CTAB (0.2M; ml)	$NaBH_4$ (0.01M; ml)	$AgNO_3$ (0.004M; ml)	A.A (0.0778M; ml)	Seeds (ml)
Seeds solution	2.50	7.50	0.60	-	-	-
Growth solution	10.00	10.00	-	0.285	0.14	0.02

Table 5.2. The list of reagents used to prepare the seeds and growth solutions of the SGNRs ($SGNR_1$ and $SGNR_2$).

Reagents		$HAuCl_4$ (0.01M; ml)	CTAB (0.1M; ml)	$NaBH_4$ (0.01M; ml)	$AgNO_3$ (0.01M; ml)	HCl (1.0M; ml)	A.A (0.1M; ml)	Seeds (ml)
Seeds solution		0.25	9.75	0.60	-	-	-	-
Growth solution	$SGNR_1$	0.50	9.00	-	0.075	0.20	0.08	1.00
	$SGNR_2$	0.50	9.00	-	0.032	0.20	0.08	1.00

5. 2. 3. Ligand exchange and functionalization of gold nanorods

Ligand exchange for the LGNR, $SGNR_1$ and the $SGNR_2$ was performed as reported in section 3. 2. 4. of chapter 3 using a round-trip phase transfer ligand exchange protocol

previously reported in the literature[25, 27]. A thiolated hairpin SYL3Cwas used to functionalize the LGNR, $SGNR_1$ and the $SGNR_2$ respectively via a salt aging process[25] as reported in section 3. 2. 5. of chapter 3.

5. 2. 4. Cell sample preparation

Prostate cancer cell line, PC3, was used as EpCAM positive sample, while healthy human kidney cell line, HEK293, was used as a control sample. The cells were cultured in the Dulbecco's modified Eagle's medium (DMEM) media containing FBS (10%) and penicillin-streptomycin (5.5ml). Prior to seeding, a hemocytometer was used to determine the cell density. The PC3 and the HEK293 cells were seeded at 1.5 x 10^6 cells per well in a 6-well plate. The PC3 cancer cells and the HEK293 cells were incubated in separate wells overnight. The experimental cell samples were incubated with the $SGNR_2$-SYL3C nanoprobes and the $SGNR_2$-MHA for 4 hours in separate wells. The cells were centrifuged at 1400 rpm for 5minutes and re-suspended in PBS buffer. The samples were excited at 488 nm for flow cytometry analysis with A MoFlo XDP cytometer (BeckmanCoulter, Brea, CA).

Furthermore, human oesophagus adenocarcinoma cell line, FLO-1 and breast cancer cell line, MCF-7 with similar cell density as above were cultured on coverslips suspended in the DMEM media in 24 well plate overnight. After the overnight incubation, the cells were washed in the PBS buffer 2x and treated with 0.1 nM of the $SGNR_2$-SYL3C nanoprobes and incubated for 0.5 hours, 1 hour and 1.5 hours respectively. After the incubation, the FLO-1 and MCF-7 cell samples were further treated with 4', 6-Diamidine-2'-phenylindole (DAPI) to stain the cell nuclei. The cell containing coverslips were fixed on a glass slide for imaging. The samples were excited at 405 nm for DAPI and 561 nm for Cy3 simultaneously with a confocal microscope (Leica Microsystems SP8+ picoEMERALDS). The DAPI and Cy3 channels were merged together in ImageJ to produce overlapped images.

5. 2. 5. Sample preparation and photothermal effect study

The photothermal effect of GNRs in cancer cells was investigated using $SGNR_1$-SYL3C and LGNR-SYL3C nanoprobes. Firstly, the FLO-1 and the HEK293 cell lines were cultured in the DMEM media. Specifically, 8.0 x 10^5 cells for each cell line were seeded per well in 2 ml of the DMEM media supplemented with 10% foetal bovine serum (FBS) and penicillin-streptomycin (5.5 ml) in a 6 well plate overnight after which the media was removed and the cells washed in phosphate buffered saline (PBS) and trypsinized to detach adherent cells. The cells were collected into a 15 ml tube and centrifuged at 1400 rpm for 5 minutes at room temperature. The supernatant was discarded and the cell pellets re-suspended in 1 ml of the fresh DMEM media in the initial 6 well plate. The cells were then incubated with 0.4 nM of the $SGNR_1$-SYL3C and the LGNR-SYL3C nanoprobes; and the $SGNR_1$-MHA and the LGNR-MHA for 1.5 hours. Thereafter, the cells were washed with PBS, trypsinized, centrifuged and re-suspended in 300 µl of phenol free DMEM media for photo-excitation. Then, 20 µl of the treated cell samples and un-treated cells were placed on an improvised chamber made from the lid of a 1.5 ml eppendorf tube. The lid was fixed on a glass slide with a masking tape as shown in figure 5.1. The cell samples were excited on resonance to the surface plasmons resonance of the $SGNR_1$ and the LGNR, namely 774 nm with laser power density 0.346±0.060W/cm^2 and 753 nm with laser power density 0.306±0.050W/cm^2 respectively. Both excitations were at 100% laser power transmission via the objective lens (10x) of a confocal laser scanning microscope (LSM510, Carl Zeiss, Göttingen, Germany) for 1minute. After laser exposure, 10 µl of the laser treated cell samples were mixed with 5 µl trypan blue (0.4%) on a glass slide to identify viable and dead cells. The trypan blue treated cell samples were image with a confocal microscope using the 10x objective lens. The quantity of viable and dead cells were determined by casting the entire laser treated cells mixed with trypan blue on a hemocytometer for counting.

Figure 5.1. The excitation of nanoprobes treated cells with a coherent laser beam passing through a confocal microscope.

5. 2. 6. Cytotoxicity effect of $SGNR_1$-SYL3C

The cytotoxicity of SYL3C based nanoprobes was evaluated by incubating the $SGNR_1$-SYL3C nanoprobe with FLO-1, MCF-7 and HEK293 cell lines in comparison with the $SGNR_1$-MHA. Specifically, 8.0 x 10^5 cells of each cell line were seeded per well in 2 ml of the DMEM media in a 6 well plate overnight after which the media was removed and the cells washed in phosphate buffered saline (PBS), trypsinized to detach adherent cells. The cells were collected into a 15 ml tube and centrifuged at 1400 rpm for 5 minutes at room temperature. The supernatant was discarded and the cell pellets re-suspended in 2 ml of the fresh DMEM media in the initial 6 well plate. The cells were then incubated with 0.4 nM of the $SGNR_1$-SYL3C nanoprobe and the $SGNR_1$-MHA for 3 hours.

Thereafter, the cells were washed with PBS, tyrpsinized, centrifuged and re-incubated in 1 ml of the fresh DMEM media for 24 hours to assess cell viability.

5. 2. 7. Optical characterization of gold nanorods nanoprobes

The extinction spectra of the $SGNR_1$, $SGNR_2$ and the LGNR samples were measured with the UV-visible spectrophotometer (Lambda 2, Perkin Elmer). A spectrofluorometer (Horiba Jobin Yvon Ltd., Middlesex, UK) was used to measure the fluorescence emission spectra of the $SGNR_1$, $SGNR_2$ and the LGNR nanoprobes at 532 nm excitations.

Time-resolved fluorescence spectroscopy was employed using the time-correlated single-photon counting (TCSPC) technique with an IBH Fluorocube fluorescence lifetime system (Horiba Jobin Yvon IBH Ltd., Glasgow, UK). The $SGNR_1$, $SGNR_2$ and the LGNR nanoprobes were excited with a 509 nm pulsed light-emitting diode (NanoLED) source respectively, operating at a repetition rate of 1 MHz. Fluorescence decay measurement was taken at the magic angle (54.7^o) to eliminate polarization artefacts. Data analysis was performed with DAS6 package. The fluorescence decay curves of the nanoprobes were fitted as explained in chapter 3. The fluorescence lifetimes were analyzed by fitting the decay curves to multi-exponentials decay model presented in equation 2.3. of chapter 2.

Flow cytometry was performed using a A MoFlo XDP cytometer (BeckmanCoulter, Brea, CA). While fluorescence imaging was performed with a single photon confocal microscope (Leica Microsystems SP8+ picoEMERALDS +CW vis lasers).

5. 3. Results and Discussion

5. 3. 1. Synthesis and functionalization of gold nanorods

Gold nanorods ($SGNR_1$, $SGNR_2$ and LGNR) were synthesized by a silver assisted seed-mediated growth method[25-26]. The longitudinal surface plasmon resonance (LSPR) of the $SGNR_1$, $SGNR_2$ and the LGNR were 789 nm, 679 nm and 760 nm respectively. The

average dimensions of the $SGNR_1$, $SGNR_2$ and the LGNR were determined from the calibration curves shown in appendix 2. The dimensions are presented in table 5.3.

Table 5.3. The dimensions of the $SGNR_1$, $SGNR_2$ and the LGNR.

Samples	LSPR (nm)	Length (nm)	Width (nm)
$SGNR_1$	789	22.0±4.6	5.8±1.3
$SGNR_2$	679	18.5±4.2	5.4±1.4
LGNR	760	45.0±7.2	11.6±2.0

Figure 5.2. shows the UV-vis extinction spectra of the $SGNR_1$, $SGNR_2$ and the LGNR before, after ligand exchange and functionalization with the SYL3C respectively. The longitudinal surface plasmon resonance of the $SGNR_1$, $SGNR_2$ and the LGNR shifted to 756 nm, 676 nm and 765 nm respectively without apparent peak broadening after the ligand exchange, indicating a successful ligand exchange as shown in figure 5.2a, c and e respectively. The blue shift after the ligand exchange could be due to the shortening of the length of $SGNR_1$, $SGNR_2$ and LGNR as a result of heating, therefore the aspect ratio of the gold nanorods decreases leading to a blue shift of the longitudinal surface plasmon resonance as predicted by Gans', Link and El-Sayed models in equations 1.2., 1.7. and 1.8. respectively[28-29]. After functionalization with the SYL3C, the LSPR of $SGNR_1$-SYL3C, $SGNR_2$-SYL3C and the LGNR-SYL3C nanopronbes were 774 nm, 634 nm and 753 nm (figure 5.2a, c and e respectively). The blue shift observed for the $SGNR_2$ and the LGNR nanoprobes is consistent with previous studies[30-31] and this could be attributed to series of repeated washing (centrifugation) which could affect the final size and the LSPR of the nanoprobes. A peak centered at ~259 nm was seen for the $SGNR_1$-SYL3C, $SGNR_2$-SYL3C and the LGNR-SYL3C nanopronbes representing the absorption wavelength of DNA (SYL3C). Upon addition of the complementary DNA (cDNA), the intensity of the absorption peak of DNA increased. The adsorption of the aptamer on the gold nanorods structures, thus, enhances their targeting abilities and stabilizes the nanoprobes from nuclease degradation for potential application in complex biological systems[19].

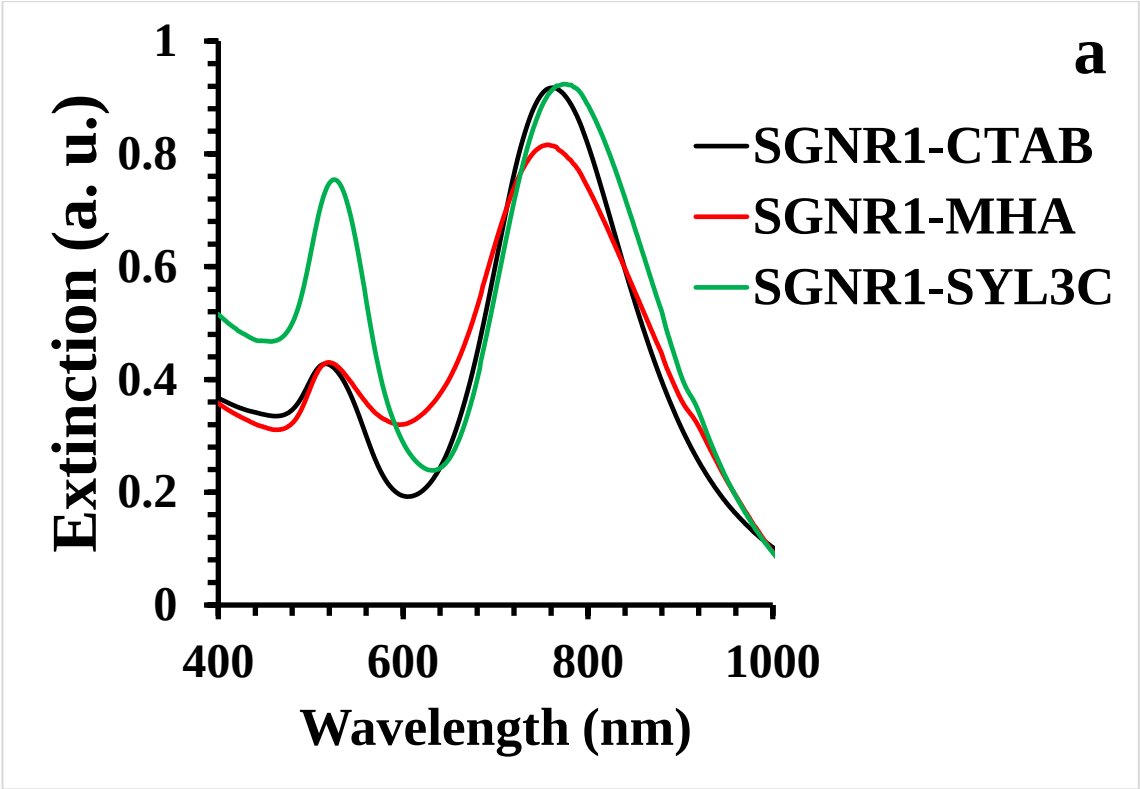
a
Extinction (a. u.)
1
0.8
0.6
0.4
0.2
0
400
600
800
1000
Wavelength (nm)
SGNR1-CTAB
SGNR1-MHA
SGNR1-SYL3C

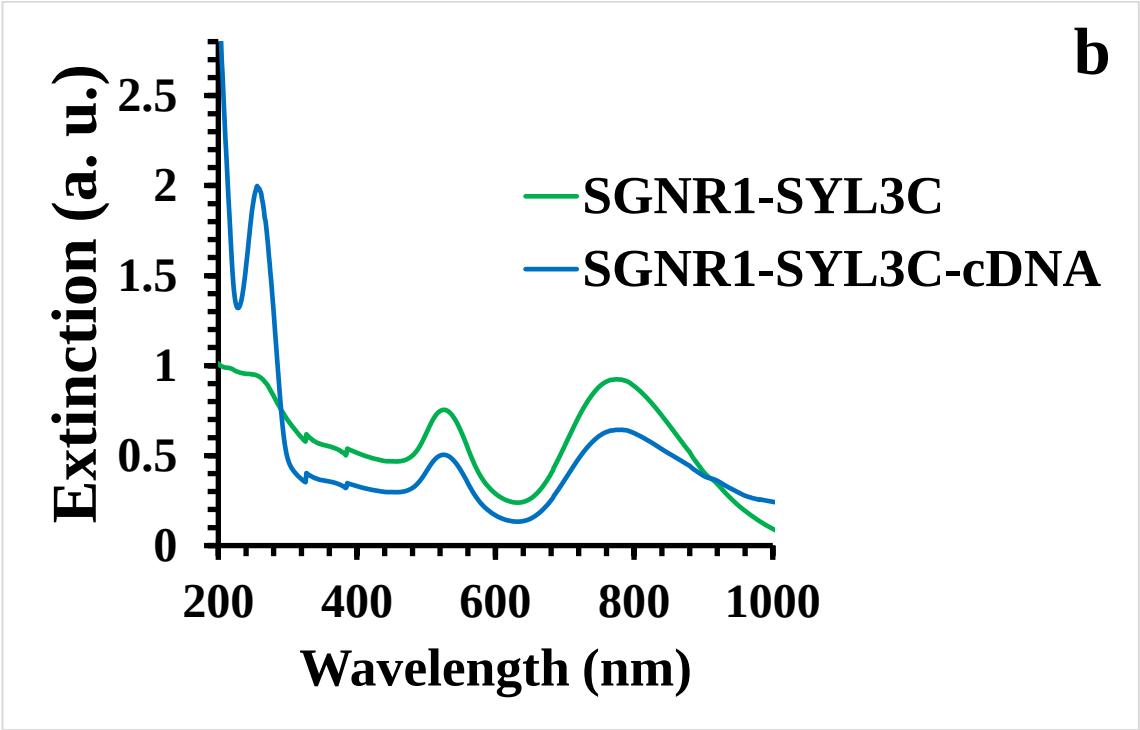
b
Extinction (a. u.)
2.5
2
1.5
1
0.5
0
200
400
600
800
1000
Wavelength (nm)
SGNR1-SYL3C
SGNR1-SYL3C-cDNA

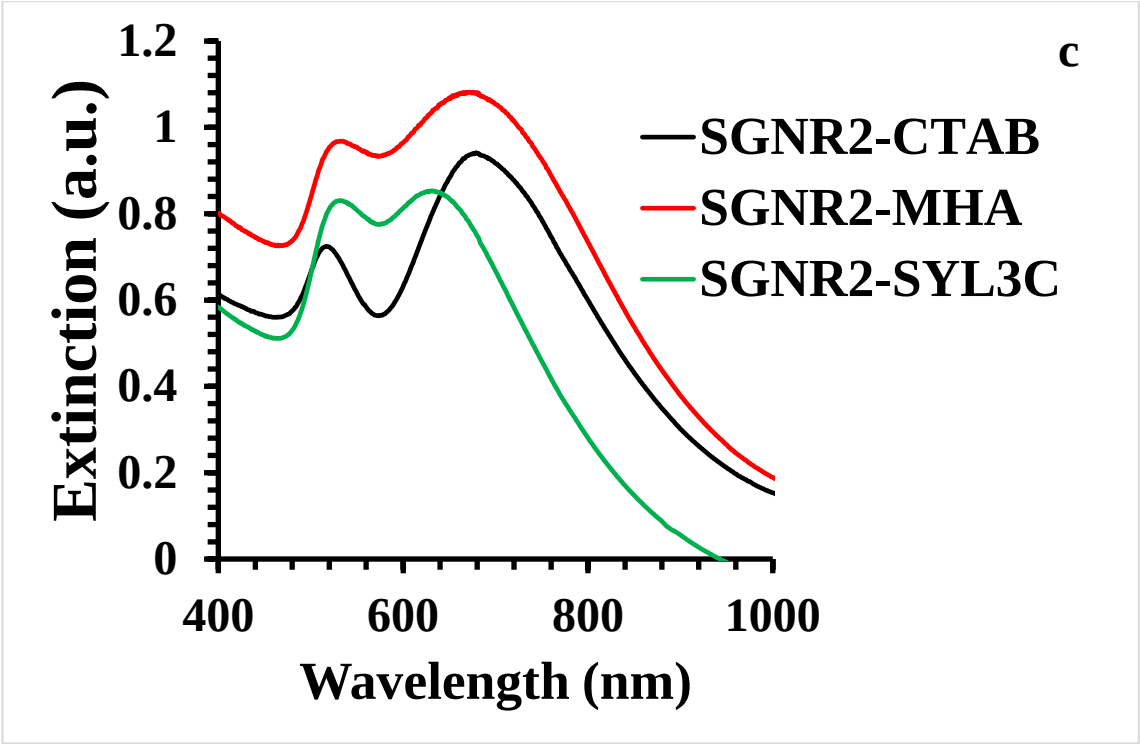
c
Extinction (a.u.)
1.2
1
0.8
0.6
0.4
0.2
0
400
600
800
1000
Wavelength (nm)
SGNR2-CTAB
SGNR2-MHA
SGNR2-SYL3C

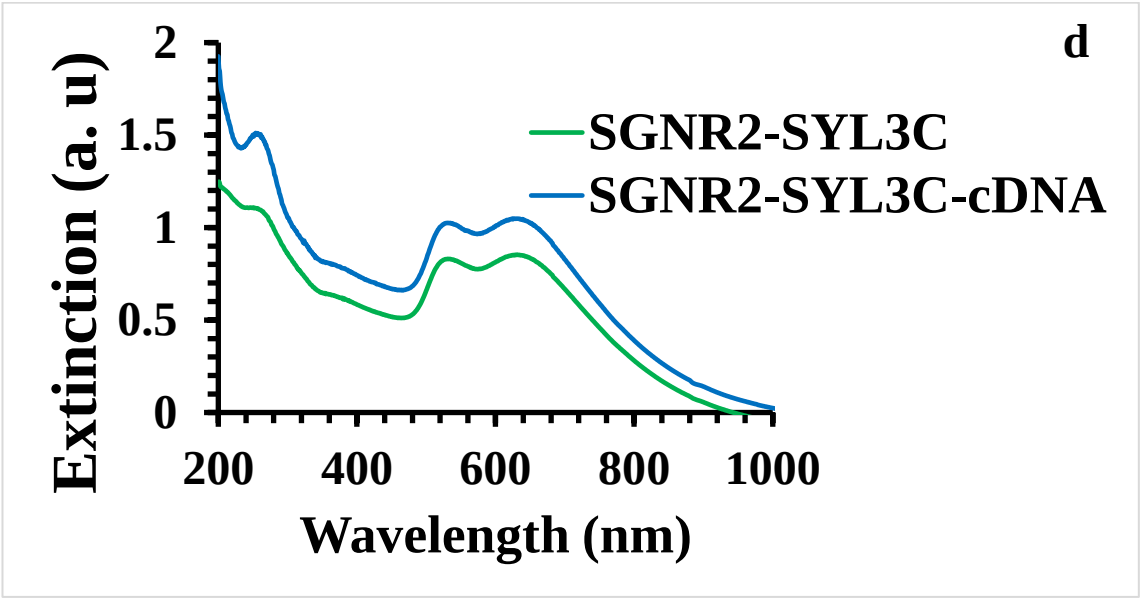
d
Extinction (a. u)
2
1.5
1
0.5
0
200
400
600
800
1000
Wavelength (nm)
SGNR2-SYL3C
SGNR2-SYL3C-cDNA

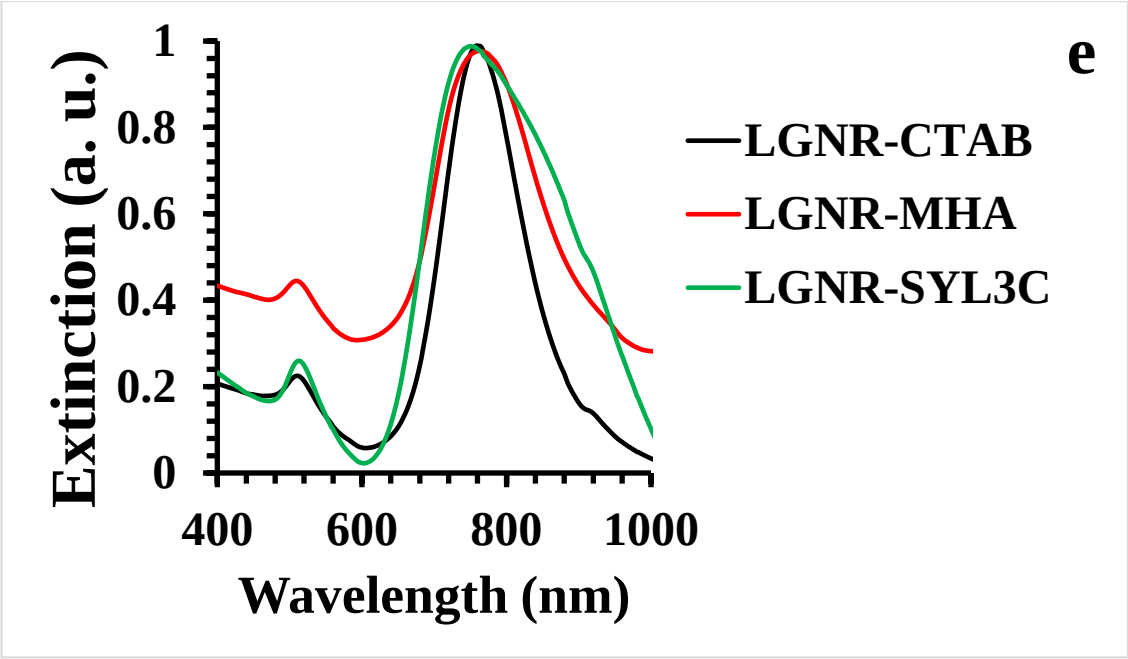

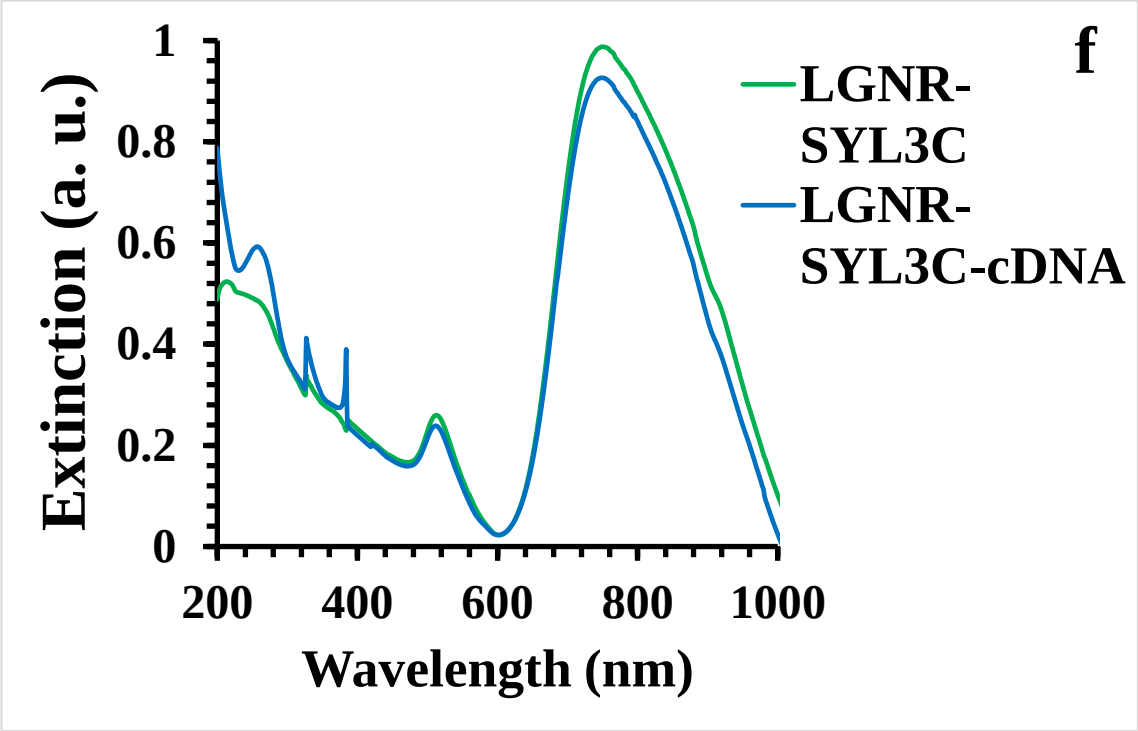

Figure 5.2. The UV-vis extinction spectra of the gold nanorods; (a) the extinction spectra of $SGNR_1$ before and after ligand exchange and functionalization with SYL3C, (b) the extinction spectra of $SGNR_1$ before and after incubating with the cDNA, (c) the extinction spectra of $SGNR_2$ before and after ligand exchange, (d) the extinction spectra of $SGNR_2$ before and after functionalization with SYL3C (e) the extinction spectra of LGNR before

and after ligand exchange, (f) the extinction spectra of LGNR before and after functionalization with SYL3C .

5. 3. 2. Fluorescence emission and lifetime of Cy3-SYL3C aptamer immobilized on gold nanorods

To understand the hybridization kinetics of the GNRs-SYL3C nanoprobes, both steady state and time-resolved fluorescence spectroscopies were performed before and after adding excess cDNA. The $SGNR_1$-SYL3C, $SGNR_2$-SYL3C and the LGNR-SYL3C nanoprobes were incubated with the cDNA in the ratio 1:1000. The samples were excited at 532 nm with a spectrofluorometer to obtain the fluorescence emission spectra. Fig. 5.3. shows the fluorescence emission spectra of the $SGNR_1$-SYL3C, $SGNR_2$-SYL3C and the LGNR-SYL3C nanoprobes before and after incubating with the cDNA. The increase of the fluorescence emission intensity of the gold nanorods nanoprobes after adding the cDNA was observed in all the three cases. Without the cDNA, aptamer was in a closed form and the Cy3 in the SYL3C (donor) is close to the gold nanorod (acceptor) surface, resulting in quenching of the fluorophores' emission due to the energy transferred from the donor to the acceptor. In the presence of the cDNA, the hybridization of the aptamer with the cDNA opened the hairpins and shifted the fluorophore away from the gold surface resulting in a recovered fluorescence emission of the fluorophore. Previous study found that the quantum yield of Cy3-ssDNA significantly reduced upon duplex formation arising from the free rotation of the carbon-carbon bond of the polymethine [32-34]. The increases in the fluorescence emission intensity of the $SGNR_1$-SYL3C, $SGNR_2$-SYL3C and the LGNR-SYL3C nanoprobes after hybridization with the cDNA imply the strong quenching in the initial closed form, thus, indicating the successful functionalization of the small gold nanorods with the aptamer.

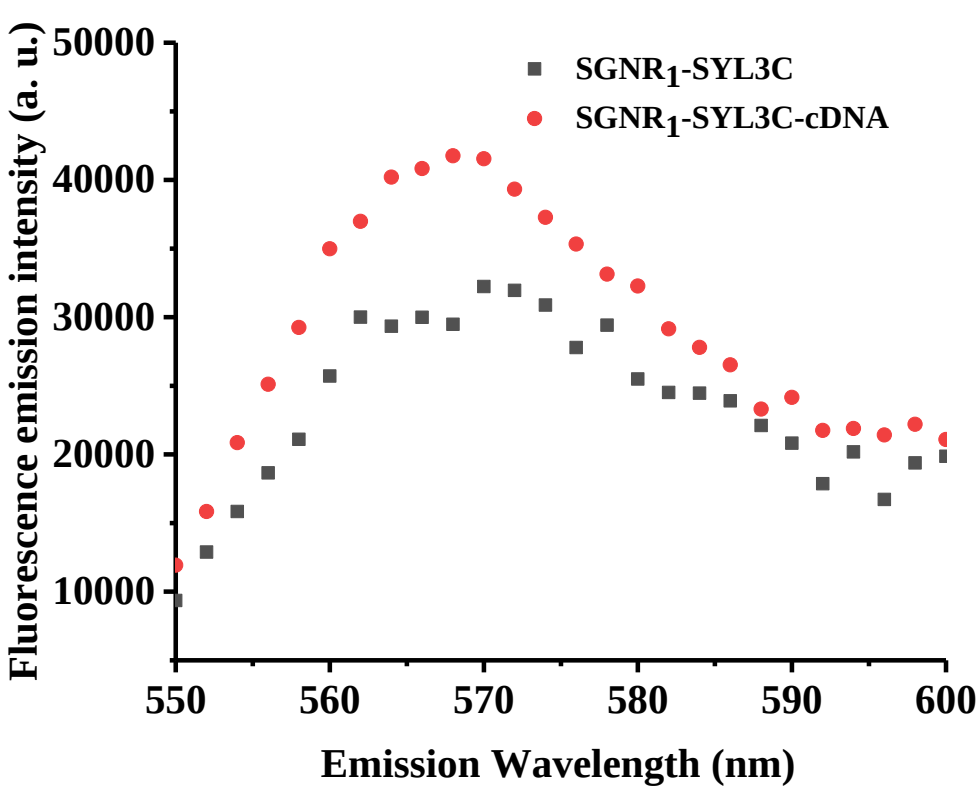
a
SGNR1-SYL3C
SGNR1-SYL3C-cDNA
Fluorescence emission intensity (a. u.)
50000
40000
30000
20000
10000
550
560
570
580
590
600
Emission Wavelength (nm)

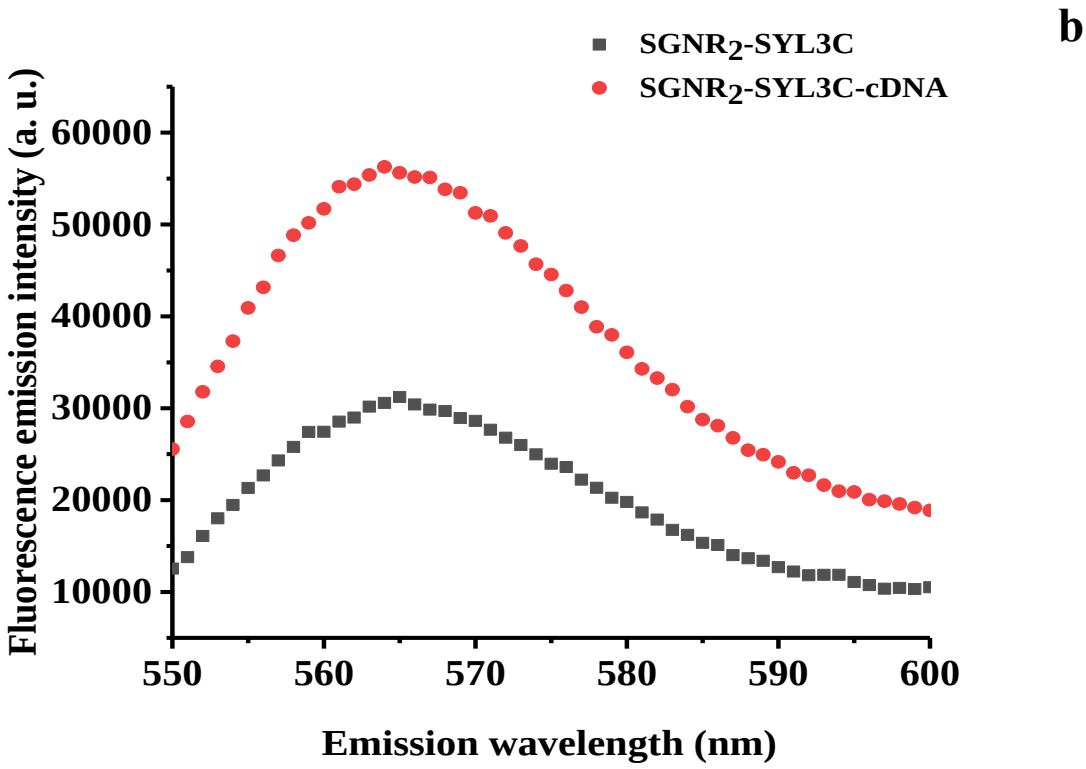
b
SGNR2-SYL3C
SGNR2-SYL3C-cDNA
Fluorescence emission intensity (a. u.)
60000
50000
40000
30000
20000
10000
550
560
570
580
590
600
Emission wavelength (nm)

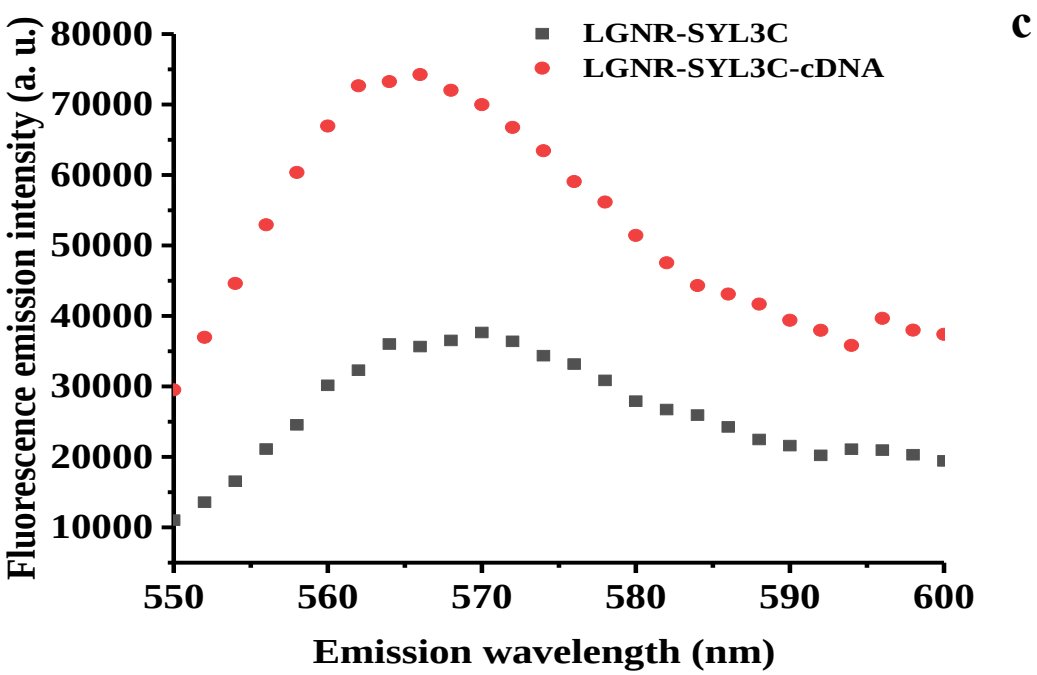

Figure 5.3. The fluorescence emission spectra of the gold nanorods nanoprobes before and after hybridization; (a) $SGNR_1$-SYL3C nanoprobe, (b) $SGNR_2$-SYL3C nanoprobe (c) LGNR-SYL3C nanoprobe.

Time-resolved fluorescence lifetime measurement was conducted to determine the fluorescence lifetimes of the $SGNR_1$-SYL3C, $SGNR_2$-SYL3C and the LGNR-SYL3C nanoprobes before and after incubation with the cDNA. Fluorescence decay curves were fitted to multi-exponentials decay model using DAS6 software as previously reported[25]. The fluorescence lifetime of free Cy3-SYL3C (i.e. without assembly onto the gold nanorods) was measured as the reference. The fluorescence lifetime of free SYL3C was fitted to a 2 exponential decay model to account for the shorter and the longer lifetimes of free SYL3C in the closed state (before hybridization with the cDNA) and the opened states (after hybridization with the cDNA). While the lifetimes of $SGNR_1$-SYL3C, $SGNR_2$-SYL3C and LGNR-SYL3C nanoprobes were fit to 3 exponential decay model to account for the longer and the shorter lifetimes of nanoprobes in the closed and the opened states, as well as the scattering from the gold nanorods. The fluorescence decay curves of the free Cy3-SYL3C, $SGNR_1$-SYL3C, $SGNR_2$-SYL3C and the LGNR-SYL3C

nanoprobes are shown in figure 5.4., while the fittings of the fluorescence decay curves are presented in figures 2 and 3 respectively of appendix 5.

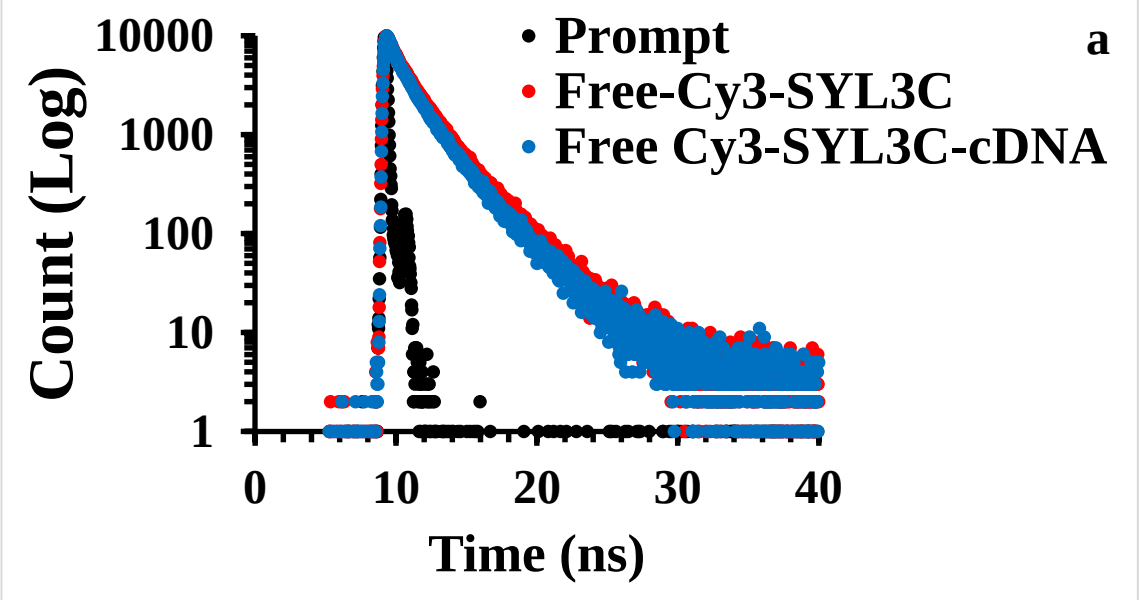

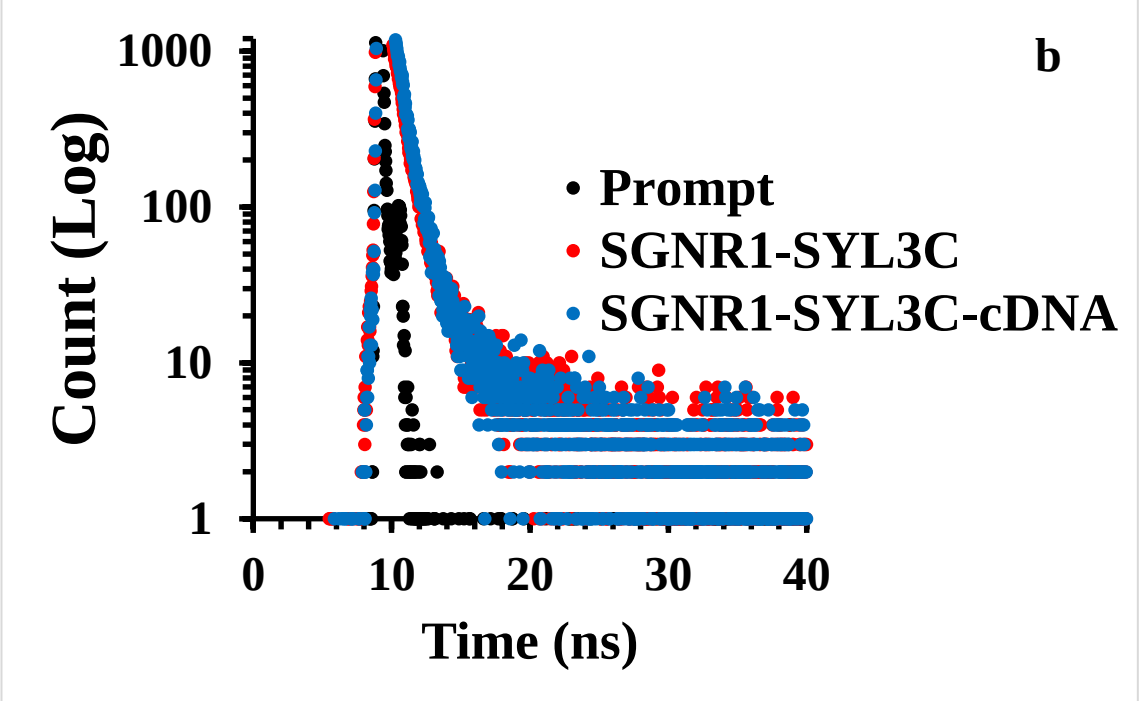

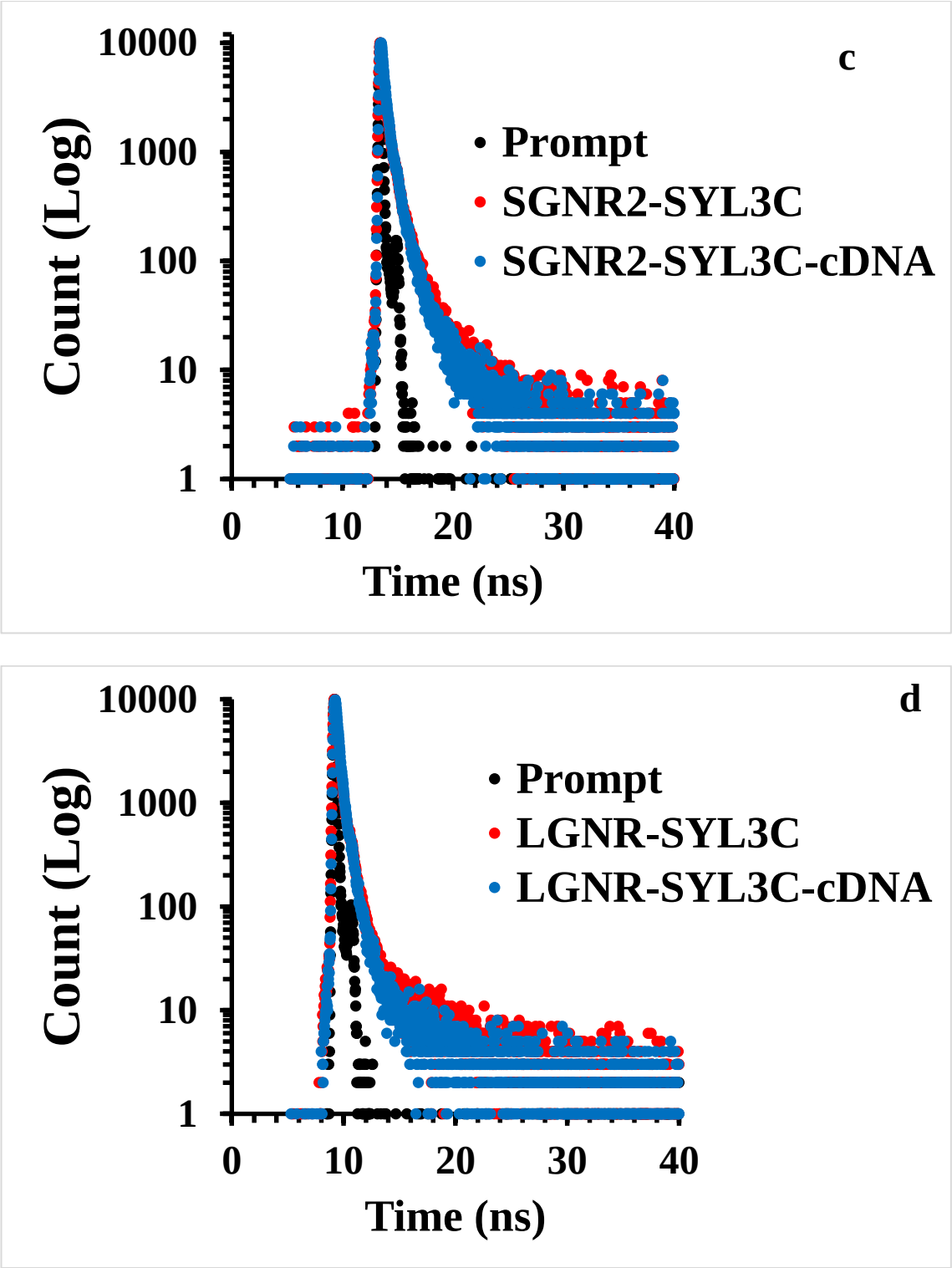

Figure 5.4. The fluorescence lifetime decays of; (a) free Cy3-SYL3C , (b) $SGNR_1$-SYL3C nanoprobe, (c) $SGNR_2$-SYL3C nanoprobe (d) LGNR-SYL3C nanoprobe.

Table 5.4. shows the fluorescence lifetimes of the free Cy3-SYL3C, $SGNR_1$-SYL3C, $SGNR_2$-SYL3C and the LGNR-SYL3C nanoprobes. The fluorescence lifetime of the free Cy3-SYL3C shows two fluorescence lifetime components denoted by τ_1 and τ_2, where τ_1 and τ_2 are the shorter and the longer lifetime components of the free Cy3-SYL3C in both the closed state and the opened state respectively. It has been reported that the energy transferred from the fluorophore to the nucleotide bases could occur by photo induced electron transfer when both the fluorophore and the bases are in a close proximity[25, 35], hence the shorter lifetime component of the free Cy3-SYL3C. The average lifetime of the free Cy3-SYL3C is denoted by $\bar{\tau}$ in both states. The average fluorescence lifetime of the free Cy3-SYL3C in the closed state is 1.65 ns while its average lifetime in the opened state is 1.53 ns. It can be seen that the average fluorescence lifetime of the free Cy3-SYL3C decreases after hybridization with the cDNA as shown in table 5.4. This could be due to the rotation of the carbon-carbon bond of the polymethine chain upon hybridization, inducing a decrease in the quantum yield of Cy3[33], hence the decrease of the average fluorescence lifetime of the free Cy3-SYL3C after hybridization with the cDNA.

Table 5.4. The fluorescence lifetimes of a free Cy3-SYL3C.

Sample	τ_1 (ns)	B_1 (%)	τ_2 (ns)	B_2 (%)	$\bar{\tau}$ (ns)	χ^2
Free-Cy3-SYL3C	1.07±0.01	43.69	2.88±0.01	56.31	1.65	1.04
Free-Cy3-SYL3C - cDNA	1.04±0.01	49.94	2.84±0.01	50.06	1.53	1.00

Table 5.5. shows the fluorescence lifetimes of the $SGNR_1$-SYL3C, $SGNR_2$-SYL3C and the LGNR-SYL3C nanoprobes before and after incubating with the cDNA. The fluorescence lifetimes of the $SGNR_1$-SYL3C, $SGNR_2$-SYL3C and the LGNR-SYL3C nanoprobes show three lifetime components where τ_1 and τ_2 represent the shorter and the longer lifetime components of the Cy3 in $SGNR_1$-SYL3C, $SGNR_2$-SYL3C and LGNR-

SYL3C nanoprobes in the closed and the opened states respectively, τ_3 being the scattering from the gold was fixed at 0.5 channel during curve fitting to eliminate the scattering contribution of the gold nanorods. Table 5.5. shows that the shorter lifetime components, τ_1 of the nanoprobes in the closed state, $SGNR_1$-SYL3C (0.54 ns), $SGNR_2$-SYL3C (0.44 ns) and LGNR-SYL3C (0.44 ns), are shorter in comparison to the shorter lifetime component of the free Cy3-SYL3C (1.07 ns) in the closed state. The decrease of the average decay time ($\bar{\tau}$) of the GNRs-SYL3C nanoprobes (1.34 ns, 1.31 ns and 1.45 ns) in comparison to that of the free Cy3-SYL3C (1.65 ns) was apparent which could be due to the strong quenching effect of the gold nanorod. Studies have shown that gold nanorods are good quenchers of fluorescence via donor-acceptor energy transfer mechanism when both the donor and acceptor are within the interaction range[25, 36-37]. This confirmed again that the Cy3-SYL3C is attached to the gold nanorods. In the opened (hybridization) state, τ_1 of the GNRs-SYL3C nanoprobes are shorter than that of the free Cy3-SYL3C (tables 5.4. and 5.5.) indicating that the Cy3 is still anchored on the GNR after hybridization[38]. Furthermore, the average lifetimes, $\bar{\tau}$ of the $SGNR_1$-SYL3C, $SGNR_2$-SYL3C and the LGNR-SYL3C nanoprobes decreased after hybridization (1.34 vs. 1.05 ns, 1.31 vs. 1.14 ns and 1.45 vs. 0.91 ns respectively). A reduction in the fluorescence decay of Cy3-ssDNA upon duplex formation was reported before[33-34]. The observed lifetime decreases observed here could be due to the reduced quantum yield of the Cy3 arising from the free rotation of the carbon-carbon bond of the polymethine chain upon duplex formation of the Cy3-SYL3C aptamer nanoprobe[32-34].

Table 5.5. The fluorescence lifetimes of the $SGNR_1$-SYL3C, $SGNR_2$-SYL3C and the LGNR-SYL3C nanoprobes.

Sample	τ_1 (ns)	B_1 (%)	τ_2 (ns)	B_2 (%)	τ_3 (ns)	B_3 (%)	$\bar{\tau}$ (ns)	$\chi 2$
$SGNR_1$-SYL3C	0.54±0.01	35.89	2.71±0.05	4.21	0.01	61.90	1.34	1.04
$SGNR_1$-SYL3C-cDNA	0.49±0.00	40.81	2.03±0.04	5.70	0.01	53.49	1.05	1.03
$SGNR_2$-SYL3C	0.44±0.01	34.08	2.08±0.03	8.32	0.01	57.60	1.31	1.06
$SGNR_2$-SYL3C-cDNA	0.44±0.01	35.97	1.94±0.03	7.16	0.01	56.87	1.14	1.02
LGNR-SYL3C	0.46±0.01	30.08	3.49±0.08	2.87	0.01	67.03	2.89	1.06
LGNR-SYL3C-cDNA	0.35±0.00	40.03	2.11±0.07	3.10	0.01	56.87	0.91	1.03

5. 3. 3. Biocompatibility of small gold nanorods aptamer nanoprobe

Cell viability was determined to evaluate the biocompatibility of the $SGNR_1$-SYL3C nanoprobe on the cells after incubation for 24 hours. The total cells (viable and dead cells) were counted and the percentage of viable cells (viable cells/total cells x 100%) was determined. Figure 5.5. displays bar chart representing the percentage of the viable cells after incubation with the $SGNR_1$-SYL3C nanoprobe and the MHA coated $SGNR_1$. The cytotoxicity effect of both the nanoprobe and the MHA coated SGNR on the viability of cells was found to be very small. It can be seen that >90% of the cells incubated with the

nanoprobe were viable after 24 hours consistent with the previous report[6]. This indicates that the $SGNR_1$-SYL3C nanoprobe is biocompatible to the cells.

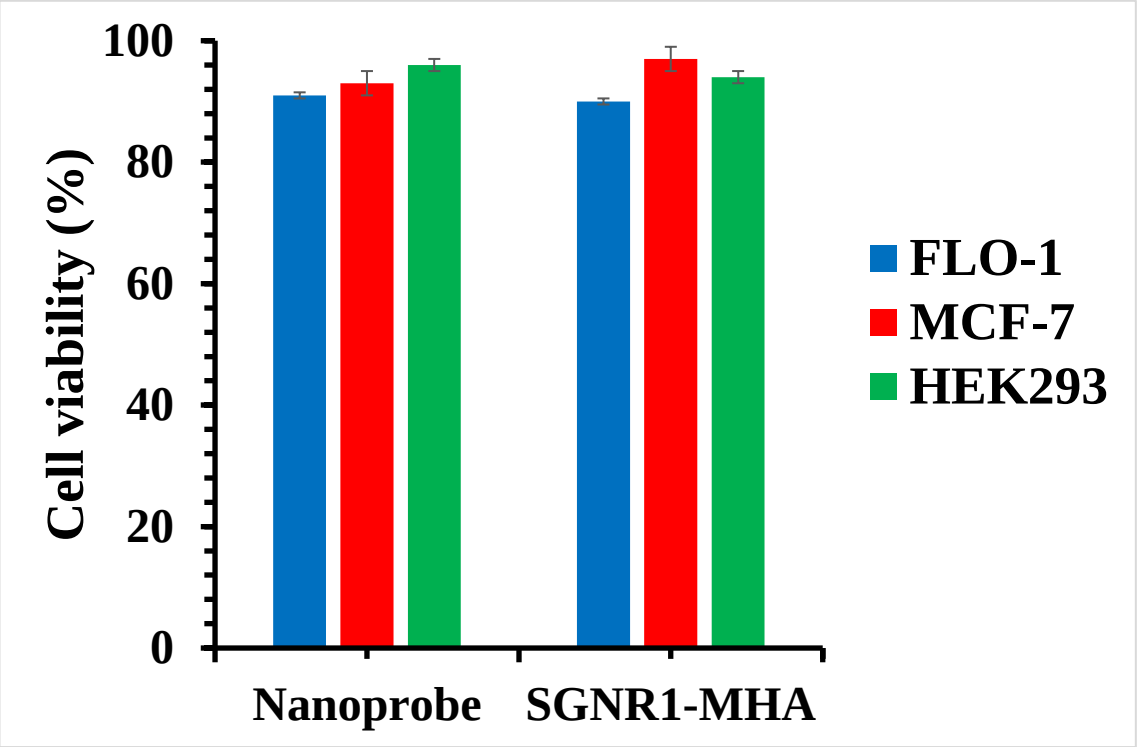

Figure 5.5. The biocompatibility of $SGNR_1$-SYL3C aptamer nanoprobe.

5. 3. 4. Targeting EpCAM expressed cancer cells with SGNR-SYL3C nanoprobes

Cancer cells co-exist with healthy cells in the living systems, thus, a targeting ligand is required to deliver therapeutic interventions to destroy specific cancer cells thereby minimizing adverse effect on the healthy cells[39]. Hence, the SGNRs were functionalized with the SYL3C to target EpCAM over-expressed cancer cells. Flow cytometry and fluorescence microscopy techniques were employed to monitor the binding and the location of the SGNR-SYL3C nanoprobes on the cancer cells. Figure 5.6. depicts the distribution of the histogram of fluorescent intensity from the 6 samples obtained from the flow cytometry. It shows that the fluorescence intensity of the PC3 treated with the nanoprobes (X-med 0.76) increased by 0.46 in comparison to 0.30 being the autofluorescence from the PC3 and the PC3 treated with the MHA-GNRs. This indicates the attachment of the nanoprobes to the PC3 cells. On the other hand, the increase of the

fluorescence intensity of the nanoprobe treated HEK293 cells is 0.24 higher than that from its two controls. The near doubled difference (0.46 vs. 0.24) in the increase of X-med from the nanoprobe treated PC3 and the HEK293 against their controls indicates a higher amount of $SGNR_2$-SYL3C nanoprobes bound to the PC3 cells. The PC3 has high expression of EpCAM[40-42] , while the HEK293 cell line is a healthy kidney cells and does not over-express EpCAM[43]. Therefore less $SGNR_2$-SYL3C nanoprobes are bound to the HEK293, hence the weak fluorescence signal from the probe treated HEK293 cells. This demonstrates the specificity of the $SGNR_2$-SYL3C nanoprobe to recognize EpCAM on the cancer cells[44].

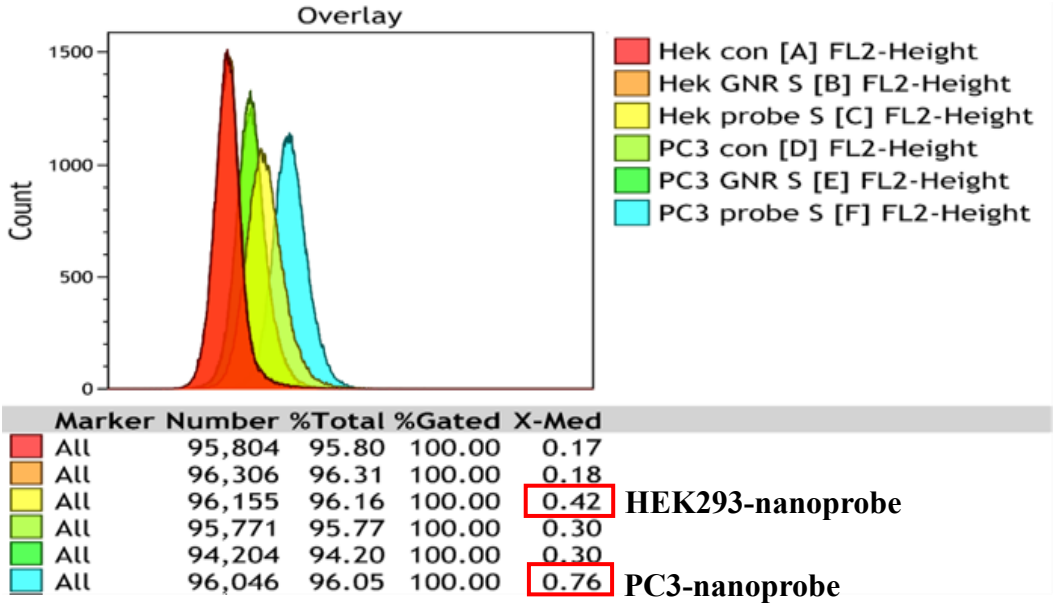

Figure 5.6. The histogram of the distribution of fluorescent intensity.

To futher understand the uptake dynamics of the $SGNR_2$-SYL3C nanoprobe by the EpCAM over-expressed cancer cells, cellular imaging and Z-stack analysis were performed on the nanoprobe treated cancer cells in comparison with the two controls. Fig. 5.7. shows the fluorescent microscopic images of the cell control (un-treated), $SGNR_2$-MHA treated cells and the nanoprobe treated cells. It can be seen that the cells treated with the $SGNR_2$-SYL3C nanoprobe display strong fluorescence signals in constrast with the weak background in the Cy3 channel observed in the control group and the small gold

nanorods treated cells. At 0.5 hours, a few bright spots correlated to the nanoprobes attached to the cancer cells as highlighted by the red circles were observed. With the increase of incubation time, more bright spots were found on the cells after incubation for 1 hour and 1.5 hours. In addition, more nanoprobes were found on the MCF-7 cancer cells than the FLO-1 cancer cells.

The weak fluorescence signal observed for the control and the small gold nanorod treated group could be due to autofluorescence from the cancer cells. However, the samples treated with the nanoprobe recorded strong fluorescent signal indicating the binding of the nanoprobe to the EpCAM over-expressed cancer cells. The increase of bright areas observed at longer incubation time suggests that more nanoprobes were attached to the cancer cells at longer incubation time [44]. The binding of the nanoprobes on the cancer cell could be as a result of the EpCAM over- expression on the membrane of cancer cells of epithelia origin as previously reported[14, 16]. The expression levels of EpCAM in the MCF-7 cancer cells is more than that in the FLO-1 cancer cells, hence, the presence of more nanoprobes on the MCF-7 than the FLO-1[15-17].

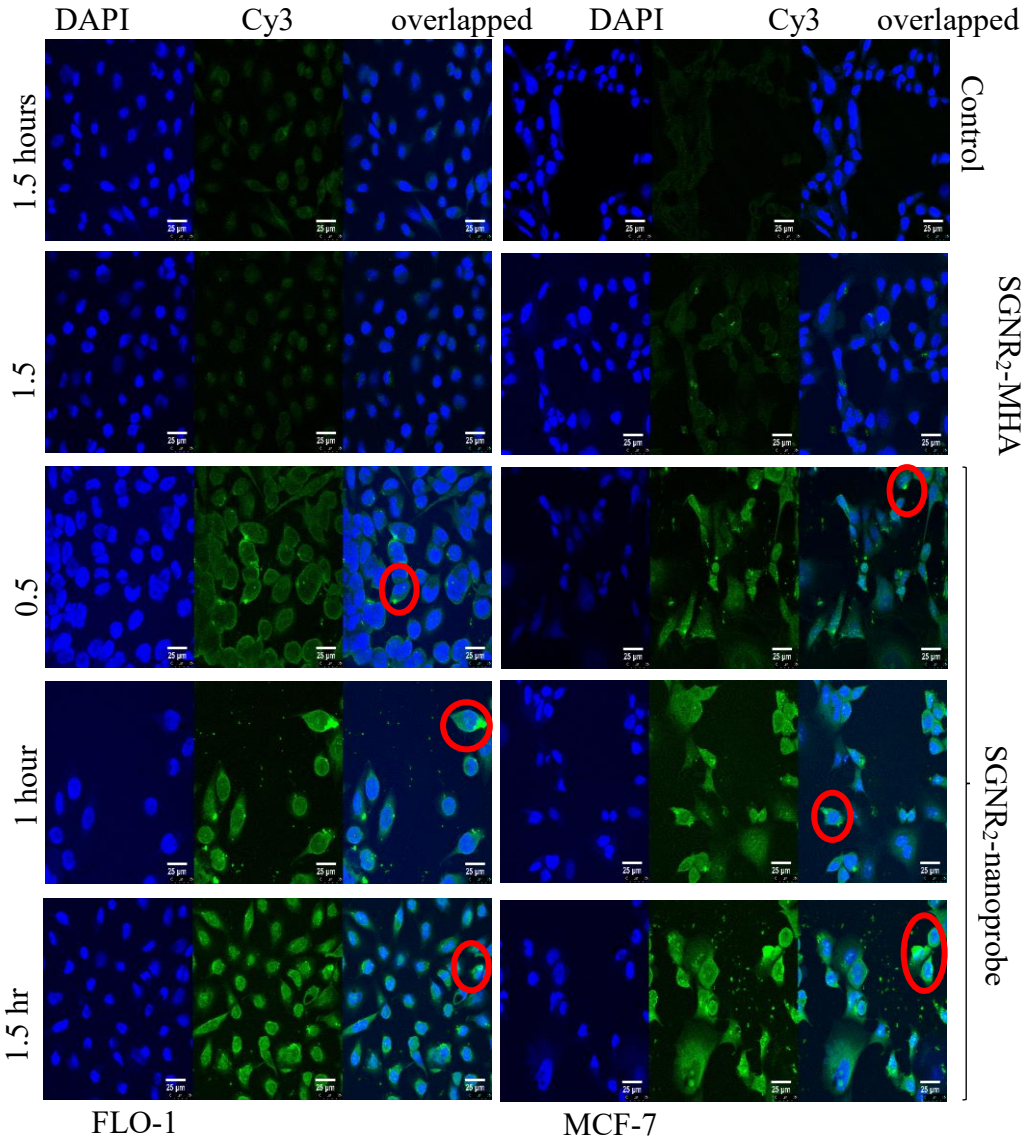

Figure 5.7. The confocal microscopic images of the FLO-1 and the MCF-7 cancer cells treated with the $SGNR_2$-SYL3C nanoprobes for 0.5 hours, 1 hour and 1.5 hours in comparsion to the cell control and the cell treated with the $SGNR_2$-MHA for 1.5 hours.

Z-stack analysis was further performed to reveal the localization of the nanoprobes on the cancer cell. The Z-stack images depicting the localization of nanoprobes on the FLO-1 and MCF-7 cancer cells are shown in fig. 5.8. The nucleus of the cells was stained in blue by DAPI while the bright green spots seen on the cell membrane signalled the

fluorescence emission from the Cy3. The z-plane scanning as indicated by the trajectory of the red arrows reveals that the nanoprobes are located on the cell membrane as expected because the receptor (EpCAM) resides on the cell membrane. The bright green spots seen could be an indication of the location of the nanoprobes on the cell membrane of FLO-1 cells and MCF-7 (fig. 5.8a-b). At half an hour, few bright green spots were seen on the cell membrane of the FLO-1 cells (fig.5.8a-b). The bright green spot increased at longer incubation time (1.5 hours) indicating that more nanoprobes got attached on the membrane at longer incubation time. In comparison, more nanoprobes were seen on the membrane of the MCF-7 cells than the FLO-1 cells at half hour (fig. 5.8a vs 5.8b).

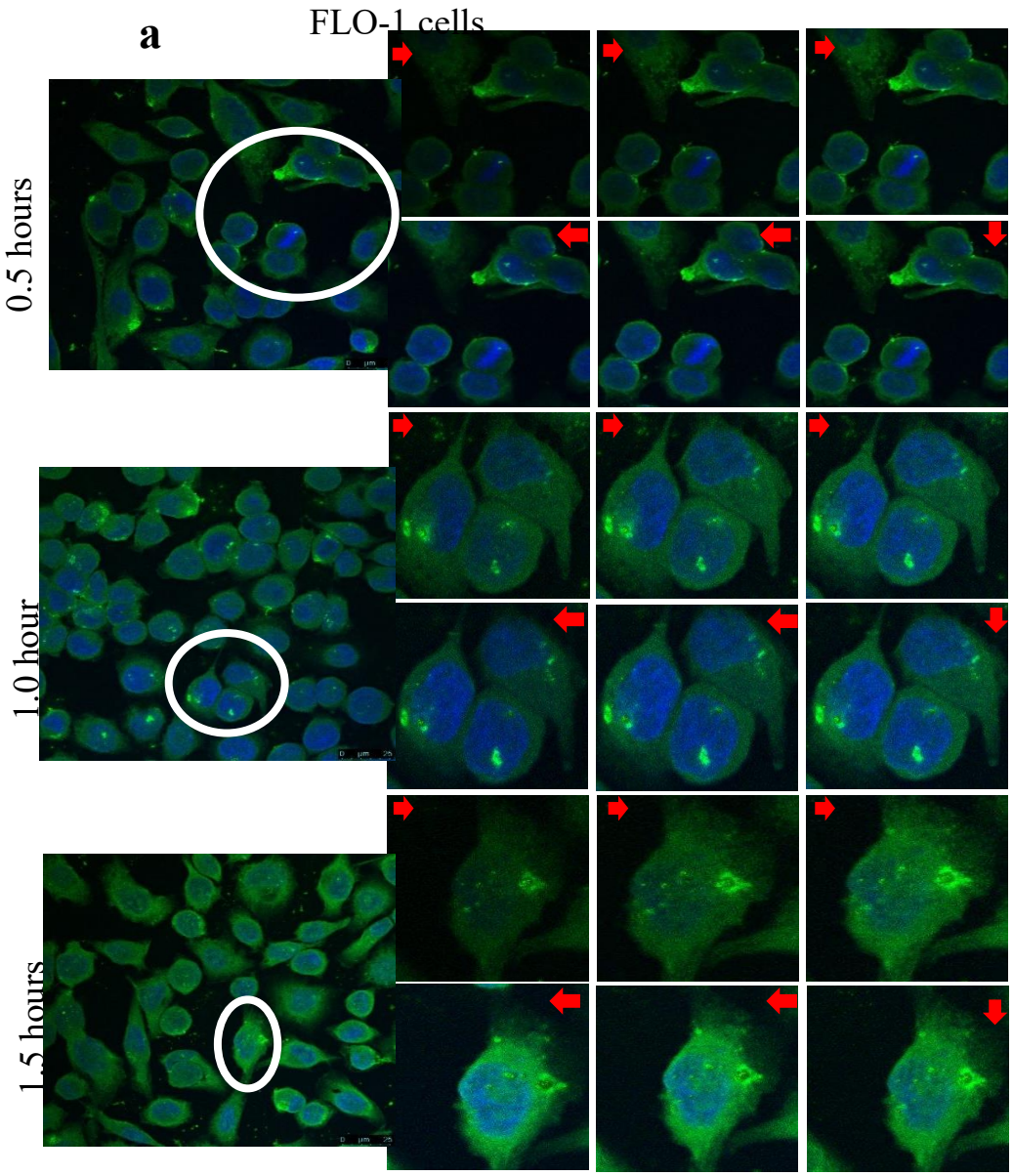

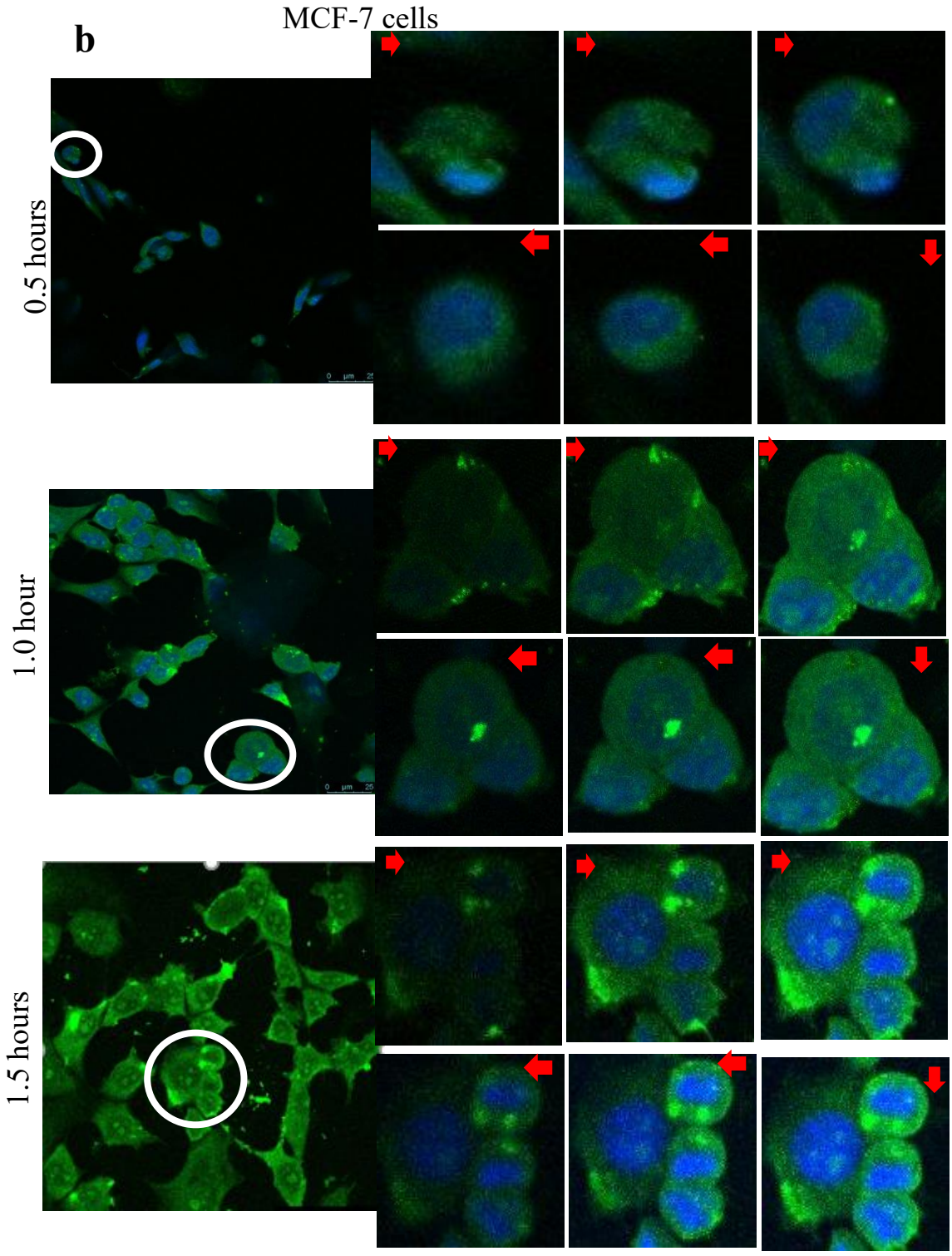

Figure 5.8. The Z-stack of the $SGNR_2$-SYL3C nanoprobe incubated with the cancer cells for 0.5 hours-1.5 hours; (a) FLO-1 cell, (b) MCF-7 cells.

5. 3. 5. Photothermal effect of the SGNR and the LGNR based SYL3C nanoprobes

The size-dependent photothermal effect of the GNRs-SYL3C nanoprobes was demonstrated by exciting the FLO-1 cells and the HEK293 cells treated with the $SGNR_1$-SYL3C and the LGNR-SYL3C nanoprobes in comparison to the two controls for 1 minute. Figure 5.9. depicts the optical images of the FLO-1 and the HEK293 cell samples illuminated at the surface plasmon resonance wavelength of the nanoprobes. More blue stained cells were observed on the nanoprobes ($SGNR_1$-SYL3C and LGNR-SYL3C) treated FLO-1 cells than the HEK293 cells (fig 5.9a-d). This indicates that more FLO-1 cells treated with the nanoprobes died in comparison to the nanoprobe treated HEK293 after exposure to the laser illumination. The FLO-1 cells treated with the $SGNR_1$-SYL3C nanoprobe died more than the FLO-1 cells treated with the LGNR-SYL3C nanoprobe as depicted by the red circles (fig. 5.9a and 5.9c). In comparison, the GNRs-MHA treated FLO-1 and HEK293 cells and the control samples displayed less blue stained cells (fig. 5.9 e-l) indicating fewer dead cells. No significant difference of the dead cells was seen for the FLO-1 cells treated with the $SGNR_1$-MHA and the LGNR-MHA respectively.

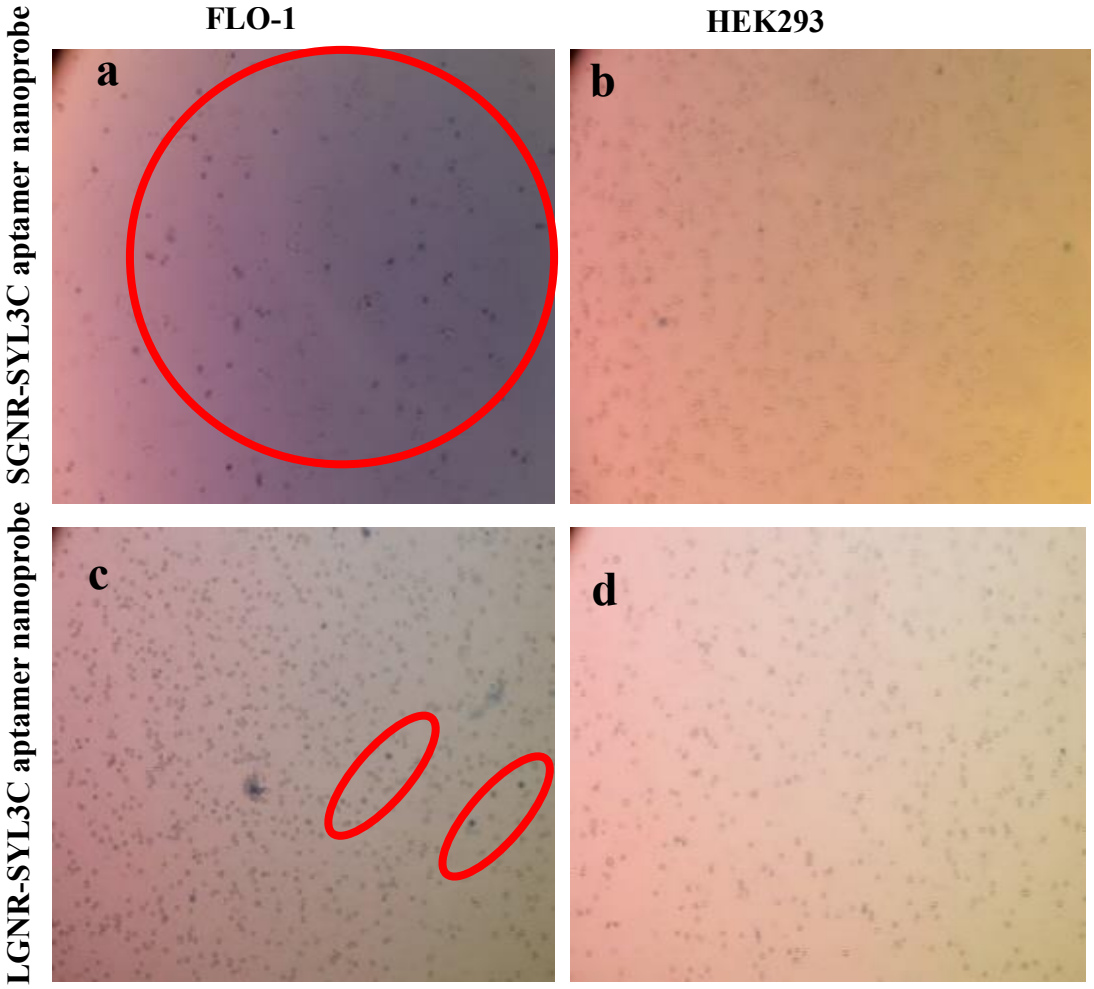
FLO-1
HEK293
SGNR-SYL3C aptamer nanoprobe
LGNR-SYL3C aptamer nanoprobe
a
b
c
d

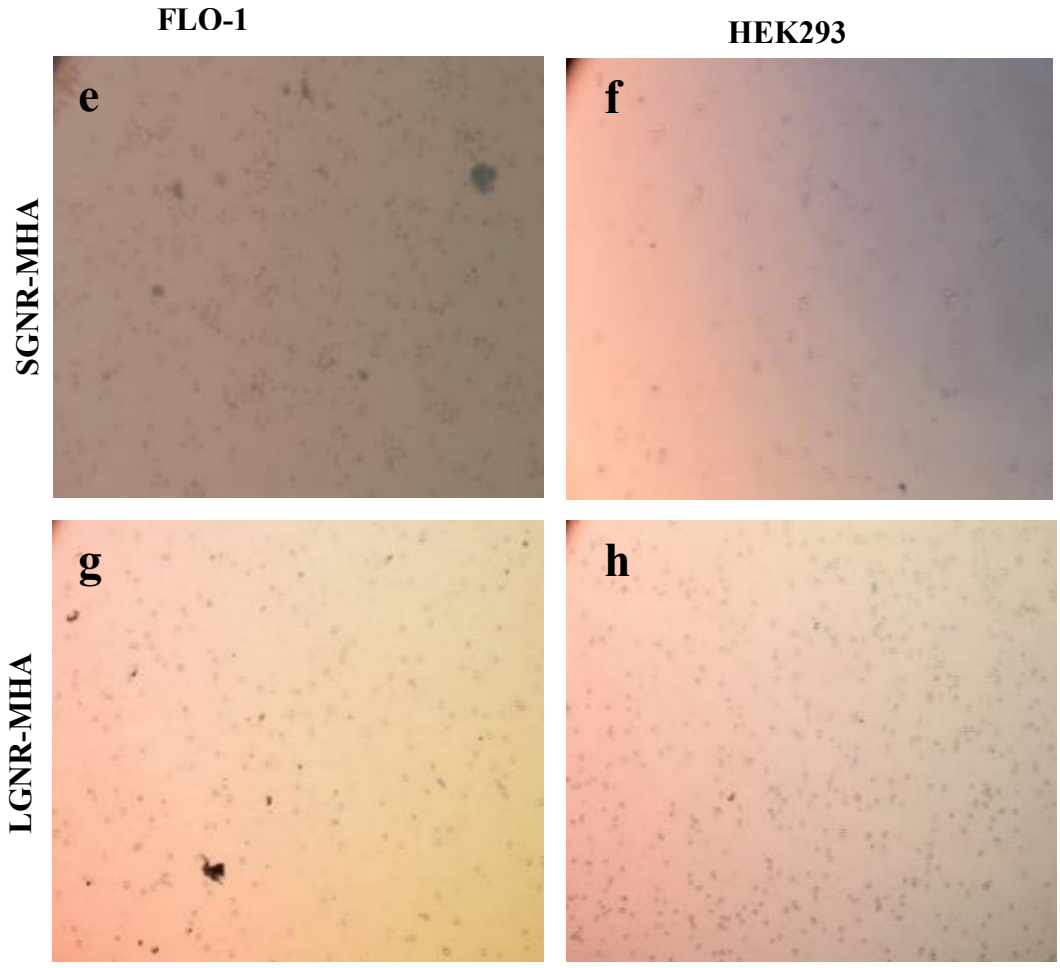
FLO-1
HEK293
SGNR-MHA
LGNR-MHA
e
f
g
h

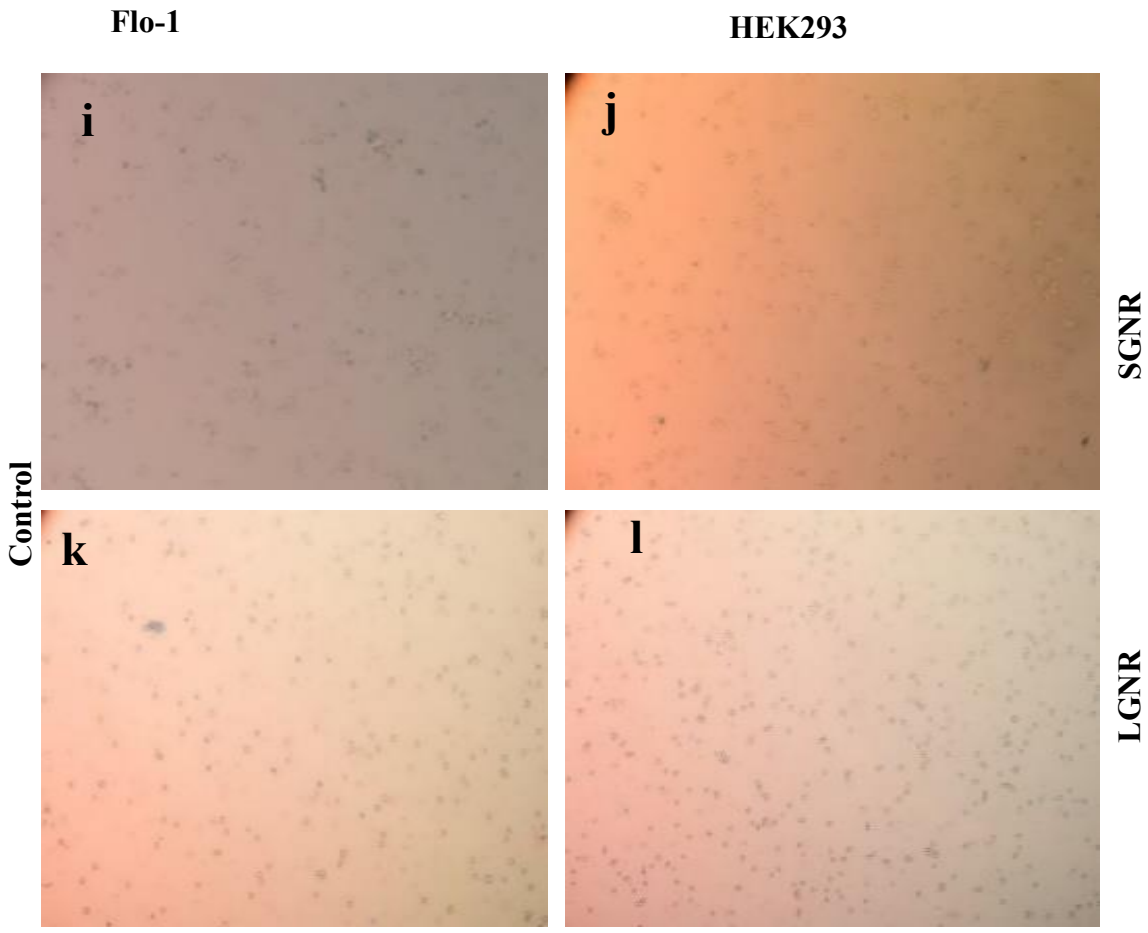

Figure 5.9. The bright field images of the cells exposed to the laser for 1 minute; (a) SGNR-SYL3C nanoprobe for FLO-1. (b) SGNR-SYL3C nanoprobe for HEK293.(c) LGNR-SYL3C nanoprobe for FLO-1. (d) LGNR-SYL3C nanoprobe for HEK293, (e) SGNR-MHA for FLO-1. (f) SGNR-MHA for HEK293. (g) LGNR-MHA for FLO-1. (h) LGNR-MHA for HEK293, (i, k) Control for FLO-1. (j, l) Control for HEK293.

Cell necrosis was determined by counting the total dead FLO-1 and HEK293 cells per a sample after the laser illumination. That is, the total cells (dead and live cells) were counted and the percentage of the dead cells (dead cells/total cells x 100%) after illumination was determined. Figure 5.10. displays the bar chart of the cell necrosis for photo-excited treated cell samples. This shows that the illuminated FLO-1 cells treated with the $SGNR_1$-SYL3C and the LGNR-SYL3C nanoprobes have 27% and 9% dead cells respectively, higher than 12% and 7 % dead cells of the illuminated FLO-1 cells

treated with the $SGNR_1$-MHA and the LGNR-MHA, while the illuminated control FLO-1 cell sample was 2% dead. Illuminated HEK293 cells treated with the $SGNR_1$-SYL3C and the LGNR-SYL3C nanoprobes have 4% and 1% dead cells, while the illuminated HEK293 cells treated with the $SGNR_1$-MHA and the LGNR-MHA have 3% and 4% dead cells respectively. The illuminated control HEK293 cell sample has 1% dead cells. Thus, it is evident that the GNRs-SYL3C nanoprobes treatment induced more dead FLO-1cells than the GNRs-MHA (without SYL3C) and the un-treated cells after laser illumination. Significantly, the $SGNR_1$-SYL3C nanoprobe induced more than double dead cells in comparison to the cell line treated with the same GNRs without aptamer functionalization and more than 13 times in comparison to the cell line without nanoprobes. In addition, the FLO-1 cells treated with the same laser illuminated GNRs-SYL3C nanoprobes died more than the HEK293 cells with similar treatment. This is because the GNRs-SYL3C nanoprobes have higher binding affinity and specificity for the EpCAM over-expressed cancer cells[1-2, 45] and better targeting abilities than the GNRs-MHA[24], therefore more SYL3C nanoprobes bind to the FLO-1 cell membrane than the HEK293 (negative to EpCAM) cells[43], manifesting the benefit of targeted nanoprobes in the photothermal therapy of cancer. Moreover, the FLO-1 cells treated with the $SGNR_1$-SYL3C nanoprobe died 3x more in comparison to the same cells treated with the LGNR-SYL3C nanoprobe; similarly more FLO-1 cells treated with the $SGNR_1$-MHA died than the FLO-1 cells treated with the LGNR-MHA after the laser illumination (fig 5.10a-b). This is not surprising as our previous study revealed that the SGNRs generate more heat energy than the LGNRs at the surface plasmon resonance excitation (fig.4.9., chapter 4).

These results demonstrate the specificity of the GNRs-SYL3C nanoprobes for targeting EpCAM over-expression in the cancer cells and the efficacy of the nanoprobes for photothermal therapy of cancer. Furthermore, the $SGNR_1$-SYL3C nanoprobes have shown superior photothermal effect compared to the LGNR-SYL3C nanoprobes.

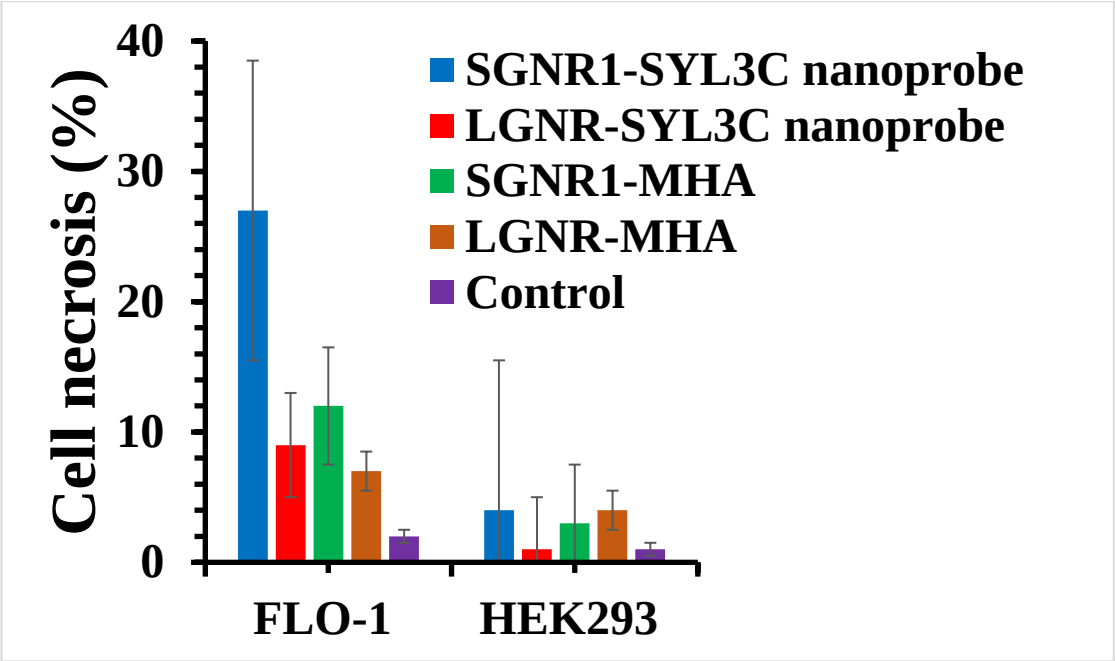

Figure 5.10. The histogram of cell necrosis for laser exposed FLO-1 and HEK293.

5. 4. Conclusion

In conclusion, this study has successfully synthesized and functionalized SGNRs-SYL3C nanoprobes for targeting EpCAM over-expressed cancer cells. The SGNRs-SYL3C nanoprobes have shown low toxicity effect on the viability of cells. It is found that the SGNRs-SYL3C nanoprobes binds specifically on the membrane of the FLO-1 and the MCF-7 cells with EpCAM over-expression. GNRs-SYL3C nanoprobes induce higher death rate on the FLO-1 cells than the GNRs without targeting ligand and the death rate of the FLO-1 cells treated with the SGNR-nanoprobe is higher than that of the FLO-1 cells treated with the LGNR. This demonstrates an enhanced efficacy of the GNRs-SYL3C nanoprobes in the photothermal therapy resulting from an increased affinity to EpCAM expressed cancer cells and the enhanced photothermal effect of the SGNRs. These findings may guide researchers in the design of gold nanorods nanoprobes with superior photothermal effect for photothermal therapy of cancer.

References

1. Song, Y.; Zhu, Z.; An, Y.; Zhang, W.; Zhang, H.; Liu, D.; Yu, C.; Duan, W.; Yang, C. J., Selection of DNA aptamers against epithelial cell adhesion molecule for cancer cell imaging and circulating tumor cell capture. *Anal. Chem.* **2013,** *85*, 4141-4149.
2. Minhee, K.; Kim, D.; Kim, K.; Jung, W.; Kim, D., Applications of cancer cell-specific aptamers in targeted delivery of anticancer therapeutic agents. *Molecules* **2018,** *23* (4), 830-849.
3. Shamaila, S.; Zafar, N.; Riaz, S.; Sharif, R.; Nazir, J.; Naseem, S., Gold nanoparticles: an efficient antimicrobial agent against enteric bacterial human pathogen *Nanomaterials* **2016,** *6* (4), 71-80.
4. Warrier, P.; Yuan, Y.; Beck, M. P.; Teja, A. S., Heat transfer in nanoparticle suspensions: modeling the thermal conductivity of nanofluids. *AIChE Journal* **2010,** *56* (12), 3243-3256.
5. An, L.; Wang, Y.; Tian, Q.; Yang, S., Small gold nanorods: recent advances in synthesis, biological imaging, and cancer therapy. *Materials* **2017,** *10* (12), 1372-1392.
6. Jia, H.; Fang, C.; Zhu, X. M.; Ruan, Q.; Wang, Y. X.; Wang, J., Synthesis of absorption-dominant small gold nanorods and their plasmonic properties. *Langmuir* **2015,** *31* (26), 7418-7426.
7. Huang, X.; El-Sayed, M. A., Plasmonic photo-thermal therapy (PPTT). *Alexandria Journal of Medicine* **2011,** *47* (1), 1-9.
8. Tauber, R.; Reuter, W.; Gerok, W., Role of membrane glycoproteins in mediating trophic responses. *Gut* **1987,** *28* (S1), 71-77.
9. Quick, M.; Javitch, J. A., Monitoring the function of membrane transport proteins in detergent-solubilized form. *Proceedings of the National Academy of Sciences* **2007,** *104* (9), 3603-3608.
10. Wang, N.; Liu, H.; Hao, J.; Bai, X.; Li, H.; Zhang, Z.; Wanga, H.; Tang, J., Single molecular recognition force spectroscopy study of a DNA aptamer with the target epithelial cell adhesion molecule. *Analyst* **2015,** *140*, 6226-6229.
11. Amaya-Gonzalez, S.; Ide-los-Santos-Alvarez, N.; Miranda-Ordieres, A. J.; Lobo-Castanon, M. J., Aptamer-based analysis: a promising alternativefor food safety control. *Sensors* **2013,** *13*, 16292-16311.

12. Wang, Y.; Li, J.; Qiao, P.; Jing, L.; Song, Y.; Zhang, J.; Chen, Q.; Han, Q., Screening and application of a new aptamer for the rapid detection of Sudan dye lll. *European Journal of Lipid Science and Technology* **2018,** *120*, 1700112-1700118.

13. Pu, Y.; Liu, Z.; Lu, Y.; Yuan, P.; Liu, J.; Yu, B.; Wang, G.; Yang, C. J.; Liu, H.; Tan, W., Using DNA aptamer probe for immunostaining of cancer frozen tissues. *Analytical Chemistry* **2015,** *87* (3), 1919-1924.

14. Munz, M.; Baeuerle, P. A.; Gires, O., The emerging role of EpCAM in cancer and stem cell signaling. *Cancer Res.* **2009,** *69* (14), 5627-5629.

15. Zheng, T.; Zhang, Q.; Feng, S.; Zhu, J.-J.; Wang, Q.; Wang, H., Robust non-enzymatic hybrid nanoelectrocatalysts for signal amplification toward ultrasensitive electrochemical cytosensing. *Journal of the American Chemical Society* **2014,** *136* (6), 2288-2291.

16. Garcia, E.; Hayden, A.; Birts, C.; Britton, E.; Cowie, A.; Pickard, K.; Mellone, M.; Choh, C.; Derouet, M.; Duriez, P.; Noble, F.; White, M. J.; Primrose, J. N.; Strefford, J. C.; Rose-Zerilli, M.; Thomas, G. J.; Ang, Y.; Sharrocks, A. D.; Fitzgerald, R. C.; Underwood, T. J.; consortium, O.; MacRae, S.; Grehan, N.; Abdullahi, Z.; de la Rue, R.; Noorani, A.; Elliott, R. F.; de Silva, N.; Bornschein, J.; O'Donovan, M.; Contino, G.; Yang, T.-P.; Chettouh, H.; Crawte, J.; Nutzinger, B.; Edwards, P. A. W.; Smith, L.; Miremadi, A.; Malhotra, S.; Cluroe, A.; Hardwick, R.; Davies, J.; Ford, H.; Gilligan, D.; Safranek, P.; Hindmarsh, A.; Sujendran, V.; Carroll, N.; Turkington, R.; Hayes, S. J.; Ang, Y.; Preston, S. R.; Oakes, S.; Bagwan, I.; Save, V.; Skipworth, R. J. E.; Hupp, T. R.; O'Neill, J. R.; Tucker, O.; Taniere, P.; Owsley, J.; Crichton, C.; Schusterreiter, C.; Barr, H.; Shepherd, N.; Old, O.; Lagergren, J.; Gossage, J.; Davies, A.; Chang, F.; Zylstra, J.; Sanders, G.; Berrisford, R.; Harden, C.; Bunting, D.; Lewis, M.; Cheong, E.; Kumar, B.; Parsons, S. L.; Soomro, I.; Kaye, P.; Saunders, J.; Lovat, L.; Haidry, R.; Eneh, V.; Igali, L.; Welch, I.; Scott, M.; Sothi, S.; Suortamo, S.; Lishman, S.; Beardsmore, D.; Anderson, C.; Smith, M. L.; Secrier, M.; Eldridge, M. D.; Bower, L.; Achilleos, A.; Lynch, A. G.; Tavare, S., Authentication and characterisation of a new oesophageal adenocarcinoma cell line: MFD-1. *Scientific Reports* **2016,** *6*, 32417-32429.

17. Chen, Y.; Cheng, B.; He, Z.; Wang, S.; Wang, Z.; Sun, M.; Song, H.; Fang, Y.; Chen, F.; Xiong, B., Capture and identification of heterogeneous circulating tumor cells

using transparent nanomaterials and quantum dots-based multiplexed imaging. *Journal of Cancer* **2016,** *7* (1), 69-79.

18. Lai, X.; Zou, Y.; Wang, S.; Zheng, M.; Hu, X.; Liang, H. Y.; Wang, X.; Ding, D.; Chen, L.; Chen, Z.; Tan, W., Modulating the morphology of gold graphitic nanocapsules for plasmon resonance-enhanced multimodal imaging. *Anal. Chem.* **2016,** *88*, 5385−5391.

19. Song, Y.; Shi, Y.; Huang, M.; Wang, W.; Wang, Y.; Cheng, J.; Lei, Z.; Zhu, Z.; Yang, C., Bioinspired engineering of a multivalent aptamer-functionalized nanointerface to enhance the capture and release of circulating tumor cells. *Angew. Chem. Int. Ed.* **2019,** *58*, 2236-2240.

20. Liu, Z.; Lu, Y.; Pu, Y.; Liu, J.; Liu, B.; Yu, B.; Chen, K.; Fu, T.; Yang, C. J.; Liu, H.; Tan, W., Using aptamers to elucidate esophageal cancer clinical samples. *Science Reports* **2015,** *5* 18516-18524.

21. Manivasagan, P.; Hoang, G.; Moorthy, M. S.; Mondal, S.; Doan, V. H. M.; Kim, H.; Phan, T. T. V.; P, N. T.; Oh, J., Chitosan/fucoidan multilayer coating of gold nanorods as highly efficient near infrared photothermal agents for cancer therapy. *Carbohydrate Polymers* **2019,** *211*, 360-369.

22. Bucharskaya, A. B.; Maslyakova, G. N.; Chekhonatskaya, M. L.; Terentyuk, G. S.; Navolokin, N. A.; Khlebtsov, B. N.; Khlebtsov, N. G.; Bashkatov, A. N.; Genina, E. A.; Tuchi, V. V., Plasmonic photothermal therapy: approaches to advanced strategy. *Lasers in Surgery and Medicine* **2018,** *50*, 1025-1033.

23. Turcheniuk, K.; Dumych, T.; Bilyy, R.; Turcheniuk, V.; Bouckaert, J.; Vovk, V.; Chopyak, V.; Zaitsev, V.; Mariot, P.; Prevarskaya, N.; Boukherroub, R.; Szunerits, S., Plasmonic photothermal cancer therapy with gold nanorods/reduced graphene oxide core/shell nanocomposite. *RSC Adv.* **2016,** *6*, 1600-1610.

24. Yang , H.; Chen , Z.; Zhang , L.; Yung , W.-Y.; Leung , K. C.-F.; Chan , H. Y. E.; Choi , C. H. J., Mechanism for the cellular uptake of targeted gold nanorods of defined aspect ratios. *small* **2016,** *12* (37), 5178-5189.

25. Wei, G.; Yu, J.; Wang, J.; Gu, P.; Birch, D. J. S.; Chen, Y., Hairpin DNA functionalized gold nanorods for mRNA detection in homogenous solution *J. Biomed. Opt.* **2016,** *21* (9), 097001-097009.

26. Mbalaha, Z. S.; Edwards, P. R.; Birch, D. J. S.; Chen, Y., Synthesis of small gold nanorods and their subsequent functionalization with hairpin single stranded DNA. *ACS Omega* **2019,** *4* (9), 13740-13746.

27. Wijaya, A.; Hamad-Schifferli, K., Ligand customization and DNA functionalization of gold nanorods via round-trip phase transfer ligand exchange. *Langmuir* **2008,** *24*, 9966-9969.

28. Gans, R., Über die Form ultramikroskopischer Goldteilchen. *Ann. Phys.* **1912,** *342* (5), 881-900.

29. Link, S.; Mohamed, M. B.; El-Sayed, M. A., Addition and correction. *J. Phys. Chem. B* **2005,** *109* (20), 10531-10532.

30. Shi, W.; Casas, J.; Venkataramasubramani, M.; Tang, L., Synthesis and characterization of gold nanoparticles with plasmon absorbance wavelength tunable from visible to near infrared region. *ISRN Nanomaterials* **2012,** *2012*, 659043-659052.

31. Sharma, V.; Park, K.; Srinivasarao, M., Shape separation of gold nanorods using centrifugation. *Proceedings of the National Academy of Sciences* **2009,** *106* (13), 4981-4985.

32. Muddana, H. S.; Morgan, T. T.; Adair, J. H.; Butler, P. J., Photophysics of Cy3-encapsulated calcium phosphate nanoparticles. *Nano Lett.* **2009,** *9* (4), 1559-1566.

33. Sanborn, M. E.; Connolly, B. K.; Gurunathan, K.; Levitu, M., Fluorescence properties and photophysics of the sulfoindocyanine Cy3 linked covalently to DNA. *J. Phys. Chem. B* **2007,** *111*, 11064-11074.

34. Spiriti, J.; Binder, J. K.; Levitus, M.; Vaart, A., Cy3-DNA stacking interactions strongly depend on the identity of the terminal basepair. *Biophysical Journal* **2011,** *100* (4), 1049-1057.

35. Lakowicz, J. R., *Principles of Fluorescence Spectroscopy*. 3rd ed.; Springer: New York, 2006.

36. Racknor, C.; Singh, M. R.; Zhang, Y.; Birch, D. J. S.; Chen, Y., Energy transfer between a biological labelling dye and gold nanorods. *Methods and Applications in Fluorescence* **2014,** *2*, 015002-015008.

37. Zhang, Y.; Wei, G.; Yu, J.; Birch, D. J. S.; Chen, Y., Surface plasmon enhanced energy transfer between gold nanorods and fluorophores: application to endocytosis study and RNA detection. *Faraday Discuss* **2015,** *178*, 383-394.

38. Wei, G.; Simionesie, D.; Sefcik, J.; Sutter, J. U.; Xue, Q.; Yu, J.; Wang, J.; Birch, D. J. S.; Chen, Y., Revealing the photophysics of gold-nanobeacons via time-resolved fluorescence spectroscopy. *Opt Lett* **2015,** *40* (24), 5738-5741.

39. National Cancer Institute, Targeted therapy to treat cancer. National Cancer Institute: 2020.

40. Massoner, P.; Thomm, T.; Mack, B.; Untergasser, G.; Martowicz, A.; Bobowski, K.; Klocker, H.; Gires, O.; Puhr, M., EpCAM is overexpressed in local and metastatic prostate cancer, suppressed by chemotherapy and modulated by MET-associated miRNA-200c/205. *Br J Cancer* **2014,** *111* (5), 955-964.

41. Ni, J.; Cozzi, P.; Beretov, J.; Duan, W.; Bucci, J.; Graham, P.; Li, Y., Epithelial cell adhesion molecule (EpCAM) is involved in prostate cancer chemotherapy/radiotherapy response in vivo. *BMC Cancer* **2018,** *18* (1), 1092-1104.

42. de Wit, S.; Manicone, M.; Rossi, E.; Lampignano, R.; Yang, L.; Zill, B.; Rengel-Puertas, A.; Ouhlen, M.; Crespo, M.; Berghuis, A. M. S.; Andree, K. C.; Vidotto, R.; Trapp, E. K.; Tzschaschel, M.; Colomba, E.; Fowler, G.; Flohr, P.; Rescigno, P.; Fontes, M. S.; Zamarchi, R.; Fehm, T.; Neubauer, H.; Rack, B.; Alunni-Fabbroni, M.; Farace, F.; De Bono, J.; Ijzerman, M. J.; Terstappen, L. W. M. M., EpCAM(high) and EpCAM (low) circulating tumor cells in metastatic prostate and breast cancer patients. *Oncotarget* **2018,** *9* (86), 35705-35716.

43. Tretter, J. Y.; Schorpp, K.; Luxenburger, E.; Trambauer, J.; Steiner, H.; Hadian, X. K.; Gires, O.; Niessing, X. D., A high-content screen for small-molecule regulators of epithelial cell-adhesion molecule (EpCAM) cleavage yields a robust inhibitor. *J. Biol. Chem.* **2018,** *293* (23), 8994-9005.

44. Wang, J.; Zhu, G.; You, M.; Song, E.; Shukoor, M. I.; Zhang, K.; Altman, M. B.; Chen, Y.; Zhu, Z.; Huang, C. Z.; Tan, W., Assembly of aptamer switch probes and photosensitizer on gold nanorods for targeted photothermal and photodynamic cancer therapy. *ACS Nano* **2012,** *6* (6), 5070-5077.

45. Li, Z.; Tang, S.; Wang, B.; Li, Y.; Huang, H.; Wang, H.; Li, P.; Li, C.; Chu, P. K.; Yu, X.-F., Metabolizable small gold nanorods: size-dependent cytotoxicity, cell uptake and *in vivo* biodistribution. *ACS Biomaterials Science & Engineering* **2016,** *2* (5), 789-797.

Chapter 6

Detection of RNA biomarkers in biological systems with the small gold nanorod based nanoprobes

6. 1. Introduction

Prostate cancer is one of the leading causes of mortality among men globally[1-2]. Prostate cancer occurs in many forms and this include prostate adenocarcinomas, small cell carcinomas, sarcomas, transitional cell carcinomas and neuroendocrine prostate cancer[3]. Neuroendocrine prostate cancer (NEPC) evolves from prostate adenocarcinoma[4]. NEPC is considered as a big threat to men's health because it is resistant to hormonal therapies[2]. In addition, the current screening methods for prostate cancer are androgen receptor (AR) and prostate specific antigen (PSA) testing[5]. Prostate specific antigen testing for example, lacks the specificity and sensitivity to detect early stage of prostate cancer[6]. Moreover, NEPC does not express neither androgen receptor nor prostate specific antigen biomakers[7-9], making the diagnosis of NEPC very challenging. Furthermore, both normal cells and prostate cancer cells express PSA; and an elevated PSA level does not necessarily implicate prostate cancer[10]. For example, benign prostate hyperplasia, prostatisis or urinary tract infection could induce elevated PSA levels[11-12]. Moreover, PSA test is susceptible to false positive or false negative result[11]. This obligates the use of other tests (e.g. trans rectal ultrasound, x-ray and cystoscopy) to make informed prognosis[13]. The delay in conducting further tests to establish a prima facie of prostate cancer could exacerbate the morbidity of the patient leading to death. Hence, the need for new techniques to enable sensitive and facile detection of cancer biomarkers for early diagnosis of NEPC.

It has been reported that cancer cells secrete substantial amount of exosomes at the early stage of cancer development[14]. Therefore, exosomes can be harnessed as potential biomarkers for early diagnosis of NEPC because the exosomes exhibit biological characteristics reminiscent of their originating parent cell[15-16]. Exosomes are nanoscale extracellular vesicles released by the living systems[17]. Exosomes occur in abundance in cells and other biological fluids such as saliva, urine and blood alongside other

extracellular vesicles[16-22]. Exosomes can be 30-200 nm in diameter and are composed of proteins, mRNA, microRNA (miRNA) and lipids[15, 22-23]. Exosomes facilitate intercellular communication[24], exosomes contain proteins and nucleic acids[15] and can be used as nano-vectors for delivery of therapeutic agents. Compared to the circulating tumour cells, exosomes occur in abundance in serum, are very stable and can penetrate the blood-brain barrier[22]. In addition, cellular biomarkers could be characterised by bio-molecular impurities that may affect the sensitivity of nanoprobes[17]. However, cell derived exosomes can be purified to enhance the sensitivity and specificity of nanoprobes in targeting applications. These biophysical features make exosomes interesting scaffolds for biomedical sensing applications.

Jiang et al. have demonstrated that gold nanocluster-carbon dot nanoprobes assembled on the cancer derived exosomes can be used to track the intracellular distribution of the exosomes via the fluorescence signal of the labeled exosomes internalized by the cells[15]. Zhang et al. have shown that the gold nanospheres coupled to the exosomes enhanced the Raman scattering signal of cancer derived exosomes in discriminating cancer cells from the healthy cells[16]. This approach was used to classified exosomes derived from different cancer cells. Shao et al. utilized magnetic microbeads in capturing glioblastoma multiforme derived exosomes to analyse the mRNA levels of the exosomes[22]. The study found that analysing the mRNA level of cancer exosomes could be a promising approach for monitoring cancer patients' response to drugs therapy.

Blood serum offers another opportunity for early diagnosis of cancer biomakers because cancer cells release enzymes and exosomes into the blood stream[25]. Blood serum could be defined as a yellow fluid derived from blood after coagulation. Uludag et al. utilized antibody functionalized gold nanospheres to detect the concentration of PSA in the human serum for diagnosis of prostate cancer[26]. Choi et al. demonstrated that fluorescein isothiocyanate (FITC)/peptide-conjugated gold nanoparticle biosensor amplifies fluorescence signal upon addition of PSA[27]. An aptasensor based on DNA aptamer functionalized gold nanosphere adsorb on the gold planer surface detected the level of PSA in the human serum[28]. Ageing and urinary tract infections could induce high PSA level in human beings; however, these may not necessarily implicate prostate cancer

infection[11-12], hence, the need for alternative biomarkers with high specificity for detecting prostate cancers.

In comparison to the gold nanospheres, the longitudinal surface plasmon resonance (LSPR) of the SGNRs can be tuned to the near infrared region where biological tissue transmission is very high, making the SGNRs suitable for deep tissue applications[29]. Moreover, the LSPR of SGNRs between 650 nm and700 nm overlaps the emission of organic dyes such as cyanine 5 and 5.5 (Cy5 and Cy5.5). Thus, the fluorescence emission intensities of Cy5 on the SGNR nanoprobes with LSPR in this range (650 nm-700 nm) could be enhanced when the dyes are in an optimal distance from the gold surface in the hybridization state[30-31]. Furthermore, overlapping the LSPR of the GNR with the absorption of Cy5 enhances energy transfer between the Cy5 and the GNRs when the nanoprobes are in their initial closed states. These features are capable of amplifying signal/background ratio of the SGNR nanoprobes. In addition, it has been found that more targets bind to the small nanoparticles than the large size nanoparticles because the small size nanoparticles have larger surface area to volume ratio[29]. Thus, the SGNR nanoprobes are expected to yield higher sensitivity than the large gold nanorods (LGNR) nanoprobes in detecting RNA biomarkers. Previously, the gold nanorods nanoprobes have been utilized in detecting c-myc in the messenger RNA (mRNA)[30, 32]. A c-myc gene is an oncogene encoded in the mRNA from a DNA molecule and it is reported to be over-expressed in prostrate cancers[5, 33]. A mRNA is transcribed from the DNA in the cell nucleus and transported to the ribosome in the cell cytoplasm where it is translated for the synthesis of protein [34]. Recently, Mather et al. identified the neuroendocrine long non-coding RNA (NEAR1) that is expressed in the prostate cancer cell line (PC3)[35]. Targeting the NEAR1 biomaker with the gold nanorod nanoprobe could be an alternative approach for early diagnosis of the NEPC. Hence, the functionalization of the SGNR with the targeting ligands to enhance the sensitivity and specificity of the gold nanoprobes for early diagnosis of NEPC.

This chapter focuses on developing the GNR based nanoprobes for detecting the RNA biomarkers in the prostate cancer cells, cellular exosomes and the blood serum. The SGNR and the LGNR nanoprobes were functionalized with the c-myc-Cy5-hpDNA and

the LINC261-Cy5-hpDNA for targeting the mRNA and the NEAR1 in the cancer cells, cancer derived exosomes and the blood serum.

6. 2. Experimental section

6. 2. 1. Materials

All chemicals were used as received without further purification. Chloroauric acid ($HAuCl_4$, 49%), Hexadecyltrimethylammonium bromide (CTAB, 99%), Ascorbic acid (AA), Sodium borohydride ($NaBH_4$, 99.8%), Silver nitrate ($AgNO_3$), Dodecanethiol (DDT, 98%), Mercaptohexanoic acid (MHA, 99.8%), Acetone (99.9%), Isopropanol (99.5%), Toluene (99.8%) and methanol were purchased from Sigma Aldrich while hydrochloric acid (HCL) was purchased from Fluka. Blood sera of prostate cancer infected mouse and healthy mouse were provided by Dr Francesco Crea, School of Life and Health and Chemical Sciences, The Open University.

LINC261-Cy5-hpDNA:

5'-/5Cy5/CTGACTTGGCTGTTGGTCTATTGGTTCACAAGTCAGAA/3THIOMC3-D/-3'

cDNA: 5'-TGAACCAATAGACCAACAGC-3'. The LINC261-hpDNA and the cDNA were purchased from Integrated DNA Technologies (IDT).

C-myc-Cy5-hpDNA:

5'-Cy5-CTGACTTGGTGAAGCTAACGTTGAGCAAGTCAG-AA-$(CH_2)_6$-HS-3'

cDNA: 5'- CCT CAA CGT TAG CTT CAC CAA- 3'. The C-myc-hpDNA and the cDNA were purchased from Sigma Aldrich.

6. 2. 2. Synthesis of gold nanorods

Two large gold nanorods ($LGNR_1$ and $LGNR_2$) and small gold nanorods (SGNRs) were synthesised by a similar protocol of silver assisted seed mediated growth method as reported in section 3. 2. 2 of chapter 3. The gold nanorods were centrifuged at 13000 rpm

for 15 minutes and re-suspended in 2 ml of distilled water in a conventional plastic cuvette (1 cm path length) for UV-vis extinction measurement. The reagents for the synthesis of LGNRs and SGNRs are presented in table 6.1. and 6.2. respectively.

Table 6.1. The list of reagents used to prepare the seeds and the growth solutions of the LGNRs ($LGNR_1$ and $LGNR_2$).

Reagents		$HAuCl_4$ (0.001M; ml)	CTAB (0.2M; ml)	$NaBH_4$ (0.01M; ml)	$AgNO_3$ (0.004M; ml)	A.A (0.0778M; ml)	Seeds (ml)
Seeds solution		2.50	7.50	0.60	-	-	-
Growth solution	$LGNR_1$	100.00	100.00	-	1.400	1.400	0.20
	$LGNR_2$	10.00	10.00	-	0.135	0.14	0.02

Table 6. 2. The list of reagents used to prepare the seeds and the growth solutions of the SGNR.

Reagents	$HAuCl_4$ (0.01M; ml)	CTAB (0.1M; ml)	$NaBH_4$ (0.01M; ml)	$AgNO_3$ (0.01M; ml)	HCl (1.0M; ml)	A.A (0.1M; ml)	Seeds (ml)
Seeds solution	0.25	9.75	0.60	-	-	-	-
Growth solution	0.50	9.00	-	0.04	0.20	0.08	1.00

6. 2. 3. Ligand exchange and functionalization of gold nanorods

Ligand exchange and functionalization were performed as reported in section 3. 2. 3 of chapter 3.

6. 2. 4. Preparation of samples for flow cytometry measurements

A prostate cancer cell line (PC3) was chosen as a model cell line because the expression level of the NEAR1 and the mRNA cancer biomakers in PC3 is high[5, 8]. A human kidney cell line (HEK293) was chosen as a control cell line because it is non-cancerous with low expression of the NEAR1 and the mRNA[33, 36] cancer biomakers. The cells were cultured in the Dulbecco's modified Eagle's medium (DMEM) media containing FBS (10%) and penicillin-streptomycin (5.5 ml). Prior to seeding, a hemocytometer was used to determine the cell density. The PC3 and the HEK293 cells were seeded at 5.0 x 10^5 cells per well in a 12-well plate. The PC3 cancer cells and the HEK293 cells were incubated in separate wells overnight. The cells were washed in the PBS buffer the following day and resuspended in 1 ml of the DMEM media. The experimental cell samples were incubated with 0.2 nM concentration of the SGNR-LINC261 nanoprobe and the SGNR-MHA for 3 hours in separate wells. The control samples were equally incubated for 3 hours without the nanoprobe treatment. The cells were washed 2x in the PBS buffer and centrifuged at 1400 rpm for 5 minutes. and re-suspended in 1ml of the PBS buffer for flow cytometry analysis. The samples were excited with the 638 nm excitation laser using Invitrogen Attune NxT acoustic focusing cytometer (Life Technologies, Carlsbad, USA) for flow cytometry analysis.

6. 2. 5. Extraction of exosomes

Exosomes can be extracted by various methods and these include ultracentrifugation, density gradient, and size exclusion chromatography. These methods are characterised by low yield, low throughput and time consuming[17, 37]. Therefore, exosomes were extracted according to a commercial exosomes extraction protocol[38] because of high yield of exosomes and its simplicity[39]. Firstly, a prostate cancer cell line (PC3) and a heathy human kidney cell line (HEK293) were cultured separately in the DMEM media supplemented with foetal bovine serum (FBS, 10%) and penicillin-streptomycin (5.5 ml) in 25 cm^3 flask until a confluence level of >90 % was attained. Then, the cells were washed in the PBS buffer and trypsinized to detach adherent cells. The washed cells were later incubated in a fresh FBS free DMEM media (5 ml) overnight to ensure that sufficient amount of the exosomes released in the media originated strictly from the cells[38]. The cell

media (4 ml) was harvested the next day into a 15 ml tube by decantation, while the cell pellets were re-suspended in a fresh FBS contained DMEM media for future use. The 4 ml of harvested cell media were centrifuged at 2000g for 30 minutes at room temperature to remove residual cells and debris. After centrifuge, the 4 ml of harvested cell media were gently decanted into another 15 ml, while the pellet discarded. The 4 ml of harvested cell media were mixed properly with 2 ml of the Total Exosomes Isolation reagent and incubated overnight at 4 ^{o}C. After the incubation, the mixture was centrifuged at 10,000g for 1 hour at 4 ^{o}C to sediment the exosomes. The supernatant was discarded, while the precipitated exosomes were re-suspended in a fresh PBS buffer and stored at 4 ^{o}C for future use.

By a similar approach, 90 µl of the blood serum were taken from a non-tumor bearing mouse (NTM) and a prostate cancer infected mouse (PCM). The blood serum of the NTM and the PCM were incubated with 45 µl of the Total Exosomes Isolation reagent under similar experimental conditions as above to isolate the exosomes.

6. 2. 6. Determination of the concentration and the hydrodynamic size of the cell exosomes

The concentration and the hydrodynamic size of the exosomes were determined with the NanoSight LM10 system (NanoSigth Ltd., Minton Park, Amesbury, Wiltshire, UK). Prior to the measurement, 10 µl of the PC3 and the HEK293 exosomes were separately diluted in 400 µl of the PBS buffer. The temperature of the diluent was measured with a thermocouple (Omega, HH804). The diluents were then aspirated with a syringe and loaded onto the sample chamber of the LM10 viewing unit. The exosomes were excited with a blue laser 405 nm. Nanoparticle tracking analysis (NTA) analytical software version 3.0 was used to determine the concentration and the hydrodynamic size of the cellular exosomes. The screen gain and camera level on the software were set at 5.3 and 13 respectively to ensure that the camera (SCMOS) visualizes the nanoparticle clearly.

6. 2. 7. Preparation of the PC3 exosomes and the HEK293 exosomes for incubation with the SGNR and the LGNR nanoprobes.

The stock of the PC3 exosomes and the HEK293 exosomes were diluted in the PBS buffer to obtain appropriate concentration of the PC3 exosomes and the HEK293 exosomes for analysis. The PC3 exosomes were incubated with the SGNR-LINC261 and the SGNR-c-myc nanoprobes to detect the high expression of the NEAR1, and the mRNA cancer biomarkers respectively, while the HEK293 exosomes with low expression of the NEAR1, and the mRNA cancer biomarkers were used as control. The PC3 exosomes and the HEK293 exosomes each with 1.0 x 10^{10} particles/ml were incubated with 0.5 nM of the SGNR-LINC261 nanoprobe in 100 µl of the PBS buffer in a quartz cuvette at 37 ^{o}C for 2 hours to detect the high expression of the NEAR1. A similar concentration of the PC3 and the HEK293 exosomes as above were incubated with 0.3 nM of the SGNR-c-myc nanoprobe in 100 µl of the PBS buffer in a quartz cuvette at 37 ^{o}C for 2 hours to detect the high expression of mRNA.

The size effect of the GNRs on the sensitivity of the gold nanoprobes in detecting the NEAR1 and the mRNA in the cellular exosomes was investigated by incubating the cellular exosomes with the LGNR nanoprobes and the SGNR nanoprobes. Firstly, 0.5 nM of the $LGNR_1$- LINC261 nanoprobe and the SGNR- LINC261 nanoprobe were incubated with 1.0 x 10^{10} particles/ml of the PC3 and the HEK293 cells respectively in 100 µl of the PBS buffer in a quartz cuvette at 37 ^{o}C for 2 hours. In addition, 0.37nM of the $LGNR_2$-c-myc nanoprobe and the SGNR-c-myc nanoprobe were incubated with 1.0 x 10^{10} particles/ml of the PC3 and the HEK293 cells respectively in 100 µl of the PBS buffer in a quartz cuvette at 37 ^{o}C for 2 hours. In addition, the effect of the concentration of cancer cell exosomes on the sensitivity of the SGNR nanoprobes in detecting the NEAR1 biomarker was investigated by incubating a fixed amount (0.5 nM) of the SGNR-LINC261 nanoprobe with varying concentrations of the PC3 exosomes.

Furthermore, 1.0 x 10^{10} particles/ml exosomes from the NTM and the PCM were each incubated with 0.5 nM of the SGNR- LINC261 nanoprobe in 100 µl of the PBS buffer in a quartz cuvette at 37 ^{o}C for 2 hours. Then 5 µl of the blood serum of the NTM and the

PCM were directly incubated with 0.5 nM of the SGNR- LINC261 nanoprobe in 100 µl of the PBS buffer in a quartz cuvette at 37 ^{o}C for 1 hour.

6. 2. 8. Characterization of gold nanorods, nanoprobes and exosomes

The extinction spectra of the gold nanorods covering 400-1100 nm wavelength was measured with a UV-visible spectrophotometer (Lamda 2, Perkin Elmer). A scanning electron microscope (SEM, FEI Quanta FEG 250) was used for morphological characterization of the gold nanorods using a 30kV electron beam and bright field/dark field scanning transmission electron detectors. ImageJ software was used for the size analysis. A spectrofluorometer (Horiba Jobin Yvon Ltd., Middlesex, UK) was used to measure the fluorescence emission spectra at an excitation of 635 nm. The fluorescence lifetime measurement was performed with an IBH Fluorocube (Horiba Jobin Yvon IBH Ltd., Glasgow, UK) using the time-correlated single-photon counting (TCSPC) technique as reported in section 3. 2. 7. of chapter 3. The flow cytometry measurements were performed using an Invitrogen Attune NxT acoustic focusing cytometer (Life Technologies, Carlsbad, USA). The concentration and the hydrodynamic size of the cellular exosomes were determined with a Nanosight LM10 (Nanosight Ltd., Minton Park, Amesbury Wiltshire, UK).

6. 3. Results and Discussion

6. 3. 1. Synthesis and functionalization of gold nanorods

The UV-vis extinction spectra of the two large gold nanorods $LGNR_1$ and $LGNR_2$ are shown in figure 6.1. The longitudinal surface plasmon resonance (LSPR) of the $LGNR_1$ and the $LGNR_2$ were 660nm and 679 respectively. The longitudinal surface plasmon resonance of the $LGNR_1$ and the $LGNR_2$ shifted to 657 nm and 680 nm respectively after the ligand exchange, thus indicating a successful ligand exchange (fig. 6.1a). The blue shift observed for the $LGNR_1$ after the ligand exchange could be due to a heating effect, thus shortening the length of the gold nanorods. The shortening of the length reduces the aspect ratio of the $LGNR_1$ leading to a blue shift of the LSPR as predicted by Gans', Link

and El-Sayed models in equations 1.2 and 1.7 respectivley[40-41]. The LSPR of the $LGNR_1$-LINC261 and the $LGNR_2$-c-myc- hpDNA nanoprobes were 649 nm and 653 nm respectively after functionalization (fig.6.1a-b). The blue shift of the $LGNR_1$-LINC261 nanoprobe and the $LGNR_2$-cmyc nanoprobe could be attributed to series of repeated washing (centrifugation) which might have affected the size distribution and the LSPR of the LGNRs nanoprobes[42-43].

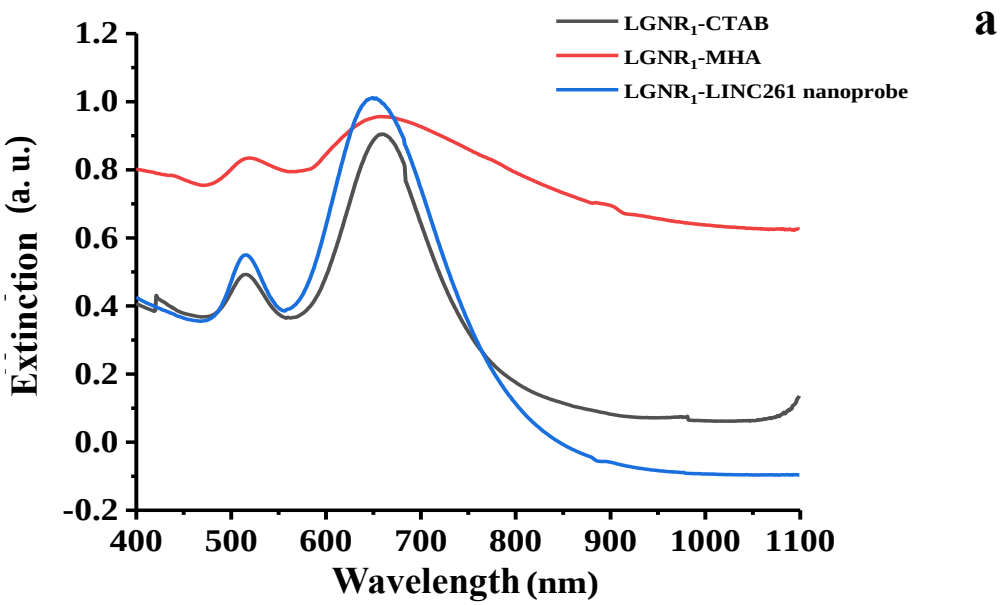

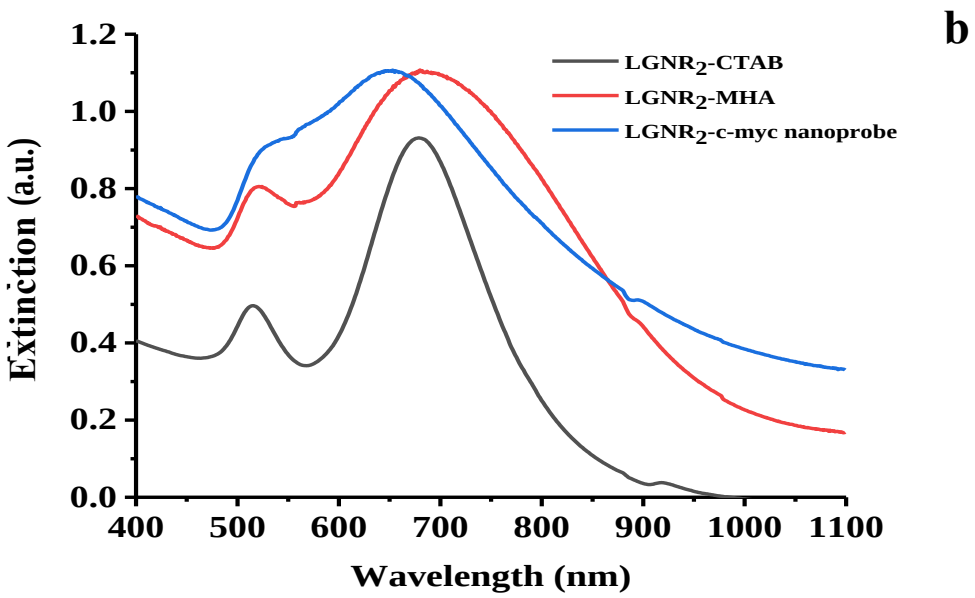

Figure 6.1. The UV-vis extinction spectra of the gold nanorods; (a) the extinction spectra of the $LGNR_1$ before, after ligand exchange and functionalization with the LINC261-hpDNA (b) the extinction spectra of the $LGNR_2$ before, after ligand exchange and functionalization with the c-myc-hpDNA.

Figure 6.2. shows that the LSPR of the SGNR was 680 nm after synthesis, but blue shifted to 668 nm without a broadened peak after ligand exchange. The same SGNR sample was separately functionalized with the LINC261-hpDNA and the c-myc-hpDNA as two distinct nanoprobes. After functionalization, the LSPR of the SGNR-LINC261nanoprobe was 676 nm while the LSPR of the SGNR-c-myc nanoprobe was 672 nm (fig. 6.2a-b). The adsorption of the oligonucleotides on the gold nanorods structures, thus, enhances their targeting abilities and stabilizes the nanoprobes from nuclease degradation for potential application in complex biological systems[44-46].

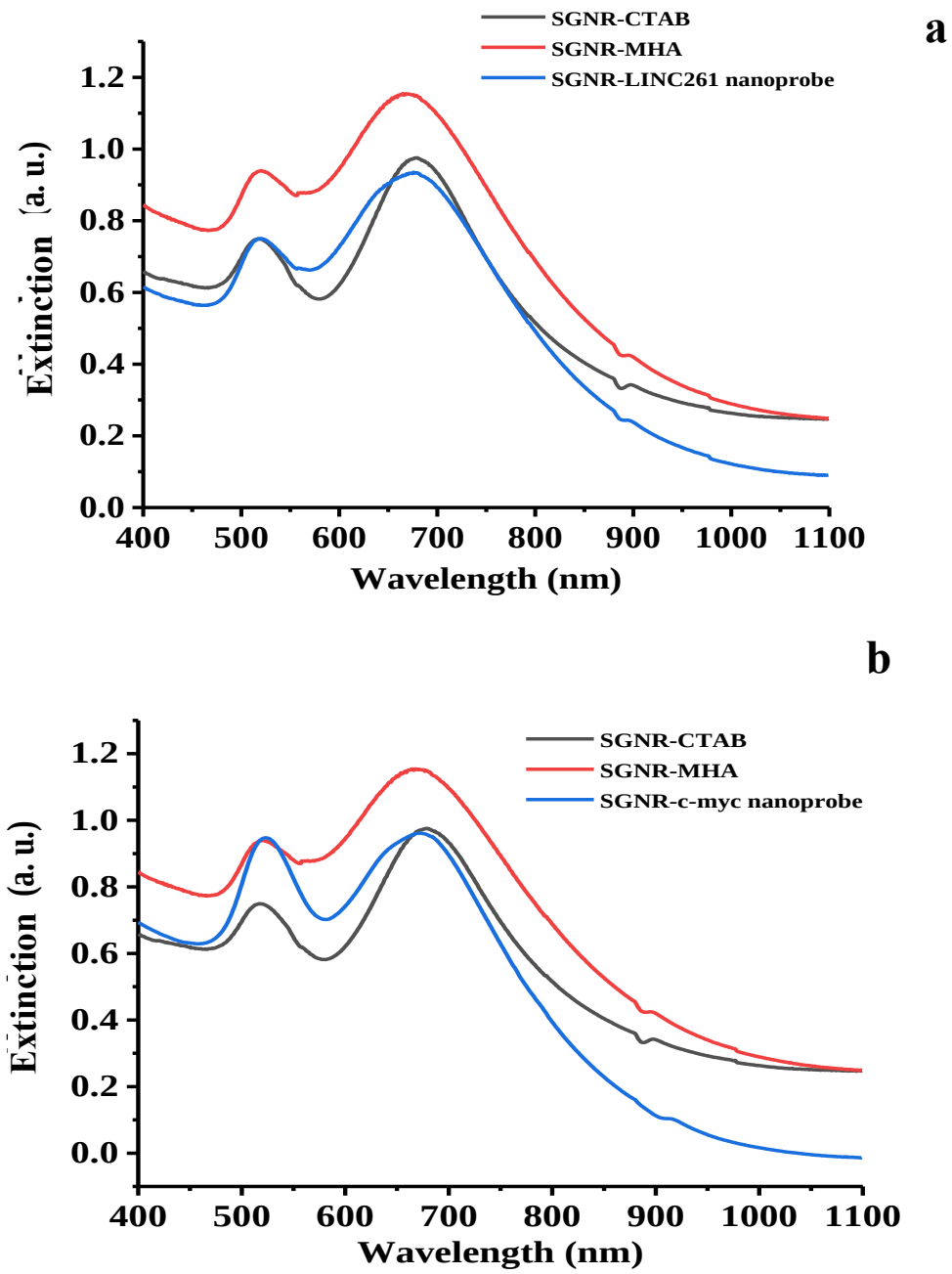

Figure 6.2. The UV-vis extinction spectra of the gold nanorods; (a) the extinction spectra of the SGNR before, after ligand exchange and functionalization with the LINC261-hpDNA and (b) the extinction spectra of the SGNR before, after ligand exchange and functionalization with the c-myc-hpDNA.

The SEM images of the synthesized $LGNR_1$ and SGNR are shown in figures 6. 3a-b respectively. It can be observed that the length of $LGNR_1$ is longer compared to SGNR. In addition, the width of $LGNR_1$ is broader compared to that of the SGNR. In general, the size of the $LGNR_1$ is larger compared to the SGNR as expected.

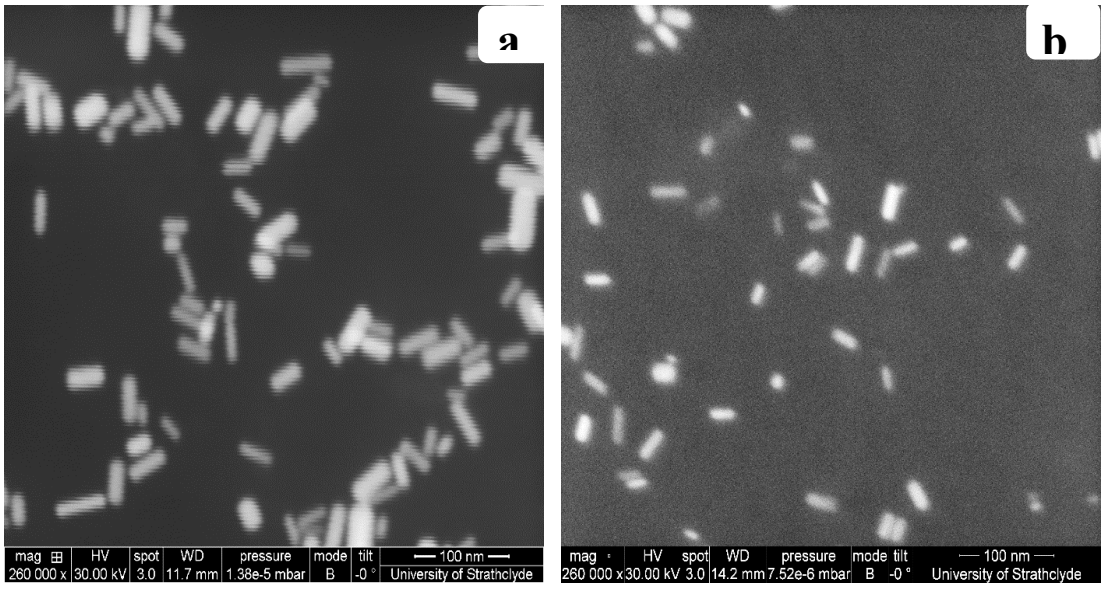

Figure 6.3. SEM images of (a) $LGNR_1$ and (b) SGNR.

Table 6.3. displays the dimensions of the $LGNR_1$, $LGNR_2$, and the SGNR samples. The dimensions of the $LGNR_1$ and the SGNR samples were determined by ImageJ software from the SEM images above while the dimensions of $LGNR_2$ was determined from the calibration curve shown in fig. 2 of appendix 2. The average length and the average width of $LGNR_1$ were found to be 38.2±7.0 nm and 11.3±2.7 nm respectively. While the average length and the average width of SGNR were found to be 18.1±5.4 nm and 5.2±1.3 nm respectively. The histograms showing the distribution of the length and the width of $LGNR_1$ and SGNR are presented in appendix 3. The average length and the average width of $LGNR_2$ sample obtained by a calibration curve shows 37.2±6.4 nm and 11.2±2.5 nm respectively.

Table 6.3. The dimensions of the large and the small gold nanorods.

Samples	LSPR (nm)	Length (nm)	Width (nm)
$LGNR_1$	660	38.2±7.0	11.1±2.7
$LGNR_2$	679	37.2±6.4	11.2±2.5
SGNR	680	18.1±5.4	5.2±1.3

6. 3. 2. Fluorescence emission intensities and lifetimes of the LINC261-nanoprobe and the c-myc-nanoprobe immobilized on the gold nanorods

The performance of the LINC261-nanoprobe and the c-myc-nanoprobe was evaluated using both steady state and time-resolved fluorescence spectroscopies. All the nanoprobes were excited at 635 nm to measure the fluorescence emission intensity using a spectrofluorometer. The nanoprobes were incubated with the complementary DNA (cDNA) in the ratio 1:1000. The fluorescence emission spectra of the nanoprobes before and after adding the cDNA are displayed in fig. 6.4. It can be seen that the fluorescence emission intensity of the $LGNR_1$-LINC261 nanoprobe and the $LGNR_2$-c-myc nanoprobe increased by 2.4 fold and 1.8 fold respectively after hybridization, thus, indicating that the targeting sequences in the hairpin DNA (hpDNA) bind to the complementary sequences of the targets (fig.6.4a-b). Similarly, it can be seen that the fluorescence emission intensities of the SGNR-LINC261 nanoprobe and the SGNR-c-myc nanoprobe increased by 3.7 fold and 2.1 fold respectively after hybridization (fig. 6.4c-d). This is because the fluorescence emissions of the nanoprobes were quenched due to the surface plasmon (SP) enhanced energy transfer to the gold nanorods in the absence of targets. However, the fluorescence emission intensity of the nanoprobes increases after hybridization. This indicates that the fluorescence emission intensities of the gold nanorods nanoprobes are determined by the interaction of the fluorophores with the gold nanorods surface and the rate of hydrization[32, 47-48].

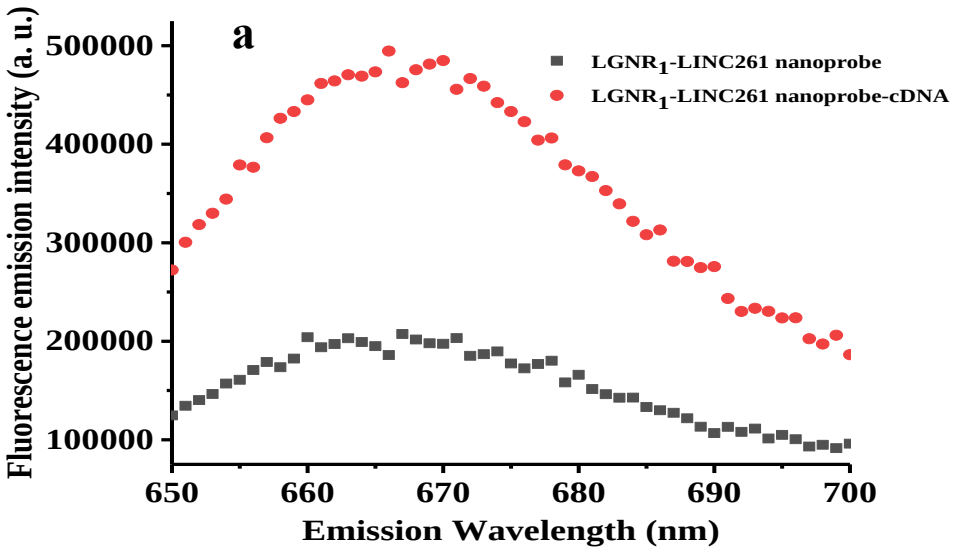
a
Fluorescence emission intensity (a. u.)
500000
400000
300000
200000
100000
650
660
670
680
690
700
Emission Wavelength (nm)
LGNR1-LINC261 nanoprobe
LGNR1-LINC261 nanoprobe-cDNA

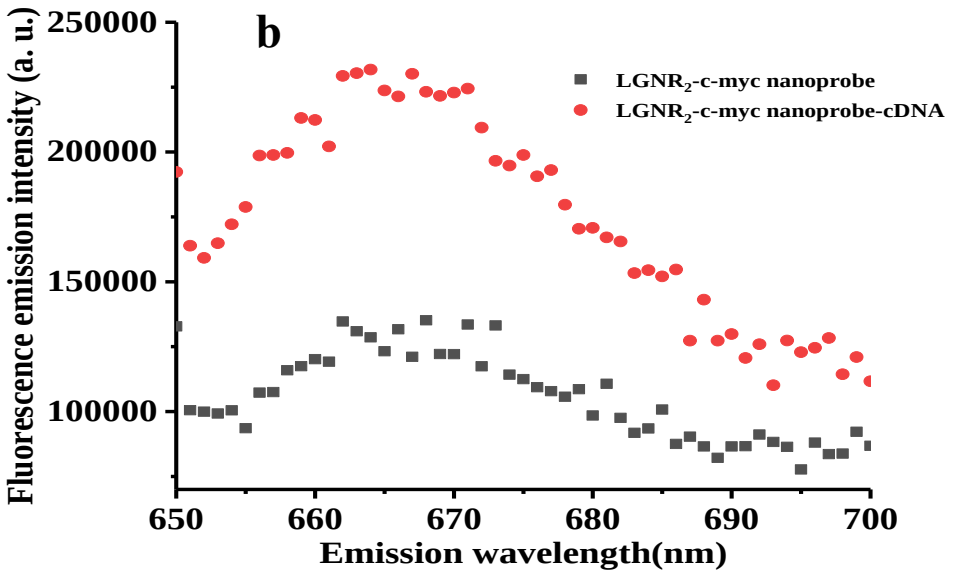
b
Fluorescence emission intensity (a. u.)
250000
200000
150000
100000
650
660
670
680
690
700
Emission wavelength(nm)
LGNR2-c-myc nanoprobe
LGNR2-c-myc nanoprobe-cDNA

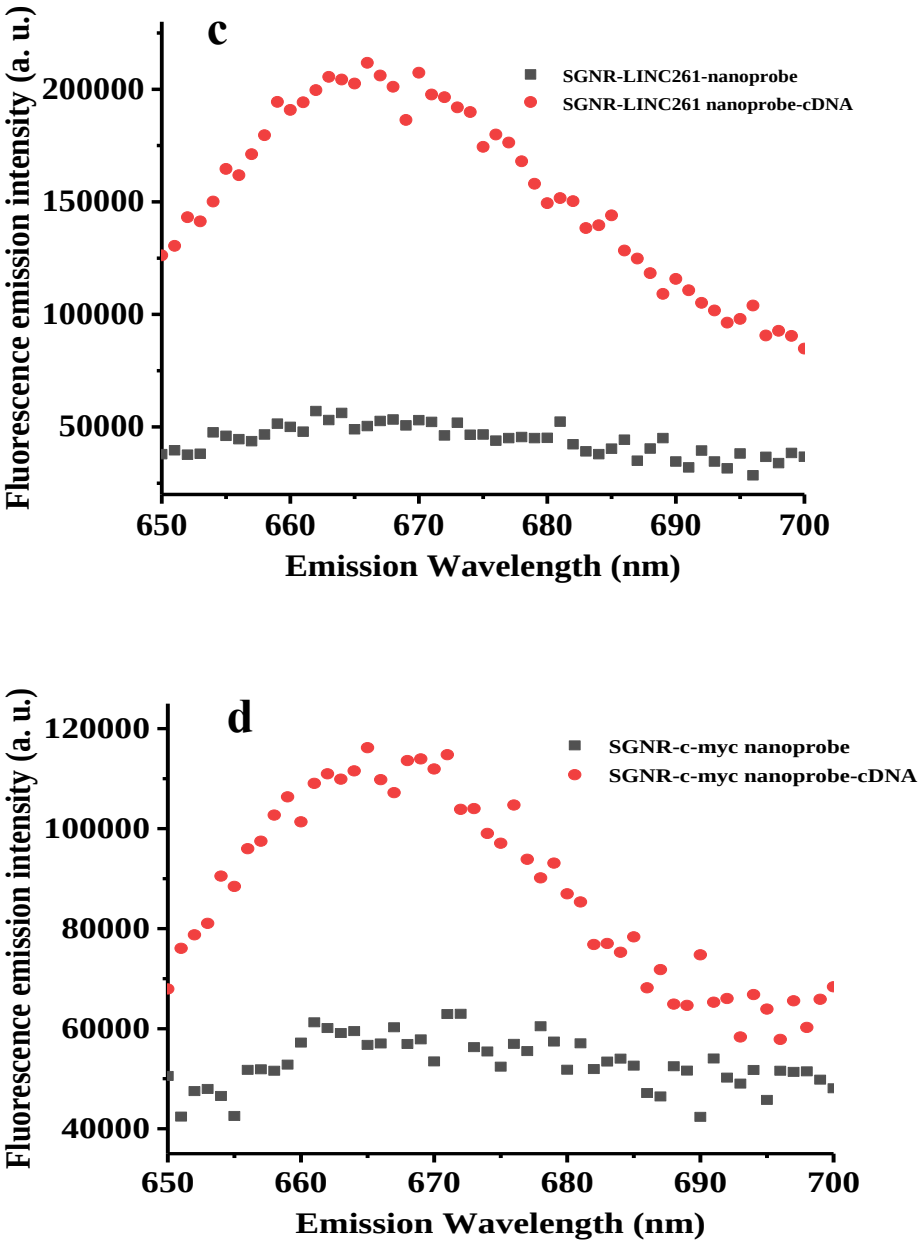

Figure 6.4. The fluorescence emission spectra of the gold nanorods nanoprobes before and after hybridization at 2 hours incubation; (a) $LGNR_1$-LINC261 nanoprobe, (b) $LGNR_2$-c-myc nanoprobe, (c) SGNR-LINC261 nanoprobe, (d) SGNR-c-myc nanoprobe.

Table 6.4. shows the ratio of fluorescence emission intensities of the $LGNR_1$-LINC261, $LGNR_2$-c-myc, SGNR-LINC261 and the SGNR-c-myc nanoprobes with and without the

cDNA. In comparison, the fluorescence emission intensity increase of the SGNR-LINC261 nanoprobe (3.7 fold) is higher than that of the $LGNR_1$-LINC261 nanoprobe (2.4 fold). Similarly, the fluorescence emission intensity increase of the SGNR-c-myc-Cy5-hpDNA nanoprobe (2.7 fold) is higher than 1.8 fold of the $LGNR_2$-c-myc nanoprobe. This could be attributed to the higher packing density of hairpin DNA on the SGNRs surface due to the high surface curvature of the SGNRs and the large ratio of the surface area to volume of the SGNRs. It has been reported that the DNA molecules bind more to a curved surface than on a flat surface; and the surface curvature increases as the size of the gold nanoparticle decreases[49]. Moreover, Wei et al. have demonstrated that the fluorescence intensity of the GNR nanoprobe increases with the hpDNA packing density[32], hence, the higher increases of the fluorescence emission intensities of the SGNR nanoprobes than that of the LGNRs nanoprobes. In addition, it has been reported that targets from the surrounding environment bind more to the small size nanoparticles than the large size nanoparticles because the small size nanoparticle have larger surface area to volume ratio[29] for enhanced binding of the targets leading to the higher fluorescence intensity increase than the large size nanoparticles.

Table 6.4. The ratio of the fluorescence emission intensities of the $LGNR_1$-LINC261, $LGNR_2$-c-myc, SGNR-LINC261 and the SGNR-c-myc nanoprobes with and without the cDNA.

Sample	The ratio of fluorescence emission intensity with and without the cDNA (fold)
$LGNR_1$-LINC261 nanoprobe	2.4
SGNR-LINC261 nanoprobe	3.7
$LGNR_2$-c-myc nanoprobe	1.8
SGNR-c-myc nanoprobe	2.1

To evaluate the performance of the $LGNR_2$-cmyc-nanoprobe and the SGNR-cmyc-nanoprobe, the fluorescence lifetimes of the free-cmyc-Cy5-hpDNA (i.e. without assembly onto GNRs) was measured as the reference. Figure 6.5a-b shows the fluorescence decays of the free cmyc-Cy5-hpDNA, $LGNR_2$-cmyc-nanoprobe and the SGNR-cmyc-nanoprobe in the closed state (before hybridization) and the opened state (after hybridization), while the fittings of the fluorescence decay curves of the free Cy5-c-myc-hpDNA, $LGNR_2$-c-myc nanoprobe and SGNR-c-myc nanoprobe are presented in figure 4 of appendix 5. The fluorescence decays of the $LGNR_2$-cmyc-nanoprobe and the SGNR-cmyc-nanoprobe were faster prior to hybridization than those after hybridization because the Cy5 fluorophore on the nanoprobes moves away from the GNR surface upon hybridization with the targets. This results in a longer fluorescence decay time in the case of the $LGNR_2$-cmyc-nanoprobe and the SGNR-cmyc-nanoprobe respectively, which is consistent with their fluorescence intensity increase. In comparison, the fluorescence decay of the SGNR-cmyc-nanoprobe after hybridization is longer than that of the $LGNR_2$-cmyc-nanoprobe (fig.6.5b) indicating a longer fluorescence decay time for Cy5 in the SGNR based nanoprobes than that in the LGNR based nanoprobe after hybridization.

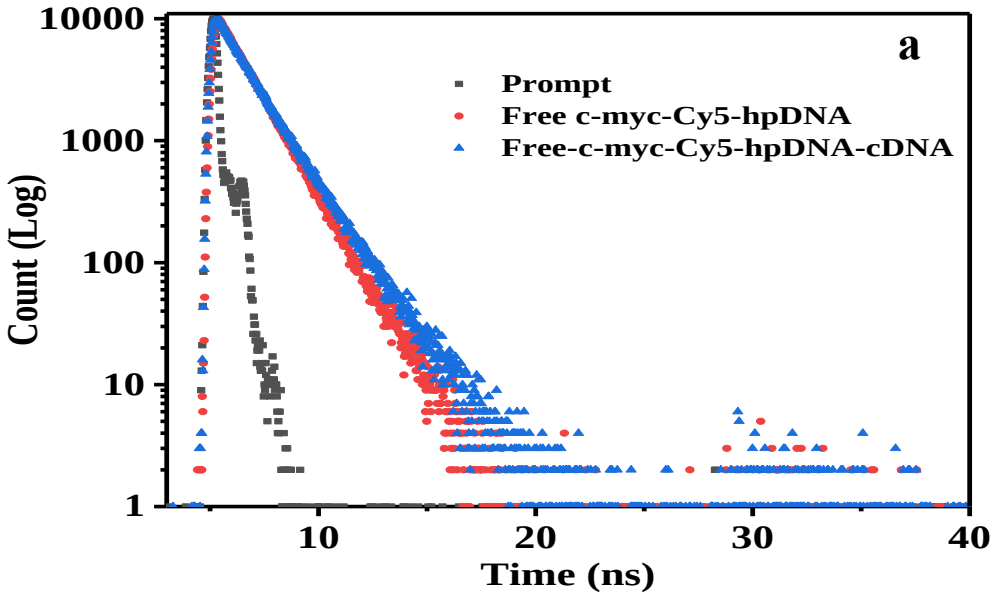

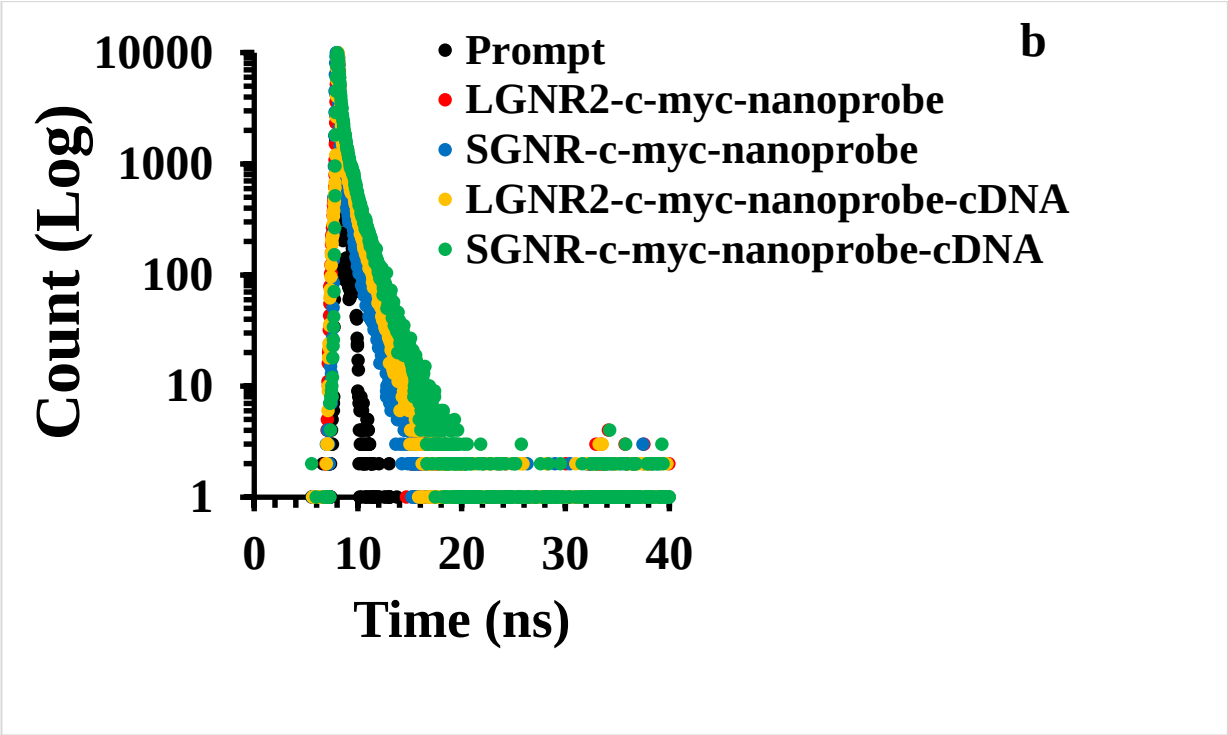

Figure 6.5. The fluorescence lifetime decays of; (a) free c-myc-Cy5-hpDNA, (b) $LGNR_2$-c-myc nanoprobe and SGNR-c-myc nanoprobe.

Table 6.5. shows the fluorescence lifetimes of the free c-myc-Cy5-hpDNA , $LGNR_2$-c-myc nanoprobe and the SGNR-c-myc nanoprobe denoted by τ_1 (short lifetime), τ_2 (long lifetime) and τ_3 (scattering contribution from gold core) respectively in both closed and opened states. The free c-myc-Cy5-hpDNA shows a short lifetime (τ_1) of 0.57 ns and a long lifetime (τ_2) of 1.42 ns in the closed state. The short lifetime could be due to photo-induced electron transfer from the Cy5 fluorophore to the nucleotide bases. It has been reported that energy transfer from the fluorophore to the nucleotide bases could occur by photo-induced electron transfer when both the fluorophore and the bases are in closed proximity[32, 50], hence the shorter lifetime of Cy5 in the free c-myc-Cy5-hpDNA. However, after hybridization (i.e. opened state) with the complementary sequence, both the τ_1 (0.62 ns) and the τ_2 (1.65 ns) increased respectively. The average fluorescence lifetime, $\bar{\tau}$ increase from 1.34 ns to 1.54 ns after hybridization with the cDNA indicating binding with the complementary sequence.

The average fluorescence lifetimes of all the nanoprobes in both states were calculated excluding the contribution of τ_3. Prior to hybridization, the average fluorescence lifetimes ($\bar{\tau}$) of the $LGNR_2$-c-myc nanoprobe was 1.14 ns while that of the SGNR-c-myc nanoprobe was 1.18 ns. (table 6.5). Both (1.14 ns and 1.18 ns) were shorter than the average fluorescence lifetime of free cmyc-Cy5-hpDNA (1.34 ns) prior to hybridization. The apparent reduction of the average fluorescence lifetimes of Cy5 in the $LGNR_2$-c-myc nanoprobe and the SGNR-c-myc nanoprobe is due to the strong SP enhanced energy transferred from the Cy5 to the GNR when the Cy5 is in close proximity to the GNRs[32]. After hybridization, the average fluorescence lifetimes of Cy5 in the $LGNR_2$ nanoprobes increased to 1.22 ns and that of the SGNR nanoprobes increased to 1.31 ns, indicating the opening of the hairpins. However, both are shorter in comparison to the average fluorescence lifetime of free cmyc-Cy5-hpDNA (1.54 ns). This suggests that not all the hairpins on the GNRS are opened as reported before[32]. Nevertheless, the apparent increases in the average fluorescence lifetime upon hybridization are consistent with the fluorescence intensity increases observed before[30, 32].

Similarly, the average fluorescence lifetimes ($\bar{\tau}$) of the $LGNR_1$-LINC261 nanoprobe increases from 1.11 ns to 1.27ns as expected. Interestingly, the average fluorescence lifetime of the SGNR-LINC261 nanoprobe decreases from 1.03 ns to 0.89 ns after hybridization (table 6. 6). The intensity measurement has observed a 3.7 fold increase after hybridization of this nanoprobe (table 6.4.), the highest among all the nanoprobes. This suggests that the decreases in the average lifetime is not due to a failure of the nanoprobe functioning or quenching of the fluorescence. Instead, this could be due to the surface plasmon enhanced fluorescence. When surface plasmon resonance overlaps with the emission wavelength and the Cy5 is at an optimal distance from the gold surface, coupling of the SP with the Cy5 could modify the emission rate resulting in a faster fluorescence decay and shorter lifetime[51-52]. The fittings of the fluorescence decay curves of the $LGNR_1$-LINC261 nanoprobe and the SGNR-LINC261 are presented in figure 5 of appendix 5.

Table 6.5. The fluorescence lifetimes of the $LGNR_2$-c-myc nanoprobe, and the SGNR-c-myc nanoprobe τ_3 fixed at 0.5 (0.01 ns) channel.

Sample	τ_1 (ns)	B_1 (%)	τ_2 (ns)	B_2 (%)	τ_3 (ns)	B_3 (%)	$\bar{\tau}$ (ns)	χ^2
Free-c-myc-hpDNA	0.57±0.02	20.97	1.42±0.01	79.03	-	-	1.34	1.2
Free-c-myc-hpDNA-cDNA	0.62±0.02	25.23	1.65±0.00	74.77	-	-	1.54	1.02
$LGNR_2$-c-myc nanoprobe	0.31±0.02	7.20	1.28±0.02	10.53	0.01	82.27	1.14	1.06
$LGNR_2$-c-myc nanoprobe-cDNA	0.36±0.03	5.66	1.31±0.01	14.38	0.01	79.96	1.22	1.00
SGNR-c-myc nanoprobe	0.41±0.04	5.69	1.32±0.02	10.00	0.01	84.32	1.18	1.08
SGNR-c-myc nanoprobe-cDNA	0.36±0.01	22.36	1.54±0.01	21.34	0.01	56.30	1.31	1.08

Table 6.6. The fluorescence lifetimes of the LGNR1-LINC261 nanoprobe, and the SGNR-LINC261 nanoprobe τ_3 fixed at 0.5 channel (0.01 ns).

Sample	τ_1 (ns)	B_1 (%)	τ_2 (ns)	B_2 (%)	τ_3 (ns)	B_3 (%)	$\bar{\tau}$ (ns)	χ^2
$LGNR_1$-LINC261 nanoprobe	0.32±0.02	6.86	1.30±0.02	6.99	0.01	86.15	1.11	1.00
$LGNR_1$-LINC261 nanoprobe-cDNA	0.33±0.01	12.84	1.47±0.02	13.44	0.01	73.71	1.27	1.05
SGNR-LINC261 nanoprobe	0.37±0.01	10.93	1.36±0.03	6.04	0.01	83.03	1.03	1.03
SGNR-LINC261 nanoprobe cDNA	0.36±0.01	32.86	1.30±0.02	11.61	0.01	55.53	0.89	1.03

6. 3. 3. Detection of the NEAR1 cancer biomaker in the PC3 cells

Flow cytometry was performed using the SGNR-LINC261 nanoprobe to detect the NEAR1 cancer biomaker in the PC3 while the HEK293 cells serves as a control. The fluorescence emission intensity from the flowing cells was determined from the density plot and the histogram plot. The density plot was represent by the side scatter (SSC) intensity on vertical axis and the forward scatter (FSC) intensity on the horizontal axis. The SSC describes the complexity of the cells while the FSC is proportional to the hydrodynamic size of the cells[53]. A polygon gate denoted by R1 was inserted in the density plot to analyse the fluorescence intensity of the cell population of interest. In addition to the density plot, the histogram plot was used to represent the fluorescence

intensity of the gated cell population denoted by R2. Figure 6.6. shows the density plot and the histogram plot of the gated cell population. It can be seen from gate R1 that the mean fluorescence intensity of the PC3 cells treated with the SGNR-LINC261 nanoprobe is 37, 232 higher than 262 of the SGNR-MHA treated PC3 cells and 340 of the PC3 control (fig. 6.6a). Furthermore, gate R2 shows that 19, 972 out of the total cell count (20, 000) of the SGNR-LINC261 nanoprobe treated PC3 cells have 37,283 mean fluorescence intensity, while 56 of the 20, 000 cells of the SGNR-MHA treated PC3 cells have 1,925 mean fluorescence intensity and 82 of the 20, 000 cells of the PC3 control have 19,563 mean fluorescence intensity. Clearly, the PC3 cells treated with the nanoprobe have higher fluorescence intensity than the SGNR-MHA treated PC3 and the control. The significantly enhanced fluorescence intensity from the SGNR-LINC261 nanoprobe treated PC3 cells is due to the high expression rate of the NEAR1 cancer biomaker in the PC3 cells, that is consistent with the previous report[35]. Figure 6.6b shows that the mean fluorescence intensity of the HEK293 cells treated with the nanoprobe, SGNR-MHA and the control. Gate R1 shows that the mean fluorescence intensity of the SGNR-LINC261 nanoprobe treated HEK293 is 15, 284 higher than 114 for both the SGNR-MHA treated HEK293 cells and the HEK293 control. In addition, gate R2 shows that 19, 900 out of 20, 000 cells of the SGNR-LINC261 nanoprobe treated HEK293 cells have 15, 358 mean fluorescence intensity, while 8 of the 20, 000 cells of the SGNR-MHA treated HEK293 cells have 3, 822 mean fluorescence intensity and 9 of the 20, 000 cells of the HEK293 control have 5, 648 mean fluorescence intensity. In comparison, the mean fluorescence intensity of the PC3 cells treated with the SGNR-LINC261 nanoprobe is twice higher than that of the HEK293 cells treated with the SGNR-LINC261 nanoprobe. This is due to the higher expression of the NEAR1 cancer biomaker in the PC3 cells compared to the HEK293 cells, thus, leading to a strong fluorescence signal from the PC3 cells. This result demonstrates the ability of the SGNR-LINC261 nanoprobe to descriminate a neuroendocrine prostate cancer cells from a healthy cells.

a

SGNR-LINC261 nanoprobe-PC3

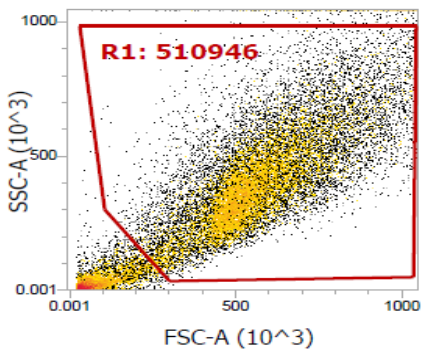

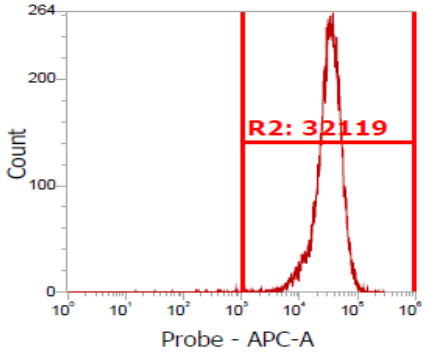

Name	Gate	X Parameter	Y Parameter	Count	%Total	%Gated	X Mean	X Median	X Peak
All Events	All Events	Probe-APC - RL1-A		28,014	100.000	100.000	36,286	32,491	-42
R1	R1	Probe-APC - RL1-A		20,000	71.393	71.393	37,232	34,989	32,119
R2	R2	Probe-APC - RL1-A		19,972	71.293	99.860	37,283	35,009	32,119

SGNR-MHA-PC3

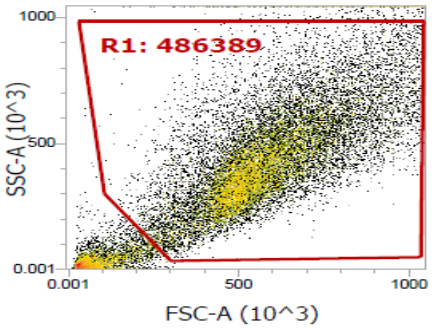

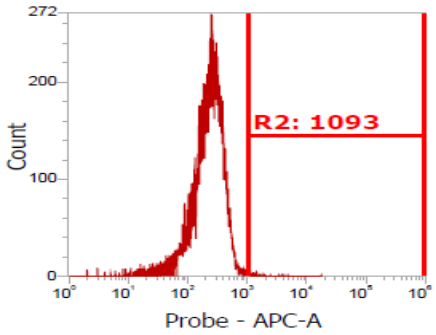

Name	Gate	X Parameter	Y Parameter	Count	%Total	%Gated	X Mean	X Median	X Peak
All Events	All Events	Probe-APC - RL1-A		28,866	100.000	100.000	318	242	-24
R1	R1	Probe-APC - RL1-A		20,000	69.286	69.286	262	243	266
R2	R2	Probe-APC - RL1-A		56	0.194	0.280	1,925	1,364	1,093

PC3-control

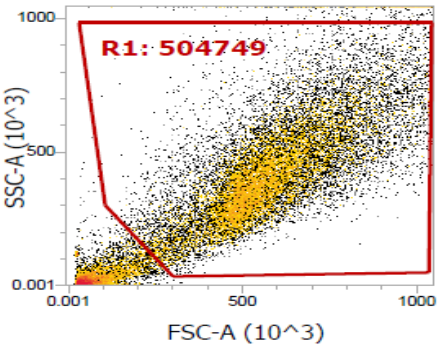

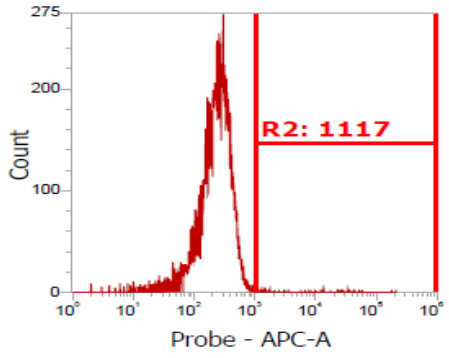

Name	Gate	X Parameter	Y Parameter	Count	%Total	%Gated	X Mean	X Median	X Peak
All Events	All Events	Probe-APC - RL1-A		29,065	100.000	100.000	536	236	-25
R1	R1	Probe-APC - RL1-A		20,000	68.811	68.811	340	247	232
R2	R2	Probe-APC - RL1-A		82	0.282	0.410	19,563	6,419	1,117

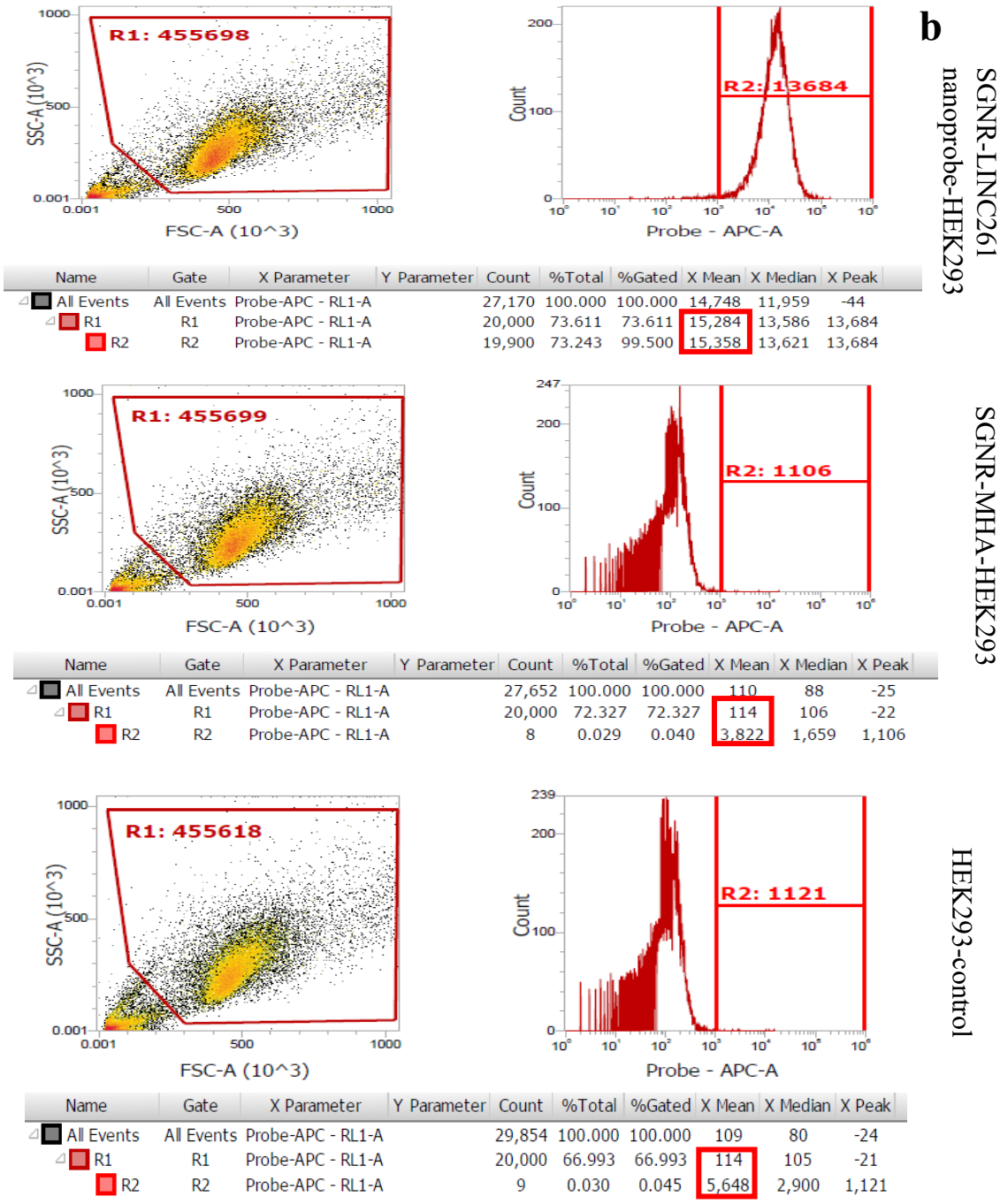

Figure 6.6. The density plot and histogram plot of the PC3 cells and the HEK293 cells incubated with the SGNR-LINC261 nanoprobes for 3 hours; (a) SGNR-LINC261 nanoprobe-PC3 cells/SGNR-MHA-PC3 cells/PC3 cells control, (b) SGNR-LINC261 nanoprobe-HEK293 cells/SGNR-MHA-HEK293 cells/ HEK293 cells control.

6. 3. 4. Determination of the concentration and the hydrodynamic size of the cellular exosomes

The concentration of the exosomes in suspension could be a very important parameter for diagnostic applications. It has been observed that $>10^9$ exosomes/ml can be found in about 100 μl of blood serum[22]. The concentration of the cellular exosomes was determined by the NTA software by counting the number of exosomes captured by the Nanosight' SCMOS camera. While the hydrodynamic size of the exosomes was determined by tracking the trajectory of the exosomes undergoing a Brownian motion to the centre of the exosomes. Then, the NTA software automatically determines the diffusion coefficient of the exosomes and computes the hydrodynamic size according to equation 2.7. The concentration of the PC3 cellular exosomes was found to be 1.60 $x10^{11}$particles/ml, while the concentration of the HEK293 exosomes was found to be 1.76 x 10^{11} particles/ml. Figure 6.7a displaying the hydrodynamic size of the PC3 cellular exosomes shows a dominant particle size of 115 nm and a smaller fraction of 425 nm and 665 nm larger size particles. The larger size particles could be due to the exosomes aggregation and other macromolecules. On the other hand, the distribution of the hydrodynamic size of the HEK293 cellular exosomes shows a dominant particle size of 45 nm mixed with 175 nm larger size particles (figure 6.7b). The size of the PC3 cellular exosomes and the HEK293 cellular exosomes measured are in agreement with the previous studies[14-15, 17, 38, 54]. The size distribution of the PC3 cellular exosomes and the HEK293 cellular exosomes are displayed in figure 6.7.

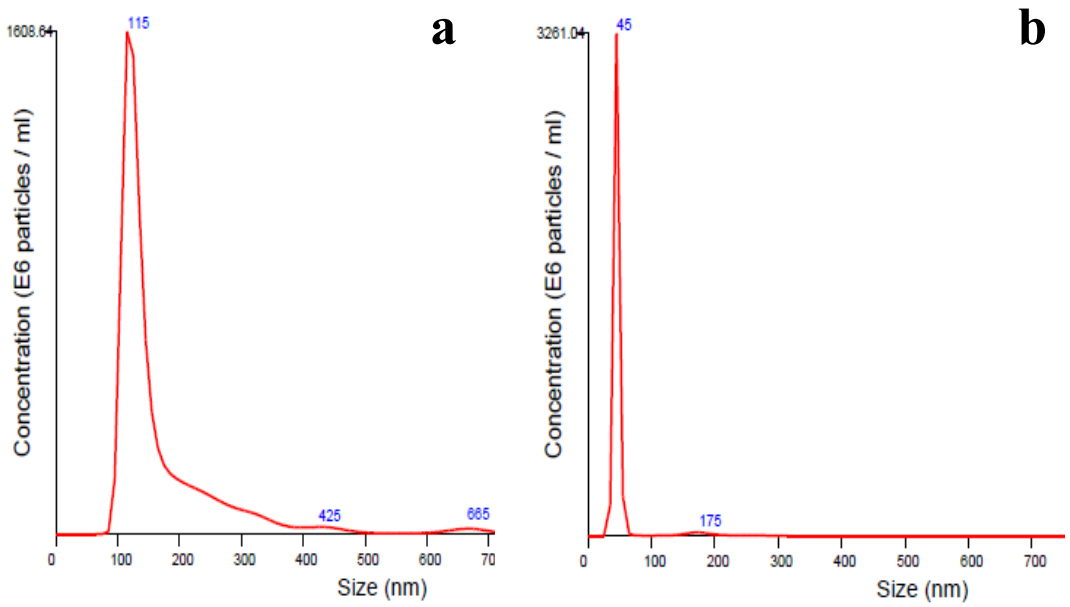

Figure 6.7. The distribution of the concentration and the hydrodynamic size of the; (a) PC3 cellular exosomes, (b) HEK293 cellular exosomes.

6. 3. 5. Detection of the mRNA and the NEAR1cancer biomarkers over-expression in the PC3 exosomes with the LGNR and the SGNR nanoprobes.

Since cancer cells secrete exosomes at the early stage, cellular exosomes were extracted from PC3 cell line, and HEK293 cell line to detect the mRNA cancer biomarker over-expressed in the cell-derived exosomes. Figure 6.8. shows the fluorescence emission intensity of the $LGNR_2$-c-myc nanoprobes and the SGNR-c-myc nanoprobes incubated with the cellular exosomes. It can be seen that the fluorescence intensity of both nanoprobes increased after 2 hours of incubation with the PC3 cellular exosomes respectively. The fluorescence emission intensity of the $LGNR_2$-c-myc nanoprobe incubated with the PC3 cellular exosomes is slightly higher than the $LGNR_2$-c-myc nanoprobe without the PC3 cellular exosomes (fig. 6.8a). On the other hand, the fluorescence emission intensity of the $LGNR_2$-c-myc nanoprobe incubated with the HEK293 cellular exosomes was similar to the $LGNR_2$-c-myc nanoprobe without the HEK293 cellular exosomes (fig. 6.8b). The ratio of the fluorescence emission intensity of the $LGNR_2$-c-myc nanoprobe incubated with the PC3 cellular exosomes is 1.39 fold

higher than 1.02 fold of the fluorescence emission intensity of the $LGNR_2$-c-myc nanoprobe incubated with the HEK293 cellular exosomes (table 6.7.). Furthermore, the fluorescence emission intensity of the SGNR-c-myc nanoprobe incubated with the PC3 cellular exosomes is higher than that of the SGNR-c-myc nanoprobe without the PC3 cellular exosomes (fig 6.8c). On the other hand, the fluorescence intensity of the SGNR-c-myc nanoprobe incubated with the HEK293 cellular exosomes was similar to the SGNR-c-myc nanoprobe without the HEK293 cellular exosomes (fig. 6.8d). The ratio of the fluorescence emission intensity of the SGNR-c-myc nanoprobe incubated with the PC3 cellular exosomes is 2.43 fold higher than 1.00 fold of the fluorescence emission intensity of the SGNR-c-myc nanoprobe incubated with the HEK293 cellular exosomes (table 6.7.). The higher fluorescence emission intensity observed for both the $LGNR_2$-c-myc nanoprobe and the SGNR-c-myc nanoprobe with the PC3 cellular exosomes compared to the HEK293 cellular exosomes could be due to the over-expression of c-myc gene in the mRNA of PC3 cellular exosomes [33, 36]. In contrast, the fluorescence emission intensity of the SGNR-c-myc nanoprobe with the PC3 cellular exosomes is enhanced by 2.43 fold more than 1.39 fold of the fluorescence emission intensity of the $LGNR_2$-c-myc nanoprobe as shown in fig 6.8e and table 6.7. respectively. The enhancement of the fluorescence emission intensity of the SGNR-c-myc nanoprobe with the PC3 cellular exosomes compared to the $LGNR_2$-c-myc nanoprobe could be due to a higher uptake of the SGNR-c-myc nanoprobe by the PC3 cellular exosomes. The size of the SGNR-c-myc nanoprobe is smaller compared to the size of the $LGNR_2$-c-myc nanoprobe, hence the higher uptake of the SGNR-c-myc nanoprobe.

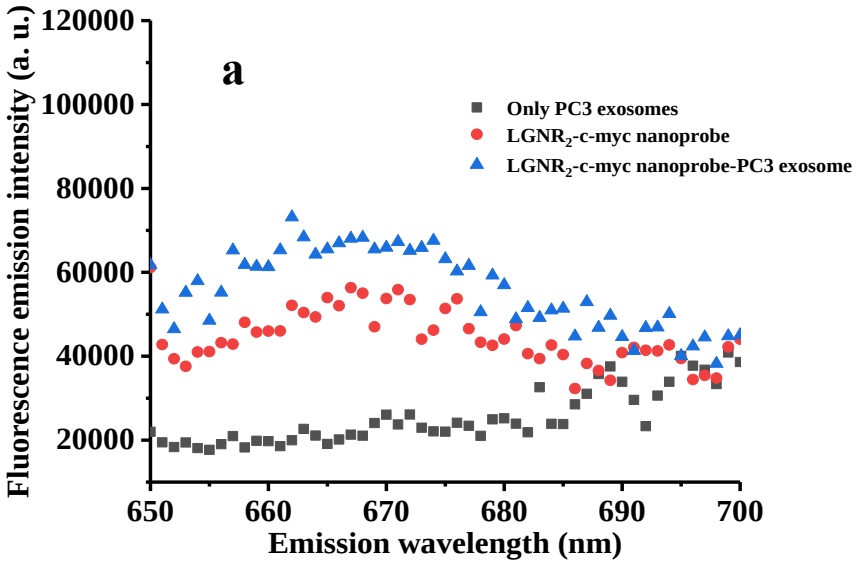
a
Only PC3 exosomes
LGNR2-c-myc nanoprobe
LGNR2-c-myc nanoprobe-PC3 exosome
Fluorescence emission intensity (a. u.)
120000
100000
80000
60000
40000
20000
650
660
670
680
690
700
Emission wavelength (nm)

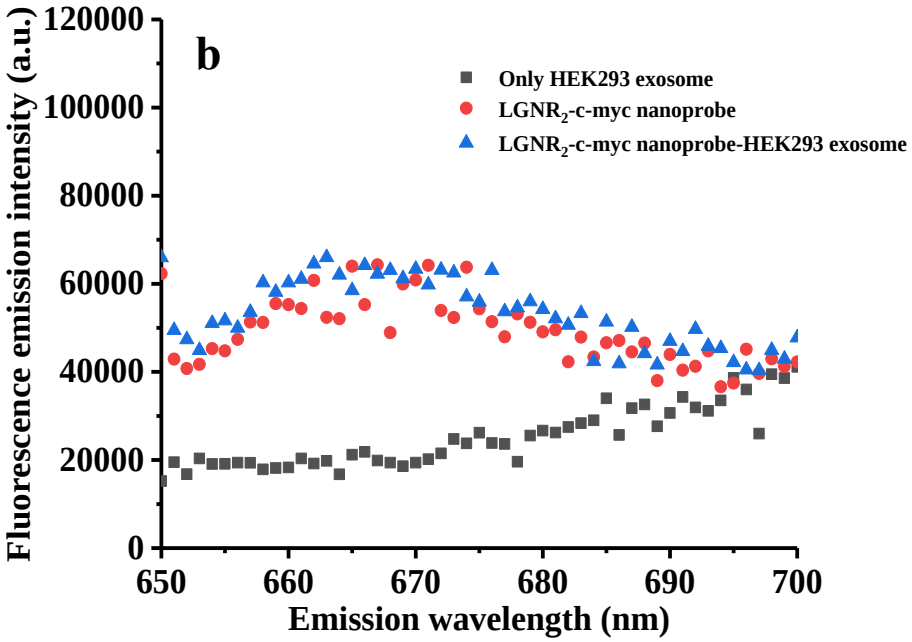
b
Only HEK293 exosome
LGNR2-c-myc nanoprobe
LGNR2-c-myc nanoprobe-HEK293 exosome
Fluorescence emission intensity (a.u.)
120000
100000
80000
60000
40000
20000
0
650
660
670
680
690
700
Emission wavelength (nm)

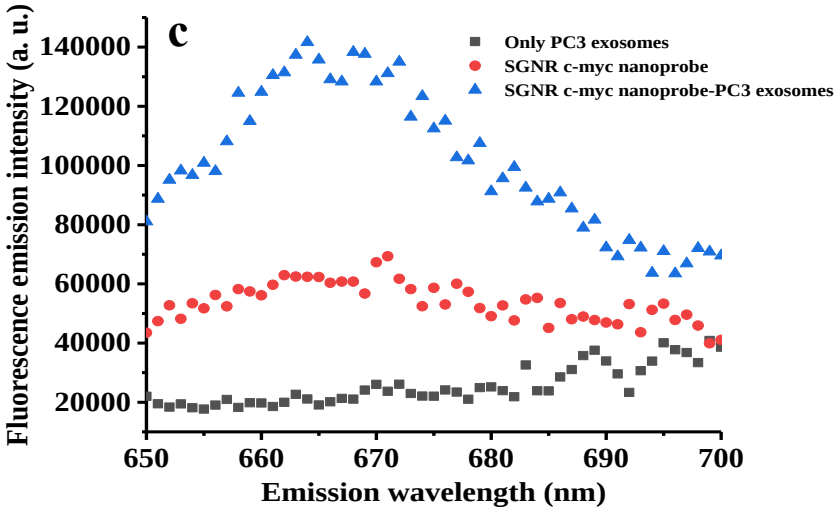
c
Only PC3 exosomes
SGNR c-myc nanoprobe
SGNR c-myc nanoprobe-PC3 exosomes
Fluorescence emission intensity (a. u.)
140000
120000
100000
80000
60000
40000
20000
650
660
670
680
690
700
Emission wavelength (nm)

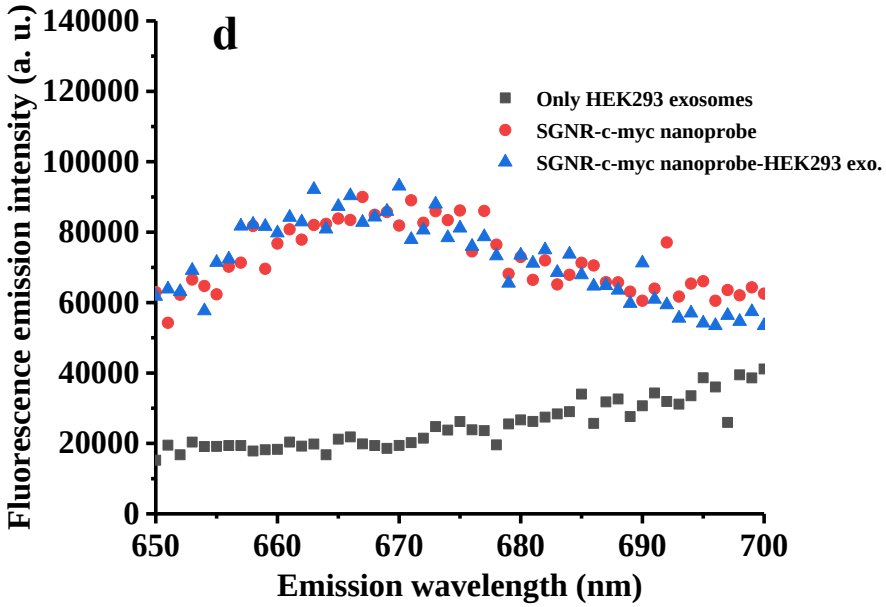
d
Only HEK293 exosomes
SGNR-c-myc nanoprobe
SGNR-c-myc nanoprobe-HEK293 exo.
Fluorescence emission intensity (a. u.)
140000
120000
100000
80000
60000
40000
20000
0
650
660
670
680
690
700
Emission wavelength (nm)

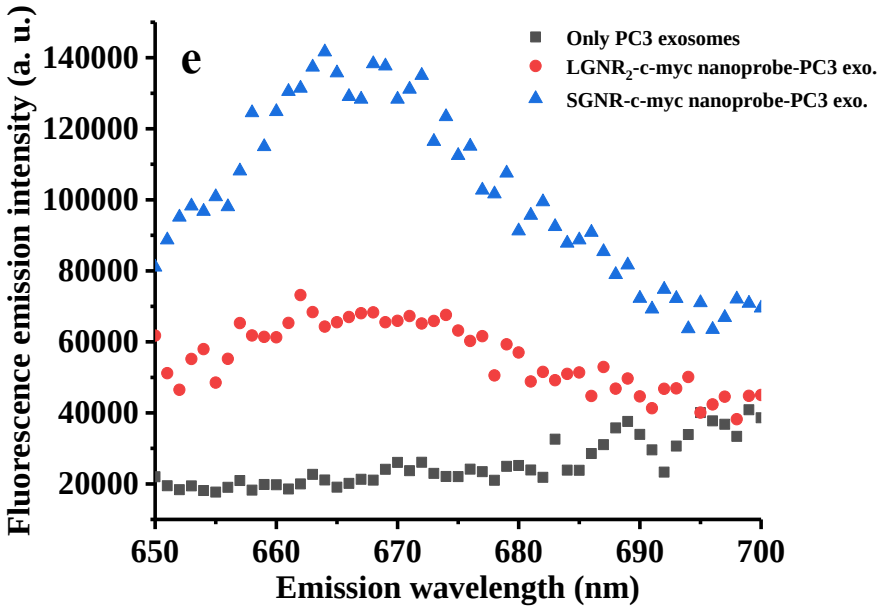

Figure 6.8. The fluorescence emission spectra of the $LGNR_2$-c-myc nanoprobe and the SGNR-c-myc nanoprobes incubated with the PC3 and the HEK293 cellular exosomes 2 hours; (a) $LGNR_2$-c-myc nanoprobe and PC3 exosomes, (b) SGNR-c-myc nanoprobes and PC3 exosomes, (c) $LGNR_2$-c-myc nanoprobe and HEK exosomes, (d) SGNR-c-myc nanoprobes and HEK exosomes and (e) $LGNR_2$-c-myc nanoprobe-PC3 exosomes and SGNR-c-myc nanoprobe-PC3 exosomes.

Table 6.7. The ratio of the fluorescence emission intensities of the $LGNR_2$-c-myc nanoprobe and the SGNR-c-myc nanoprobe incubated with the PC3 and the HEK293 cellular exosomes.

Sample	The ratio of fluorescence emission intensity increases	
	PC3 cellular exosomes (fold)	HEK293 cellular exosomes (fold)
$LGNR_2$-c-myc nanoprobe	1.39	1.02
SGNR-c-myc nanoprobe	2.43	1.00

Cancer derived exosomes manifest various biomakers[15, 22-23], thus, cellular exosomes positive for NEAR1 biomaker were extracted from the PC3 cell line, while cellular exosomes negative for NEAR1 biomaker were extracted from the HEK293 cell line as a control for early diagnosis of NEPC. Figure 6.9. shows the fluorescence intensities of the $LGNR_1$-LINC261 and the SGNR-LINC261 nanoprobes incubated with the cellular exosomes. It can be seen that the fluorescence emission intensities of both nanoprobes increased after 2 hours of incubation with the PC3 cellular exosomes respectively. On the contrary, no significant fluorescence emission intensity increment was observed after 2 hours of incubating both nanoprobes ($LGNR_1$-LINC261 nanoprobe and SGNR-LINC261 nanoprobe) with the HEK293 cellular exosomes respectively. This could be an indication that both the $LGNR_1$-LINC261 nanoprobe and the SGNR-LINC261 nanoprobe are sensitive to the NEAR1 biomaker that is highly over-expressed in the PC3 cellular exosomes. Table 6.8. shows that the ratio of the fluorescence intensity of the $LGNR_1$-LINC261 nanoprobe with the PC3 cellular exosomes increase by 1.34 fold, while that of the SGNR-LINC261 nanoprobe with the PC3 cellular exosomes increase by 2.11 fold. Clearly, the fluorescence intensity increase of the SGNR-LINC261 nanoprobe with the PC3 cellular exosomes is significantly higher than the fluorescence intensity increase of the $LGNR_1$-LINC261 nanoprobe with the PC3 cellular exosomes. This could be due to the large amount of the SGNR-LINC261 nanoprobe uptaken by the PC3 cellular exosomes in comparison to the LGNR1-LINC261 nanoprobe, thus leading to a higher fluorescence intensity. It is very interesting to note that fluorescence intensity of the SGNR-LINC261 nanoprobe with the HEK293 cellular exosomes remains unchange after 2 hours as shown in table 6.8. and fig.6.9b. These results clearly demonstrate that the small gold nanorods nanoprobes have better sensitivity in detecting the NEAR1 cancer biomaker in the neuroendocrine prostate cancer exosomes compared to the large gold nanorod nanoprobes.

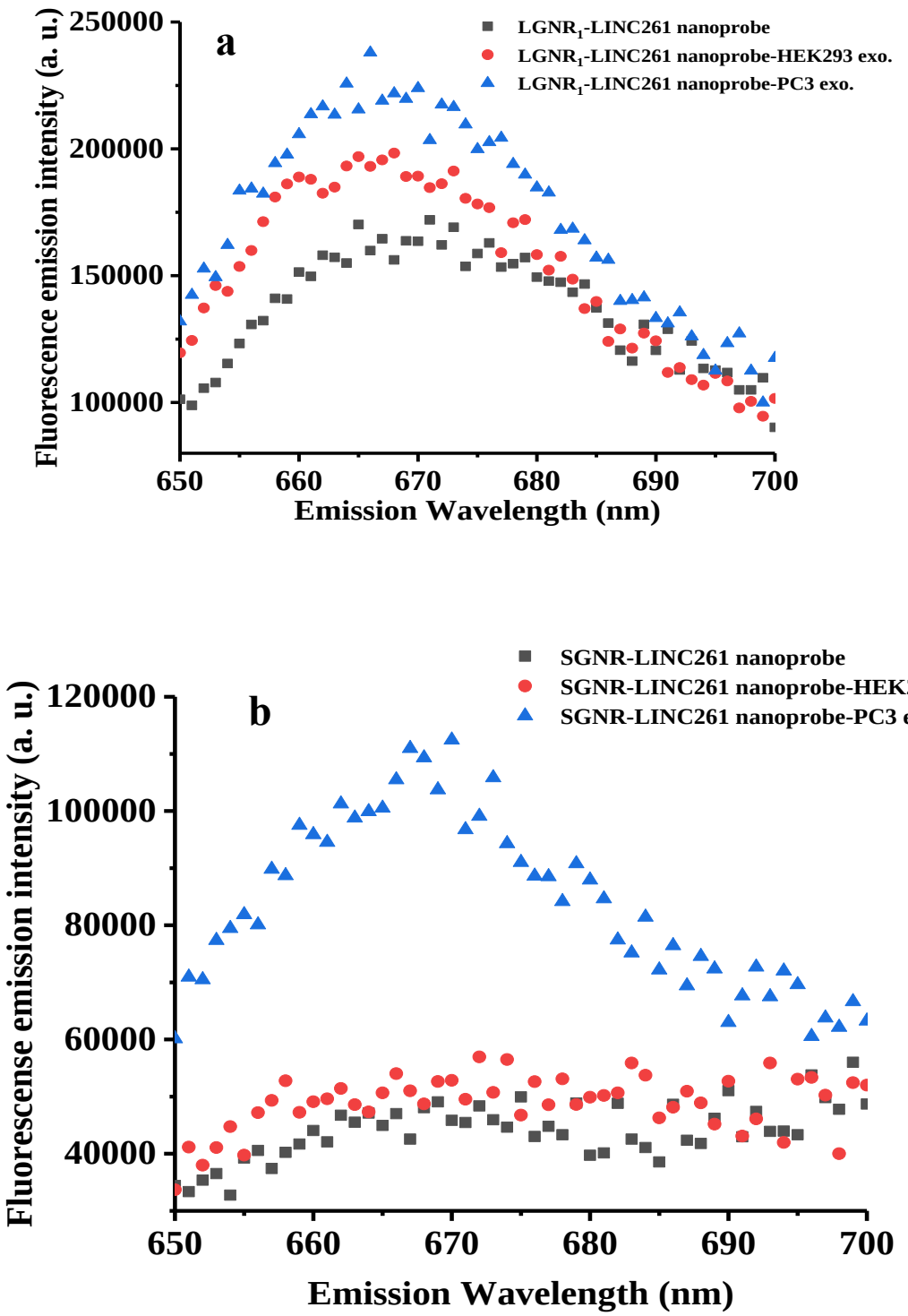

Figure 6.9. The fluorescence emission spectra of the gold nanorods nanoprobes with the cellular exosomes for 2 hours; (a) $LGNR_1$-LINC261 with the PC3 and the HEK293

cellular exosomes, (b) SGNR-LINC261 nanoprobes with the PC3 and the HEK293 cellular exosomes.

Table 6.8. The ratio of the fluorescence emission intensity increases of the $LGNR_2$-c-myc nanoprobe and the SGNR-c-myc nanoprobe incubated with the PC3 and the HEK293 cellular exosomes respectively.

Sample	The ratio of fluorescence intensity increases	
	PC3 cellular exosomes (fold)	HEK293cellular exosomes (fold)
$LGNR_1$-LINC261 nanoprobe	1.34	1.15
SGNR-LINC261 nanoprobe	2.11	1.07

Furthermore, the efficacy of the SGNR-LINC261 nanoprobe in detecting NEAR1 cancer biomaker was evaluated by incubating the SGNR-LINC261 nanoprobe with the exosomes extracted from the blood serum of a prostate cancer infected mouse (PCM) and that of the non-tumor bearing mouse (NTM). Figure 6.10. displays the fluorescence emission intensity of the SGNR-LINC261 nanoprobe incubated with the PCM and the NTM exosomes. The fluorescence emission intensity of the SGNR-LINC261 nanoprobe in the PCM exosomes was apparently increased in comparison to that from the nanoprobes control and the PCM exosomes control. Moreover, the 2. 2 fold increase in the intensity of the SGNR-LINC261 nanoprobe in the PCM exosomes against the nanoprobes control is higher than 1.7 fold increase of the same nanoprobes in the NTM exosomes. This confirms the capability of the SGNR-LINC261 nanoprobes in detecting the NEAR1 target in the blood serum derived exosomes. Moreover, the SGNR-LINC261 nanoprobe was directly applied to the blood serum of the PCM and the NTM and incubated for 1 hour. It was found that the fluorescence intensity of the SGNR-LINC261 nanoprobe in the PCM blood serum increased by 3.0 fold in comparison to the nanoprobe control, which is clearly higher than the 2.2 fold increase of the nanoprobes in the NTM

blood serum against the control as shown in fig. 6.10b. Further study is needed to investigate the influence of incubation time on the fluorescence intensity change. Nevertheless, this preliminary results suggests that the SGNR-LINC261 nanoprobe has the capacity to descriminate between a NEPC infected mouse and a healthy mouse in the blood serum and blood serum derived exosomes.

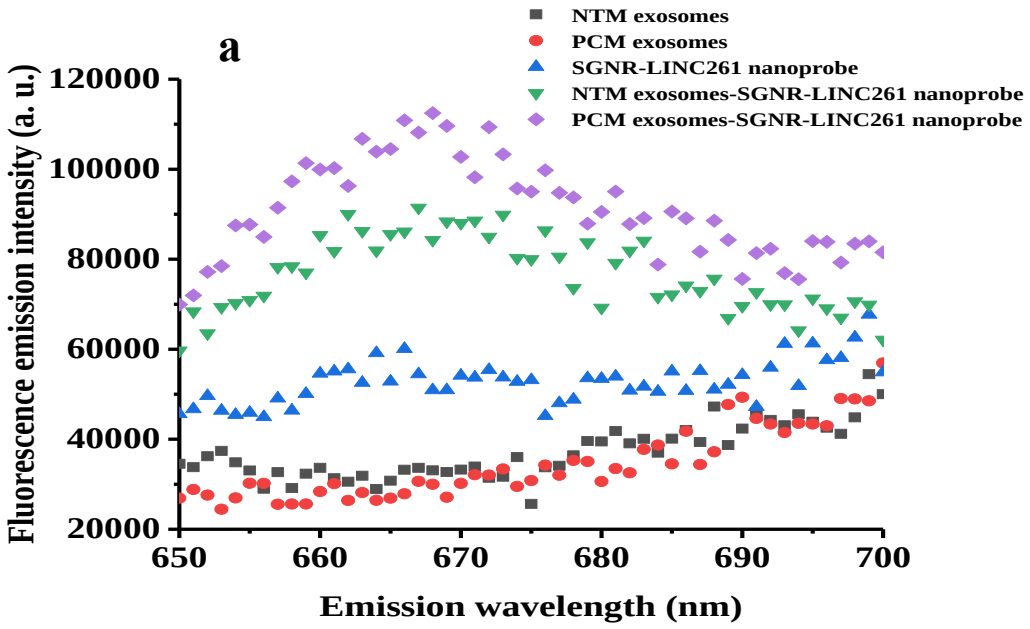

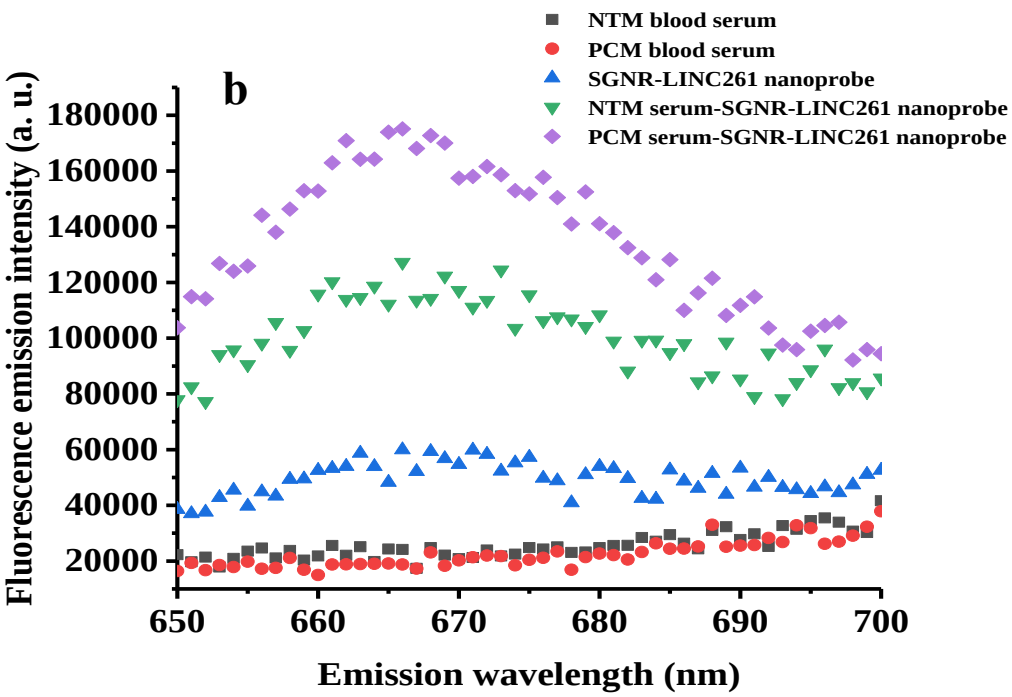

Figure 6.10. The fluorescence emission spectra of the SGNR-LINC261 nanoprobes targeting NEAR1 cancer biomaker in the blood serum; (a) SGNR-LINC261 nanoprobe incubated with the PCM and the NTM blood serum exosomes for 2 hours and (b) SGNR-LINC261 nanoprobe incubated with the PCM and the NTM blood serum for 1 hour.

6. 3. 6. Correlation of the fluorescence emission intensity of the SGNR-LINC261 nanoprobe with the exosome concentration

To investigate the influence of the PC3 exosome concentration on the fluorescence emission intensity of the SGNR-LINC261 nanoprobes, 6.93 x 10^2 – 1.00 x 10^{10} particles/ml of exosome were incubated with a fixed 0.5 nM of the SGNR-LINC261 nanoprobes. Table 1 of appendix 3 shows the fluorescence emission intensity of the SGNR-LINC261 nanoprobe with the exosome concentration. Figure 6.11. shows that the fluorescence emission intensity of the SGNR-LINC261 nanoprobe increases as the concentration of the PC3 cellular exosomes increases indicating the ability of the SGNR-

LINC261 nanoprobe to detect the NEAR1 biomaker at different concentrations of the PC3 cellular exosomes.

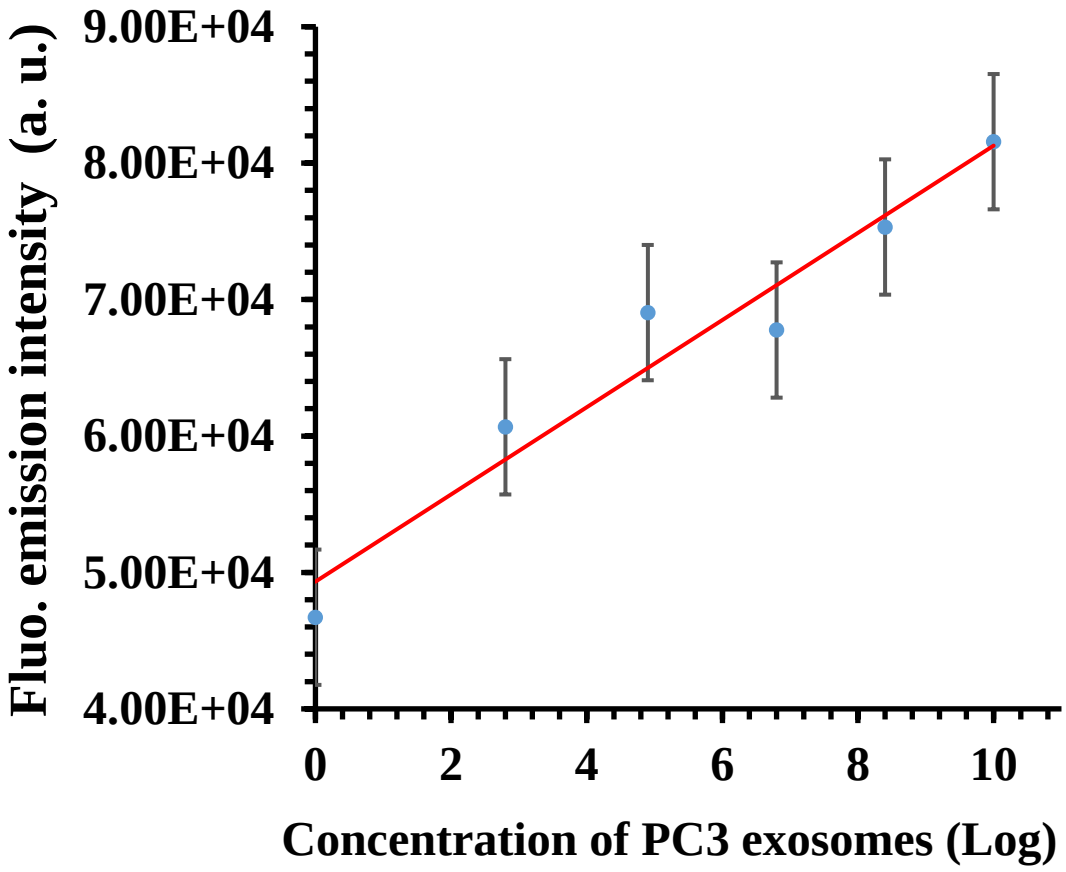

Figure 6.11. The effect of the concentration of the PC3 cellular exosomes on the sensitivity of the SGNR-LINC261 nanoprobe.

6. 4. Conclusion

Early diagnosis of prostate cancer is very essential for successful treatment of prostate cancer. This objective can only be achieved if roburst techniques are exploited to identify and target the prostate cancer biomakers with high specificity and sensitivity at the early stage of the tumorigenesis. By assembling targeting ligands on the gold nanorods nanostructure, it is demonstrated that the gold nanorods nanoprobes can be utilized in detecting biomakers associated to the prostate cancer cells. In addition to ultilizing cancer cells as models for detecting cancer, the cancer cell derived exosomes and the blood

serum exosomes are secreted at the early stage of the tumor, therefore, exosomes can be utilized as alternative models for the early diagnosis of prostate cancer. For facile and real time detection, the blood serum of prostate cancer infected mouse incubated with the SGNR nanoprobes can be used to detect prostate cancer. Flow cytometry analysis revealed that the fluorescence intensity of PC3 cells treated with the SGNR-LINC261 nanoprobes is higher than that of the HEK293 cells treated with the same nanoprobe under similar experimental conditions. Furthermore, the fluorescence intensity measurements revealed that both the small and the large gold nanorods nanoprobes were uptaken by the PC3 derived exosomes. The fluorescence intensity of the small nanorods nanoprobes incubated with the PC3 derived exosomes is more enhanced compared to that of the large gold nanorods nanoprobes.

References

1. Zhang, H.; Guo, H., Long non-coding RNA NORAD induces cell proliferation and migration in prostate cancer. *Journal of International Medical Research* **2019,** *47* (8), 3898-3904.
2. Huang, Y.-H.; Zhang, Y.-Q.; Huang, J.-T., Neuroendocrine cells of prostate cancer: biologic functions and molecular mechanisms. *Asian Journal of Andrology* **2019,** *21* (3), 291-295.
3. American Cancer Society, What is prostate cancer? https://www.cancer.org/cancer/prostate-cancer/about/what-is-prostate-cancer.html (accessed 28/022020).
4. Conteduca, V.; Oromendia, C.; Eng, K. W.; Bareja, R.; Sigouros, M.; Molina, A.; Faltas, B. M.; Sboner, A.; Mosquera, J. M.; Elemento, O.; Nanus, D. M.; Tagawa, S. T.; Ballman, K. V.; Beltran, H., Clinical features of neuroendocrine prostate cancer. *European Journal of Cancer* **2019,** *121*, 7-18.
5. Hanafi, M. M. M.; Afzan, A.; Yaakob, H.; Aziz, R.; Sarmidi, M.; Wolfender, J.-L.; Prieto, J., In vitro pro-apoptotic and anti-migratory effects of Ficus deltoidea L. plant

extracts on the human prostate cancer cell Lines PC3. *Frontiers in Pharmacology* **2017,** *8, 895-914*.

6. Bai, V.; Kaseb, A.; Tejwani, S.; Divine, G.; Barrack, E.; Menon, M.; Pardee, A.; Reddy, G., Identification of prostate cancer mRNA markers by averaged differential expression and their detection in biopsies, blood, and urine. *Proceedings of the National Academy of Sciences of the United States of America* **2007,** *104*, 2343-2348.

7. Tsai, H.; Lehrer, J.; Alshalalfa, M.; Erho, N.; Davicioni, E.; Lotan, T., Gene expression signatures of neuroendocrine prostate cancer and primary small cell prostatic carcinoma. *BMC Cancer* **2017,** *17*, 759-779.

8. Tai, S.; Sun, Y.; Squires, J.; Zhang, H.; Oh, W.; Liang, C.-Z.; Huang, J., PC3 is a cell line characteristic of prostatic small cell carcinoma. *The Prostate* **2011,** *71*, 1668-1679.

9. Mitobe, Y.; Takayama, K.; Horie-Inoue, K.; Inoue, S., Prostate cancer-associated lncRNAs. *Cancer Letters* **2018,** *418*, 159-166.

10. Das, R.; Feng, F. Y.; Selth, L. A., Long non-coding RNAs in prostate cancer: Biological and clinical implications. *Molecular and Cellular Endocrinology* **2019,** *480*, 142-152.

11. National Cancer Institute, Prostate specific antigen test. National Cancer Institute: 2017.

12. Damborska, D.; Bertok, T.; Dosekova, E.; Holazova, A.; Lorencova, L.; Kasak, P.; Tkac, J., Nanomaterial-based biosensors for detection of prostate specific antigen. *Mikrochim Acta* **2017,** *184* (9), 3049-3067.

13. Caram, M. E. V.; Skolarus, T. A.; Cooney, K. A., Limitations of prostate-specific antigen testing after a prostate cancer diagnosis. *Eur Urol* **2016,** *70* (2), 209-210.

14. Belsareb, S. Targeting and Enrichment of Exosomes using Magnetic Nanoparticles. MSc thesis, University of Florida, 2017.

15. Jiang, X.; Zong, S.; Chen, C.; Zhang, Y.; Wang, Z.; Cui, Y., Gold–carbon dots for the intracellular imaging of cancer-derived exosomes. *Nanotechnology* **2018,** *29* (17), 175701-175710.

16. Zhang, P.; Wang, L.; Fang, Y.; Zheng, D.; Lin, T.; Wang, H., Label-free exosomal detection and classification in rapid discriminating different cancer types based on

specific Raman phenotypes and multivariate statistical analysis. *Molecules* **2019,** *24* (16), 2947-2961.

17. Li, A.; Zhang, T.; Zheng, M.; Liu, Y.; Chen, Z., Exosomal proteins as potential markers of tumor diagnosis. *Journal of Hematology & Oncology* **2017,** *10* (1), 175-183.

18. Abramowicz, A.; Marczak, L.; Wojakowska, A.; Zapotoczny, S.; Whiteside, T. L.; Widlak, P.; Pietrowska, M., Harmonization of exosome isolation from culture supernatants for optimized proteomics analysis. *PloS one* **2018,** *13* (10), 0205496-0205510.

19. Nonaka, T.; Wong, D. T. W., Saliva-exosomics in cancer: molecular characterization of cancer-derived exosomes in saliva. *Enzymes* **2017,** *42*, 125-151.

20. Huebner, A. R.; Somparn, P.; Benjachat, T.; Leelahavanichkul, A.; Avihingsanon, Y.; Fenton, R. A.; Pisitkun, T., Exosomes in urine biomarker discovery. In *Urine Proteomics in Kidney Disease Biomarker Discovery*, Gao, Y., Ed. Springer Netherlands: Dordrecht, 2015; pp 43-58.

21. Ye, G.; Guo, L.; Xing, Y.; Sun, W.; Yuan, M., Identification of prognostic biomarkers of prostate cancer with long non-coding RNA-mediated competitive endogenous RNA network. *Experimental and Therapeutic Medicine* **2019,** *17*, 3035-3040.

22. Shao, H.; Chung, J.; Lee, K.; Balaj, L.; Min, C.; Carter, B. S.; Hochberg, F. H.; Breakefield, X. O.; Lee, H.; Weissleder, R., Chip-based analysis of exosomal mRNA mediating drug resistance in glioblastoma. *Nature Communications* **2015,** *6* (1), 6999-7007.

23. Matsuno, Y.; Kanke, T.; Maruyama, N.; Fujii, W.; Naito, K.; Sugiura, K., Characterization of mRNA profiles of the exosome-like vesicles in porcine follicular fluid. *PloS one* **2019,** *14* (6), 0217760-0217775.

24. Dragomir, M.; Chen, B.; Calin, G. A., Exosomal lncRNAs as new players in cell-to-cell communication. *Transl Cancer Res* **2018,** *7* (S2), S243-S252.

25. Flournoy, B., What Is Serum? https://sciencing.com/what-is-serum-4673561.html (accessed 18/09/2020).

26. Uludag, Y.; Tothill, I. E., Cancer biomarker detection in serum samples using surface plasmon resonance and quartz crystal microbalance sensors with nanoparticle signal amplification. *Analytical Chemistry* **2012,** *84* (14), 5898-5904.

27. Choi, J. H.; Kim, H. S.; Choi, J.-W.; Hong, J. W.; Kim, Y.-K.; Oh, B.-K., A novel Au-nanoparticle biosensor for the rapid and simple detection of PSA using a sequence-specific peptide cleavage reaction. *Biosensors and Bioelectronics* **2013,** *49*, 415-419.

28. Jolly, P.; Zhurauski, P.; Hammond, J. L.; Miodek, A.; Liébana, S.; Bertok, T.; Tkáč, J.; Estrela, P., Self-assembled gold nanoparticles for impedimetric and amperometric detection of a prostate cancer biomarker. *Sensors and Actuators B: Chemical* **2017,** *251*, 637-643.

29. Singh, P.; Pandit, S.; Mokkapati, V. R. S. S.; Garg, A.; Ravikumar, V.; Mijakovic, I., Gold nanoparticles in diagnostics and therapeutics for human cancer. *International journal of molecular sciences* **2018,** *19* (7), 1979-1994.

30. Mbalaha, Z. S.; Edwards, P. R.; Birch, D. J. S.; Chen, Y., Synthesis of small gold nanorods and their subsequent functionalization with hairpin single stranded DNA. *ACS Omega* **2019,** *4* (9), 13740-13746.

31. M, O. J.; Wang, P. C.; Tseng, F. G., Probing quenched dye fluorescence of Cy3-DNA-Au-nanoparticle hybrid conjugates using solution and array platforms. *J Colloid Interface Sci.* **2012,** *371* (1), 34-41.

32. Wei, G.; Yu, J.; Wang, J.; Gu, P.; Birch, D. J. S.; Chen, Y., Hairpin DNA-functionalized gold nanorods for mRNA detection in homogenous solution. *Journal of Biomedical Optics* **2016,** *21* (9), 097001-097009.

33. Rebello, R. J.; Pearson, R. B.; Hannan, R. D.; Furic, L., Therapeutic approaches targeting MYC-driven prostate cancer. *Genes* **2017,** *8* (2), 71-86.

34. Feher, J., *Quantitative Human Physiology*: *An introduction*. Academic Press: London, 2017.

35. Mather, R.; Venalainen, E.; Pucci, P.; Lin, D.; Xue, H.; Wang, Y.; Crea, F., The long non-coding RNA NEAR1 promotes neuroendocrine prostate cancer cell proliferation and survival. In *3rd International Cancer Symposium, Cancer Research Center of Lyon (CRCL), 25-27 Sep 2017,*, Lyon, France., 2017.

36. Liu, H.; Zhou, M.; Luo, X.; Zhang, L.; Niu, Z.; Peng, C.; Ma, J.; Peng, S.; Zhou, H.; Xiang, B.; Li, X.; Li, S.; He, J.; Li, X.; Li, G., Transcriptional regulation of BRD7 expression by Sp1 and c-Myc. *BMC Mol Biol* **2008,** *9*, 111-124.

37. Lobb, R.; Becker, M.; Wen, S.; Wong, C.; Wiegmans, A.; Leimgruber, A.; Möller, A., Optimized exosome isolation protocol for cell culture supernatant and human plasma. *Journal of extracellular vesicles* **2015,** *4*, 27031-27042.

38. Thermo Fisher Scientific, Total Exosome Isolation Reagent (from cell culture media). https://www.thermofisher.com/order/catalog/product/4478359#/4478359.

39. Patel, G. K.; Khan, M. A.; Zubair, H.; Srivastava, S. K.; Khushman, M. d.; Singh, S.; Singh, A. P., Comparative analysis of exosome isolation methods using culture supernatant for optimum yield, purity and downstream applications. *Scientific Reports* **2019,** *9* (1), 5335-5344.

40. Gans, R., Über die Form ultramikroskopischer Goldteilchen. *Ann. Phys.* **1912,** *342* (5), 881-900.

41. Link, S.; Mohamed, M. B.; El-Sayed, M. A., Addition and correction. *J. Phys. Chem. B* **2005,** *109* (20), 10531-10532.

42. Shi, W.; Casas, J.; Venkataramasubramani, M.; Tang, L., Synthesis and characterization of gold nanoparticles with plasmon absorbance wavelength tunable from visible to near infrared region. *ISRN Nanomaterials* **2012,** *2012*, 659043-659052.

43. Sharma, V.; Park, K.; Srinivasarao, M., Shape separation of gold nanorods using centrifugation. *Proceedings of the National Academy of Sciences* **2009,** *106* (13), 4981-4985.

44. Song, Y.; Shi, Y.; Huang, M.; Wang, W.; Wang, Y.; Cheng, J.; Lei, Z.; Zhu, Z.; Yang, C., Bioinspired engineering of a multivalent aptamer-functionalized nanointerface to enhance the capture and release of circulating tumor cells. *Angew. Chem. Int. Ed.* **2019,** *58*, 2236-2240.

45. Unser, S.; Bruzas, I.; He, J.; Sagle, L., Localized surface plasmon resonance biosensing: current challenges and approaches. *Sensors* **2015,** *15* (7), 15684-15716.

46. Saha, K.; Agasti, S. S.; Kim, C.; Li, X.; Rotello, V. M., Gold nanoparticles in chemical and biological sensing. *Chemical Reviews* **2012,** *112* (5), 2739-2779.

47. Zhang, Y.; Wei, G.; Yu, J.; Birch, D. J. S.; Chen, Y., Surface plasmon enhanced energy transfer between gold nanorods and fluorophores: application to endocytosis study and RNA detection. *Faraday Discuss* **2015,** *178*, 383-394.

48. Zhang, Y.; Birch, D. J. S.; Chen, Y., Two-photon excited surface plasmon enhanced energy transfer between DAPI and gold nanoparticles: opportunities in intra-cellular imaging and sensing. *Appl. Phys. Lett.* **2011,** *99*, 103701-103703.

49. Hill, H. D.; Millstone, J. E.; Banholzer, M. J.; Mirkin, C. A., The role radius of curvature plays in thiolated oligonucleotide loading on gold nanoparticles. *ACS Nano* **2009,** *3* (2), 418-424.

50. Lakowicz, J. R., *Principles of Fluorescence Spectroscopy*. 3rd ed.; Springer: New York, 2006.

51. Ray, K.; Zhang, J.; Lakowicz, J. R., Fluorescence lifetime correlation spectroscopic study of fluorophore-labeled silver nanoparticles. *Analytical Chemistry* **2008,** *80* (19), 7313–7318.

52. Zhang, J.; Fu, Y.; Chowdhury, M. H.; Lakowicz, J. R., Single-molecule studies on fluorescently labeled silver particles: effects of particle size. *The Journal of Physical Chemistry C* **2008,** *112* (1), 18-26.

53. Adan, A.; Alizada, G.; Kiraz, Y.; Baran, Y.; Nalbant, A., Flow cytometry: basic principles and applications. *Critical Reviews in Biotechnology* **2017,** *37* (2), 163-176.

54. Rajagopal, C.; Harikumar, K. B., The Origin and Functions of Exosomes in Cancer. *Frontiers in Oncology* **2018,** *8* (66), 1-13.

Chapter 7

Summary and conclusion

Small gold nanorods (SGNRs) have been demonstrated in various biomedical applications due to their fascinating features such as large absorption and scattering cross-sections, enhanced heat generation for photothermal applications, photostability, biocompatibility, deep tissue penetration, tunable size and shape. Utilization of these features requires synthesis of stable SGNRs for biomedical applications. A systematic study on the growth conditions was carried out and a reliable method has been developed for the synthesis of stable SGNRs with good control over size and shape, and high yield of rods. These SGNRs were successfully functionalized with hairpin DNA (hpDNA) for targeting messenger RNA (mRNA).

It is found that the peaks of the extinction spectra determined by experimental study matched well with that predicted by Gans model. The extinction cross-section of both the SGNRs and the LGNRs is enhanced as the longitudinal surface plasmon resonance overlaps the incident wavelength. The SGNRs and the LGNRs experienced a blue shift of longitudinal surface plasmon resonance in agarose gel media; the blue shift is more significant for the LGNRs compared to the SGNRs. The concentration of agarose gel has significant influence on the longitudinal surface plasmon resonance of gold nanorods. Moreover, this work investigated the influence of the size of gold nanorods and media on their photothermal effects. Theoretical calculation revealed that the SGNRs have higher photothermal efficiency than the LGNRs in solution. However, experimental study revealed that the SGNRs generated slightly more heat than the LGNRs at off-resonance illumination, while the LGNRs generated more heat than the SGNRs at plasmon resonance excitation in solution. Nevertheless, the SGNRs generated more heat than the LGNRs when both are in gel media that is close to a cell enviroment.

Cancer cells manifest multiple biomarkers both on the cell membrane and in the cell cytoplasm. Thus, the SGNRs and the LGNRs have been functionalized with SYL3C aptamer probes for targeting EpCAM over-expression on the cell membrane of cancer cells of epithelia origin. Microscopic imaging revealed that the SYL3C aptamer based SGNRs nanoprobes bind on the cell membrane of EpCAM over-expressed cancer cells. The aptamer functionalized SGNRs based nanoprobes were found to have higher

photothermal effect in cancer cells compared to the aptamer functionalized LGNRs nanoprobes. Furthermore, the SGNRs and the LGNRs were functionalized with LINC261 hairpin DNA for targeting neuroendocrine long non-coding RNA 1 (NEAR1) biomarker in the cells and the exosomes. The SGNRs based nanoprobes were found to be more sensitive than the LGNRs based nanoprobes in detecting NEAR1 cancer biomarker in cells and exosomes.

In conclusion, this work has demonstrated the synthesis and functionalization of stable SGNRs based nanoprobes for detecting cancer biomarkers. The nanoprobes have demonstrated capacity to detect cancer biomarkers and strong photothermal effect to treat cancer disease. However, quantification of the packing density of hpDNA molecules on the SGNRs and the LGNRs was not investigated. Characterization of the gold nanorods nanoprobes in a mouse model was not explored in this work. Further research is urgently needed to quantify the effect of the packing density of hpDNA molecules assembled on both the SGNRs and the LGNRs nanoprobes efficiency. Future work is planned to test the SGNRs-LINC261 nanoprobes on clinical samples such as blood serum from a prostate cancer patient and a non-prostate cancer patient to ascertain the specificity and sensitivity of these nanoprobes in targeting cancer biomarkers in clinical samples.

Appendix 1

Histogram of the length and width distribution of the small gold and the large nanorods

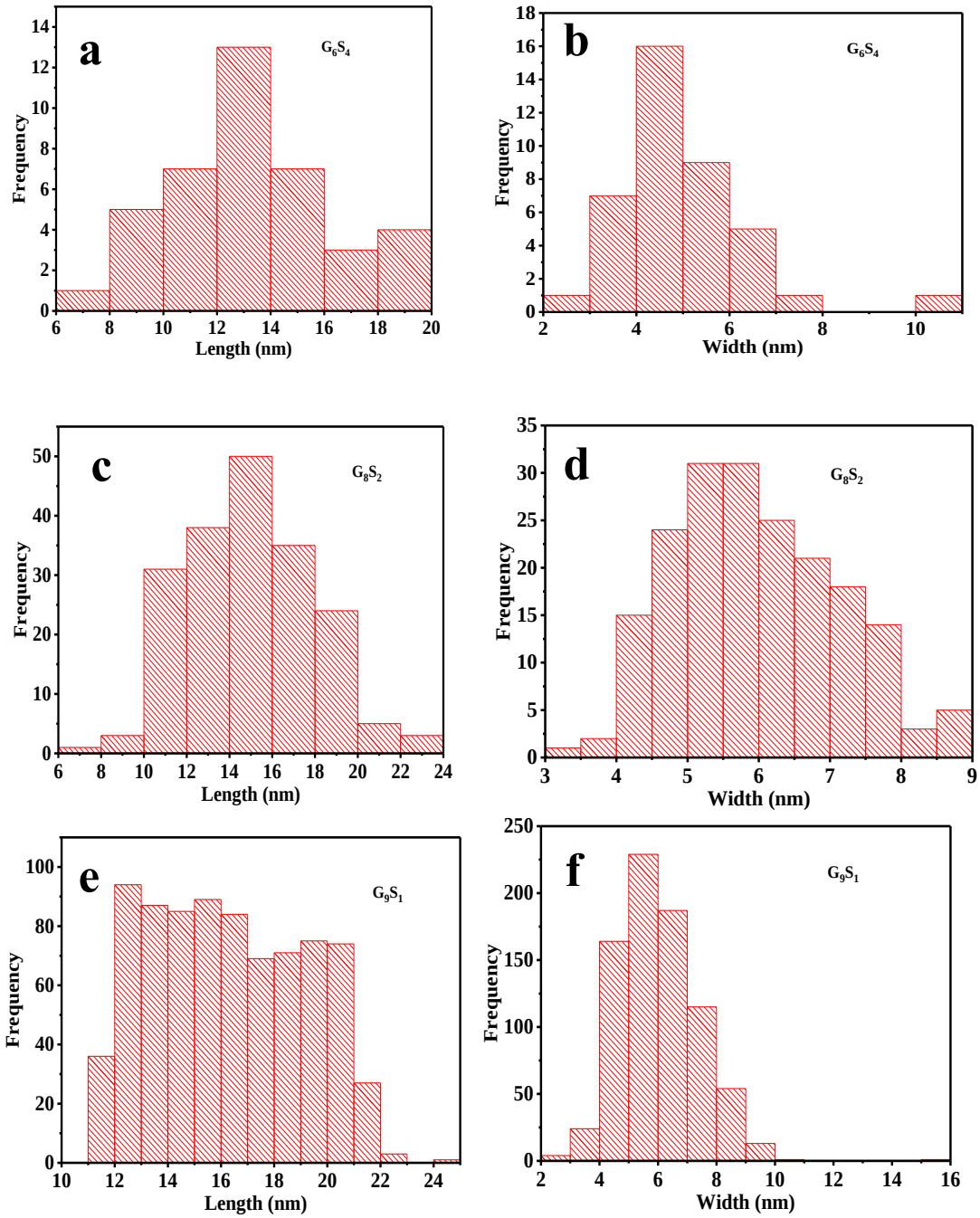

Figure 1. Histogram of length and width of distribution; (a, b) length and width of G_6S_4 (c, d) length and width of G_8S_2 and (e, f) length and width of G_9S_1.

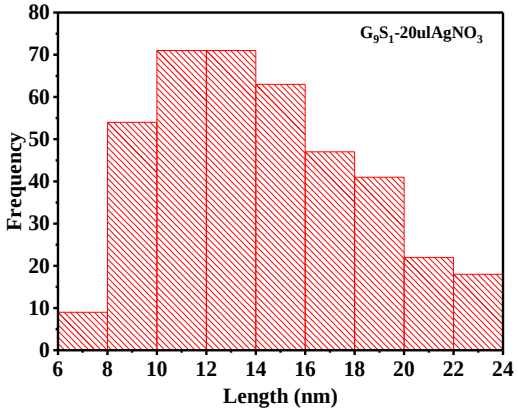
G_9S_1-20ulAgNO$_3$
Frequency
Length (nm)

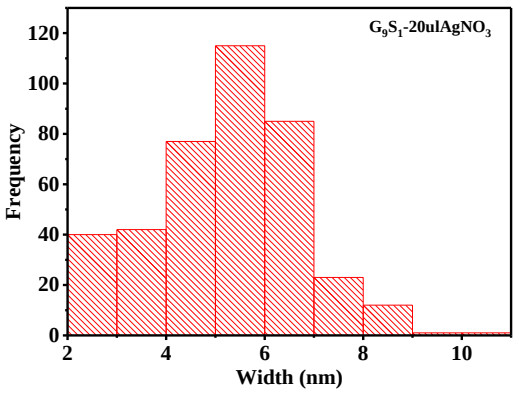
G_9S_1-20ulAgNO$_3$
Frequency
Width (nm)

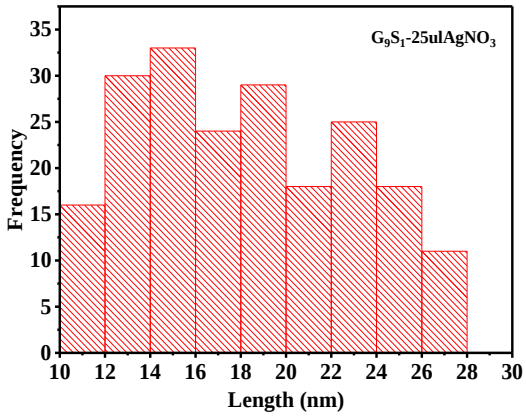
G_9S_1-25ulAgNO$_3$
Frequency
Length (nm)

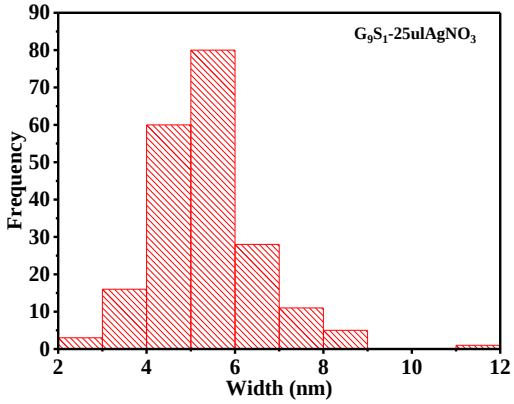
G_9S_1-25ulAgNO$_3$
Frequency
Width (nm)

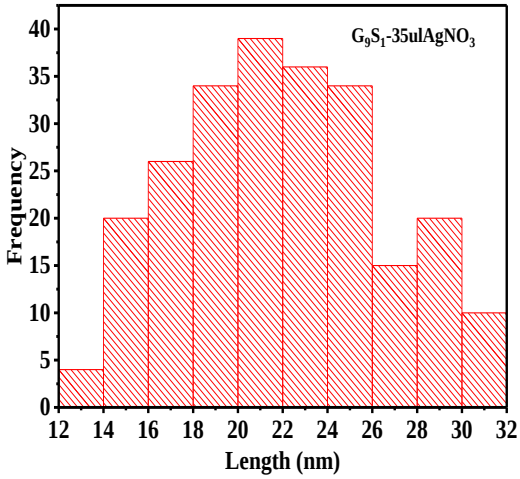
G_9S_1-35ulAgNO$_3$
Frequency
Length (nm)

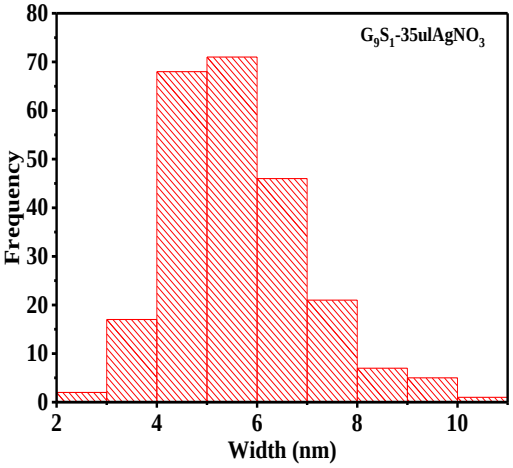
G_9S_1-35ulAgNO$_3$
Frequency
Width (nm)

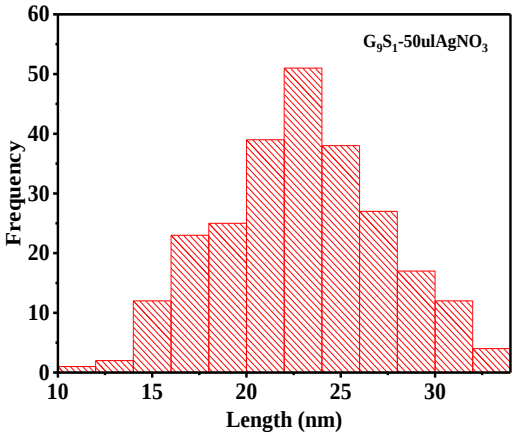
G_9S_1-50ulAgNO$_3$
Frequency
Length (nm)

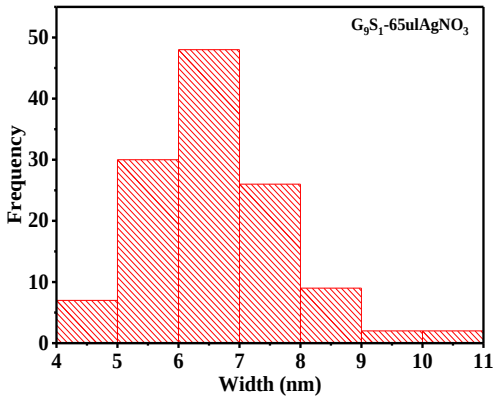
G_9S_1-65ulAgNO$_3$
Frequency
Width (nm)

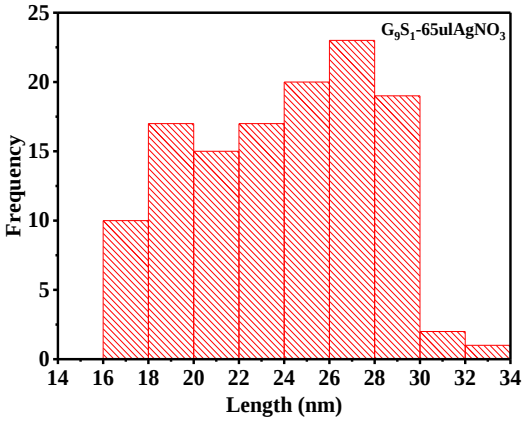
G_9S_1-65ulAgNO$_3$
Frequency
Length (nm)

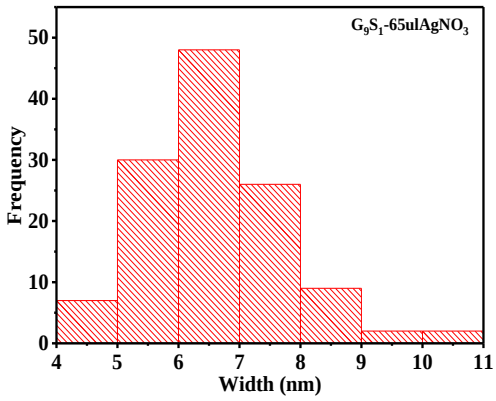
G_9S_1-65ulAgNO$_3$
Frequency
Width (nm)

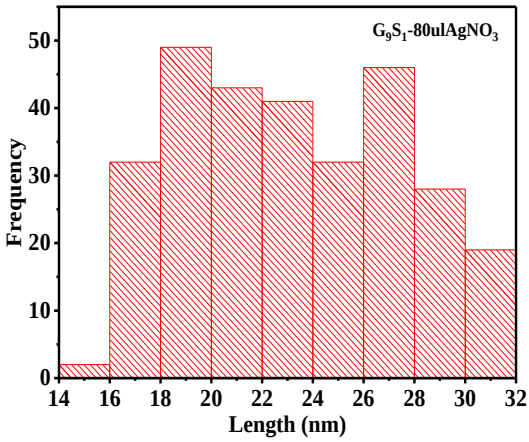
G_9S_1-80ulAgNO$_3$
Frequency
Length (nm)

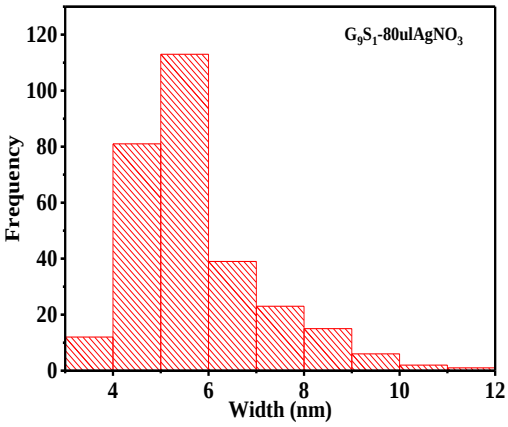
G_9S_1-80ulAgNO$_3$
Frequency
Width (nm)

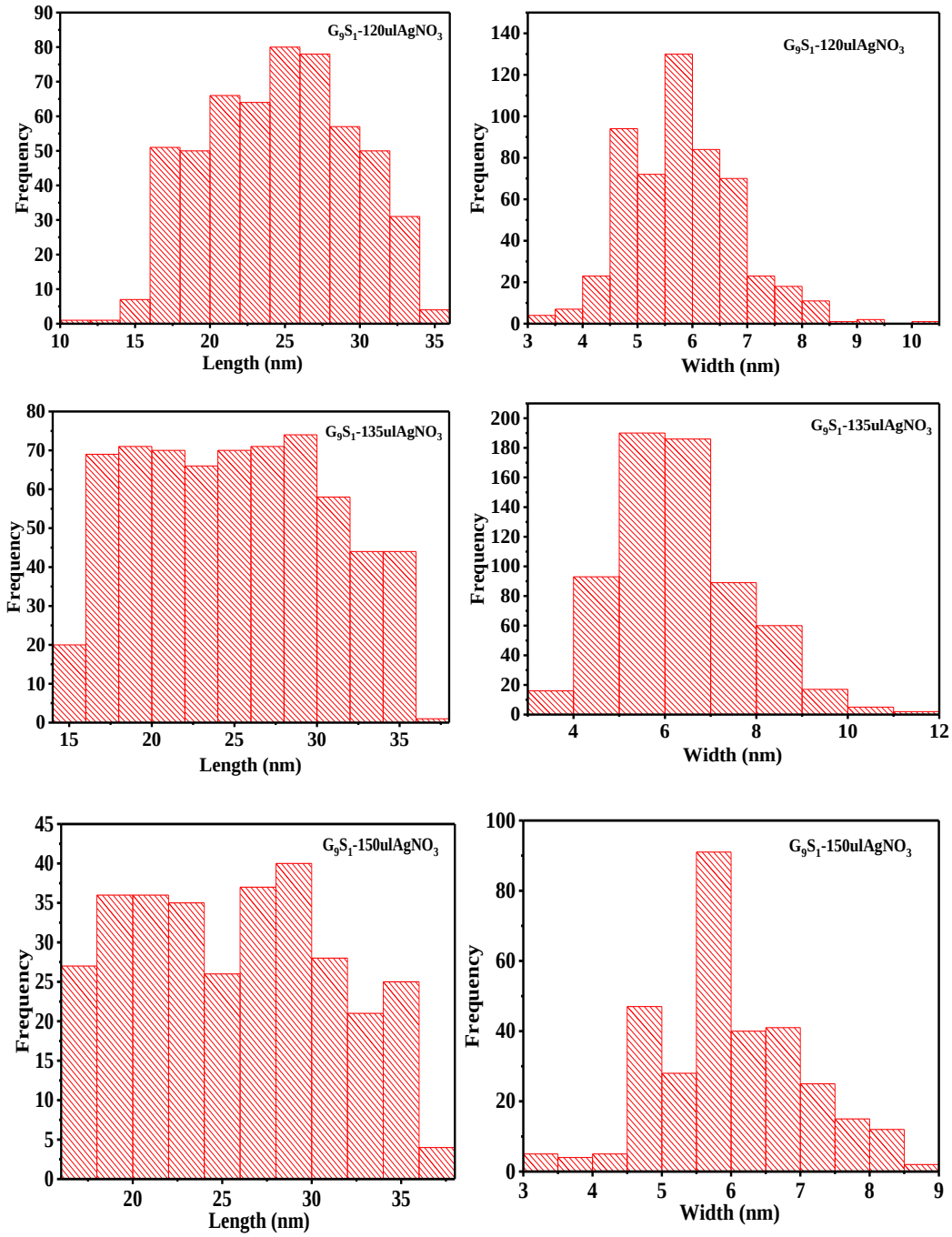

Figure 2. Histogram of length and width of G_9S_1-20ul$AgNO_3$ to G_9S_1-150ul$AgNO_3$. Histogram of the length and width distribution of L816 and S817 samples.

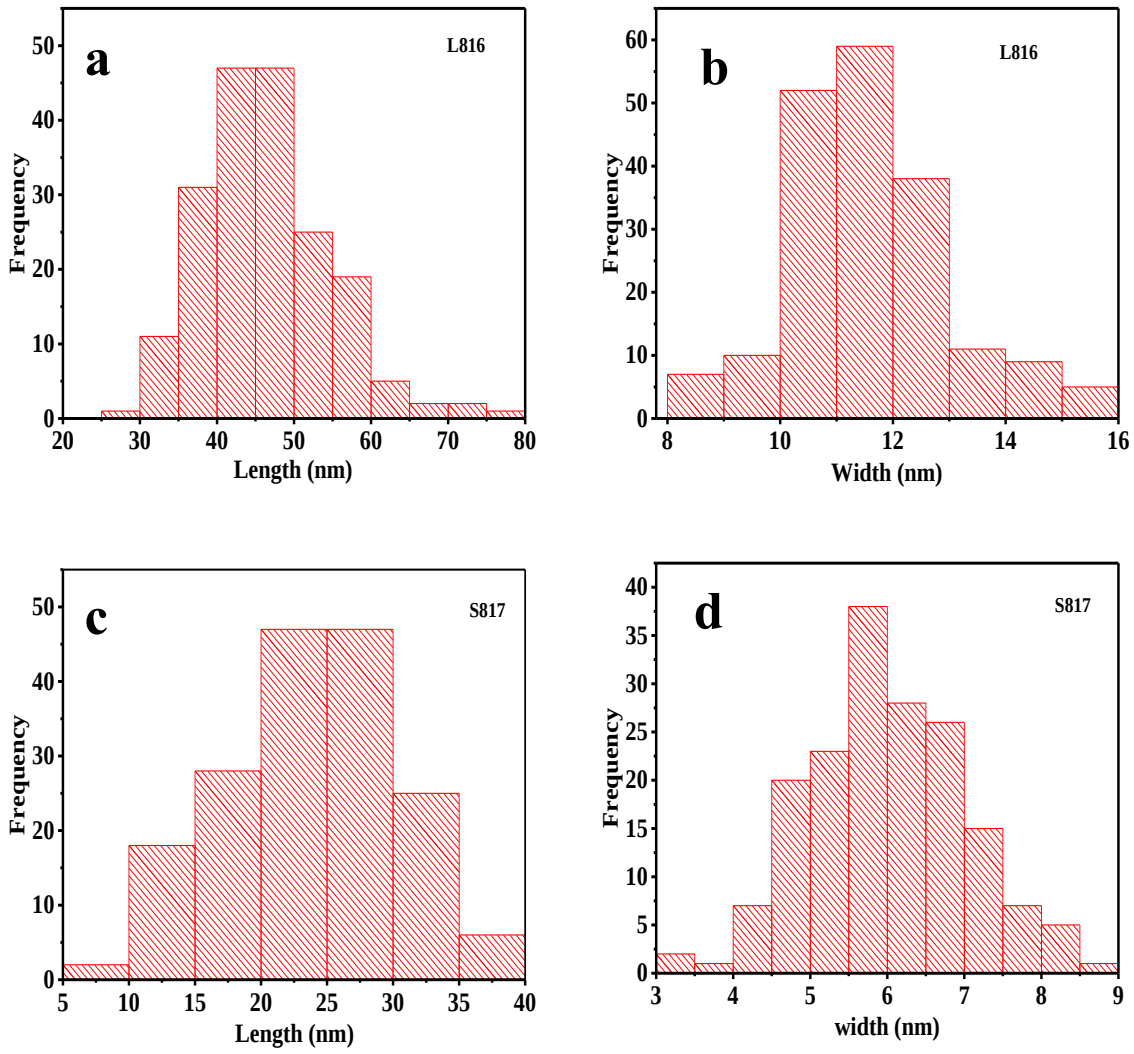

Figure 3. Histogram of length and width of distribution; (a, b) length and width of L816. (c, d) length and width of S817.

Appendix 2

Calibration curve of the SGNRs and the LGNRs, blue shift at varying concentrations of TBE buffer and water agarose gel, and the temperature profiles of SGNRs and LGNRs in water and agarose gel.

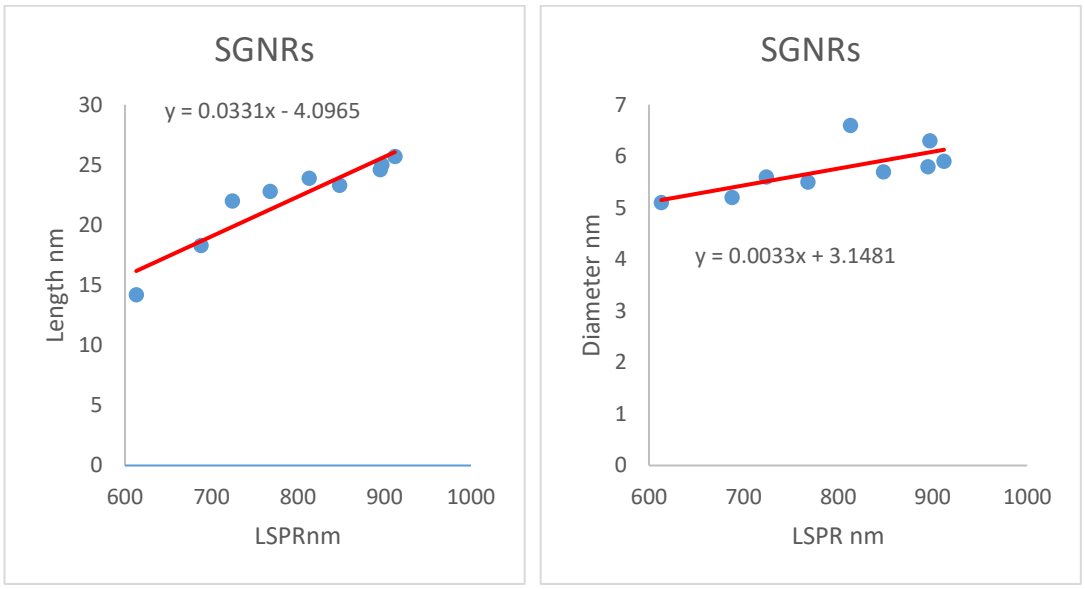

Figure 1. Standard calibration curve of the dimensions of SGNRs

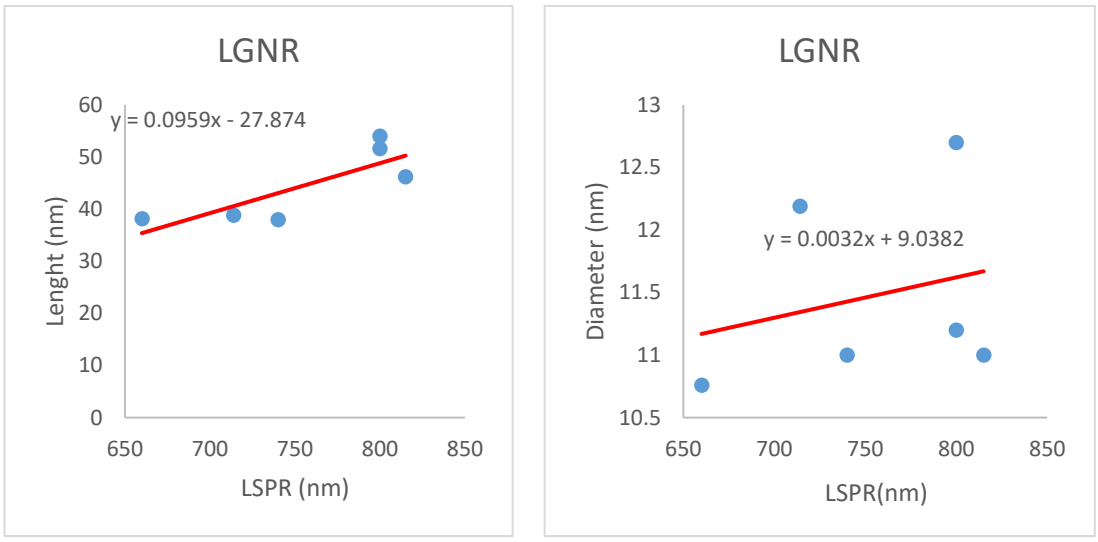

Figure 2. Standard calibration curve of the dimensions of LGNRs

Temperature profile of the SGNRs and the LGNRs excited at different wavelength in water and agarose gel.

Table 1a. Normalised temperature profile of SGNRs excited at different wavelength in water.

Time (mins.)	Temperature (^{0}C)								
	Excitation:715nm (2.74±0.16W/cm^2)			Excitation: 750nm 2.74±0.16W/cm^2			Excitation:800nm (2.74±0.16W/cm^2)		
	S720	**S754**	**S817**	**S720**	**S754**	**S817**	**S720**	**S754**	**S817**
2	25.05	25.11	22.96	23.05	23.10	22.90	22.57	22.87	22.96
4	28.15	28.52	26.27	26.35	26.65	26.20	25.23	26.27	26.27
6	30.23	30.71	28.24	28.50	29.00	28.10	27.01	28.83	28.24
8	31.72	32.41	29.57	30.05	30.95	29.70	28.83	30.70	29.57
10	32.89	33.69	30.51	31.25	32.40	30.75	30..41	32.08	30.57
12	33.05	34.60	31.24	32.25	33.40	31.60	30.01	32.87	31.24
14	33.48	33.85	31.83	32.90	33.55	32.10	31.10	33.31	31.83
16	33.69	34.01	32.13	33.30	33.40	32.05	31.79	33.17	32.13

Table 1b. Normalised temperature profile of LGNRs excited at different wavelength in water.

Time (mins.)	Temperature (^{0}C)								
	Excitation:715nm (2.74±0.16W/cm^2)			Excitation: 750nm 2.74±0.16W/cm^2			Excitation:800nm (2.74±0.16W/cm^2)		
	L719	**L755**	**L816**	**L719**	**L755**	**L816**	**L719**	**L755**	**L816**
2	25.43	24.57	22.71	23.40	24.10	22.55	22.27	22.52	23.95
4	29.59	27.40	23.94	27.10	27.50	24.75	24.99	25.63	27.40
6	32.52	29.53	24.89	29.45	30.00	26.75	26.76	27.84	29.96
8	34.22	30.92	25.80	31.15	32.10	28.40	27.99	29.52	31.54
10	35.72	31.72	26.44	32.05	33.30	29.45	28.83	30.60	32.87
12	35.72	30.71	26.76	32.55	34.20	30.40	29.42	31.00	32.82
14	35.13	31.88	26.55	33.10	35.20	30.30	29.57	30.50	33.12
16	36.41	32.58	26.92	33.15	35.10	30.35	28.98	30.31	34.30

Longitudinal surface plasmons resonance of L784 in water and agarose gel.

Table 2. The longitudinal surface plasmons resonance of L784 at different concentration of agarose hydrogel dissolved in TBE buffer and water solvents.

Concentration of agarose gel media (%)	LSPR (nm)			
	TBE buffer-agarose hydrogel	Water-agarose hydrogel	Blue shift in TBE buffer-agar. hydrogel	Blue shift in water-agarose hydrogel
0.3	764	784	20	0
0.5	761	784	23	0
0.7	761	784	23	0
1.1	760	784	24	0
1.5	743	783	41	1
2.0	717	778	67	6
2.5	717	758	67	26

Table 3a. Normalised temperature profile of SGNR excited at different wavelength in TBE buffer agarose gel.

Time (mins.)	Temperature (^{0}C)								
	Excitation:715nm (2.74±0.16W/cm^2)			Excitation: 750nm 2.74±0.16W/cm^2			Excitation:800nm (2.74±0.16W/cm^2)		
	S720	**S754**	**S817**	**S720**	**S754**	**S817**	**S720**	**S754**	**S817**
2	21.59	21.43	21.32	20.00	20.02	20.75	19.71	20.01	21.39
4	23.67	23.30	22.71	21.70	21.80	22.90	20.75	22.47	24.94
6	26.12	25.37	24.36	23.60	23.90	24.90	22.08	24.54	27.45
8	28.31	26.97	26.44	25.20	25.90	26.40	23.26	26.17	28.98
10	30.33	28.25	27.51	26.25	27.75	27.45	24.30	27.30	30.26
12	31.72	28.84	27.67	27.00	31.75	28.35	25.03	27.89	31.19
14	31.13	28.36	27.72	26.30	31.00	29.00	24.94	27.30	32.03
16	30.54	28.95	28.68	26.85	32.20	28.70	24.49	27.60	32.57

Table 3b. Normalised temperature profile of LGNRs excited at different wavelength in TBE buffer agarose gel.

Time (mins.)	Temperature (^{0}C)								
	Excitation:715nm 2.57±0.15W/cm^2			Excitation: 750nm 2.74±0.16W/cm^2			Excitation:800nm 2.78±0.05W/cm^2		
	L719	**L755**	**L816**	**L719**	**L755**	**L816**	**L719**	**L755**	**L816**
2	22.12	21.38	23.03	20.70	19.85	20.90	19.91	19.76	20.89
4	23.56	22.66	25.32	21.85	20.90	22.40	20.60	20.70	22.18
6	25.27	24.09	27.24	22.90	22.15	23.60	21.54	21.68	23.01
8	25.75	25.27	28.31	23.90	23.40	23.85	22.32	22.82	23.90
10	26.49	26.17	28.47	24.65	24.20	23.95	22.92	23.75	24.59
12	27.56	26.44	29.21	25.25	24.90	24.80	23.01	24.59	25.38
14	28.25	26.92	29.96	25.70	25.10	25.75	23.16	24.79	25.92
16	28.95	27.40	30.76	25.05	25.40	26.65	23.75	24.69	26.22

Appendix 3

Histogram of the length and width distribution of $LGNR_1$and SGNR samples

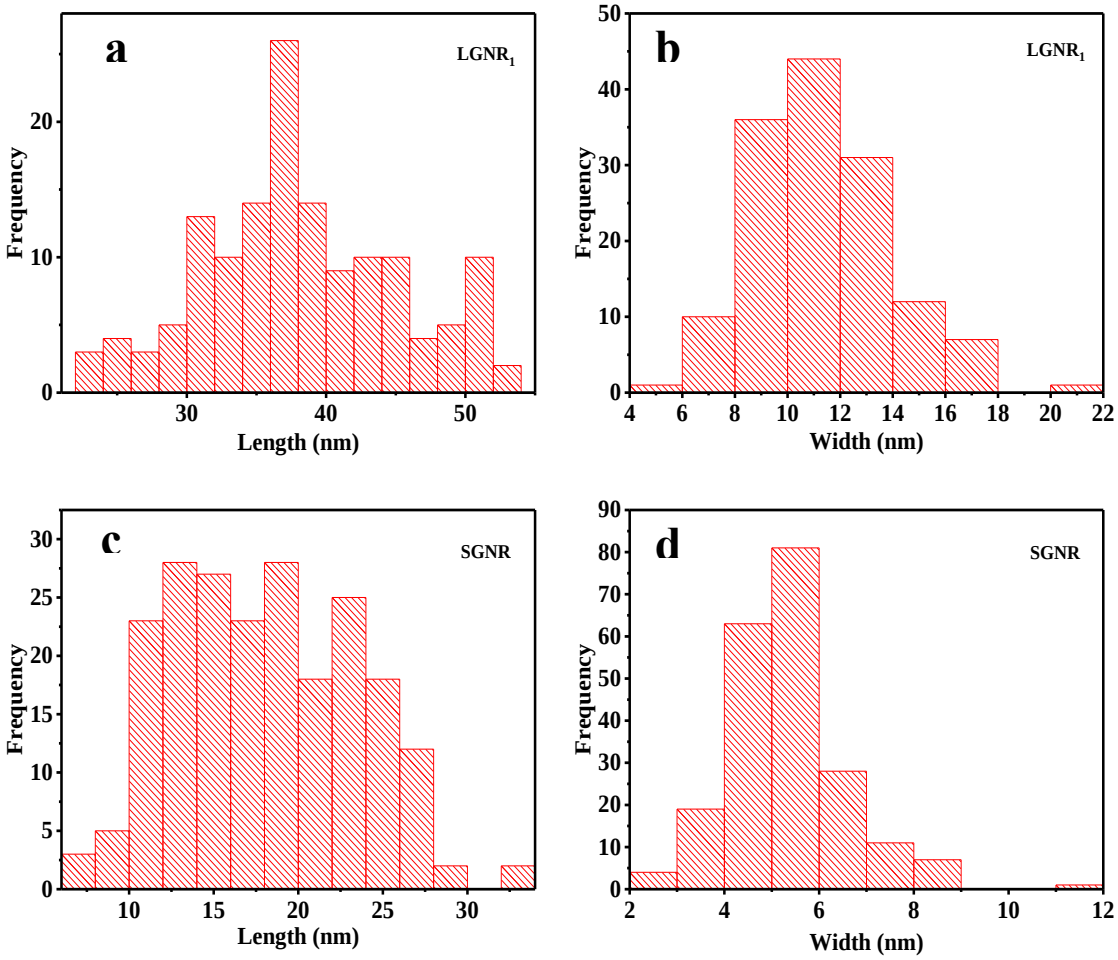

Figure 1. Histogram of length and width of distribution; (a, b) length and width of $LGNR_1$. (c, d) length and width of SGNR.

Table 1. The correlation of fluorescence emission intensity of SGNR-LINC261 nanoprobe and exosome concentration.

Conc. of PC3 cellular exosomes (particles/ml)	Conc. of PC3 cellular exosomes (Log)	Fluorescence emission intensity of SGNR-LINC261 nanoprobe (a. u.)
6.93×10^2	2.8	60673.23
8.00×10^4	4.9	69043.78
6.25×10^6	6.8	67768.94
2.50×10^8	8.4	75320.03
1.00×10^{10}	10.0	81572.38

Appendix 4.

Procedure for fitting the fluorescence lifetime decay curve with a multi-exponential decay model

DAS6 software was used to fit the fluorescence lifetime decay curve using a multi-exponential decay model. The decay as a function of time is given by[1]:

$$F(t) = A + B_1 \exp\left(-\frac{t}{\tau_1}\right) + B_2 \exp\left(-\frac{t}{\tau_2}\right)$$

where A is the original amount, B is the relative amplitude, t is the time and τ is the lifetime. Displayed in fig. 1. is the dialogue box of a fluorescence lifetime decay curve of a dummy sample saved in DAS6 software.

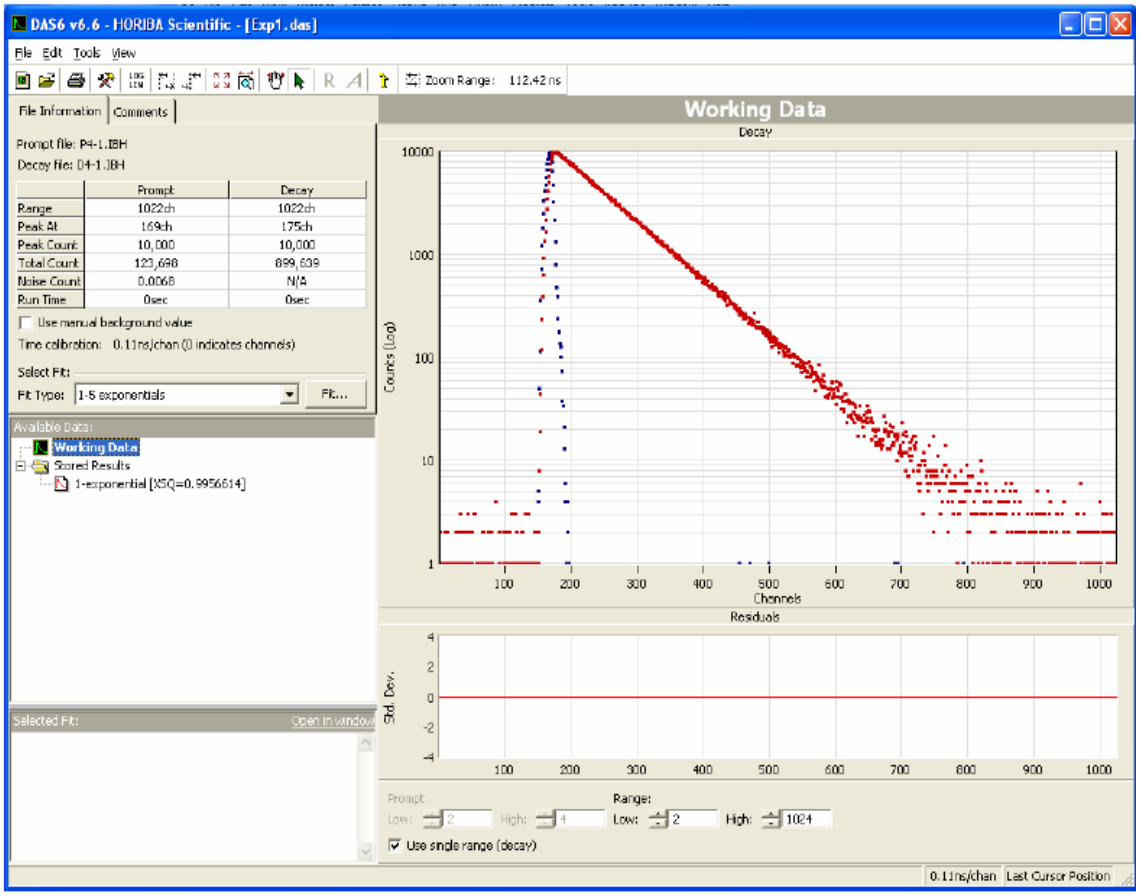

Figure 1. The dialogue box of fluorescence decay curve saved in DAS6 software.

1. Select the range of fluorescence decay (red curve) from the beginning to the end of the fluorescence decay curve.

2. Click fit tab on the middle left. Then a dialogue box shown in fig 3.2. will be displayed

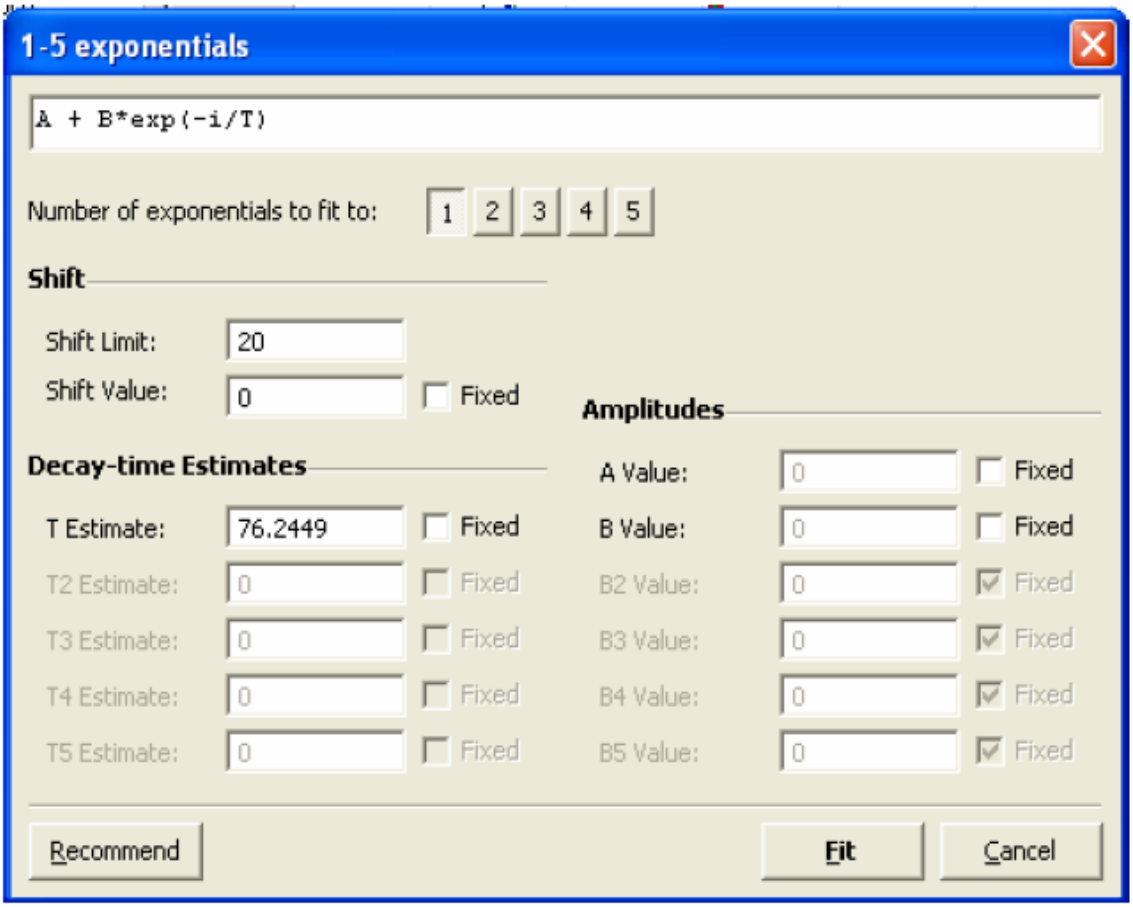

Figure 2. The dialogue box showing the number of exponentials to fit to.

3. The number of exponential decays to be selected is determined by the number of lifetimes from different species in the microenvironment. For free fluorophores in solution, the opened and closed fluorophores exist, thus 2 exponential decays are recommended to determine the fluorescence lifetime of free fluorophore opened and closed in the solution. For fluorophore labeled gold nanorod based nanoprobes, the lifetime of opened and closed fluorophore and gold cores (scattering excitation) co-exist in the solution, thus 3 exponential decays are recommended. However, to eliminate the contribution of the scattered excitation, it is recommended that τ_1 should be fixed at 0.5. channel. After the appropriated number of exponential decays are selected, then click on the fit button at bottom right. The fitting displays the result as shown in fig 3.3.

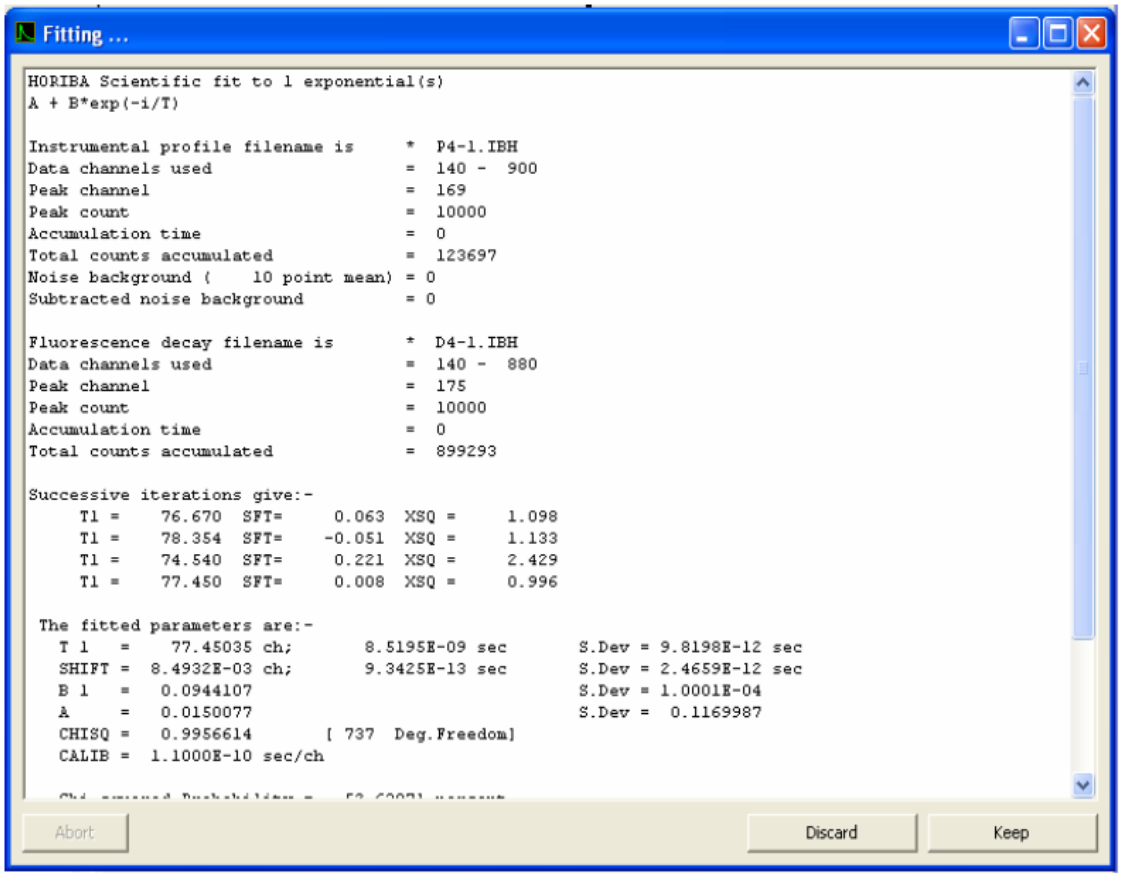

Figure 3. The dialogue box showing measured parameters.

4. For a good fit, χ^2 should be near 1.0 but ≤ less 1.2. In addition, the prior knowledge of the lifetimes is required to either accept the measured lifetime or discard it.

5. The average lifetime can be determined by calculation using equation 2.5.

Reference

1. Horiba Scientific, DAS-6 operational manual. Part number J81119 rev. A.

Appendix 5.

Fittings of the fluorescence lifetime decay curves of the gold nanorods based nanoprobes

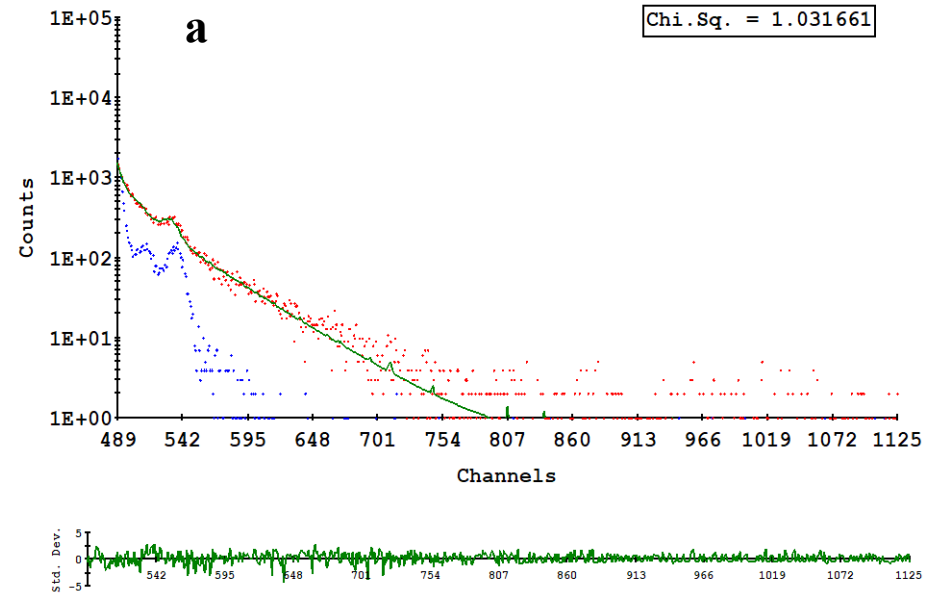

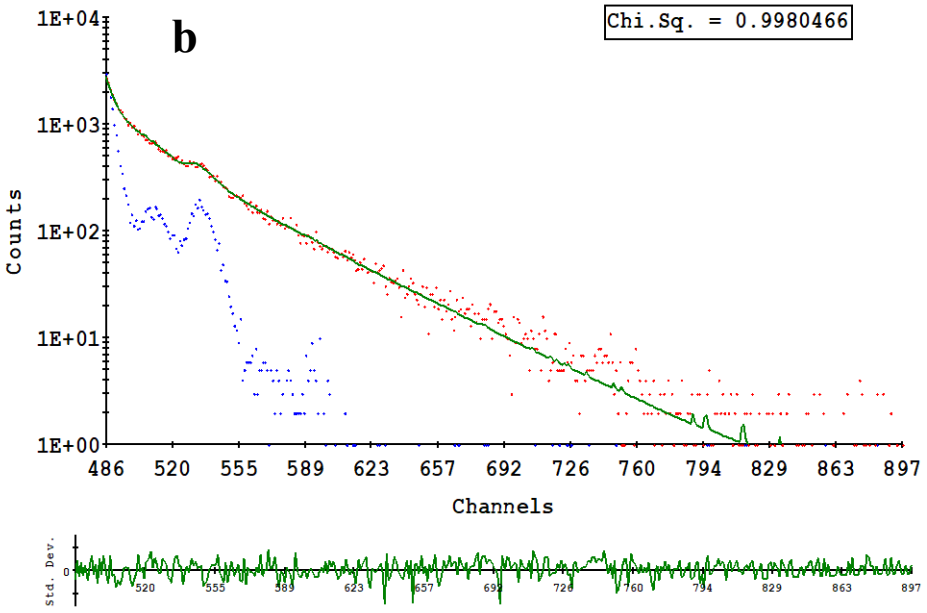

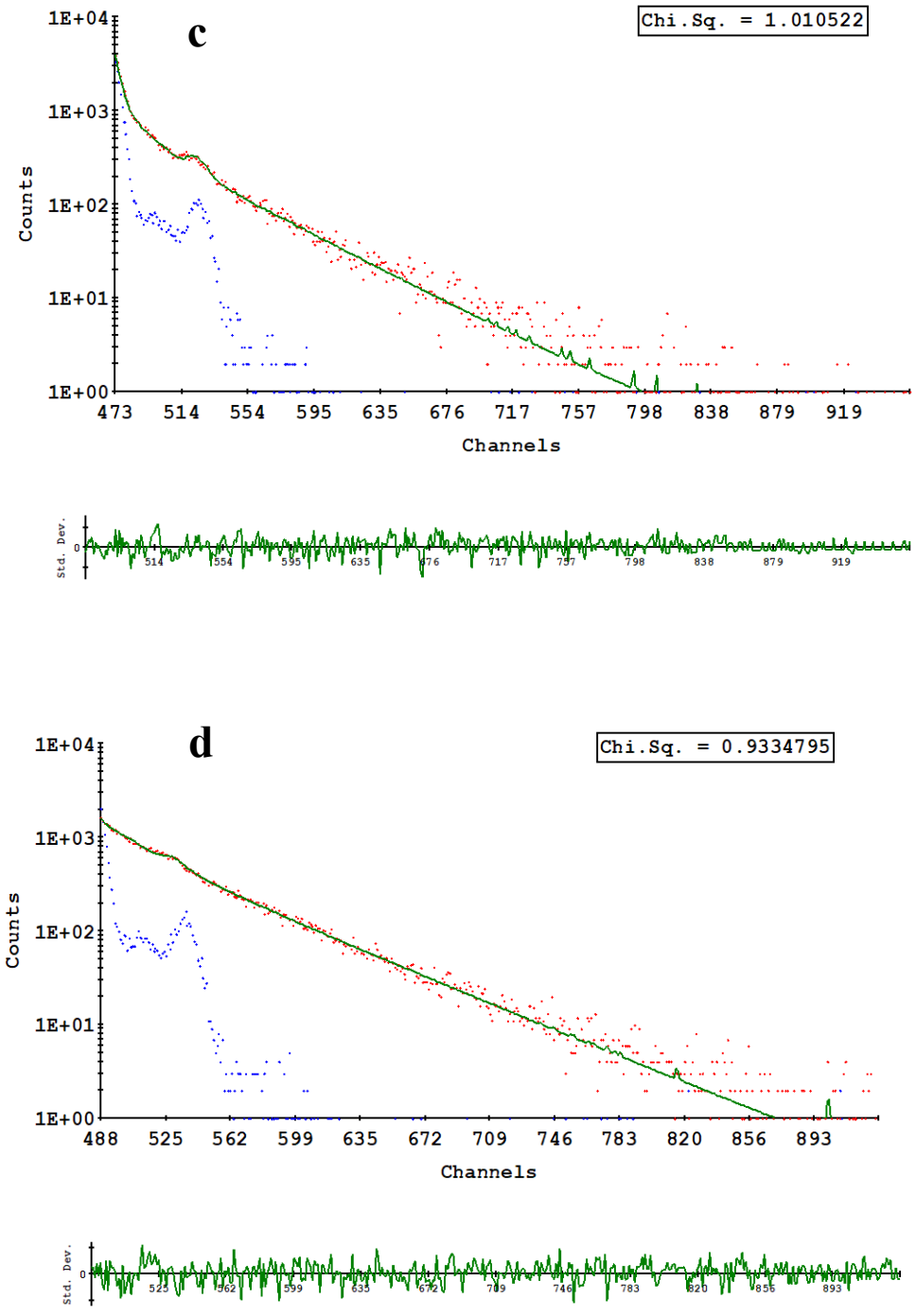

Figure 1. The fittings of the fluorescence decay curves of the SGNRs nanoprobes; (a) $SGNR_1$-hpDNA, (b) $SGNR_1$-hpDNA-cDNA, (c) $SGNR_2$-hpDNA, (d) $SGNR_2$-hpDNA-cDNA.

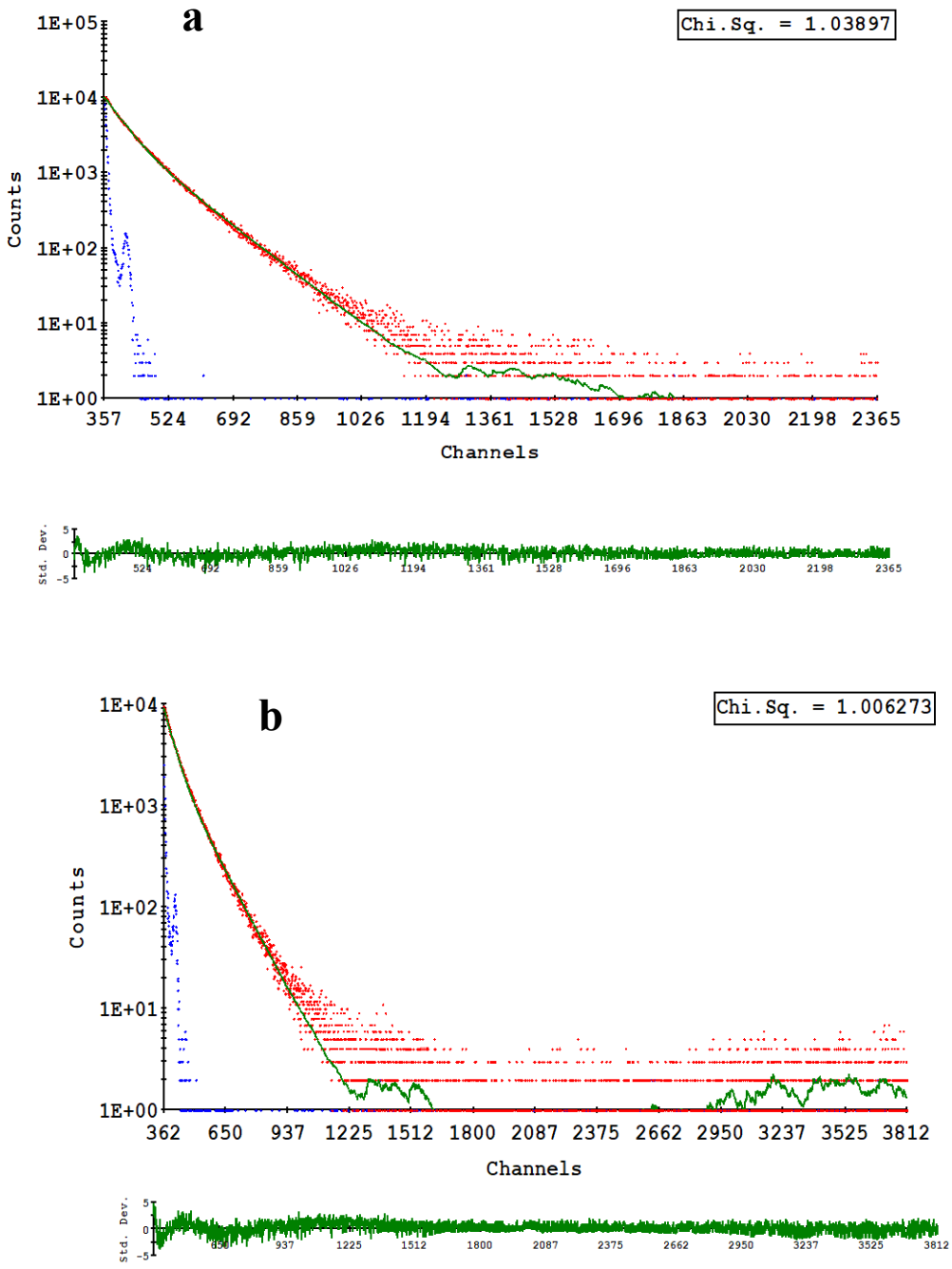

Figure 2. The fittings of the fluorescence decay curves of the free Cy3-SYL3C; (a) free Cy3-SYL3C and (b) free Cy3-SYL3C-cDNA.

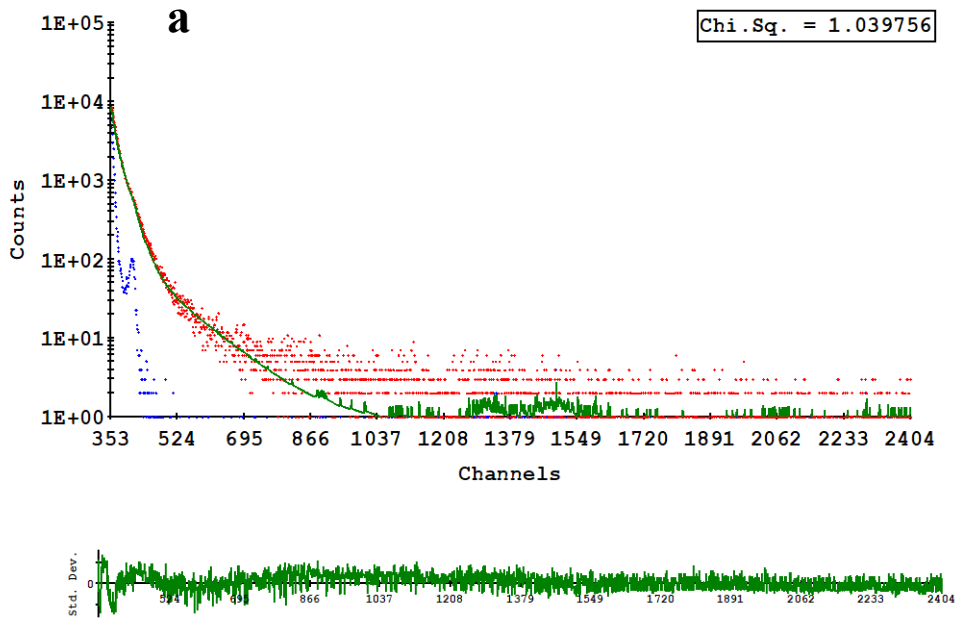
a
Chi.Sq. = 1.039756
Counts
1E+05
1E+04
1E+03
1E+02
1E+01
1E+00
353 524 695 866 1037 1208 1379 1549 1720 1891 2062 2233 2404
Channels
Std. Dev.
0

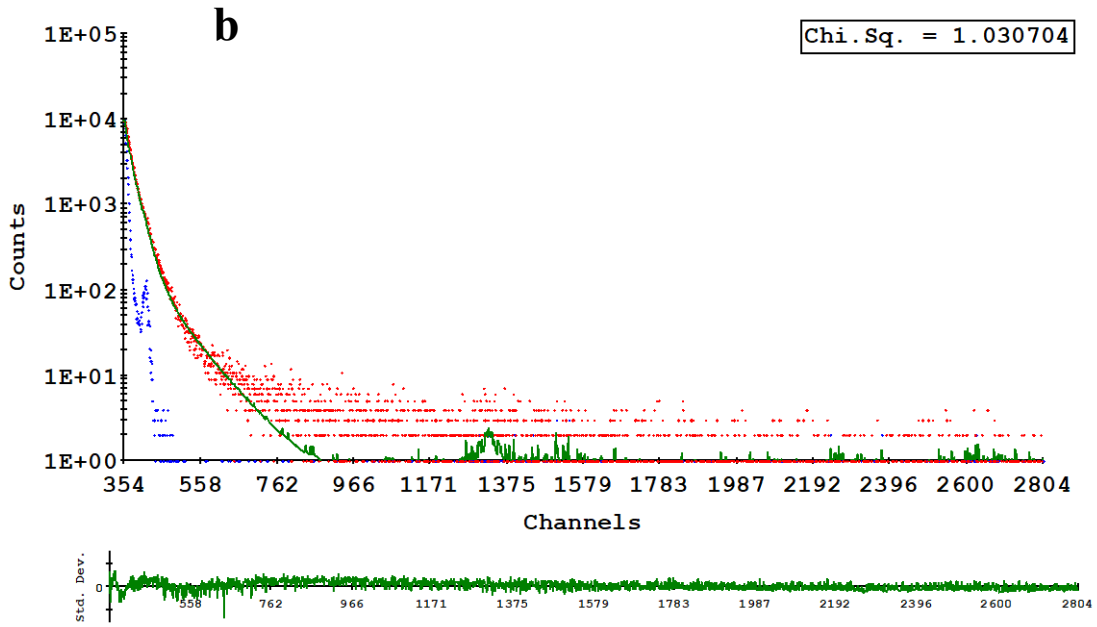
b
Chi.Sq. = 1.030704
Counts
1E+05
1E+04
1E+03
1E+02
1E+01
1E+00
354 558 762 966 1171 1375 1579 1783 1987 2192 2396 2600 2804
Channels
Std. Dev.
0

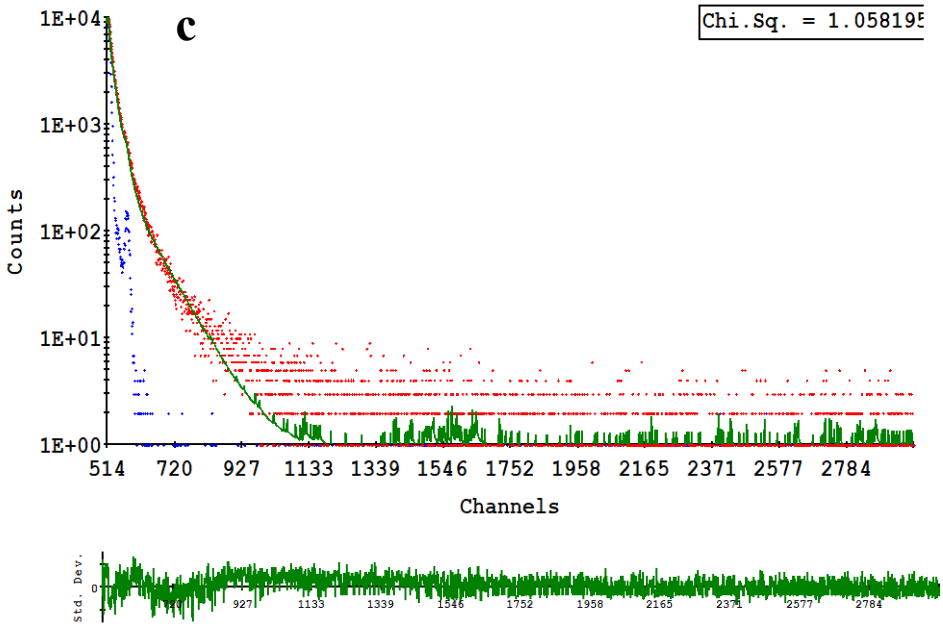
c
Chi.Sq. = 1.058195
1E+04
1E+03
1E+02
1E+01
1E+00
Counts
514 720 927 1133 1339 1546 1752 1958 2165 2371 2577 2784
Channels
Std. Dev.
0
927 1133 1339 1546 1752 1958 2165 2371 2577 2784

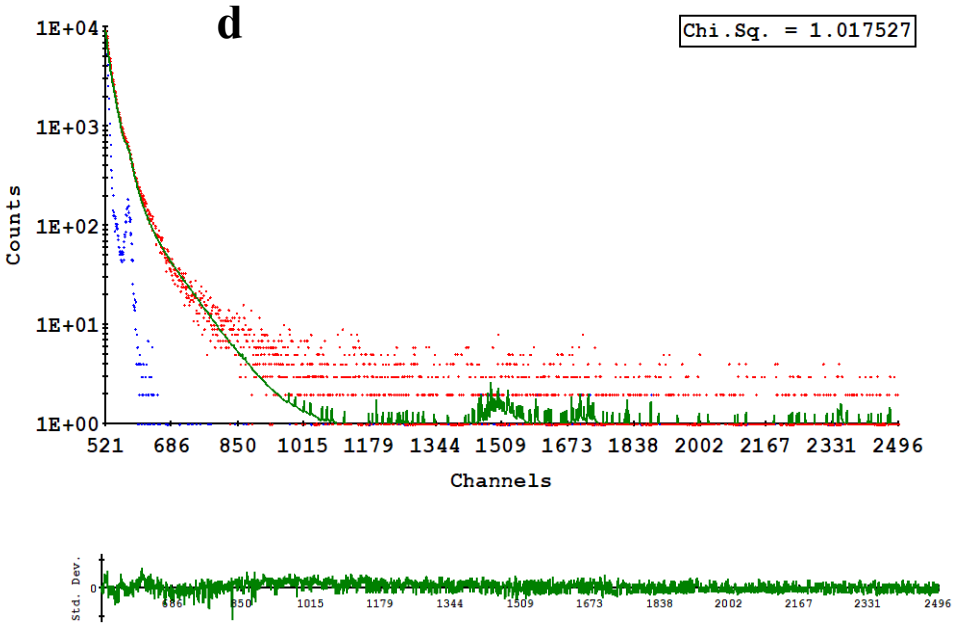
d
Chi.Sq. = 1.017527
1E+04
1E+03
1E+02
1E+01
1E+00
Counts
521 686 850 1015 1179 1344 1509 1673 1838 2002 2167 2331 2496
Channels
Std. Dev.
0
686 850 1015 1179 1344 1509 1673 1838 2002 2167 2331 2496

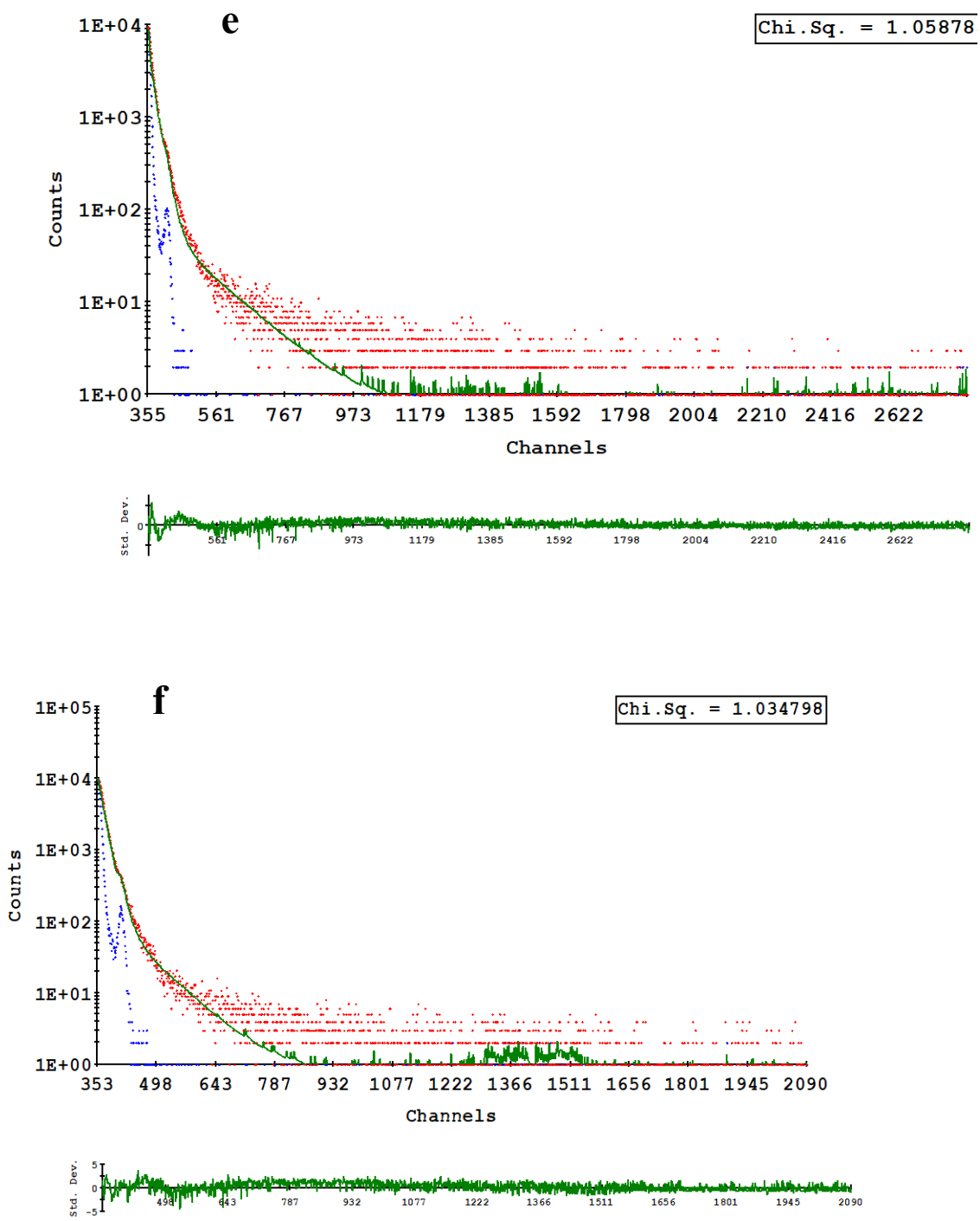

Figure 3. The fittings of the fluorescence decay curves of the SGNRs and LGNRs nanoprobes; (a) $SGNR_1$-SYL3C, (b) $SGNR_1$-SYL3C-cDNA, (c) $SGNR_2$-SYL3C, (d) $SGNR_2$-SYL3C-cDNA, (e) LGNR-SYL3C, (f) LGNR-SYL3C-cDNA,

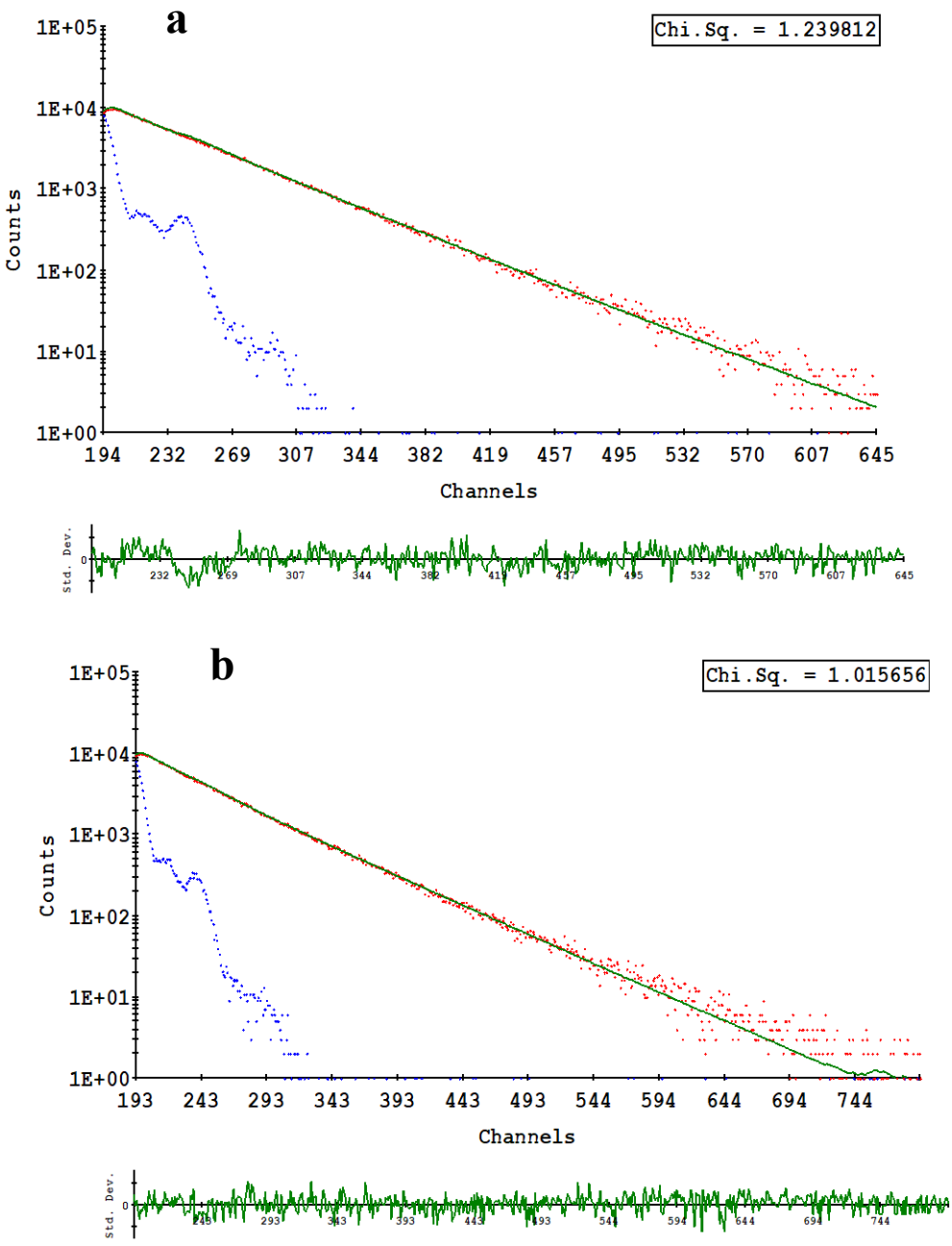
a
Chi.Sq. = 1.239812
Counts
1E+05
1E+04
1E+03
1E+02
1E+01
1E+00
194 232 269 307 344 382 419 457 495 532 570 607 645
Channels
Std. Dev.
0
b
Chi.Sq. = 1.015656
Counts
1E+05
1E+04
1E+03
1E+02
1E+01
1E+00
193 243 293 343 393 443 493 544 594 644 694 744
Channels
Std. Dev.
0

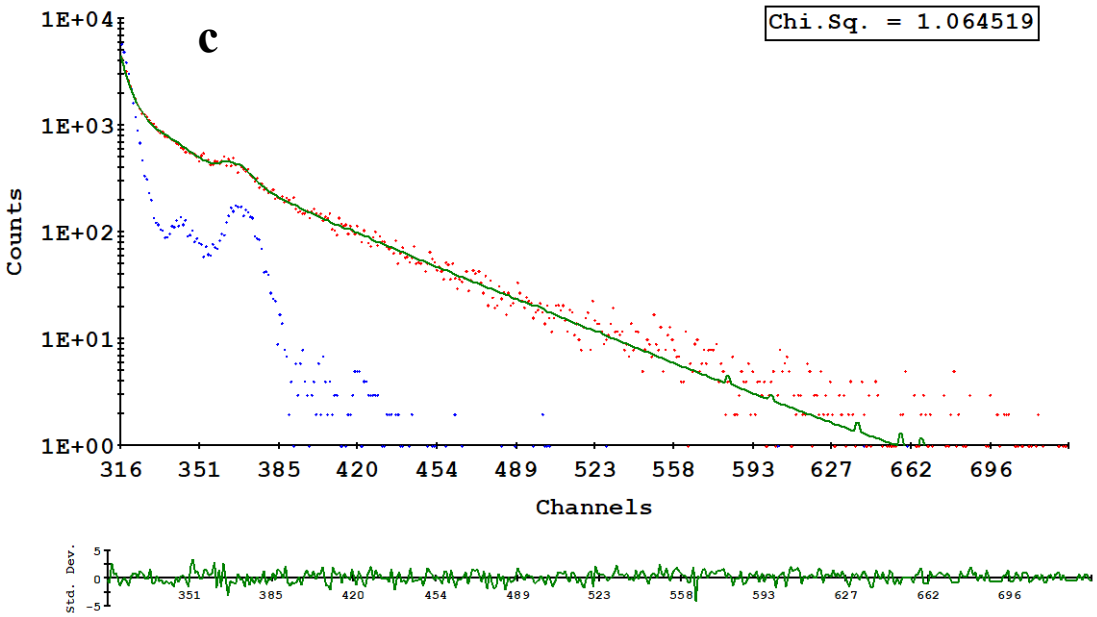
c
Chi.Sq. = 1.064519
1E+04
1E+03
1E+02
1E+01
1E+00
Counts
316 351 385 420 454 489 523 558 593 627 662 696
Channels
Std. Dev.
5
0
-5
351 385 420 454 489 523 558 593 627 662 696

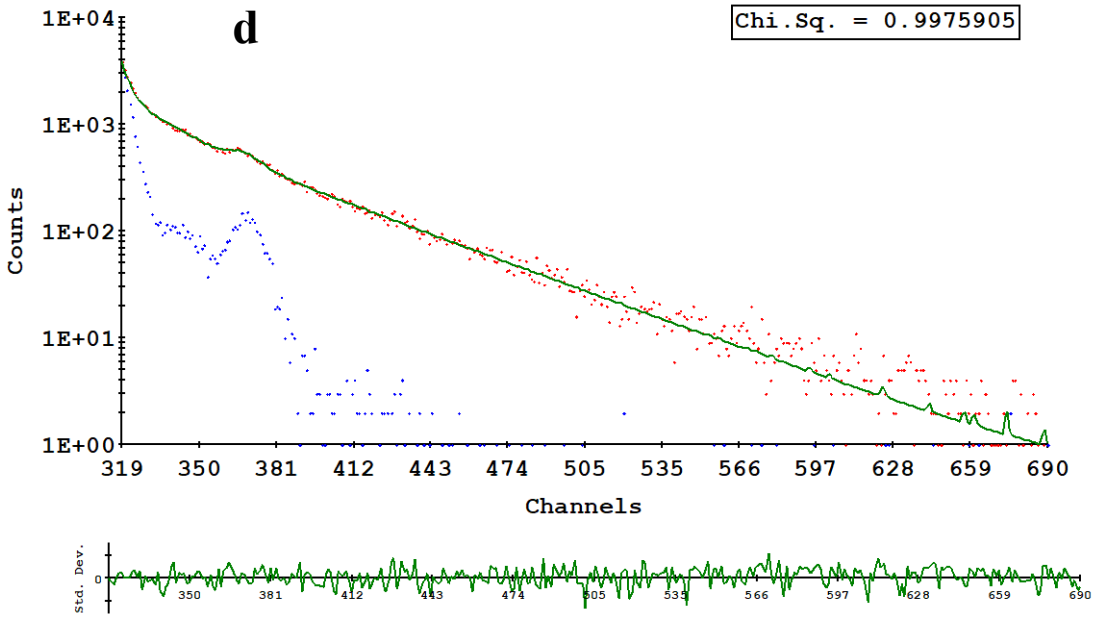
d
Chi.Sq. = 0.9975905
1E+04
1E+03
1E+02
1E+01
1E+00
Counts
319 350 381 412 443 474 505 535 566 597 628 659 690
Channels
Std. Dev.
0
350 381 412 443 474 505 535 566 597 628 659 690

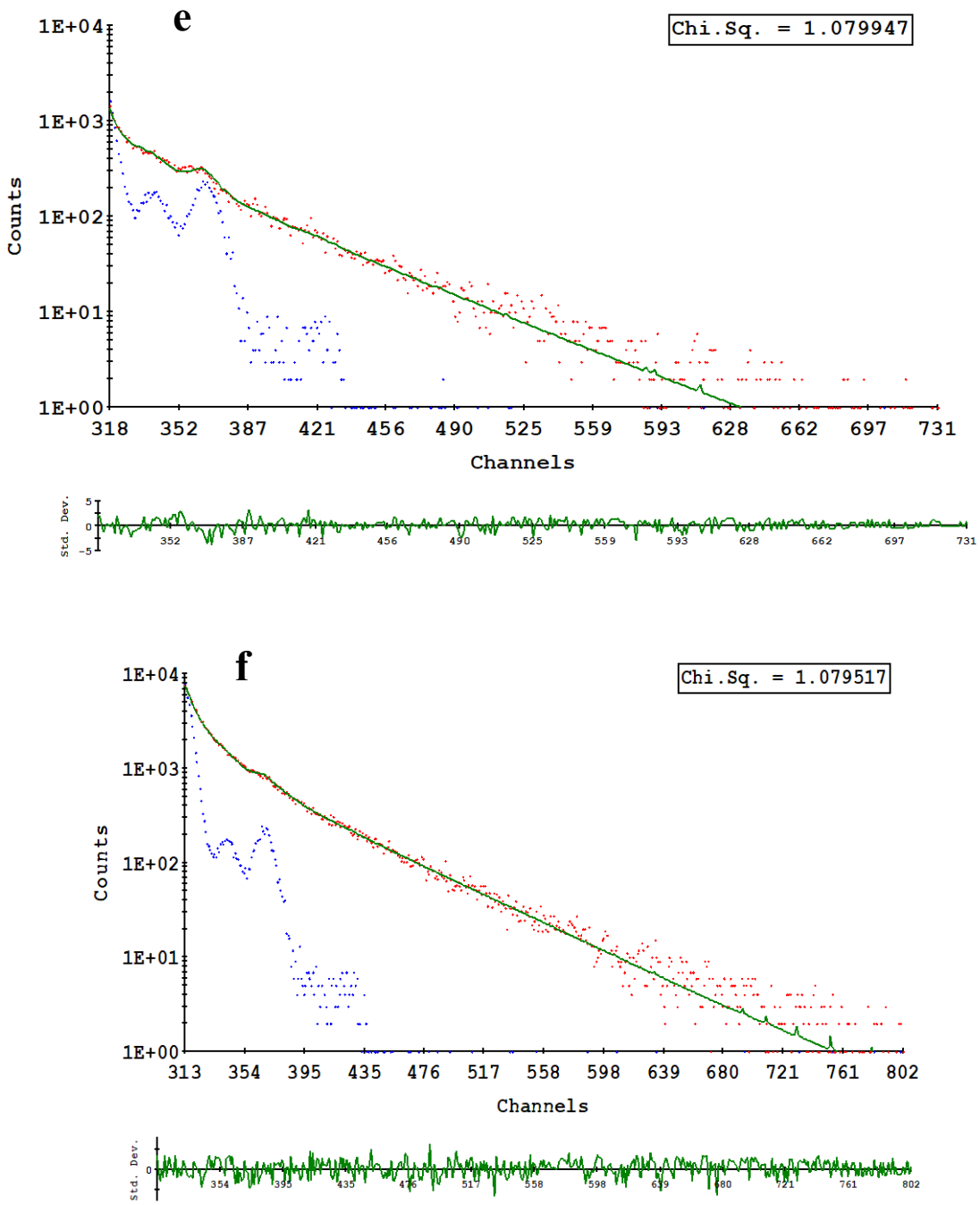

Figure 4. The fittings of the fluorescence decay curves of the free c-myc-Cy5-hpDNA LGNRs nanoprobe and SGNRs nanoprobe; (a) free c-myc-Cy5-hpDNA, (b) free c-myc-Cy5-hpDNA-cDNA, (c) $LGNR_2$- c-myc nanoprobe, (d) $LGNR_2$- c-myc nanoprobe-cDNA, (e) SGNR- c-myc nanoprobe, (f) SGNR- c-myc nanoprobe -cDNA.

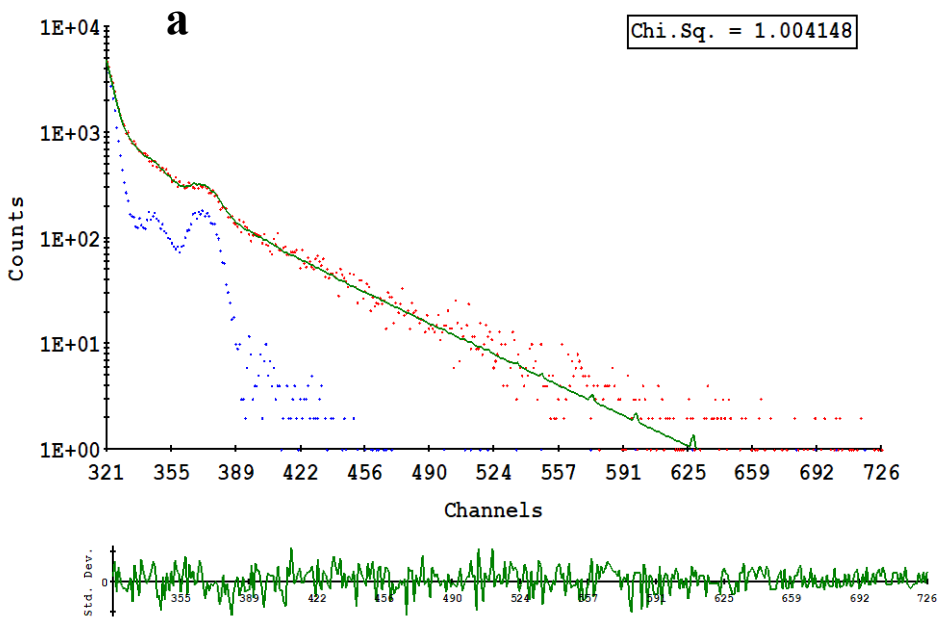
a
Chi.Sq. = 1.004148
1E+04
1E+03
1E+02
1E+01
1E+00
Counts
321 355 389 422 456 490 524 557 591 625 659 692 726
Channels
Std. Dev.
0
355 389 422 458 490 524 557 591 625 659 692 726

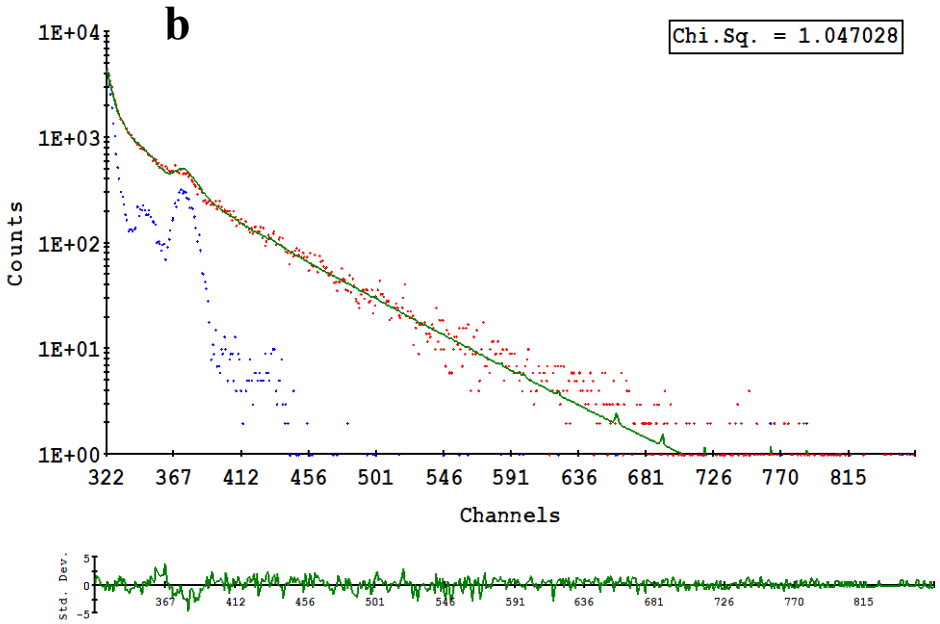
b
Chi.Sq. = 1.047028
1E+04
1E+03
1E+02
1E+01
1E+00
Counts
322 367 412 456 501 546 591 636 681 726 770 815
Channels
Std. Dev.
5
0
-5
367 412 456 501 546 591 636 681 726 770 815

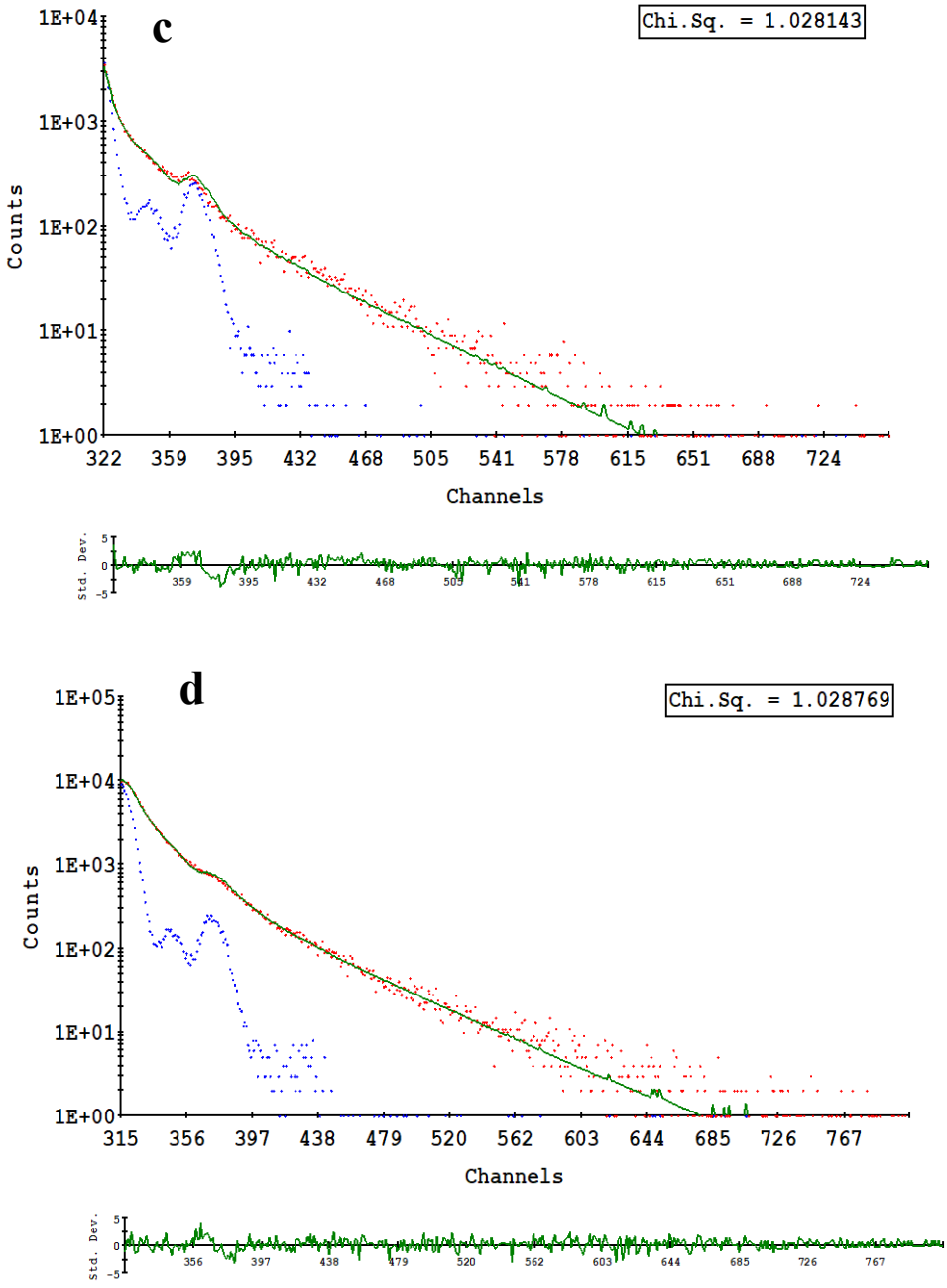

Figure 5. The fittings of the fluorescence decay curves of the LGNRs nanoprobe and SGNRs nanoprobe; (a) $LGNR_1$-LINC261 nanoprobe, (b) $LGNR_1$-LINC261 nanoprobe-cDNA, (c) SGNR-LINC261 nanoprobe, (d) SGNR-LINC261 nanoprobe -cDNA.